22 August 2008 | $10

Science

AAAS

Volume 321, Issue 5892

COVER

Using sunlight to rearrange the chemical bonds of water into hydrogen and oxygen, as in photosynthesis, would constitute a practical way to store solar energy as a fuel. Such an energy source will depend on new catalysts that promote this fuel-forming reaction cheaply and efficiently. See page 1072.

Photo illustration: Paul Montie (images: iStockphoto.com; Getty Images)

DEPARTMENTS

EDITORIAL

NEWS OF THE WEEK

NEWS FOCUS

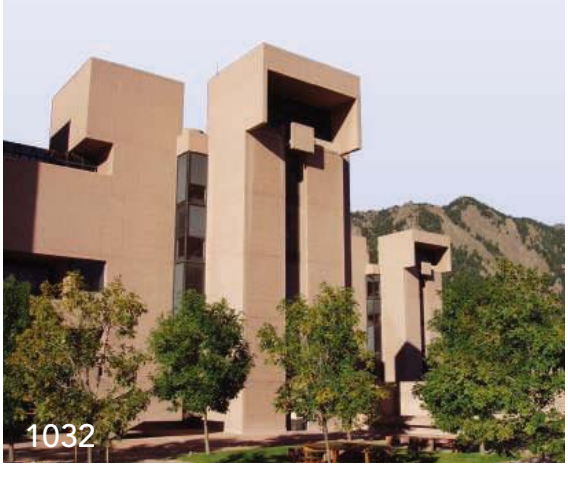

LETTERS

BOOKS *ET AL.*

1042

POLICY FORUM

PERSPECTIVES

CONTENTS continued >>

Science

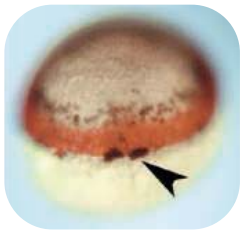

SCIENCE EXPRESS

www.sciencexpress.org

PHYSICS

Quantum Communication with Zero-Capacity Channels
G. Smith and J. Yard
Two quantum communication channels, each of which is so noisy that it has zero-capacity to independently transmit information, can do so when used together.
10.1126/science.1162242

CELL BIOLOGY

High-Quality Binary Protein Interaction Map of the Yeast Interactome Network
H. Yu et al.
Comparison of existing methods for mapping protein-protein interactions in yeast cells shows that the high-throughput approaches are complementary to one another.
10.1126/science.1158684

DEVELOPMENTAL BIOLOGY

Chemokine Signaling Controls Endodermal Migration During Zebrafish Gastrulation
S. Nair and T. F. Schilling
During zebrafish gastrulation, chemokines are required for integrin-dependent adhesion of endodermal cells to mesoderm, a role distinct from their action as chemoattractants.
10.1126/science.1160038

PHYSICS

Coupled Superconducting and Magnetic Order in $CeCoIn_5$
M. Kenzelmann et al.
Unlike other superconductors, magnetic ordering coexists with and is stabilized by superconductivity in the exotic superconductor CeCoIn.
10.1126/science.1161818

TECHNICAL COMMENT ABSTRACTS

PALEONTOLOGY

REVIEW

GEOLOGY

BREVIA

ATMOSPHERIC SCIENCE

REPORTS

ASTRONOMY

PHYSICS

MATERIALS SCIENCE

CONTENTS continued >>

REPORTS *CONTINUED...*

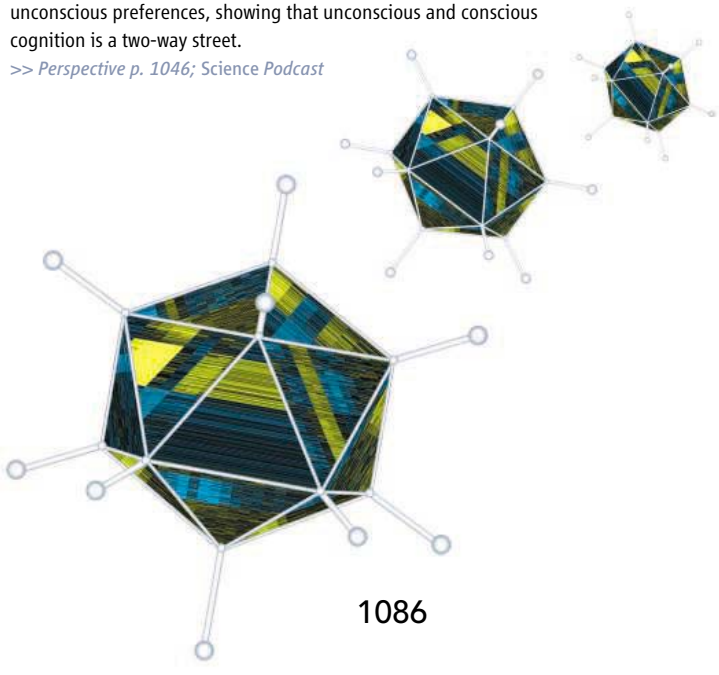

1086

AAAS
ADVANCING SCIENCE, SERVING SOCIETY

SCIENCE (ISSN 0036-8075) is published weekly on Friday, except the last week in December, by the American Association for the Advancement of Science, 1200 New York Avenue, NW, Washington, DC 20005. Periodicals Mail postage (publication No. 484460) paid at Washington, DC, and additional mailing offices. Domestic individual membership and subscription (51 issues): $144 ($74 allocated to subscription). Domestic institutional subscription (51 issues): $770; Foreign postage extra: Mexico, Caribbean (surface mail) $55; other countries (air assist delivery) $85. First class, airmail, student, and emeritus rates on request. Canadian rates with GST available upon request, GST #1254 88122. Publications Mail Agreement Number 1069624. SCIENCE is printed on 30 percent post-consumer recycled paper. **Printed in the U.S.A.**

Change of address: Allow 4 weeks, giving old and new addresses and 8-digit account number. **Postmaster:** Send change of address to AAAS, P.O. Box 96178, Washington, DC 20090–6178. **Single-copy sales:** $10.00 current issue, $15.00 back issue prepaid includes surface postage; bulk rates on request. The identification code for *Science* is 0036-8075. *Science* is indexed in the *Reader's Guide to Periodical Literature* and in several specialized indexes.

Printed on 30% post-consumer recycled paper.

CONTENTS continued **>>**

Head-turner.

SCIENCE**NOW**

www.sciencenow.org

HIGHLIGHTS FROM OUR DAILY NEWS COVERAGE

Oh, Brad, You're So . . . Symmetrical
Balanced bodies are more attractive, study shows.

Ancient Beavers Take Silver in Log-Chomping Olympics
Fossilized logs peg today's beavers as the true lumberjacks.

Sniffing for Mr. Right
Birth control could change a woman's sense of the perfect man.

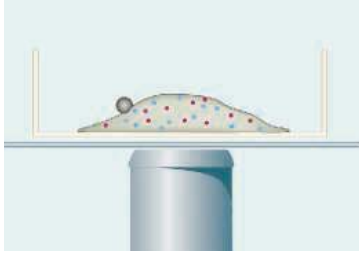

Measuring responses to mechanical force.

SCIENCE **SIGNALING**

www.sciencesignaling.org

THE SIGNAL TRANSDUCTION KNOWLEDGE ENVIRONMENT

PROTOCOL: Application of Fluorescence Resonance Energy Transfer and Magnetic Twisting Cytometry to Quantify Mechano-Chemical Signaling Activities in a Living Cell
S. Na and N. Wang
Get detailed instructions for delivering biologically relevant mechanical stress to individual cells and observing the intracellular signaling activities that ensue.

PRESENTATION: Defining Drug Targets in Yeast Haploinsufficiency Screens—Application to Human Translational Pharmacology
M. Roberge
Identifying targets of drugs in yeast using genome-wide drug-induced haploinsufficiency is a viable approach to predicting drug targets in humans.

A better retirement for scientists.

SCIENCE **CAREERS**

www.sciencecareers.org/career_development

FREE CAREER RESOURCES FOR SCIENTISTS

Tooling Up: Defying Gravity
D. Jensen
To succeed in science—especially in industry—intellectual brilliance may be necessary, but it's not sufficient.

A Comfortable Retirement
G. Sinha
European countries are working to improve pensions for mobile scientists.

***Science* Careers Poll Results: A Realistic Readership**
J. Austin
Grad students and postdocs are guardedly optimistic about their career prospects.

From the Archives: Choosing a Thesis Lab
S. Brass
For M.D./Ph.D. students, the thesis-lab choice poses special challenges.

SCIENCE**PODCAST**

www.sciencemag.org/multimedia/podcast

FREE WEEKLY SHOW

Download the 22 August *Science* Podcast to hear about a new strategy for developing antibiotics, predicting conscious decisions, updating a U.S. climate change model, and more.

CREDITS: (*SCIENCE NOW*) WILLIAM BROWN/BRUNEL UNIVERSITY; (*SCIENCE CAREERS*) PEDRO SIMÕES; (*SCIENCE SIGNALING*) PRESTON HUEY/*SCIENCE*

Separate individual or institutional subscriptions to these products may be required for full-text access.

EDITED BY STELLA HURTLEY

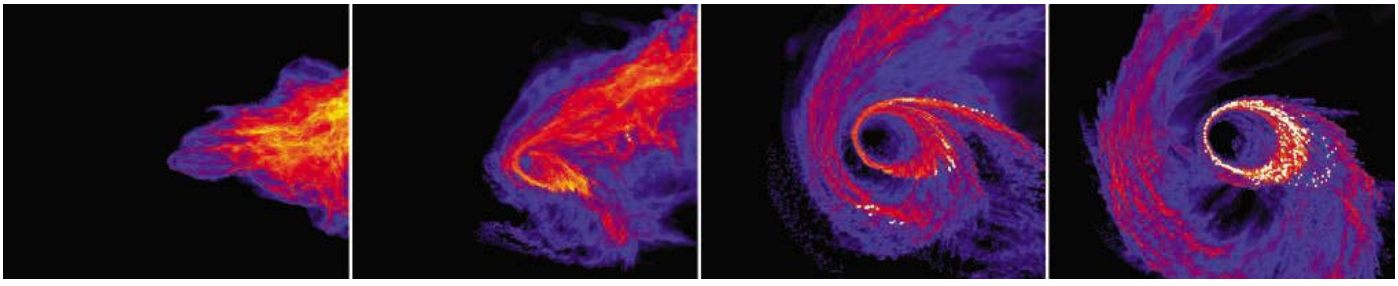

Black Hole Rising >> Our Galaxy contains a massive black hole, which was discovered by carefully observing the elliptical motions of stars around it. But this raises the questions of how did these stars get there, and why are they mostly massive stars? The black hole should have disrupted and consumed a molecular cloud from which such stars generally form, and capture of material from farther out seems unlikely. **Bonnell and Rice** (p. 1060; see the Perspective by **Armitage**) present a series of simulations that show that, although a molecular cloud is greatly disrupted by a black hole, sufficient gas remains to form a disrupted disk that can nucleate stars, and, under appropriate conditions, most of these become massive stars. These results thus explain the observations, confirm that the stars are indeed revealing a black hole, and provide an explanation for this type of star formation.

Tibetan Uprising

The Tibetan plateau, the highest extensive region on Earth, formed broadly in response to the collision of India with Asia. But the cause and timing of the uplift of the plateau have been difficult to resolve. **Royden *et al.*** (p. 1054; see the News story by **Kerr**) review the geologic history of the collision, focusing on Tibet, and propose that the history of the plateau is closely tied to tectonics in the Pacific. Before about 20 million years ago, Pacific and Indonesian trenches were migrating away from the Himalayan collision zone, which allowed some accommodation of the excess crustal mass produced by the collision. Once trench migration ceased or slowed, extensive uplift of Tibet commenced.

Circulating More

Earth's atmosphere receives more solar energy at low latitudes than at high latitudes, resulting in more heating near the equator than at the poles. Because such a thermal gradient cannot be maintained by the fluid atmosphere, poleward transport by atmospheric circulation redistributes heat to correct the imbalance. The conventional picture is that air rises predominantly in the tropics, within a structure known as a Hadley Cell, and begins its movement toward the poles at high altitudes. That view, however, is predicated on the representation of entropy that ignores the water content of the air. By considering atmospheric moisture, **Pauluis *et al.*** (p. 1075) show that considerably more air rises in the mid-latitudes than previously realized. The resulting mass transport by atmospheric circulation is nearly twice the canonical value, with as much as half of the air ascending into the upper troposphere doing so in the mid-latitudes.

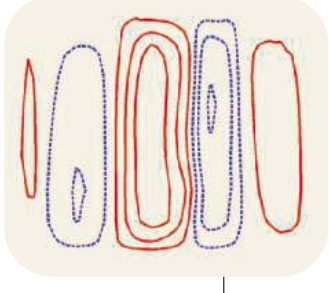

Cs_2 Unspun

Rotational and vibrational degrees of freedom have hampered full cooling of molecules required for the formation of Bose Einstein condensates (BECs), which can now be achieved regularly with atomic samples. **Danzl *et al.*** (p. 1062, published online 10 July) show that by using a coherent Raman pumping scheme, discrete packets of energy can be removed from loosely bound cesium dimers in an atomic BEC to create tightly bound, translationally cold Cs_2 molecules in specific rotational-vibrational levels of the electronic ground state. The experiment effectively removes all rotational excitation, but leaves in vibrational energy that could possibly be dissipated in a second pumping cycle. Key to the technique is preservation of phase coherence between two pumping lasers tuned to substantially different frequencies, achieved by referencing to a frequency comb.

Fine Wire Finesse

An electron-current can drive atomic diffusion, a process known as electromigration. In very small copper wires, this can lead to the formation of voids or breaks in a wire, which presents a significant problem in modern electronics. Using in situ electron microscopy, **Chen *et al.*** (p. 1066) find that the electromigration process can be influenced by the presence of specific microstructural features. Atomic diffusion is significantly reduced where a twinned grain meets a grain boundary. At this junction, new steps on the crystal need to form for migration to occur, which adds an incubation or nucleation time to the process. It is thus possible that the lifetime of fine copper wires can be improved by engineering crystal grains in copper wires.

Jam the Signal

Many bacterial pathogens sense that they are in a potential host because they can detect adrenergic molecules. These organisms share a sensor kinase that picks up the signal and relays it to virulence gene loci, thus kicking in the responses needed to ensure bacterial establishment. This pathway makes a good target for broad spectrum antibiotic development because virulence inhibition should not present a strong selective pressure for resistance. **Rasko *et al.*** (p. 1078) have had some success with this approach using a non-toxic small molecule inhibitor of the sensor kinase QseC, which blocks signaling in a sensitive and specific manner. In animal models, the inhibitor was somewhat effective against gastrointestinal infections with enterohemorrhagic *Escherichia coli* and *Salmonella typhimurium*. Encouragingly, the lead molecule was more effective against the systemic pathogen *Francisella tularensis*: A single oral dose protected 80% of infected mice from death.

CREDITS (TOP TO BOTTOM): BONNELL AND RICE; PAULUIS *ET AL.*

Fixed But Flexible

To what extent is stochastic noise responsible for phenotypic variability in biological systems? **Feinerman *et al.*** (p. 1081) combine computer modeling with measurements of expression levels of multiple proteins required for signaling in populations of T cells, along with the response of the same cells to antigenic stimulation. Together, these revealed how stochastic variation in expression of different components of antigen-induced signaling pathway had distinct effects on the response potential of T cells. For a clone of T cells responding to a given antigen, this could help by optimizing flexibility within the responding cell population, while maintaining the overall uniformity required for reliable antigen discrimination.

The Making of a Centromere

Centromeres play a critical role during cell division in ensuring that eukaryotic chromosomes are evenly distributed between daughter cells. How and where centromeres form on chromosomes remains something of a mystery, because during evolution new centromeres seem to have arisen independently of the underlying DNA sequence. **Ishii *et al.*** (p. 1088) developed a system for generating new centromeres at will in fission yeast, by snipping out the existing centromere from one of the three chromosomes. Survivors of this generally fatal event were found either to form a new centromere at one of the subtelomeric regions of the eviscerated chromosome, or to fuse the aberrant chromosome with another chromosome. The formation of new centromeres required components of the RNA interference machinery.

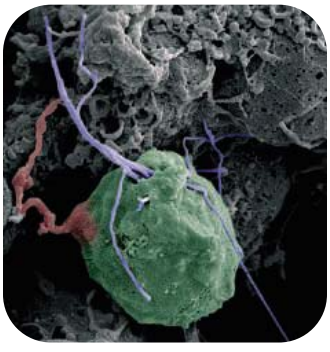

Sensing Alarm

In 1973, Hans Grueneberg observed the presence of a structure at the tip of the rodent nose that, he thought, belonged to the Nervus terminalis. Recently, using transgenic techniques, several groups reported the rediscovery of this structure. They named this structure the Grueneberg ganglion in memory of the original work. However, the function of these cells remains a matter of controversy. Despite the lack of typical olfactory neuronal features, the ganglion was suggested to have some olfactory function, based on the expression of olfactory marker protein and on its neural connections to the olfactory bulb of the brain. **Brechbühl *et al.*** (p. 1092) have now identified a function for the Grueneberg ganglion cells. A combination of anatomical, surgical, and behavioral techniques were used to suggest that the Grueneberg ganglion is involved in alarm pheromone detection.

To Divide or Not to Divide

Cells can stop dividing and remain in a nonproliferative state (like most differentiated cells in an organism), but, under some conditions, the cells can reenter the cell division cycle and begin to proliferate again. **Sang *et al.*** (p. 1095) provide evidence that a transcriptional repressor known as Hairy and Enhancer of Split1 (HES1) has an important role in determining whether or not a cell can resume cell division. When proliferation of human fibroblast cells in culture was inhibited, reduction of HES1 activity prevented cells from reinitiating cell division once the block to proliferation was removed. Inappropriate reentry into the cell cycle is a property of tumor cells, and treatments that inhibited Hes1 function in skeletal muscle tumor cells also inhibited proliferation and promoted differentiation.

Deciding the Undecided

How do our unconscious biases affect rational decision-making, and can the decisions we make affect these biases? **Galdi *et al.*** (p. 1100; see the Perspective by **Wilson and Bar-Anan**) find in a longitudinal study of voting intentions in a population of voters that, as expected, the conscious beliefs of already-decided voters predict the choices that they made when quizzed again at a later date, and that the automatic associations of undecided voters likewise predicted their choices later on. Surprisingly, however, the conscious beliefs of the decided voters, which, at the first question period, showed no correlation with their automatic or implicit preferences, did, in fact, predict their implicit preferences during the second session, suggesting that the interaction between unconscious and conscious cognition is a two-way street.

CREDIT: BRECHBÜHL *ET AL.*

Donald Kennedy is Editor Emeritus of *Science*.

Science and Security, Again

THE STRUGGLE BETWEEN OPEN SCIENCE AND NATIONAL SECURITY IS AN OLD STORY. BACK IN 1981, government attempts to limit foreign visitors to U.S. laboratories and control access to fundamental research projects led to widespread academic anger. The Department of Defense–Universities Forum in the early 1980s, of which I was co-chair, struggled to resolve difficulties presented by applications (for example, of international arms traffic regulations) to withhold access to basic, nonmilitary research. For years, only limited gains were made, but in 1985, to everyone's surprise, President Ronald Reagan ended this long-running controversy by executing National Security Decision Directive (NSDD) 189. NSDD 189 provided that only classification could be used to limit the disclosure of basic research results. It was a stunning policy shift that delighted the scientific community.

Well, we now find ourselves in a post-9/11 world and are learning that even good things don't last forever. Scientists now live in a strange alternative universe. On the one hand, Secretary of State Condoleezza Rice, during her earlier term as the National Security Advisor, announced that NSDD 189 still applied to basic research. But in this new security-conscious environment, that principle came to be honored primarily in the breach; soon scientists were complaining right and left that "Sensitive But Unclassified" (SBU) designations were being used to restrict publication. *Science* published accounts of this epidemic of faux classification in its News section and on the Editorial page, emphasizing the ambiguity under which the scientific community must labor. Restrictions short of classification were absolutely not permitted—but they were all over the place!

A number of universities were uncomfortable enough about this to attempt some documentation of the difficulties. For example, in 2004, a 20-institution task force of the Association of American Universities and the Council on Governmental Relations was charged to identify contract and grant language inconsistent with the stated policy embodied in NSDD 189. They combed their records and found many cases of publication restrictions, limitations on the access of foreign nationals to fundamental research projects, and others; amounting to 138 instances in total. In some cases, the differences were negotiated out; in others, the universities accepted the restrictions; and in many, the universities simply decided not to do the research. Last month, the task force released its 2007 follow-up survey and report, indicating 180 such instances.

In 2005, a commission jointly organized by the Department of Homeland Security program of the Center for Strategic and International Studies—not an organization notably soft on security—issued a white paper in which it strongly recommended that NSDD 189 be the central and only provision regarding security controls over fundamental research. It added strong advice to the effect that implementation should be done carefully so as to "avoid incursions on openness." Late last year, a National Academies committee issued *Science and Security in a Post-9/11 World*, an excellent report on the present status. The committee's co-chairs, Alice Gast and Jacques Gansler, summarized these findings last month in the *Chronicle of Higher Education*.

Although it's clear that some of the old problems are still with us, there is some really good news about the future. Secretary of Defense Robert M. Gates recently undertook a review of the situation. The result was a tough memorandum this June from John J. Young Jr., the undersecretary of Defense responsible for acquisition. Young's memo fully endorsed NSDD 189 and supplied blunt "clarifying guidance" to Department of Defense (DOD) officers and units. The basic message is that SBU is dead on arrival and that compliance with NSDD 189 is the order of the day.

Secretaries Rice and Gates deserve the thanks of the scientific community for upholding the central principle of NSDD 189. The tough procedural talk from Undersecretary Young should end the practice whereby middle-level officials can invent restrictive categories to reflect their individual convictions about security. So if your next research grant or contract from the DOD should turn up with a publication restriction based on SBU, you might write Undersecretary Young about it, and then see if anything happens. It should.

– Donald Kennedy

10.1126/science.1163738

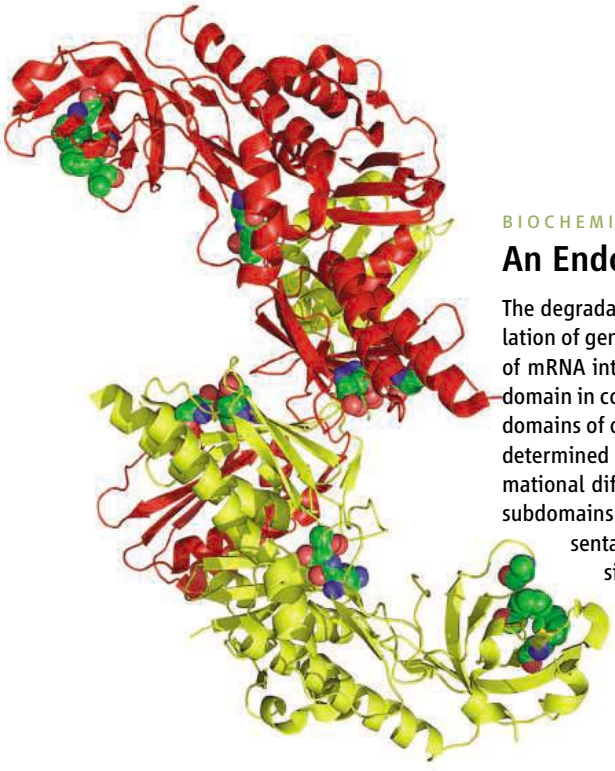

BIOCHEMISTRY

An Endonuclease Tango

The degradation of mRNA transcripts is an important cellular mechanism contributing to the regulation of gene expression. In *Escherichia coli*, the first step of this process involves internal cleavage of mRNA into fragments by the endoribonuclease RNase E. The structure of the RNase E catalytic domain in complex with short RNA substrates revealed a tetramer in which RNA is bound by two subdomains of one monomer and cleaved at the catalytic site of another monomer. Koslover *et al.* have determined the structure of the unliganded RNase E catalytic domain and discovered large conformational differences relative to the substrate-bound protein. In the unliganded structure, the two subdomains of each monomer that furnish the RNA binding residues (shown in space-filling representation) are rotated away from the rest of the monomer and from the neighboring catalytic site by about 60°, which allows the substrate easy access. Pivoting then carries the RNA into close proximity to the catalytic site. In addition, the quaternary structure of the tetramer is substantially reorganized in unliganded RNase E, suggesting a high degree of structural flexibility that may permit the enzyme to accommodate RNA molecules of various sizes and shapes by using different combinations of binding and catalytic sites within the tetramer. — NM*

Structure **16**, 1238 (2008).

NEUROSCIENCE

Storing the Latest Update

How memories are formed and stabilized has been a central question for decades. Recent research has shown that reactivating apparently stable memories can render them fragile and open to modification and to another round of stabilization in a process called reconsolidation. Hupbach *et al.* explored the conditions leading to the updating of episodic memory. They found that memory plasticity at reactivation provides a mechanism for updating memories, and that the latter are determined by the spatial context; that is, the "where" of episodic memory. Only when the memory was reactivated in the same context as when it was learned could new learning be incorporated into the existing store of knowledge; if reactivated in a new context, no updating occurred. — PRS

Learn. Mem. **15**, 574 (2008).

SYSTEMS BIOLOGY

Be My Partner?

Although evolutionary pressures may alter the spatial and temporal aspects of gene expression and thus dictate whether the proteins encoded by these genes have the opportunity to recognize each other, protein-protein interactions may in fact be mediated through largely independent modular domains. To date, most network mapping studies have been based on the whole protein as the unit. Boxem *et al.* have begun a long-term project to build interactome maps derived from protein domains. They describe a resource of 800 early-embryogenesis proteins that are present after the first two cell divisions in *Caenorhabditis elegans*. They systematically fragmented the open reading frames to create a library of yeast two-hybrid fusions; multiple fragments of each protein were generated to minimize the possibility of missing an interaction because the fusion products had not folded properly. Taking the fragment out of its native protein context did not result in promiscuous liaisons but increased the ability to detect interactions, which confirmed those already reported in the literature via other means. New interactions were also identified, and because they tended to connect proteins with similar phenotypes and functional annotations, will probably be functionally relevant. Minimum regions of interaction (defined as the smallest region shared by all interacting fragments) were studied in 200 proteins, and interaction maps within two molecular complexes—the nuclear pore and the centrosome—were assembled. — BJ

Cell **134**, 534 (2008).

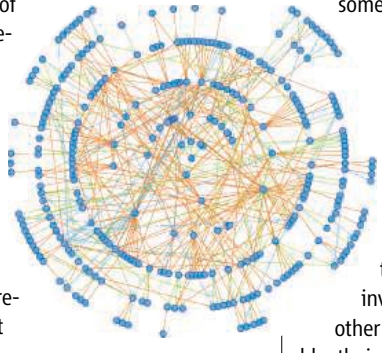

A network graph of early-embryo proteins.

CHEMISTRY

Stable Pyramids

Lead sulfide commonly crystallizes into cubes, dominated by the stability of the {100} faces, with the occasional formation of an octahedron or tetrahedron that involves the growth of {111} faces. Though other growth faces such as the {113} are possible, their much lower stability means that they are not observed during fast crystallization processes. Fan *et al.* combined a toluene solution of lead diethyldithiocarbamate with an aqueous solution containing a slight stoichiometric excess of sodium sulfide. At the interface, they observed the slow growth of upright pyramids of PbS with only {113} facets. The pyramids were uniform in size and randomly distributed across the water/toluene fluid interface, as a result of the capillary and van der

*Nilah Monnier is a summer intern in *Science*'s editorial department.

CREDITS (TOP TO BOTTOM): KOSLOVER *ET AL.*, *STRUCTURE* **16**, 1238 (2008); BOXEM *ET AL.*, *CELL* **134**, 534 (2008)

Waals forces overcoming the intrinsic dipolar repulsion of the highly charged crystals. The authors believe that at the interface, an emulsive supersaturated layer forms, which serves as the growth medium for the pyramids and also limits the number of growth directions. They found that the height of the toluene column was critical in determining the type of crystal that formed, thus offering an additional variable to consider for the growth of kinetically unfavored crystal habits. — MSL

J. Am. Chem. Soc. **130**, 10892 (2008).

MATERIALS SCIENCE

An Inside View of Foam

From lending texture to a perfect pint, to mediating fluid flow in porous rock, and even capturing space dust in the wake of a comet, foams have a diverse set of mechanical properties, geometrical structures, and applications. Their

Aerogel.

remarkable strength-to-weight ratio makes them sought after as physical supports, with their large surface area making them ideal scaffolds for catalytic applications. They tend to be rather delicate, however, and the mechanisms whereby the various structures form and then limit the resulting physical properties have not been clear. Barty *et al.* use coherent x-ray diffraction to provide a detailed three-dimensional image of the internal structure of the highly porous form of tantalum oxide known as aerogel, often described as "frozen smoke." Combining the exquisite structural information with detailed simulations, they show that the observed blob-and-beam network structure explains why the materials are weaker than expected. Such insight offers a route toward improving the properties through better control of the preparation process. — ISO

Phys. Rev. Lett. **101**, 55501 (2008).

IMMUNOLOGY

An Entrapment Defense

Eosinophils are white blood cells that play a critical role in protecting vertebrates from parasitic infections and also are believed to participate more broadly in immune defense. Yousefi *et al.* suggest that eosinophils serve to protect the gastrointestinal tract from unwanted bacterial invaders, and they do so by engaging an unusual mechanism. Analyzing colon tissue from patients with Crohn's disease (a chronic intestinal inflammatory disorder), they found that a subset of the infiltrated eosinophils were associated with extracellular structures that contained DNA and eosinophil-derived granule proteins. In vitro studies revealed that when treated with lipopolysaccharide from bacterial pathogens, eosinophils released their mitochondrial DNA in an explosive fashion. This DNA release was dependent on priming of the cells with cytokines and resulted in rapid death of cocultured bacteria, although the eosinophils themselves remained viable. Mice that had been manipulated genetically to overproduce eosinophils displayed similar extracellular structures in their intestine in response to surgically induced sepsis, and they survived longer than control mice. Thus, these eosinophil-derived structures appear to trap and kill bacterial invaders in the gut. Other researchers had shown previously that neutrophils and mast cells also produce extracellular traps with antimicrobial activity, but in those instances the expelled DNA was nuclear rather than mitochondrial, and that strategy resulted in the death of the immune cells. — PAK

Nat. Med. **14**, 10.1038/nm.1855 (2008).

MICROBIOLOGY

Trawling Hidden Waters

Lake Vostok is a vast lake currently buried under a 4-km-thick glacier in Antarctica; it has long been an object of curiosity to microbiologists. What could possibly live at −2°C, under 400 atm, in complete darkness, and with few available nutrients? D'Elia *et al.* have anticipated the delayed breakthrough by the Russian drilling team in their microbiological examinations of the frozen lake surface that has accreted on the underside of the glacier. They were surprised to discover that more than 60 taxa of cold-tolerant bacteria grew in their long-term cultures, all related to known environmental species. Microscopy revealed algal cells and evidence of fungi. Because a variety of samples were taken, distinct ecological zones could also be distinguished. Despite these apparent riches, there were still far fewer organisms in the lake ice than in other environments on Earth. When the Russian team do bore through the entire ice sheet, they are very unlikely to find a microbiological paradise, unless it is one they have brought with them. — CA

Appl. Environ. Microbiol. **74**, 4962 (2008).

CREDIT: AIMEE WHALEN, RON BAALKE, JAMES D. ROSE/STARDUST OUTREACH TEAM/JPL/NASA

www.sciencemag.org

Science

1200 New York Avenue, NW
Washington, DC 20005
Editorial: 202-326-6550, FAX 202-289-7562
News: 202-326-6581, FAX 202-371-9227
Bateman House, 82-88 Hills Road
Cambridge, UK CB2 1LQ
+44 (0) 1223 326500, FAX +44 (0) 1223 326501

Subscription Services For change of address, missing issues, new orders and renewals, and payment questions: 866-434-AAAS (2227) or 202-326-6417, FAX 202-842-1065. Mailing addresses: AAAS, P.O. Box 96178, Washington, DC 20090-6178 or AAAS Member Services, 1200 New York Avenue, NW, Washington, DC 20005

Institutional Site Licenses please call 202-326-6755 for any questions or information

Reprints: Author Inquiries 800-635-7181
Commercial Inquiries 803-359-4578

Permissions 202-326-7074, FAX 202-682-0816

Member Benefits AAAS/Barnes&Noble.com bookstore www.aaas.org/bn; AAAS Online Store http://www.apisource.com/aaas/ code MKB6; AAAS Travels: Betchart Expeditions 800-252-4910; Apple Store www.apple/eppstore/aaas; Bank of America MasterCard 1-800-833-6262 priority code FAA3YU; Cold Spring Harbor Laboratory Press Publications www.cshlpress.com/affiliates/aaas.htm; GEICO Auto Insurance www.geico.com/landingpage/go51.htm?logo=17624; Hertz 800-654-2200 CDP#343457; Office Depot https://bsd.officedepot.com/portalLogin.do; Seabury & Smith Life Insurance 800-424-9883; Subaru VIP Program 202-326-6417; VIP Moving Services http://www.vipmayflower.com/domestic/index.html; Other Benefits: AAAS Member Services 202-326-6417 or www.aaasmember.org.

science_editors@aaas.org	(for general editorial queries)
science_letters@aaas.org	(for queries about letters)
science_reviews@aaas.org	(for returning manuscript reviews)
science_bookrevs@aaas.org	(for book review queries)

Published by the American Association for the Advancement of Science (AAAS), *Science* serves its readers as a forum for the presentation and discussion of important issues related to the advancement of science, including the presentation of minority or conflicting points of view, rather than by publishing only material on which a consensus has been reached. Accordingly, all articles published in *Science*—including editorials, news and comment, and book reviews—are signed and reflect the individual views of the authors and not official points of view adopted by AAAS or the institutions with which the authors are affiliated.

AAAS was founded in 1848 and incorporated in 1874. Its mission is to advance science, engineering, and innovation throughout the world for the benefit of all people. The goals of the association are to: enhance communication among scientists, engineers, and the public; promote and defend the integrity of science and its use; strengthen support for the science and technology enterprise; provide a voice for science on societal issues; promote the responsible use of science in public policy; strengthen and diversify the science and technology workforce; foster education in science and technology for everyone; increase public engagement with science and technology; and advance international cooperation in science.

Information for Authors
See pages 634 and 635 of the 1 February 2008 issue or access www.sciencemag.org/about/authors

EDITED BY CONSTANCE HOLDEN

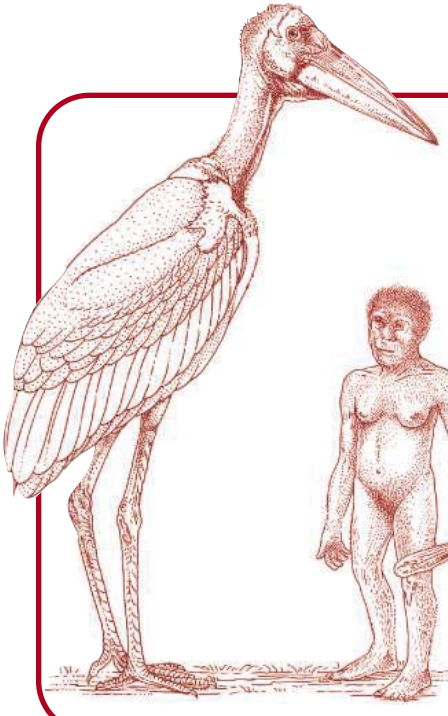

Who Ate Whom?

Big leg bones from the Indonesian island of Flores show that the meter-high "hobbit" people (*Homo floresiensis*) who once lived there shared the island with enormous flesh-eating storks, researchers say. Hanneke Meijer of the National Museum of Natural History in Leiden, the Netherlands, and Rokus Awe Due of the Indonesian Centre for Archaeology in Jakarta found the bones in Liang Bua cave in the same layers as the hobbits—dated to at least 18,000 years ago. They identified them as a new species of extinct giant marabou. The scientists say the 1.8-meter-tall bird was a carnivore and top predator on the island; whether hobbits were among its fare is open to speculation. They reported on the find this week at the meeting of the Society of Avian Paleontology and Evolution in Sydney, Australia.

Batterers' Brains

Scientists have now turned their brain-imaging equipment on a particularly troublesome population: wife-beaters.

In a paper published last month in *Molecular Psychiatry*, criminologist Adrian Raine of the University of Pennsylvania and colleagues in Hong Kong report that spouse abusers' brains have unusually strong reactions to emotional stimuli.

They studied 10 Chinese men referred by police or welfare agencies for repeatedly hitting, choking, pushing, or throwing things at their wives. The researchers compared them with 13 men who had never hit their wives, matched for age, level of education, and years of marriage. The subjects performed both cognitive and emotional tasks while their brains were being scanned.

The two groups showed no differences on the cognitive task, but emotionally it was a different story. In the test, which monitored reactions to either neutral words or aggressive words such as "kill," the cognitive brain areas related to control over emotions reacted to aggressive words less in the wife-beaters than in the controls; at the same time, their emotional brain areas responded more. The researchers speculate that wife-beaters may have "insufficient prefrontal regulatory resources" to rein in their own violent reactions to negative situations.

The finding "makes sense," says psychologist Nelly Alia-Klein of Brookhaven National Laboratory in Upton, New York, who also does brain-imaging studies of aggression. "It really brings attention to the study of domestic abuse from the disease-model perspective," she says, and may help spur research on drugs to target impairments in emotional regulation.

Secrets of a Green Sahara

About 5300 years ago, near the center of modern-day Niger, a woman and two children died; how it happened is unclear. They were buried carefully, on a bed of flowers—the woman, the 8-year-old, and the 5-year-old cuddled in a last embrace.

Millennia later, paleontologist Paul Sereno of the University of Chicago in Illinois and his team were looking for dinosaurs when they discovered the trio's remains. "It brought tears to our eyes," Sereno said at a press event held last week at the National Geographic Society in Washington, D.C. Carbon dating revealed they were Tenerians, who lived in Gobero when the Sahara was a lush savanna. Further excavation revealed an entire cemetery—the Sahara's largest. The team also found the remains of Kiffians, who lived in the area 5000 years earlier, Sereno said.

The Gobero site also contained pottery shards, flower pollen, jewelry, and fossils that should help scientists fill out the picture of both groups. For example, skull measurements show that Kiffians stood more than 2 meters tall. And marks left by muscle attachments reveal that the Tenerians and Kiffians were fairly healthy, said Christopher Stojanowski, a bioarchaeologist at Arizona State University in Tempe. Findings were reported last week in *PLoS ONE*.

MOTORMOUTH

Meet AnTon, so named for its animatronic tongue. Built by doctoral student Robin Hofe of the University of Sheffield, U.K., and his adviser Roger K. Moore, the device consists of a plastic skull and silicon tongue, both cast from human counterparts, and various filaments and motors that seek to duplicate the musculature and movement needed for speech.

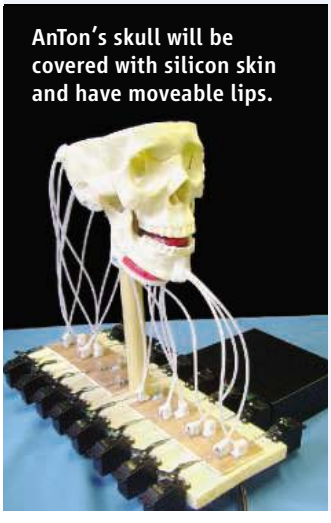

AnTon's skull will be covered with silicon skin and have moveable lips.

AnTon won't be able to make any noise until Hofe closes up the back to create a vocal cavity. But the tongue, which is embedded with wire mesh to allow attachment of "muscles," can already move and form shapes needed for speech sounds such as "oh."

Hofe, who unveiled AnTon this month at the Artificial Life XI conference in Winchester, U.K., hopes to use the device to study the energetics and mechanics of speech production. He believes it can ultimately help improve voice-recognition programs. He may also deactivate selected muscles to replicate and test remedies for speech pathologies seen in stroke victims.

AnTon is "a very cool system," says Matthias Scheutz, director of the Human Robot Interaction Laboratory at Indiana University, Bloomington. He notes that other teams have created robotic or artificial mouths with tongues but says he's impressed by how closely this one mimics a human.

CREDITS (TOP TO BOTTOM): I. VAN HOORTWIJK; MIKE HETTWER/NATIONAL GEOGRAPHIC, 2008; ROBIN HOFE AND ROGER K. MOORE

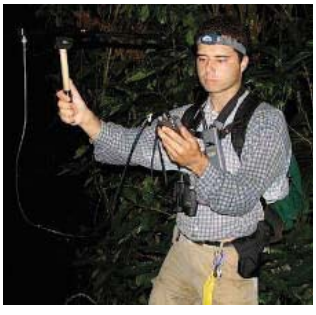

In the Field

NIGHTMARE AT DUSK. Catching a glimpse of the elusive Pacific screech owl in the dry forests of Costa Rica this month was a special moment for Stanford University ornithologist and nature photographer Cagan Sekercioglu (bottom left). But it came at a high price: a mob attack that left his colleague, Jim Zook, with 12 stitches.

The attack came after locals mistook the two birders for bandits who had stolen electrical wiring from a nearby farm. After smashing the windshield, five assailants slashed Zook, a U.S. citizen who's lived in Costa Rica for 30 years, on the hand and back with a machete. Sekercioglu was also detained, but luckily the captors ended up summoning the police, who extricated the scientists from the angry mob.

That's when Sekercioglu spotted a screech owl and grabbed his camera. "My heart is pounding, and it's a mixture of emotions seeing this thing," he says. "I press and the flash goes off and there's this perfect photo."

CELEBRITIES

A BALANCING ACT. Emma Pooley's ride to the Olympic silver medal in cycling last week required some juggling of her scientific career. When she's not on a bicycle, the 25-year-old British graduate student studies the instability of lumpy soils at the Institute for Geotechnical Engineering at ETH Zürich in Switzerland.

It helps that her supervisor, Sarah Springman, is an accomplished triathlete and rower. In addition to working part-time, Pooley also won permission to spend several months this winter at the University of Western Australia in Perth "rather than sitting in the snow in Zürich," says co-supervisor Jan Laue. Pooley finished 25 seconds behind American Kristin Armstrong in the 23.5-km women's time trial held on 13 August in Beijing.

MOVERS

WONDERLAND. Jessica Hodgins wants to make a robot's gaze as lifelike as possible. Markus Gross is developing a three-dimensional video-recording system. The two computer scientists, at Carnegie Mellon University (CMU) in Pittsburgh, Pennsylvania, and the Swiss Federal Institute of Technology (ETH) in Zürich, respectively, will now have the backing of one of the world's largest entertainment companies as heads of research labs being funded by the Walt Disney Co.

The two new labs are the first Disney research facilities to be set up in collaboration with academic institutions. Hodgins hopes to draw on the faculty and technical resources at CMU's nearby School of Computer Science to collaborate with Disney Research Pittsburgh on efforts such as developing robots that can play games with guests at Disney's theme parks. Current Disney researchers will also be encouraged to take research sabbaticals at the university. Gross anticipates a similar relationship between ETH and Disney Research–Zurich, including joint efforts to improve animation quality and enhance cinematography.

Disney isn't saying how much it plans to spend, but each lab expects to hire seven or eight primary researchers. "My kids are excited," says Gross. "My 20-year-old daughter likes [Disney] Pixar movies very much."

To **S. Blair Hedges,** a biologist at Pennsylvania State University in State College, identifying a tiny snake found in Barbados as a new species and naming it *Leptotyphlops carlae* after his wife, Carla Hass, was standard practice. But his 4 August announcement in *Zootaxa* infuriated some residents of the Caribbean island nation, who for generations have known it simply as the threadsnake.

Q: Isn't it rude to name a snake after your wife?
Most people consider something named after them an honor. She happened to be with me when I collected the specimen from the edge of a forest in Barbados. And besides, she is a herpetologist.

Q: Why is it a discovery if residents already knew about the snake?
"Discovery" is a relative term. The threadsnake has probably been there for a million years, but the discovery happened at my lab in Pennsylvania when it was determined that the snake that everybody thought they knew was a distinct species endemic to the island.

Q: What's the added value of knowing that the snake is unique?
Learning that it exists only on an island [means] it is much more likely to be threatened with extinction if its habitat disappears. Now that we know that the species occurs only in forest patches in Barbados, we can make the argument that the forests need to be preserved for the sake of biodiversity.

Got a tip for this page? E-mail people@aaas.org

CREDITS (TOP LEFT-HAND IMAGES); (TOP AND BELOW RIGHT) CAGAN HAKKI SEKERCIOGLU (BELOW LEFT) SCOTT R. LOARIE; (RIGHT-HAND IMAGES) (TOP TO BOTTOM) PAT LITTLE/AP PHOTO; S. BLAIR HEDGES /PENN STATE; (BOTTOM LEFT) STEFANO RELLANDINI/REUTERS

Skirmish over Endangered Species Act
1030

Wanted: Math education faculty
1031

Contaminated. Environmental workers donned protective gear on 29 November 2001 before attempting to clean up the Hart Senate Office Building after the anthrax attacks.

ANTHRAX INVESTIGATION

FBI Discusses Microbial Forensics—But Key Questions Remain Unanswered

WASHINGTON, D.C.—Facing growing public skepticism, impatient politicians, and a blogosphere rife with conspiracy theories, the Federal Bureau of Investigation (FBI) on Monday sought to bolster its case that Army scientist Bruce Ivins was the perpetrator of the 2001 anthrax attacks by extensively discussing the scientific evidence. Backed by six outside researchers who lent a hand in the investigation, FBI officials explained during two press briefings how they linked spores from the envelopes sent to Congress and the media back to a flask at Ivins's lab at the U.S. Army Medical Research Institute of Infectious Diseases (USAMRIID). Although the agents did add a few new details to the picture that has emerged over the past 3 weeks, several scientists say that many questions still remain unanswered (see sidebar).

The briefings confirmed the scientific process that sources close to the investigation, as well as independent microbiologists who analyzed a key court document, had described before (*Science*, 15 August, p. 898), a process that relied on whole-genome sequencing to find four mutations unique to the spores used in the attacks. The bureau also hammered home that, in contrast to widespread reports, no special additives, such as silica, were added to the spore preparation, and that Ivins—who killed himself on 29 July—would have been able to produce the letters on his own 7 years ago using standard lab equipment.

To reinforce the scientific message, the FBI took the unusual step of organizing two briefings, one for reporters from scientific journals, including *Science*, so that it had ample time to delve into the scientific nitty-gritty, and the other for the general press. It also brought in microbiology heavyweights such as Rita Colwell, who helped fund the sequencing of the attack strain in 2001 while she was head of the National Science Foundation.

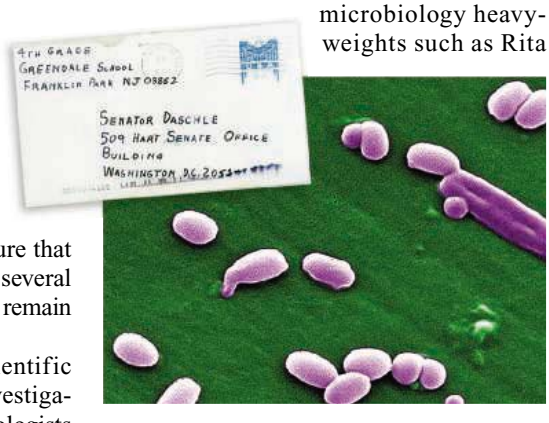

Dangerous mail. Senator Tom Daschle's office received one of the letters tainted with the deadly anthrax spores, later found to be from the widely used Ames strain (*above*).

More answers may come out over the next couple of months, because the bureau has given its scientific collaborators permission to discuss the case and publish their findings. Claire Fraser-Liggett, the former head of The Institute for Genomic Research (TIGR) who is now at the University of Maryland School of Medicine in Baltimore, says she and her colleagues expect to have a draft manuscript about their piece of the puzzle ready for submission in a month's time. The numerous "technical reports we have had to produce for the FBI over the years is making manuscript-writing that much easier," she says.

A key moment in the investigation came when TIGR researchers sequenced the anthrax sample taken from the spinal fluid of Robert Stevens, the first victim of the anthrax letter attacks that ultimately killed five people and sickened 17. When they compared that strain with the first anthrax strain ever sequenced—a project finished about the time of the attacks—they found a few small differences between the two, as they reported in *Science* (14 June 2002, p. 2028). Because *Bacillus anthracis* is extremely homogenous genetically and both isolates came from the Ames strain, researchers "had no idea" that they could reliably pinpoint a few changes in its genome, says Jacques Ravel, a former TIGR researcher now at the University of Maryland School of Medicine. The finding gave them confidence that they might be able to differentiate the anthrax samples stored at dozens of labs, says Fraser-Liggett—and finger the one involved in the letters.

The FBI confirmed on Monday that a preliminary analysis at the U.S. Centers for Disease Control and Prevention showed that the powder in each of the four letters was not a uniform population of cells but a mix that, when grown in a petri dish, yielded some colonies that were different in texture, color, and size. Paul Keim's group at Northern Arizona University in Flagstaff extracted DNA from these variants and supplied it to TIGR, where 12 DNA samples were fully sequenced. Four mutations—all of them insertions or deletions of a DNA fragment, or "indels"—were then selected, and FBI and independent scientists developed assays to

CREDITS: (TOP) KENNETH LAMBERT/AP PHOTO; (BOTTOM) JANICE HANEY CARR/CDC; (INSET) REUTERS/DEPARTMENT OF JUSTICE

Budget squeeze threatens climate model
1032

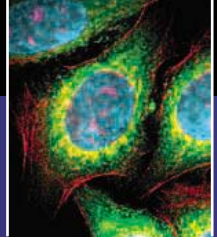

Toxicology at the nano scale
1036

look for them in a repository of more than 1000 samples of the Ames strain that the FBI had collected from labs in the United States, Sweden, the United Kingdom, and Canada. The samples were tested at about a dozen labs, including TIGR.

The FBI disclosed earlier that only eight samples had all four mutations; on Monday, it said that all but one of these came from USAMRIID. And all eight could be traced to RMR-1029—the flask of spores under Ivins's charge.

That is as far as the science took them, the FBI conceded; conventional detective work—such as checking lab notebooks and shipment records—helped rule out everyone but Ivins who had access to the spores, says Vahid Majidi, head of the agency's Weapons of Mass Destruction Directorate. He declined to give details. "I'm asking you not to second-guess our investigative approach," he said.

An analysis by materials researcher Joseph Michael at Sandia National Laboratories in Albuquerque, New Mexico, convinced the FBI that no silica or other chemicals had been added to the anthrax in the letters, as an earlier analysis by the Armed Forces Institute of Pathology (AFIP) had indicated. Transmission electron microscopy by Michael and colleagues revealed that the silicon AFIP researchers had detected in the samples was contained inside the spores—a natural occurrence documented in previous research—and not in a coating intended to make the anthrax disperse more easily.

Many experts had believed that only special coatings or electrostatic charges—which would require sophisticated chemical and physical expertise—could explain why the powder in the Senate letters seemed to float so easily (*Science*, 28 November 2003, p. 1492). If the bureau is right, "that makes it more frightening in a way," says bioterrorism expert Michael Osterholm of the University of Minnesota, Minneapolis, as it suggests that people with no special skills in those fields could make an efficient, deadly powder.

During the general press conference, Majidi admitted to a misstep in the investigation. In 2002, the FBI destroyed an anthrax sample that Ivins had submitted from his lab in February because it had not been prepared in accordance with a court-directed protocol. Keim held onto the mirror sample sent to his lab until 2006, when investigators realized it could be probed for the four mutations. (By then, investigators had already confiscated the RMR-1029 flask from Ivins.) The earlier sample was eventually shown to have all four mutations, linking it to the envelopes; but samples that Ivins gave to agents a few months later, in April 2002, did not, leading the FBI to suspect that he was trying to mislead them the second time around.

Throughout the process, the agency enlisted dozens of scientists to vet each step in the investigation and the results of the analyses to try to ensure that they would stand up to scrutiny in a court of law, says D. Christian Hassell, director of the FBI Laboratory. Groups of scientists were invited for "red-team reviews" to scrutinize the evidence, Hassell said.

Scientists involved in the case say they are relieved that after many years, they can now discuss and publish the evidence. "Suddenly, it's very relaxed," says Keim, who said he was handed a document releasing him from the nondisclosure agreement an hour before he took part in the first press conference. Adds virologist Thomas Geisbert of Boston University, "All of us who have handled the evidence have asked the FBI, and pleaded with them, to allow us to release it."

Because the evidence is unlikely to be challenged in court—the FBI expects to close the case soon—there should be a "court of science" instead, convened by the National Academy of Sciences or another independent body, suggests Osterholm. That would help alleviate the public mistrust of the official investigation and counteract conspiracy theories, like those surrounding the assassination of President John F. Kennedy, he says. But Majidi seemed resigned to the idea that the doubts will never go away entirely: "There's always going to be a spore on a grassy knoll."

–YUDHIJIT BHATTACHARJEE AND MARTIN ENSERINK

Six Anthrax Science Questions the FBI Has Yet to Answer

- What were the four mutations the FBI says it used to link the anthrax in the envelopes to Bruce Ivins at USAMRIID?
- What are the odds of a false positive—that is, the odds that the spore populations in Ivins's flask RMR-1029 and in the envelopes weren't related but shared the same four mutations by chance?
- Eight samples had anthrax with all four mutations; one of those came from a lab other than USAMRIID. On what basis was this lab ruled out as the origin of the letters?
- How did the FBI rule out the possibility that others at USAMRIID with access to Ivins's lab prepared the envelopes?
- How exactly did Ivins, if he was the perpetrator, produce an easily dispersible powder from his anthrax culture?
- What led the FBI to suspect Steven Hatfill in the earlier years of the investigation?

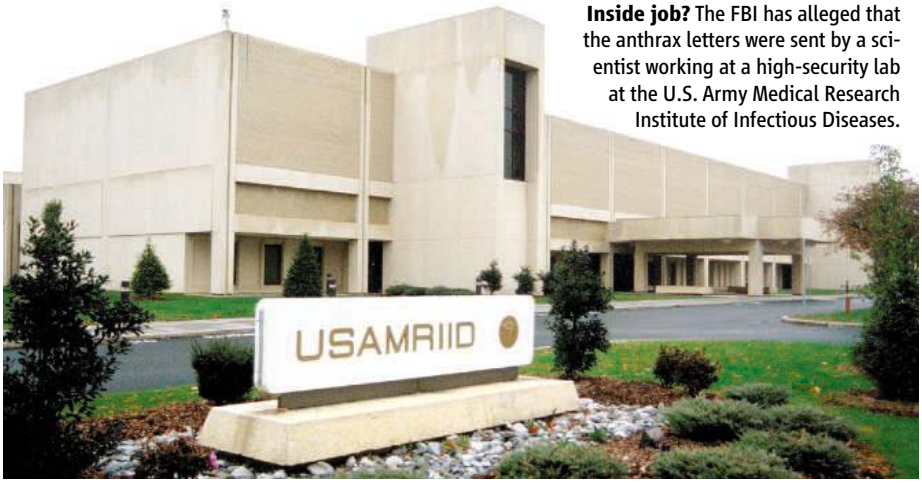

Inside job? The FBI has alleged that the anthrax letters were sent by a scientist working at a high-security lab at the U.S. Army Medical Research Institute of Infectious Diseases.

CREDITS: (IMAGE) CDC/COURTESY OF LARRY STAUFFER/OREGON STATE PUBLIC HEALTH LABORATORY; GREG MATHIESON/MAI/TIME LIFE PICTURES/GETTY IMAGES

TECTONICS

Pumping Up the Tibetan Plateau From the Far Pacific Ocean

Explaining how an area the size of Alaska got to be higher on average than the highest peak in the contiguous United States doesn't seem all that difficult: Just blame India. The roving subcontinent plowed into Eurasia beginning 50 million years ago and hasn't stopped yet. When it comes to working out the details, however, the Tibetan question remains the most contentious in tectonics. "There's a lot of gabbing, and we're not much further along than we were 20 years ago," says geochemist T. Mark Harrison of the University of California, Los Angeles (UCLA).

The problem is that researchers can't see much of what's going on beneath the plateau. Is the underlying rock strong and rigid or flowing like molasses? On page 1054, geoscientists Leigh Royden, B. Clark Burchfiel, and Robert van der Hilst of the Massachusetts Institute of Technology (MIT) in Cambridge argue that rock has flowed west to east beneath the plateau to inflate its eastern side and that the flow has been throttled by tectonic doings as far as thousands of kilometers away.

There is some agreement about how the Tibetan Plateau story begins, at least. In the western portion of the collision zone—where India smashed into the rigid and resisting block of the Tarim Basin—the colliding continents squeezed the intervening rock into the great Karakoram Range. To the east, with hot, weak rock and no rigid backstop in the way to strengthen the continents' grip, the collision sent great chunks of rock eastward. Piled 5 kilometers high to the west, crustal rock weighed heavily on the rock beneath, driving fragments toward southeast China and Indonesia without raising much of a plateau in the east.

This eastward extrusion, the MIT group is now pointing out, coincided with stirrings of the plates of the western Pacific. There, ocean plates were diving into deep-sea trenches and heading under Asia. The trenches, meanwhile, were rapidly retreating from the continent. This trench retreat made room for the crustal rock being extruded eastward and southward from Tibet, the MIT group reasons. When the trench retreat ground to a halt between 30 million and 20 million years ago, the researchers argue, the extruded material began to pile up, thickening the crust faster than before and thus pumping up the plateau.

Another, much more local gating of flow explains why the central plateau thrust upward about 10 million years ago, the group suggests. Normally, such a rise would leave deformed rock and other signs that the crust had been compressed and squeezed. No such compressional markings have been found in the east. Instead, north-south faults in the eastern plateau show that the crust was actually stretching east and west. To explain the paradox, the MIT group posits that a "dam" of strong, rigid rock beneath the plateau busted about 15 million years ago. Deep, weak crustal rock gushed eastward, stretching the central plateau by its departure and pushing up the eastern plateau. Traces of that rock monsoon may have turned up in seismic images of an apparently weak crustal layer deep beneath the eastern plateau, which van der Hilst and colleagues published earlier this year in *Geophysical Journal International*.

Not everyone agrees that crustal flow was crucial. In the May issue of *Geology*, seismologist Paul Silver of the Carnegie Institution of Washington's Department of Terrestrial Magnetism in Washington, D.C., and

GENOMICS

'Simple' Animal's Genome Proves Unexpectedly Complex

Aptly named "sticky hairy plate," *Trichoplax adhaerens* barely qualifies as an animal. About 1 millimeter long and covered with cilia, this flat marine organism lacks a stomach, muscles, nerves, and gonads, even a head. It glides along like an amoeba, its lower layer of cells releasing enzymes that digest algae beneath its ever-changing body, and it reproduces by splitting or budding off progeny. Yet this animal's genome looks surprisingly like ours, says Daniel Rokhsar, an evolutionary biologist at the University of California, Berkeley (UCB) and the U.S. Department of Energy Joint Genome Institute in Walnut Creek, California. Its 98 million DNA base pairs include many of the genes responsible for guiding the development of other animals' complex shapes and organs, he and his colleagues report in the 21 August issue of *Nature*.

Biologists had once assumed that complicated body plans and complex genomes went hand in hand. But *T. adhaerens*'s genome, following on the heels of the discovery of a similarly sophisticated genome in a sea anemone (*Science*, 6 July 2007, p. 86), "highlights a disconnect between molecular and morphological complexity," says Mark Martindale, an experimental embryologist at the University of Hawaii, Honolulu. Adds Casey Dunn, an evolutionary biologist at Brown University, "It is now completely clear that genomic complexity was present very early on" in animal evolution.

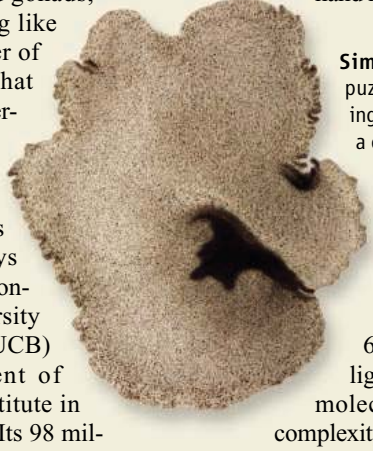

Simple—or simplified? It's a puzzle why *Trichoplax*, a seemingly primitive animal, has such a complex genome.

CREDIT: ANA SIGNOROVITCH

Ever since German zoologist Franz Eilhard Schulze first found *Trichoplax* more than a century ago in a saltwater aquarium, this disc-shaped animal has stirred debate. It has just four apparent types of cells, prompting Schulze and others to consider it a holdover from the earliest animals. They eventually assigned it to its own phylum, Placozoa.

But not everyone agrees which branch of the animal tree of life is oldest: sponges, comb jellies, or placozoans. And a few researchers have dismissively argued that placozoans are just larvae of cnidarians—jellyfish, sea anemones, and the like—or else a streamlined version of a cnidarian ancestor.

Rokhsar, his graduate student Mansi Srivastava, and their colleagues sequenced a *Trichoplax* from the Red Sea, finding an estimated 11,514 protein-coding genes.

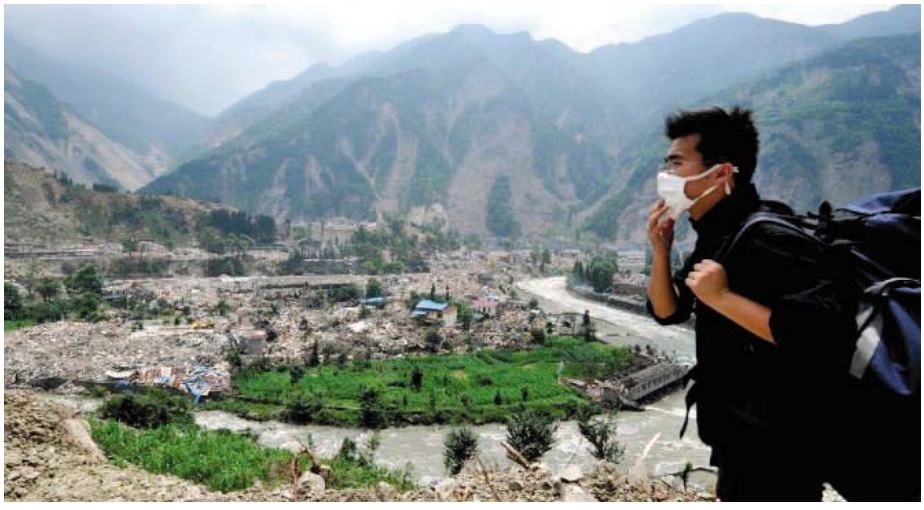

Informative disaster. The Sichuan quake holds clues to what has driven the rise of the Tibetan Plateau.

colleagues presented seismic probings of the "fabric" of the crust and deeper mantle rock of the plateau. The strong similarity of crustal and mantle fabrics "disallows the lower crustal flow model" of the MIT group, Silver says, because such flow would have disconnected the crust from the mantle, leading to different fabrics. As to the apparent absence of signs of squeezing in the eastern plateau, the heavily forested eastern area "is a good place for panda bears but a bad place for geologists to make geologic maps," writes geoscientist An Yin of UCLA in an e-mail.

May's devastating earthquake in the Sichuan region of China on the eastern edge of the plateau might eventually help resolve the Tibetan question. Burchfiel, Royden, van der Hilst, and colleagues argue in the July issue of *GSA Today* that the quake mainly reflects slow uplift, consistent with crustal flow. But so far, others see dramatic evidence of severe squeezing and crustal deformation. And how the deeper crust and mantle slowly recover from the shock of the quake could reveal just how weak and prone to flow the deeper rock of the plateau actually is. **–RICHARD A. KERR**

After comparing the sequences of 104 *Trichoplax* genes with their counterparts in other organisms, they concluded that placozoans aren't the oldest animals; they branched off after sponges but before cnidaria. Placing *Trichoplax* on the tree "will now allow us to understand how to interpret its biology in the context of animals as a whole," says Dunn.

The sequence is also clarifying what ancient genomes looked like. *Trichoplax* genes have comparable numbers of introns, noncoding regions interspersed between the coding regions, as vertebrates and as the sea anemone. And many of the same genes were linked on the chromosomes of vertebrates, *Trichoplax*, and sea anemones, the researchers report. This was not the case with the fruit fly and nematode genomes, whose genes have fewer introns and have moved about quite a bit.

Despite being developmentally simple—with no organs or many specialized cells—the placozoan has counterparts of the transcription factors that more complex organisms need to make their many body parts and tissues. It also has genes for many of the proteins, such as membrane proteins, needed for specialized cells to coordinate their function. "Many genes viewed as having particular 'functions' in bilaterians or mammals turn out to have much deeper evolutionary history than expected, raising questions about why they evolved," says Douglas Erwin, an evolutionary biologist at the Smithsonian National Museum of Natural History (NMNH) in Washington, D.C.

Trichoplax could yet be more complex than observed, perhaps having subtle differences in cell types. Or, the amoeboid form may be just one phase of a complex life cycle that's still undiscovered, says Rokhsar.

The surprises in the *Trichoplax* genome emphasize the importance of sequencing other early-arising species, such as comb jellies or different kinds of sponges, says evolutionary biologist Allen Collins of the National Marine Fisheries Service and NMNH. "The more taxa we fill in," says Collins, "the clearer our picture will be for how the entire suite of these molecules evolved over the critical time early in metazoan history." **–ELIZABETH PENNISI**

CREDIT: XINHUA/LANDOV

SCIENCESCOPE

Obama: Lunar Sooner

Both major U.S. presidential candidates looked to the heavens last week. Senator Barack Obama (D–IL) supported President George W. Bush's plan to return humans to the moon as part of a seven-page space policy white paper that also calls for increasing international efforts in space. Senator John McCain (R–AZ), during an event near NASA's Kennedy Space Center in Cape Canaveral, Florida, backed current efforts to build a successor to the shuttle to transport humans and material but did not support returning to the moon. Both men are keen to win support in the battleground state of Florida. **–ANDREW LAWLER**

Plans for Nuclear Plant Proposed

Last week, the U.S. Nuclear Regulatory Commission told Congress how it plans to license a nuclear reactor that would use technologies not yet invented or tested to produce electricity, heat, and hydrogen. The Department of Energy's (DOE's) $2.4 billion Next Generation Nuclear Plant, to be built at Idaho National Laboratory, is supposed to demonstrate the feasibility of a gas-cooled reactor that operates at 950°C, three times the temperature of current water-cooled reactors. Congress has ordered DOE to complete the plant by 2021, and last week regulators explained how it hopes to conduct research to license the plant by 2017. But that timetable is too ambitious, warns Edward Lyman of the Union of Concerned Scientists, noting that reactor materials able to withstand such high temperatures don't exist. **–ELI KINTISCH**

Vioxx Trial Criticized

Researchers combing through internal memos and other correspondence submitted by the drug company Merck in suits involving its anti-inflammatory drug Vioxx claim that a clinical trial carried out in 1999 was actually initiated by Merck's marketing department to promote sales. The trial, which compared the gastrointestinal effects of Vioxx and naproxen, a commonly used anti-inflammatory, was largely run by primary care doctors. In contrast, most clinical trials are run by specialists, suggesting that the company wanted to create buzz for the drug with the doctors likely to prescribe it. The authors of the criticism, published this week in the *Annals of Internal Medicine*, were all paid consultants to attorneys representing plaintiffs that sued Merck for heart attacks they say were caused by the drug. The company says the study, published in the *Annals* in 2003, was not done for marketing purposes.

–JENNIFER COUZIN

ENDANGERED SPECIES

New Regulation Would Lessen Influence of Fish and Wildlife Experts

For much of the past 35 years, the U.S. Endangered Species Act (ESA) has been at the center of some of the fiercest environmental battles in the United States. It has been the means by which tiny fish have held up big dams, helped bring iconic species such as the bald eagle back from the brink, and pitted environmentalists against loggers over the protection of old-growth forests in the Pacific Northwest. Now, with just 5 months left in office, the Bush Administration has proposed controversial rules that would exempt many projects from what the Administration says are unnecessary reviews by the U.S. Fish and Wildlife Service (FWS) and the National Marine Fisheries Service (NMFS). But the plan has left environmentalists sputtering. "This is a way to allow destructive projects to go forward without the check of Fish and Wildlife Service biologists," says Defenders of Wildlife's Jamie Rappaport Clark, who headed the service during the Clinton Administration.

In proposing the rule last week, the departments of the Interior and Commerce listed two main goals. The first is to prevent the ESA from being used to regulate carbon dioxide (CO_2) emissions. That became a possibility after FWS listed the polar bear as a threatened species in May (*Science*, 23 May, p. 1000). The second is to reduce the number of so-called informal consultations, which have delayed many proposed projects for months or years, according to a 2004 report by the U.S. Government Accountability Office.

Currently, when an agency is considering a proposed action (or giving a permit to a member of the public), it must first determine whether a listed species or its critical habitat might be affected. If so, then it must informally consult with biologists at the relevant service, generally FWS for terrestrial species or NMFS for marine organisms. More often than not, the agency thinks the project is unlikely to cause harm. The FWS or NMFS biologists usually agree, and the agency can proceed. But if agency or service biologists determine that harm is likely, a more involved, formal consultation takes place, and the service decides how the damage could be minimized or avoided.

Under the proposed rule, agencies have to consult the services only if indirect or direct effects of their actions are an "essential cause" of and "significant contributor" to the likely harm. This would mean that the Department of Transportation, for example, would not have to consider the impact of greenhouse gas emissions from cars on polar bears or any other listed species. The reason? Emissions from any single highway do not make a significant contribution to the melting sea ice that harms the bears, argue officials at the departments of Interior and Commerce.

Beyond CO_2, the proposed changes are sweeping as well. Under the new rule, if the agencies determine that their projects are not likely to harm a species, they would not need to seek an expert opinion from the services at all. (If the agencies suspect harm to a species, however, they still must formally consult.) Officials at the departments of Interior and Commerce argue that agencies are "fully qualified" to decide on their own whether their projects will harm a species or its habitat.

Undercut? Under a proposed rule, some logging and other federal activities might not require a review of possible harm to endangered species, such as the marbled murrelet.

Not so, say experts familiar with the ESA. Holly Doremus of the University of California, Davis, law school cites an analysis by FWS and NFMS, released in January, of similar regulations under the National Fire Plan, a federal program to reduce the risk of forest fires and restore burned ecosystems. Issued in 2003, these regulations allow the U.S. Forest Service and the Bureau of Land Management (BLM) to decide whether to consult about prescribed burning and other fire-related actions. NFMS found that the agencies failed to use the best available science in 10 out of 10 cases; FWS found other flaws in 25 out of 43 cases. "That's a very discouraging piece of evidence about how seriously the action agencies will take this job," says Doremus. A BLM spokesperson says the agency now has more expertise and expects "improved outcomes" in the future. The Forest Service has also increased training.

Although it's difficult to know exactly how well the existing system protects species, proponents say the process helps. "It's where most of the protection for endangered species occurs," says Noah Greenwald of the Center for Biological Diversity, an advocacy group in Tucson, Arizona. Without a requirement to check in with the services, Clark warns, agencies will have an incentive to put their mission—such as flood control or energy projects—ahead of protecting endangered species. According to J. B. Ruhl of Florida State University's College of Law in Tallahassee, the new rules "surely could be manipulated and abused." U.S. Department of the Interior spokesperson Chris Paolino calls those concerns unfounded. "All the penalties for harming an endangered species remain in effect," he says. "It's still in an agency's best interest to err on the side of caution."

The future of the rule, which is open for public comment until 15 September, is uncertain. A spokesperson for Senator Barack Obama (IL), the presumptive Democratic nominee for president, told the Associated Press that Obama would toss out the rule if he's elected; Senator John McCain's (R–AZ) campaign has not commented. Meanwhile, Congress could prevent any Administration from spending funds to implement it; Barbara Boxer (D–CA), who chairs the Senate Environment and Public Works Committee and opposes the rule, plans to hold a hearing 24 September. And then there are the courts. "Our biggest hope is that the rule will not be finalized," says Greenwald. "But if it is, it's likely we'll challenge it." **–ERIK STOKSTAD**

CREDITS: MATTHEW MCVAY/GETTY IMAGES; (INSET) ALL CANADA PHOTOS/ALAMY

U.S. HIGHER EDUCATION

Departments Scramble to Find Math Education Faculty

Kathryn Chval didn't have to apply for her position as a tenure-track assistant professor of math education at the University of Missouri, Columbia. And any letters of recommendation were an afterthought. Instead, after earning her Ph.D. in 2001 and joining the National Science Foundation (NSF) in suburban Washington, D.C., as a program manager, Chval simply put out the word in early 2003 that she was interested in a faculty job. She let one of the hottest job markets in academia do the rest.

Within a few weeks, 10 universities had invited her for a visit; Missouri offered to fly her out the next day. Comparing her experiences at four campuses, Chval liked the "sense of community" at Missouri and felt that the department's interests complemented her strengths in teacher education, curriculum standards, and working with disadvantaged student populations. But her husband, a lawyer, also needed to find a job. No problem: A few days later, the state attorney general's office offered him a spot in its computer crime unit.

Chval's no-hassle job search isn't unusual for those holding Ph.D.s in mathematics education. And although that may be good news for job-seekers, it's another impediment for universities trying to improve U.S. science and math education. Chval's colleague in the department of teaching, learning, and curriculum within Missouri's school of education, veteran mathematics educator Robert Reys, reports in the June/July *Notices of the American Mathematical Society* that 60% of 128 tenure-track academic jobs advertised last year in mathematics education went unfilled (see graphic). Previous surveys by Reys show that number has held steady for at least a decade. The reasons for the seller's market include a shortage of people entering the field, a growing demand by universities for their expertise as they become more involved in precollege education, a lack of consensus on how they should be trained, and a surfeit of other professional opportunities.

For starters, U.S. universities aren't keeping up with the demand. They award an average of 93 doctorates in mathematics education each year—fewer than one-tenth the number of doctorates in mathematics itself. And Reys says that many of the math ed Ph.D.s go to people not actively looking for jobs because they are already working for school districts, state education agencies, test publishers, and the like. In addition, a majority of those hired last year were already at a university, meaning that their departure simply created another vacancy.

Indeed, Reys found that the most common reason a university position wasn't filled was because the top candidate went elsewhere, part of a bidding war that Chval says has only gotten worse since she came to Missouri. "I continue to get calls," says Chval, who has built up a productive research agenda and is quietly optimistic about her chances of winning tenure next spring. "I recently received four calls from one institution, including one from the dean explaining how well my research interests fit in with their program."

Department chairs say the second most common reason for not filling a position is the inability to find an "appropriate candidate." That's code for the ongoing debate over the proper academic and professional qualifications for a faculty member who may be asked to teach math to undergraduates and education and math courses to graduate students, carry out education research, and train future teachers. Mathematics departments may require candidates to hold a Ph.D. in mathematics, meaning serious research in the discipline, while schools of education usually prefer someone who's been in the classroom and knows how the U.S. education system works. It's a rare individual who has both qualities and a rare institution that can strike the right balance. One department chair who responded to Reys's survey describes "… the third year of a failed search" that pitted mathematicians against math educators. Then he adds plaintively, "we may now lose the position to a pure math type."

Low salaries are a third reason for the dearth of qualified candidates, according to the survey, which cites a modal starting salary of $45,000 to $50,000. Chval says that she took a 40% cut in pay in moving from NSF, in suburban Virginia, to Columbia, but that the lower cost of living and other benefits of a small college town made the numbers work. Public school teachers with Ph.D.s often price themselves out of a job in higher education, notes Deborah Loewenberg Ball, dean of the school of education at the University of Michigan, Ann Arbor, a former elementary school teacher whose research has focused on improving elementary and middle school math instruction.

The federal government is doing little to address directly the shortage of math education faculty members. Earlier this decade, NSF funded 16 so-called centers for learning and teaching that aimed to improve instruction from kindergarten through graduate school in the STEM (science, technology, engineering, and mathematics) disciplines. A partner in one of the centers, Missouri doubled the size of its math ed doctoral program, says Reys. But the centers are being phased out, and Reys says he expects the number of graduates—which hit a peak of six this year—to begin dropping in a few years.

The demographics also work against any quick fixes. Just ask Chval, who was hired by the University of Illinois, Chicago, in 1989 to manage some of its NSF grants and who took 9 years to complete her Ph.D. there, taking one class a semester while raising a family and working full-time. And that's after having taught elementary school for 2 years. "It may have been free tuition, but my time sure wasn't," she laughs.

–JEFFREY MERVIS

TAKE THIS JOB, PLEASE

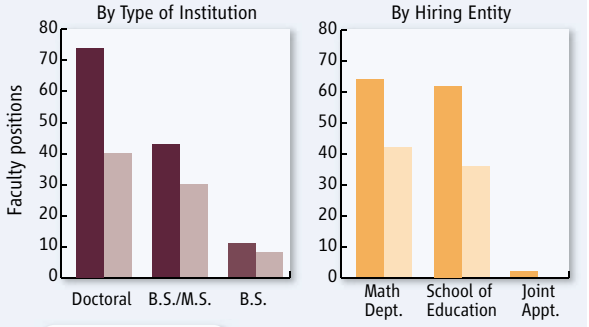

In demand. Math educators like Kathryn Chval are a prized commodity for many U.S. universities, which are having a hard time filling advertised positions.

CREDITS: (IMAGE) OSCAR CHAVEZ; (DATA SOURCE) R. REYS, JUNE/JULY 2008 *NOTICES OF THE AMS*

Turbulent Times for Climate Model

Researchers are running out of time to finish updating an important U.S. climate change model that has been hamstrung by the budget woes of its home institution, the National Center for Atmospheric Research

Every June, U.S. climate scientists descend upon Breckenridge, Colorado, to kick the tires on the nation's foremost academic global climate model. Some years there is added pressure, as scientists try to tune up the Community Climate System Model (CCSM) for simulations that will feed into the next report of the Intergovernmental Panel on Climate Change (IPCC). This is one of those years, and scientists are more worried than usual.

The question is whether they can meet a 1 October deadline for completing a critical part of their increasingly complex simulation of the interplay of Earth's atmosphere, oceans, land, and ice. "We're all very nervous," says atmospheric modeler Philip Rasch, who works remotely for the National Center for Atmospheric Research (NCAR) in nearby Boulder and who oversees the atmospheric component of the model. A big reason for the concern is the condition of the center, which hosts and manages CCSM.

In 2004, NCAR's then-director, Timothy Killeen, had launched a major restructuring that included expanding the lab, banking on a 2002 congressional promise of a 5-year doubling of the budget of its main funder, the National Science Foundation (NSF). But Congress failed to keep its promise, and NSF's contribution to NCAR, instead of rising by double-digit percentages, has grown by only 2.6% annually in the past 5 years. The resulting belt-tightening has meant pink slips for 55 employees since 2003 (out of a workforce that has averaged 800 since then) and not replacing 77 others who retired or left.

Those losses have affected CCSM. In the past 2 years, seven accomplished climate scientists among 50 researchers heavily involved in CCSM have left or announced plans to leave NCAR, including Rasch, a 27-year veteran who begins a new job this fall at Pacific Northwest National Laboratory in Richland, Washington. None has been replaced, although six scientists with less experience have been brought on since 2006 to bolster the effort.

Some climate scientists say that CCSM should have been better protected from the budget turmoil. "This hub of the nation's climate strategy has apparently not received the priority it deserves and needs," wrote members of the model's independent scientific advisory board on 8 July in an unsolicited letter to Eric Barron, who last month succeeded Killeen. Although computers are critical for climate simulation, they say, in the end it's NCAR's staff who must incorporate thousands of complex elements into a code that simulates everything from hurricanes to droughts to ocean currents.

Any erosion of CCSM's projected capabilities threatens what modeler David Randall of Colorado State University in Fort Collins calls "the closest thing we have to a national model." What sets CCSM apart from rival U.S. models at NASA and the National Oceanic and Atmospheric Administration is its widespread use by academic researchers, who also build it in partnership with NCAR. So whereas the other models rely on the expertise of teams of federal experts, CCSM's health reflects the state of overall U.S. climate research.

Although IPCC won't issue its next report until 2013, it has asked for data in 2011 from

Online
sciencemag.org
Podcast interview with the author of this article.

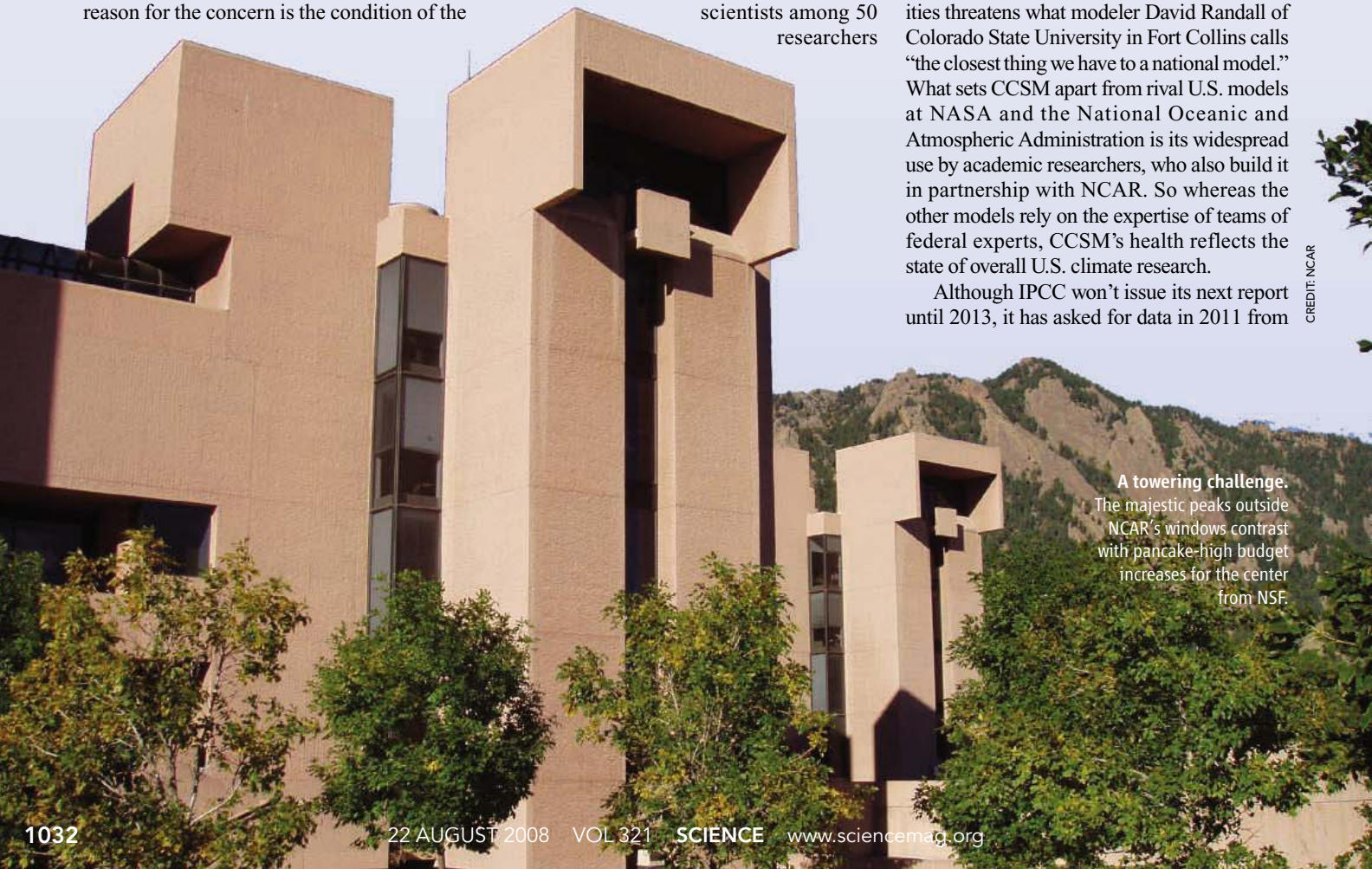

CREDIT: NCAR

A towering challenge. The majestic peaks outside NCAR's windows contrast with pancake-high budget increases for the center from NSF.

roughly two dozen models scattered around the world. Working backward, CCSM scientists gave themselves the October deadline to finalize the atmosphere, the central element of the million-line code, as well as the other segments. NCAR's deadline for connecting the pieces is 1 January 2009.

The changes will fix some flaws in the previous version of CCSM and add new features. In particular, scientists want to make tropical temperature patterns more realistic, depict ice sheets, clouds, and cycles such as El Niño more accurately, and better simulate the turbulent movement of air between the ground and an altitude of 1 km. IPCC scientists would also like models to incorporate an active carbon cycle that simulates how Earth's biological life—say, algae or swamps—shapes the biosphere.

Will NCAR come through? "CCSM is in danger of not being able to make scientifically credible contributions to [IPCC] and the climate science community," the board wrote in its July letter. Barron disagrees, saying CCSM will remain one of the world's top models. But he acknowledges that fewer bodies will mean "not being able to do as much."

Gambling on growth

Nestled at the foot of the Rocky Mountains in Boulder, NCAR was established in 1960 with NSF funding to advance climate and weather science. Its researchers have developed some of the world's best tools for predicting storms, droughts, and rising global temperatures, built on work by meteorologists, physicists, and modelers alike. In addition, NCAR provides planes, balloons, and computers to academic scientists across the country and around the world. NSF still supplies about three-fifths of its budget, $88 million of a total $149 million, including money for operations, buildings and equipment, and major facilities. The rest comes from competitive grants awarded by other government agencies and industry.

The precursor to CCSM was developed in 1983 at NCAR, and the model remains a unique partnership between academic and government scientists. Its paleoclimate runs and future projections have been the basis for hundreds of studies referenced by IPCC. The model is run out of the Earth and Sun Systems Laboratory (ESSL), the largest of five so-called laboratories at NCAR.

Along with an equally renowned short-term weather model, CCSM helped establish NCAR's reputation as the go-to resource for academic atmospheric research. But Killeen, who became director in 2000, wanted NCAR to do more, including increasingly detailed forecasts of the impacts of climate change and interdisciplinary studies on weather. So in 2004, he regrouped existing divisions into ESSL and labs for Earth observations, computing, and airborne-weather projects. He created a fifth lab to respond to growing interest in the societal impacts of climate change. Within the labs, Killeen also set up institutes devoted to interdisciplinary work and to the application of modeling and mathematical methods in geoscience. "It was a bold new initiative," says Richard Anthes, president of the University Corporation for Atmospheric Research in Boulder, which operates NCAR for NSF.

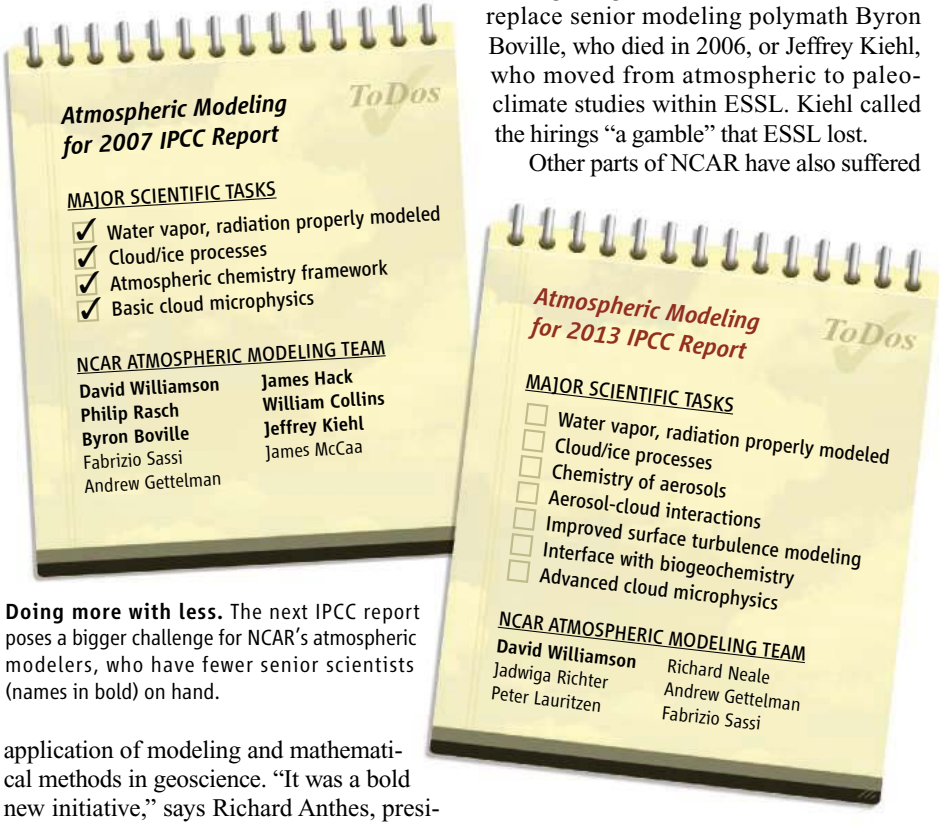

Doing more with less. The next IPCC report poses a bigger challenge for NCAR's atmospheric modelers, who have fewer senior scientists (names in bold) on hand.

Killeen hoped that NSF would finance the expansion as its overall budget grew. NSF's contribution to NCAR did rise by 19% between 2001 and 2004, but in the past 5 years it has increased by only 10%. That below-inflationary rise has triggered "chronic wasting disease" at NCAR, says Anthes. It also spawned fears among some scientists about the cost of the new bureaucracy. Managers estimate that the reorganization has added $5 million in staffing and other administrative costs over 4 years. "Shouldn't we really be about putting the money instead into scientific programs?" NCAR veteran scientist Peter Gilman recalls asking an assembly at NCAR in 2004. But without a growing contribution from NSF, Killeen was forced to ask NCAR managers to tighten their belts, including dipping into research funds to meet other expenses.

The modeling effort has also been affected by a program that Killeen began in 2001 that pays half the salaries of new hires for 2 years. ESSL used the optional funds to hire four young scientists in the climate division between 2001 and 2007, says William Large, who heads ESSL's climate division, and managers also hired five young scientists through the normal mechanism. But without a rising budget, the lab couldn't afford to replace senior modeling polymath Byron Boville, who died in 2006, or Jeffrey Kiehl, who moved from atmospheric to paleoclimate studies within ESSL. Kiehl called the hirings "a gamble" that ESSL lost.

Other parts of NCAR have also suffered from the budget shortfall. A fledgling extrasolar planets program was shuttered in 2004, and a light-detection-and-ranging station that measures aerosols will be closed next year. Before he left in June, Killeen also dissolved the lab for societal impacts that he created. (Beyond a short interview conducted before he left NCAR, Killeen declined comment for this article, citing conflict-of-interest rules related to his new job as director of NSF's geosciences division, which funds NCAR.)

The pruning has continued under Barron. This month, he ended a program run by a senior political scientist that conducted public policy research on the impacts of climate change on developing countries. The decision prompted an outcry from social scientists. But Barron says that he had no choice and that cutting it, along with the societal-impacts lab, will save NCAR $2 million annually. "We have not hurt CCSM nearly as much as other parts of NCAR," says deputy lab director C. Larrabee "Larry" Winter.

SOURCE: NCAR

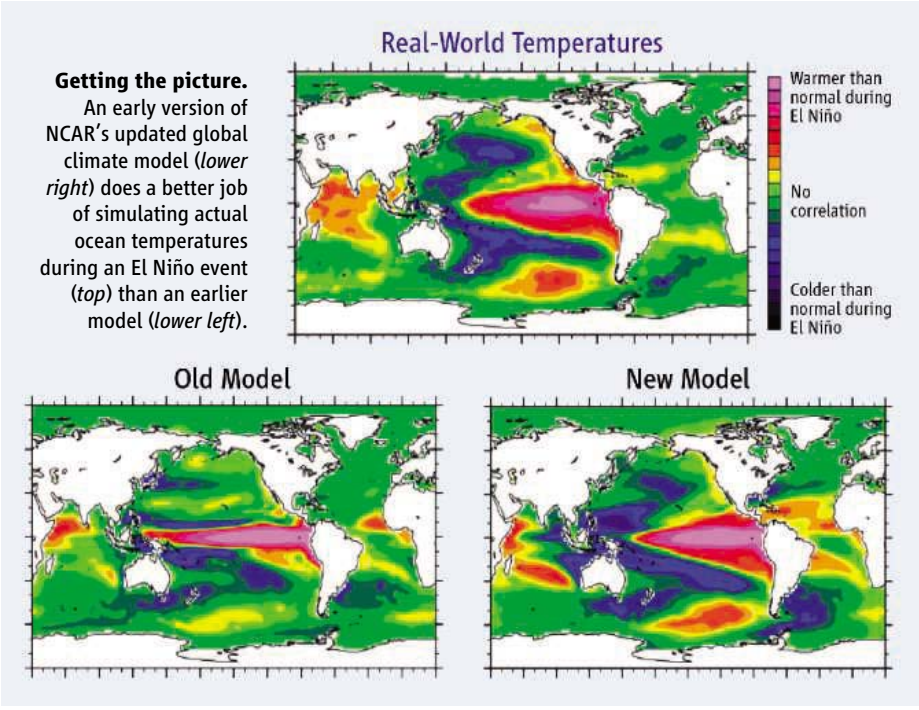

Getting the picture. An early version of NCAR's updated global climate model (*lower right*) does a better job of simulating actual ocean temperatures during an El Niño event (*top*) than an earlier model (*lower left*).

The main impact of the budget squeeze on climate modeling has been on the workload of scientists. Pressured to coordinate an increasingly complex model with fewer colleagues, Rasch says that he and others couldn't explore "the ideas they found fascinating." He says that's a big reason he left. James Hack decamped for the Department of Energy's Oak Ridge National Laboratory in Tennessee because, he says, "I had a better opportunity to build a program [there] than I did at NCAR." Joining the recent exodus of atmospheric modelers is William Collins, who went to Lawrence Berkeley National Laboratory in California. "Each in their own way found that something else was better," says Gilman. In addition, four scientists who worked on CCSM's land and chemistry components have left since last year and have not been replaced.

Modeler David Bader of Lawrence Livermore National Laboratory in California says a few million dollars spent over the past 5 years on personnel could "have made a big difference" in attracting and retaining seasoned talent. Last year, NCAR brass moved roughly $1.5 million—culled from reshuffled NCAR funds and a small NSF boost—to support the research group that does climate modeling. But that just paid the salaries of software engineers moved into that group from within NCAR. The lab is trying to hire a senior and junior atmospheric modeler.

Despite the negligible growth of NSF's contribution, NCAR has spent roughly $5 million since 2004 on equipment, including a balloon system, a mobile radar facility, and outfitting a high-altitude research jet that was completed in 2006. "It simply doesn't make sense to have a $100 million plane sitting in the hangar not doing science," says Anthes, explaining why the money wasn't spent on science and modeling efforts.

Down to the wire

Not all the news at Breckenridge was bad. Scientists there applauded, for example, a much-improved simulation of the seasonal global climate phenomenon known as El Niño–Southern Oscillation (above). The previous version depicted an unrealistic 2-year El Niño cycle; the new version offers a more realistic cycle of 3 to 6 years. Along with promising new land, ice dynamics, and depictions of the North Atlantic, CCSM's overhauled atmosphere includes new physics to describe the way clouds move heat and shift winds. "It'll be a much better model," Killeen says, thanks in part to the contributions from young researchers hired under his program.

But many of the proposed additions to the model have yet to be fully tested, making scientists uneasy. One important improvement that's behind schedule, says modeler Richard Rood of the University of Michigan, Ann Arbor, a CCSM advisory board member, is a better depiction of the turbulent movement of air from the ground to an altitude of 1 km. "I would personally worry about the fact that they're still doing major tuning [on that]," he says. Another important change would add biogeochemistry, including the complex relationship between the carbon and nitrogen cycles. Attempts to simulate dynamic nutrient cycles can lead to big crashes during testing, such as when forests in the model die unexpectedly. Progress has been slow, says Scott Doney of Woods Hole Oceanographic Institution in Massachusetts, a member of the model's biogeochemistry team, and the recent departure of two NCAR experts—Natalie Mahowald and Peter Thornton—hasn't helped. "We're going to be lucky to get a stable climate biogeochemistry system," he says.

Knitting together the model's many promising additions by January poses an even greater challenge. Researchers would like to simulate local clouds better. But when scientists inserted new parameters to do that into the full working atmosphere, polar clouds blocked too much sunlight and created excessive sea ice. The team expects to work the physics into the full atmosphere, says Rasch, but it's unclear whether the feature will work when coupled to the ocean.

The loss of seasoned modelers will be especially noticeable during the coming integration phase, says Rood. NCAR's young modelers are talented, he says, but lack valuable experience taming new parts of an unpredictable code. But NCAR atmospheric modeler Andrew Gettelman, who joined the CCSM team in 2003, says the departed veterans "are all there when we need them," reachable by e-mail or phone. And the 38-year-old modeler says the fact that he wrote some of the overhauled code will help him make the pieces fit.

Atmospheric scientists are cautiously optimistic that Barron, a paleoclimate modeler, recognizes the importance of CCSM. "There's no one else I would rather have at the helm," says atmospheric scientist Marvin Geller of Stony Brook University in New York, citing Barron's leadership of several national climate-related panels. Barron says his recent moves show that he's serious about protecting "core" activities such as CCSM, noting that he used an early version of the model for his 1980 Ph.D. thesis at the University of Miami.

Despite proposals by the White House and lawmakers to give NSF a double-digit increase in 2009, Anthes thinks that political gridlock could leave NCAR with another flat budget. So he demurs when asked if he sees light at the end of the tunnel. "I see hope," he muses. "It may be moonlight." For all his confidence about the next version of CCSM, Barron says continued flat budgets could devastate his lab's modeling efforts. "That's the real threat," he says.

–ELI KINTISCH

CREDIT: ADAPTED FROM R. B. NEALE, J. H. RICHTER, AND M. JOCHUM, *J. CLIMATE*, IN PRESS (2008)

CULTURAL HERITAGE

Shielding a Buddhist Shrine From The Howling Desert Sands

China is embarking on a major new effort to protect the Mogao Grottoes, a unique repository of murals and sculptures on the old Silk Road

DUNHUANG, CHINA—The medieval Chinese merchant prayed for good fortune before his men and their goods-laden camels and donkeys set off on a long westward journey. But the caravan soon ran into trouble: A camel tumbled off a cliff to its death, and thieves made off with reams of silk. These travails spring to life from a vivid mural, dated to the turn of the 7th century C.E., that's painted on the clay wall of Cave 420 of the Mogao Grottoes.

One of Buddhism's most revered shrines, the 492 decorated caves that make up Mogao were hewn from a cliff between the 4th and 14th centuries C.E. 25 kilometers southeast of Dunhuang, an ancient Silk Road way station in western China. Most caves feature Buddha and disciples, pre-Buddhist deities such as the nine-headed god of Earth and the 13-headed god of heaven, and scenes from sacred texts and legends. The murals—and a trove of 40,000 documents discovered in one of the caves a century ago—also offer a singular glimpse into the Silk Road's ancient rhythms, from elaborate wedding festivals and treasure hunting to sporting events with archers on horseback. The "Library Cave" cache "transformed the study of the history of China and the Silk Road," says Susan Whitfield, director of the International Dunhuang Project at the British Library in London. Highlights include the earliest known manuscript star map and the earliest dated printed document, a Buddhist sutra copied in May 868 C.E.

In designating Mogao a World Heritage Site in 1987, UNESCO hailed it as a "unique artistic achievement" whose 45,000 square meters of murals include "many masterpieces of Chinese art." "No other place compares to Mogao," says Qu Jianjun, a geographer at the Cold and Arid Regions Environment and Engineering Research Institute (CAREERI) in Lanzhou.

That's why China is launching a new effort to safeguard the caves. Earlier this year, its National Development and Reform Commission approved a $38 million project to protect Mogao's fragile artworks from three major threats: salt leaching from groundwater, exhalations and body heat from droves of tourists, and shifting sand dunes. Later this year, CAREERI plans to open an environmental research center in Dunhuang, dedicated in large part to Mogao and directed by Qu.

Cave art. On one of the Silk Road routes (dotted lines) in China lie the Mogao caves and their images of Buddhist scriptures, such as this recently restored mural.

As spectacular as the grottoes remain, damage over the centuries has diminished their grandeur. Some harm is human-wrought: After the shrines fell into disuse some 600 years ago, looters made off with scores of statues. (Some 2400 are left.) Further insults were inflicted early last century, when a retreating Russian White Army battalion holed up in the caves, blackening paintings with smoke from cooking fires and marring others with graffiti. Nature has taken a toll too. The five tiers of caves were carved along the west bank of the glacier-fed Daquan River. Spring meltwater surges occasionally flooded ground-level caves, destroying portions of murals, before engineers built embankments in the 1960s.

Then there is the constant threat of sand. "Without proper efforts, the grottoes will be entirely buried by shifting sand," says Qu. Dunhuang is an oasis on the edge of the Kumtag Desert, and searing winds whip down on Mogao from Mingsha Mountain, a 170-meter-high "megadune" of sand a few kilometers west that is creeping toward the grottoes. By the 1920s, sand had clogged the caves and they lay neglected for 40 years. "They were nearly lost," says Qu. To prevent a repeat, in 1989 the Getty Conservation Institute (GCI) of the J. Paul Getty Trust in Los Angeles, working with Dunhuang Academy and CAREERI, erected a 4.7-kilometer nylon windbreak fence on the cliff edge above the caves. That has cut wind-driven sand by about 60%, says GCI principal project specialist Neville Agnew.

To further blunt the advancing dunes, GCI and CAREERI teamed up in the mid-1990s to plant a vegetation barrier between Mogao and Mingsha. Qu and colleagues are now testing how gravel mulch—rocks of various sizes placed in grids on the sandy plateau above the caves—impedes sand flow. These and other measures have proven "highly effective," says Agnew. There's less erosion of the cliff edge, he says, and less sand cascading over it and into the caves. GCI has since turned its attention to developing techniques to preserve Mogao's artwork and to site planning and management.

Most caves, including those with some of the finest art, are off-limits. Under China's new initiative, the Institute of Computing Technology in Beijing is creating a virtual museum at Mogao's visitor center to allow tourists to experience closed caves. The initiative will also bolster efforts to mitigate sand damage and wind erosion. "The biggest challenge will be to stabilize Mingsha Mountain," says Qu. The fate of one of the more vibrant vestiges of the old Silk Road may depend on it. **–RICHARD STONE**

CREDIT: THE GETTY CONSERVATION INSTITUTE

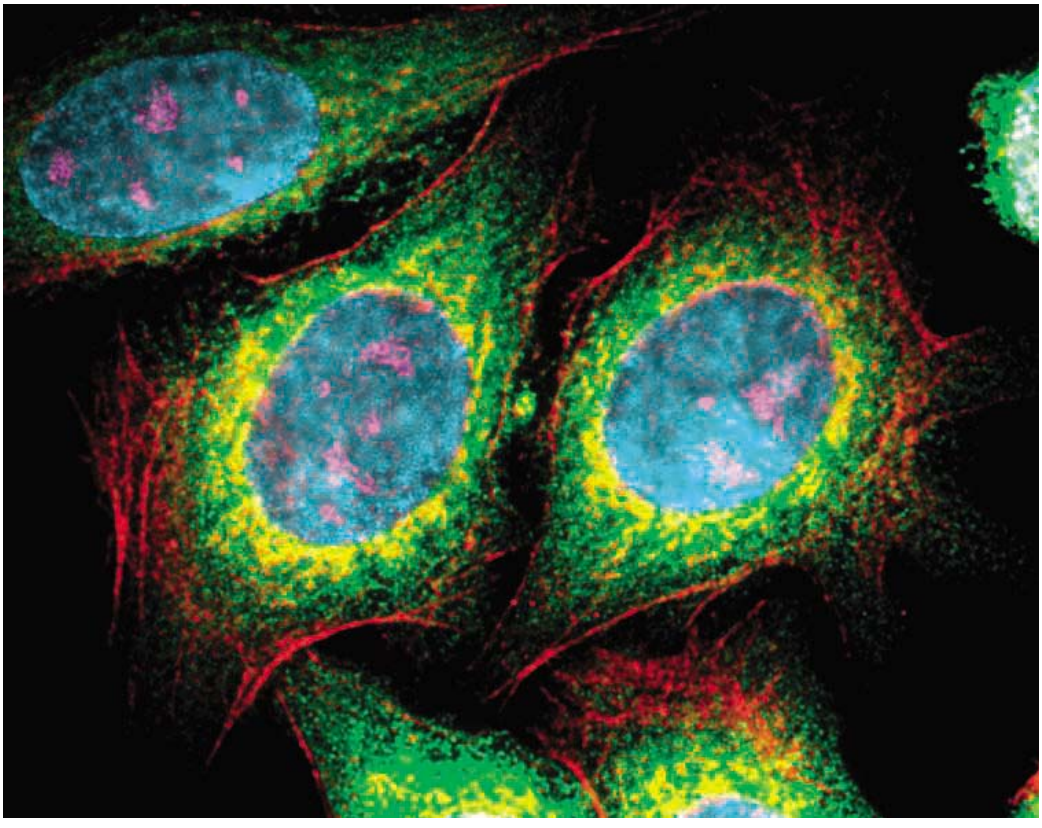

Bright invaders. Nanosized quantum dots pervade cells, tinting each structure a different color.

NANOTECHNOLOGY

Can High-Speed Tests Sort Out Which Nanomaterials Are Safe?

A flood of strange new substances based on ultrasmall particles is forcing researchers to reinvent toxicology

If you've ever marveled at a painter mixing colors on a palette, you have a taste of what nanotechnologists feel when designing materials at the smallest scale. Nanoscientists today mix collections of different atoms to create a multitude of novel pint-sized particles with a vast array of new electronic, optical, catalytic, and chemical properties. Iron oxide particles, for example, are proving exceptional as contrast agents for medical imaging. Bits of titanium dioxide harvest sunlight in solar cells. And on and on. "These are materials with wonderful properties," says Fanqing Chen, a biomedical scientist at Lawrence Berkeley National Laboratory in California. "Their contribution to science, technology, and the economy is going to be huge."

But the remarkable diversity of nanomaterials is also one of the field's biggest headaches. With potentially thousands of novel materials under investigation, health and safety regulators are left scratching their heads over which are safe and which are potentially toxic to humans or other species. That uncertainty threatens to undermine public confidence in nanotechnology and stymie the development of what is expected to be a major global economic engine. What's worse, traditional toxicology studies that test one material at a time appear woefully inadequate to the task of sorting the dangerous from the benign. "If we continue with the classical toxicological assessment [for nanomaterials], we will never catch up with this work," says Andre Nel, a nanomaterials toxicologist at the University of California, Los Angeles.

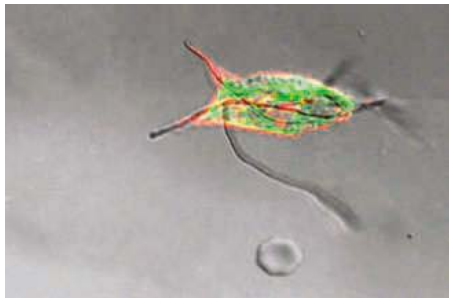

Benign or harmful? Rat lung cell attempts to ingest a carbon nanotube. Clumping nanotubes can stymie the animals' immune systems.

In hopes of picking up the pace, Nel and a handful of other toxicologists around the world are creating batteries of high-speed assays for testing the toxicity of hundreds and even thousands of different nanomaterials at the same time. The assays involve exposing different types of cells to nanoparticles and monitoring the cells for changes, such as DNA damage, alterations in gene expression, cell death, and impacts on cell growth and proliferation. It's still too early to say whether these hopes will pan out. But at a minimum, nanotoxicologists hope high-throughput studies will help them prioritize nanomaterials that should undergo conventional toxicology tests.

Clearly, there is cause for concern about the toxicity of some nanomaterials. Early studies with soccer-ball–shaped carbon fullerenes revealed, for example, that the particles can damage brain cells in fish. Conventional toxicology studies also raised yellow flags about the straw-shaped cousins of fullerenes called carbon nanotubes. When the lung tissue of rats was flushed with high levels of nanotubes, researchers found that the tubes clumped together, making it difficult for the animals' immune systems to clear them from their bodies. Still other studies have raised concerns about particles mostly considered harmless at larger sizes, such as titanium dioxide nanoparticles.

Unfortunately, such studies are slow and expensive. A single in vivo animal study can cost $50,000. In addition, it's often difficult to extrapolate how a material tested in one tissue will affect others. It's even harder to extend that one study to determine how other nanomaterials will behave. The study that showed fullerenes can damage the brain cells of fish, for example, says little about exposure to particles of iron oxide, silicon dioxide, or carbon nanotubes.

CREDITS (TOP TO BOTTOM): QUANTUM DOT CORP.; STONE AND DONALDSON, "SIGNS OF STRESS," *NATURE NANOTECHNOLOGY*, VOL. 1, 2006 OCTOBER

To confound matters further, particles can also come with different coatings that alter their properties, and they can even acquire new coatings upon entering the environment or the human body. Chen notes that some of his team's early studies reveal that the toxicity of nanoparticles can change even when they change size or shape but not composition. "They show different effects, even if they are the same material," Chen says. "It looks like there is an additional dimension … when you are dealing with nanomaterials."

Faced with such complexity, researchers have begun looking to high-throughput testing techniques as a route to better, faster, and cheaper toxicology studies. Drug companies have long used similar methods to test compounds for curing and preventing disease. But because toxicologists must look for not just one positive outcome but potentially dozens of negative ones, they face a much tougher task: developing a battery of in vitro assays using a variety of cell types to assemble a fingerprint of ways a particular nanoparticle affects different tissues.

One of the biggest such efforts to date is ToxCast, a 5-year initiative by researchers with the U.S. Environmental Protection Agency in Research Triangle Park, North Carolina. Launched in 2007 to speed up toxicity testing on chemicals in general, ToxCast is nearing the end of its pilot phase. Researchers are examining 320 different chemicals, such as pesticides, that all have previously undergone extensive conventional toxicological screens, says Keith Houck, an EPA toxicologist who is helping to develop the program. Houck says he and his colleagues are testing each chemical in a wide variety of cell-based assays, looking for 400 different "endpoints" that could signal danger to living organisms.

"What we are trying to do is get a broad bioactivity profile for each compound and correlate those with toxicology studies we have," Houck says. In the program's second phase, set to begin in 2009, Houck says ToxCast researchers will evaluate probably about another 1000 compounds, which will likely include several varieties of nanomaterials. Houck notes that the number of different starting nanomaterials, coupled with possible coatings and other molecules that could interact with them, makes it impossible to test every combination. "But we can use computational approaches to hopefully test the right ones and make some predictions about which materials are of most concern." The compounds determined to be the riskiest will then be given top priority for conventional toxicity screening.

Although the results from ToxCast won't be known for years, smaller scale efforts are already giving a sense of what the approach can offer. In a paper published in 2006 in *Nano Letters*, for example, Nel and his colleagues compared the effects of ambient ultrafine particles such as carbon black—produced in diesel exhaust—with the effects of manufactured nanoparticles such as chemically functionalized fullerenes and polystyrene. Using a series of assays that monitored levels of oxidative stress and cytotoxicity, they found clear differences in cellular responses to different particles. Functionalized polystyrene particles topped the list of materials causing the most oxidative damage to mouse macrophage cells.

"In nature, there are only a dozen or so major pathways that lead to 90% of toxicological outcomes," Nel says. So Nel and his colleagues are currently working to set up a broader set of screens to systematically monitor these pathways, conducting up to about 1000 cell-based assays a day. The screens, he says, will look for changes in addition to oxidative stress and cytotoxicity, such as DNA damage and changes in cell growth and proliferation. As ToxCast is doing, he then intends to gauge which nanomaterials are the likeliest to be harmful and put them first in line for more rigorous tests. "Instead of going through the haystack handful by handful, we've come up with a procedure to get rid of the hay," Nel says.

Chen has been developing a related approach. In another 2006 *Nano Letters* paper, he and colleagues looked at the genetic response of human skin fibroblasts when exposed to different nanoparticle-based imaging compounds. For their tests, Chen's team used gene chips that tracked how gene expression changed in about 22,000 genes in response to different types and doses of nanoparticles. Only about 50 of the genes showed significant changes. From the pattern, the Berkeley team concluded that—unlike several of the naked nanoparticles—particles coated with a polymer called polyethylene glycol induced minimal impact on exposed cells.

In a more recent study, Ralph Weissleder, a molecular imaging expert at Harvard Medical School in Boston, and colleagues have also turned to high-throughput analysis to sort out which nanoparticles have the best shot at succeeding as medicines. Nanoparticles are currently being developed as imaging agents, drug carriers, and, in some cases, therapeutic drugs themselves. A multitude of such compounds are under development, many of them coated with different small molecules to help target them to different tissues in the body, Weissleder says. But drugmakers want to avoid sinking too much time and effort into nanoparticles that have no shot at being approved for in vivo use because of their toxicity.

So Weissleder and his colleagues set out to flag potential troublemakers. They evaluated 50 different nanomaterials at four concentrations on four cell types with four different assays. In the 27 May issue of the *Proceedings of the National Academy of Sciences*, they reported that they had found broad, consistent patterns of activity, although different cell types behaved very differently. "There is not a single test that will predict how nanomaterials will behave in vivo," Weissleder says. But the batteries of cell assays can help researchers decide which ones are likely to be safest for human studies, he says.

Taken together, the early studies suggest that high-throughput assays could vastly speed up toxicological screening, Weissleder and others say. They can't do everything, Houck cautions: "In vitro assays won't ever replicate a whole body." Still, if they can begin to sort out which types of nanoparticles pose the biggest risk, they could encourage targeted testing of those compounds and thereby help shore up faith in nanotechnology's future.

–ROBERT F. SERVICE

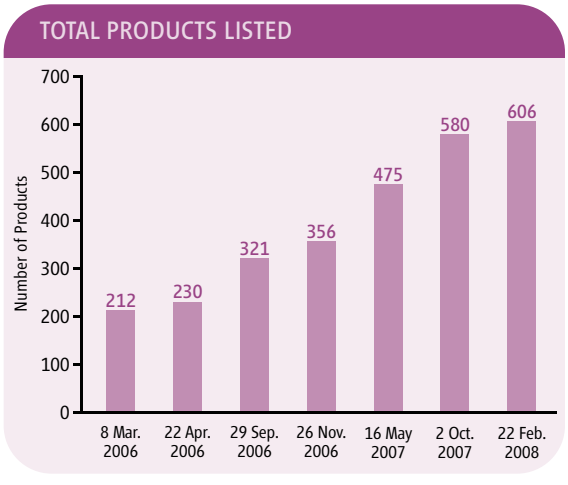

In demand. According to the Woodrow Wilson International Center for Scholars, the number of consumer products containing nanoparticles nearly doubled in 14 months.

SOURCE: THE PROJECT ON EMERGING NANOTECHNOLOGIES

Birth of a policy 1042

Monitoring biodiversity 1044

Star maker 1047

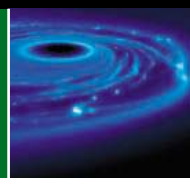

LETTERS | BOOKS | POLICY FORUM | EDUCATION FORUM | PERSPECTIVES

LETTERS

edited by Jennifer Sills

An Editor's Checklist

THE LETTER FROM M. RAFF *ET AL*. ("PAINFUL PUBLISHING," 4 JULY, P. 36) RAISES A CRUCIAL issue about peer review. A young investigator who is challenged to undertake more experiments in order to get a paper published is not usually in a position to argue. To make sure additional work is justified, an editor asking for extra experiments should be able to answer the following questions: (i) Has the reviewer rigorously justified each suggested experiment? (ii) How much time and investment of resources such as animals and materials will likely be involved? (iii) Will the additional experiments strengthen a specific, identified weakness of the manuscript rather than move the work on to the next stage or to one side? (iv) Does the reviewer have any conflicts of interest in making these requests? For example, would the reviewer's current research program benefit from information generated by the additional experiments? By asking these questions, the editor can intervene on behalf of the researcher, ensuring the best final product for publication.

R. W. GUILLERY

Department of Anatomy, Marmara University, Istanbul 34668, Turkey.

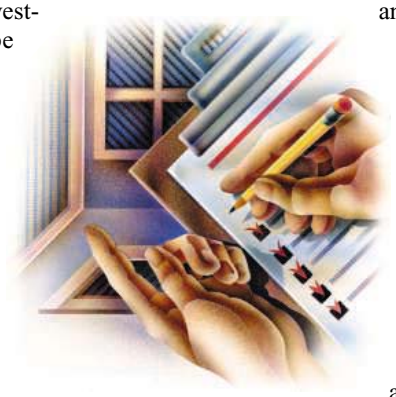

High-Profile Journals Not Worth the Trouble

RAFF, JOHNSON, AND WALTER ("PAINFUL publishing," Letters, 4 July, p. 36) make some excellent points about how peer reviewers for journals should conduct themselves. There is a fine line between being too demanding by requiring a lot of extra work and making sure a paper with important results gets out to the scientific public in a timely way.

In my laboratory, there is no pressure to publish in journals like *Science*, *Nature*, or *Cell* because we simply do not send our manuscripts to them anymore, no matter how important or high-impact we think the work may be. We have found that there is an excellent group of other, first-line journals of cell biology for which we do not need to subject ourselves to the type of competition required for publication in these three journals.

When I have served on peer-review panels, I have fought against the common practice of relating grant awards to publication in high-profile journals such as *Science*, *Nature*, and *Cell*. It is the impact and importance of the work that matters (thereby requiring the peer reviewers to read the applicant's papers quite thoroughly), not where the work is published.

JOEL L. ROSENBAUM

Department of Molecular, Cellular, and Developmental Biology, Yale University, New Haven, CT 06520–8103, USA.

Taking Responsibility for Scientific Discourse

RECENT EXPLORATION OF THE DARKER SIDE of the scientific literature (*1*) supports the idea that more than honest error plagues modern scientific discourse (*2*). Many solutions focus on improving administrative oversight (*3*). I believe that a greater burden of responsibility and potential for change falls on each of us. Here, I delineate some practices that might transform modern discourse.

Rapidly test competing hypotheses with unconventional search engines. In one example from my own experience, a Google search yielded an important paper as the first hit [(*4*), as cited in (*5*)]; this paper was much more challenging to find in a search of the same terms on PubMed. It is time-prohibitive to collect and read all cited papers, leading to a problematic compression of breadth. Multiple reviewers can ameliorate this problem, but the danger remains of creating an environment where responsibility is undesirably diffused.

Seek statistical consultation from an expert or, better, experts. Although statistical training is a core subject in graduate programs, too often the skills acquired are inadequate to deal with the actual complexity of the acquired data. Greater quantitative rigor extending to all facets of data-handling should be the common goal. Many journals now use an expert statistical reviewer; this should become the norm.

Describe your data analyses and results to a colleague who is not a coauthor. Such communication increases the likelihood of noticing an oversight in design, analysis, or logic. If such dialogue took place on a large scale, the implications for translational research could be substantial.

Fight to publish results that are clearly negative. The scientific literature and grant system are focused on positive results, but robust negative findings, if highlighted by journals, would prevent future labs from wasting time and money recreating these efforts.

Examine unspoken pressures. Too often, scientific acts are affected by influences other than those of "pure" science, such as conducting unblinded reviews, affirming popular literature conclusions despite contrary empirical evidence, meeting promotion requirements, sustaining unhealthy hierarchies in laboratories, fulfilling a priori grant data despite insufficient statistical power, and keeping one's constructed intellectual towers

CORRECTIONS AND CLARIFICATIONS

News of the Week: "Senate inquiry on research conflicts shifts to grantees" by J. Kaiser (27 June, p. 1708). The article incorrectly suggested that NIH can fine institutions for violating conflict-of-interest policies. In addition, total consulting income since 2000 reported by the three Harvard researchers was $4.2 million, not $3.6 million.

Special Issue on Forests in Flux: News: "A second chance for rainforest biodiversity" by E. Stokstad (13 June, p. 1436) states that Daniel Ludwig hoped to grow *Eucalyptus* in the Amazon. In fact, he intended to plant an Asian tree, *Gmelina arborea*. After that failed, he switched to *Eucalyptus*. In addition, the field work was managed by Jos Barlow.

Special Issue on Forests in Flux: News: "Critical time for African rainforests" by R. Koenig (13 June, p. 1439). On page 1440, the credit should read CARPE, not CAPRPE.

Reports: "Using engineered scaffold interactions to reshape MAP kinase pathway signaling dynamics" by C. J. Bashor *et al*. (14 March, p. 1539). There were two errors in Fig. 4 in describing the precise components used to construct specific circuits. In Fig. 4B, the leucine zippers attached to both the negative and positive modulators should have both been colored gray, since both modulators were fused to identical zippers (rather than to zippers with different affinity). The label was also incorrect: The resulting negative modulator does not bind with high affinity. In Fig. 4D, the leucine zipper attached to the positive modulator should have been colored black, since this modulator was fused to a zipper with higher affinity than the zipper (colored gray) fused to the negative modulator. The zipper is now black, and "high-affinity" has been added to the label. The corrected figure panels are shown here. In the main text, in the second sentence in the penultimate paragraph on page 1541, the words "high affinity" should be deleted. The correct sentence should read "In this accelerator circuit, the positive modulator (Ste50-zipper) was constitutively expressed, but the negative modulator (Msg5-zipper) was inducibly expressed." In the first sentence on page 1542, the words "higher affinity" should be inserted such that the corrected sentence reads "We built a circuit with enhanced ultrasensitive switch behavior by constitutively expressing a negative modulator (Msg5-zipper) and inducibly expressing a positive modulator (Ste50-zipper, higher affinity) (Fig. 4D)." In the legend for Fig. 4 (page 1542), the third-to-last sentence should be corrected to read "Negative modulator is displaced by inducibly expressed positive modulator fused to a higher-affinity zipper (Kd = 6.1 versus 41 nM)." The corresponding errors are also corrected in fig. S3 and tables S1 and S2 of the supporting online material, which list the exact plasmids and constructs used for construction of each circuit.

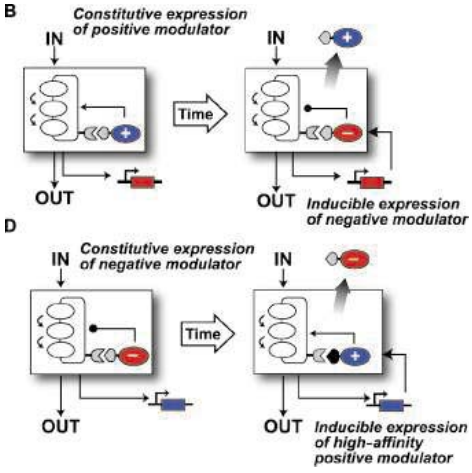

TECHNICAL COMMENT ABSTRACTS

COMMENT ON "Protein Sequences from Mastodon and *Tyrannosaurus rex* Revealed by Mass Spectrometry"

Pavel A. Pevzner, Sangtae Kim, Julio Ng

Asara *et al*. (Reports, 13 April 2007, p. 280) reported sequencing of *Tyrannosaurus rex* proteins and used them to establish the evolutionary relationships between birds and dinosaurs. We argue that the reported *T. rex* peptides may represent statistical artifacts and call for complete data release to enable experimental and computational verification of their findings.

Full text at www.sciencemag.org/cgi/content/full/321/5892/1040b

RESPONSE TO COMMENT ON "Protein Sequences from Mastodon and *Tyrannosaurus rex* Revealed by Mass Spectrometry"

John M. Asara, Mary H. Schweitzer, Lewis C. Cantley, John S. Cottrell

Endogenous peptide sequences extracted from a 68-million-year-old *Tyrannosaurus rex* fossil bone and obtained by mass spectrometry have been shown to be statistically significant based on protein database searches using two different search engines and similarity comparisons to authentic tandem mass spectrometry spectra. Specifically, we have validated the sequence GVVGLP$_{(OH)}$GQR.

Full text at www.sciencemag.org/cgi/content/full/321/5892/1040c

buffered from attack. Although these factors could be attributed to effectively playing the modern "game" of science, failure to consider their influence will guarantee their undesirable expression (*6*).

From an organizational level, refinement of guidelines for grant and paper review will be invaluable to improve both the process and products of science. However, I fear the solutions developed can only be as healthy and sustainable as an individual's resolve to infuse meaningful content. The responsibility for scientific progress has seemingly shifted from the individual to the literature as a whole, with this latter agent being a poor policeman and historian (*7*). Continued dilution of responsibility within scientific discourse and lack of personal engagement is at our collective peril. Each intentional discourse provides the opportunity for engagement. Thrown together at the collective target known as science, I have little doubt that these efforts will hit their mark.

SETH D. FRIEDMAN

Children's Hospital and Regional Medical Center, Department of Radiology, University of Washington, Seattle, WA 98195, USA.

References and Notes

1. S. L. Titus, J. A. Wells, L. J. Rhoades, *Nature* **453**, 980 (2008).
2. J. P. Ioannidis, *PLoS Med*. **2**, e124 (2005).
3. M. Raff, A. Johnson, P. Walter, *Science* **321**, 36 (2008).
4. F. G. Blankenberg, R. W. Storrs, L. Naumovski, T. Goralski, D. Spielman, *Blood* **87**, 1951 (1996).
5. S. D. Friedman, *Science* **321**, 640c (2008).
6. C. G. Jung, in *The Portable Jung*, J. Campbell, Ed. (Penguin, New York, 1971), pp. 285–286.
7. A. Tatsioni, N. G. Bonitsis, J. P. Ioannidis, *JAMA* **298**, 2517 (2007).
8. This work is supported by National Institute of Mental Health grant K01 MH069848.

The Carrageenan Diet: Not Recommended

WE READ WITH GREAT INTEREST AND CONCERN recent reports of the spread of carrageenan-producing seaweeds in coral reefs in the Bay of Bengal, as well as in Butaritari, Kiribati, and other Pacific atolls ["Seaweed invader elicits angst in India," P. Bagla, News of the Week, 6 June, p. 1271, and (*1*)]. The bioinvasion of carrageenan-producing, coral-destroying algae in remote Pacific atolls and marine reserves in the Gulf of Mannar Marine National Park is unfortunately a metaphor for the invasiveness of carrageenan in the Western diet and in other commonly used products. Although carrageenan exposure has been associated with development of inflammation in experimental models for decades (*2*), its use in processed foods (including infant formula and nutritional supplements) and other manufactured products (including pharmaceuticals, cosmetics, and toothpaste) continues to increase. In view of uncertainty about the safety of consumption of carrageenan-containing products, the efforts to cultivate carrageenan-producing seaweeds seem ill-advised.

At its 68th meeting in June 2007, the Joint Expert Committee on Food Additives (formed by the Food and Agriculture Organization of the United Nations and the World Health Organization) advised against the continued

use of carrageenan or processed Eucheuma seaweed (PES) in infant formulas (*3*). It also recommended a new dietary exposure evaluation of carrageenan intake, noting that previous estimates of carrageenan intake might be outdated. Also, the Scientific Committee on Food of the European Commission advised and the European Commission adopted the recommendation that the content of carrageenan of size less than 50,000 Da in food products should not exceed 5%, if feasible (*4*). In response to this, carrageenan manufacturers performed round-robin testing of food-grade carrageenan and PES samples and found >5% content over 50,000 Da, as well as marked variation in their determinations (*5*). We have published several reports about carrageenan-induced effects on human colonic epithelial cells in tissue culture and in ex vivo human and mouse colonic tissues. We also published a review of the harmful effects of carrageenan in many animal experiments (*6*–*10*).

With these considerations in mind, we are concerned not only about the extraordinary overgrowth associated with the attempted cultivation of carrageenan near the Gulf of Mannar Marine National Park and in Pacific sites, but the thinking associated with the spread of the use of carrageenan in products for human consumption and the increased dependence on carrageenan farming in developing economies, as in Indonesia and the Philippines. The efforts at cultivation of carrageenan-producing seaweed have demonstrated how a natural product can produce harmful effects to the marine environment; similarly, harmful effects to humans may be attributable to carrageenan exposure.

JOANNE K. TOBACMAN, SUMIT BHATTACHARYYA, ALIP BORTHAKUR, PRADEEP K. DUDEJA

Department of Medicine, University of Illinois, Chicago, IL 60612, USA.

References

1. C. Pala, "Corals, already in danger, are facing new threat from farmed algae," *The New York Times*, D3, 8 July 2008.
2. J. K. Tobacman, *Environ. Health Perspect.* **109**, 983 (2001).
3. Joint FAO/WHO Expert Committee on Food Additives, 68th meeting, Geneva, "Summary and Conclusions," 12 July 2007, JECFA 68/SC; www.fao.org/ag/agn/agns/files/jecfa68_final.pdf.
4. Scientific Committee on Food, European Commission Health & Consumer Protection Directorate-General, "Opinion of the Scientific Committee on Food on Carrageenan" (SCF/CS/ADD/EMU/199 Final, 2003); http://ec.europa.eu/food/fs/sc/scf/out164_en.pdf.
5. Marinalg Working Group on Molecular Weight Determination, "Technical position on measurements related to meeting the EC molecular weight distribution specification for carrageenan and PES" (2006); www.marinalg.org/papers/reportJan2006.pdf.
6. A. Borthakur, S. Bhattaycharyya, P. K. Dudeja, J. K. Tobacman, *Am. J. Physiol. Gastrointest. Liver Physiol.* **292**, G829 (2007).
7. S. Bhattacharyya, A. Borthakur, P. K. Dudeja, J. K. Tobacman, *J. Nutr.* **138**, 469 (2008).
8. S. Bhattacharyya *et al.*, *J. Biol. Chem.* **283**, 10550 (2008).
9. S. Bhattacharyya, P. K. Dudeja, J. K. Tobacman, *Biochim. Biophys. Acta* **1780**, 973 (2008).
10. S. Bhattacharyya, A. Borthakur, P. K. Dudeja, J. K. Tobacman, *Dig. Dis. Sci.* **52**, 2766 (2007).

Letters to the Editor

Letters (~300 words) discuss material published in *Science* in the previous 3 months or issues of general interest. They can be submitted through the Web (www.submit2science.org) or by regular mail (1200 New York Ave., NW, Washington, DC 20005, USA). Letters are not acknowledged upon receipt, nor are authors generally consulted before publication. Whether published in full or in part, letters are subject to editing for clarity and space.

POLICY-MAKING

Cybernetic Birth Control

Erik A. Mueggler

China's 1979 decision to allow only one child per couple was among the most consequential policy decisions in a century chock-full of state projects to transform populations. The one-child policy replaced a project called "later, longer, fewer," which encouraged couples to have fewer children spaced more widely apart. Relatively flexible, "later, longer, fewer" took into account the needs and values of peasants, about 80% of the population, and it cut the crude birthrate in half between 1971 and 1978. In contrast, the one-child policy was uncompromising. China's leaders employed coercive methods to achieve rapid and universal fertility reduction. Blind to the social and political realities of rural areas, the policy met immediate resistance there, countered with ruinous fines, mass sterilizations, and forced abortions. Rural cadres found the policy increasingly difficult to carry out as land use, economy, and governance were restructured in the early 1980s. It was slowly relaxed and liberalized, and by 1984–1985 it became, in many areas, a de facto two-child policy. But through the 1980s and 1990s, there were further cycles of renewed commitment to fertility reduction and slow liberalization. Today, though the goals of the policy are deemed to have been largely met, China's government continues to promote a one-child rule. Whatever the benefits of the policy in reducing fertility more quickly than socioeconomic development alone might have done, its costs have been huge: enormous human trauma, a rapidly aging population with inadequate social security, and a severely distorted sex structure (120 boys to 100 girls in 1999).

Anthropologist Susan Greenhalgh (University of California, Irvine) is our most surefooted guide to China's adventure in mass birth planning. She has pursued the topic for more than 20 years, with both detailed field studies of peasant experience and wide-ranging investigations of policy-making. In *Just One Child*, Greenhalgh focuses on the conception and birthing of the one-child policy. What was the science that convinced China's leaders that the nation was experiencing a potentially disastrous crisis in population? How was this science created, how did it gain the trust of the leaders, and how did it win out over alternative narratives about China's population? How were the goals of one child per couple and an optimal population (initially) of 700 million arrived at? How were these goals transformed into policy? Why did China's leaders decide to ignore the social and political realities of the rural areas in pursuit of these goals?

Just One Child
Science and Policy in Deng's China

by Susan Greenhalgh

University of California Press, Berkeley, 2008. 425 pp. $55, £32.95. ISBN 9780520253384. Paper, $21.95, £12.95. ISBN 9780520253391.

Greenhalgh engages these questions with a microhistory of relationships between science and policy. At the center of the book is the remarkable story of how a cybernetic science of population, employing methods developed for missile guidance systems, came to occupy the center of population policy-making. In 1978, Song Jian was a control theorist, working on missile systems. He and his fellow defense scientists were the most protected and privileged of China's scientific elite, during a time when most social and natural sciences had been decimated by the Cultural Revolution. In 1978, Song and his team, inspired by the work of an international network of population scientists known as the Club of Rome, began to apply control theory to the study of China's population. The team's projections—employing mathematics far beyond the grasp of China's policy-makers, founded on shaky and incomplete data, and completely free of any consideration of social life—presented a clear and alarming narrative. Left to grow at 1978 rates, China's population would top six billion by the year 2000. Given ideal levels of economic development, China's resource base could optimally support a population of between 650 and 700 million (the 1978 population was 980 million). Were China to rapidly adopt a universal one-child policy, it could limit the population to a manageable peak of 1.05 billion in 2004 and decrease it to optimal levels by 2080. A blanket one-child rule was, Song came to insist, the only way to ensure that China would not be crippled by unsustainable population growth in the future.

Greenhalgh draws on the field of science and technology studies (particularly as framed by Bruno Latour) to describe the development of this cybernetic science of population. She shows how Song and his team promoted their science, erected boundaries between it and older economic and social-science approaches to population, and created networks of allies that brought it to the attention of the upper echelons of the policy-making elite. China's chief policy-makers,

Promoting the one-child policy. Posters, such as this 1986 example, were widely used in the campaign to curb the projected problematic growth in China's population.

CREDIT: IISH STEFAN R. LANDSBERGER COLLECTION (WWW.IISG.NL/~LANDSBERGER)

The reviewer is at the Department of Anthropology, 101 West Hall, University of Michigan, 1085 South University Avenue, Ann Arbor, MI 48109–1107, USA. E-mail: mueggler@umich.edu

alarmed and inspired by Song's projections, ended up adopting his assumptions and proposals wholesale. Eventually, as the limitations of Song's approach began to emerge, the science behind the one-child policy was "black boxed"—made off-limits to investigation and discussion—even as the policy itself remained foundational to Chinese governance. Greenhalgh pries open this box with persistence and analytical sophistication, revealing the social mechanisms through which the science was produced and transformed into policy.

Just One Child is based on 20 years of interviews with decision-makers at many levels and the close study of Party documents and scientific articles. The book is resolutely interdisciplinary, adopting methods from anthropology, science studies, political science, and population studies. Greenhalgh does not deny that China has a "real" population problem. But she insists that this reality is co-constituted by nature, science, and politics and that any approach to understanding it must involve close investigation of these three arenas in their interaction. As a study of scientific policymaking in China, *Just One Child* is without peer. Many readers might also find it to be a useful model for investigating the relationships between science and policy in other regimes.

10.1126/science.1159273

DEMOGRAPHY

A Polemic Against Control

John C. Caldwell

Interesting and well written, *Fatal Misconception* is also deeply flawed and in essence a polemic. Matthew Connelly's account derives much of its force from the selective use of adjectives, adverbs, and nouns that make efforts to limit population growth sound at all times like a conspiracy. In the preface, the reader is disarmed by being told that the author was an eighth child who would not be alive if his parents had used contraception to constrain the size of their family. Connelly (a historian at Columbia University) also relates that his view of the population control movement changed radically as a result of an intense study of the relevant documents. His main sources are the archives of foundations, governments, and other institutions. He tells us that "This is a history of how some people systematically devalued *both* the sanctity of life *and* the autonomy of the individual."

My qualifications for commenting on the book are half a century spent largely watching the development of the population control movement, much of the time in the field examining the movement's impact on families. I was wary of being too tightly linked with efforts to limit population growth, and everywhere insisted on having a university appointment (which I managed except for one year, 1968, with the Population Council in New York). Pat Caldwell and I were apprehensive of such population programs getting out of hand, and we were acquainted at its early stages with the monstrous program (which pushed compulsory sterilization) carried out in India's Emergency of 1975–77. We rushed to Delhi to tell scholars and diplomats what was happening; the latter replied that we should not interfere with Indians doing things in their own way. I also wrote a number of papers and a book (*1*) explaining why most Africans were unlikely at that time (the late 1970s) to benefit from a smaller family.

Fatal Misconception
The Struggle to Control World Population

by Matthew Connelly

Belknap (Harvard University Press), Cambridge, MA, 2008. 537 pp. $35, £22.95, €24.50. ISBN 9780674024236.

In his attack on the family planning programs, Connelly makes several points that require brief responses. The first is that there is an intellectual thread linking eugenics groups, anti-immigration activists, racists, and the population control movement. From my experience, the leaders—and, even more so, the expatriate coordinators in developing countries—were not motivated by eugenics but by a desire to improve family life and fortunes as well as national development.

More important, the great majority of "acceptors" (who tried birth control), even those who complained of side effects, wished to continue contraception. Many of them stopped for periods of time or changed methods (*2*), but no more than we found to be the case in a study of a Western city, Melbourne, Australia (*3*). In addition, the children of acceptors almost all believed that their parents had been right to limit family size (*2*).

Connelly's charge that proof was lacking for the proposition that reduced natural increase would foster economic growth is more difficult to evaluate. The evidence is ambiguous. The more salient argument is that the early start of family planning programs may have lowered the eventual global population by one or two billion people, a margin that could prove critical in terms of pressure on food, petroleum, water, and other resources. Without that reduction, our carbon footprint would certainly be greater.

The author clearly feels that fertility decline would have begun spontaneously as death rates of children fell and incomes and educational levels rose. The delay in restricting population growth would probably have been greater than Connelly believes. Throughout our work in rural south Asia and sub-Saharan Africa, couples almost invariably explained that their parents could not have controlled fertility because contraception had not been explained to them and they had no access to contraceptives. The couples attested that they would have been in the same situation if family planning programs had not arrived.

The book implies that the West was ruthlessly applying its own experience to non-Western countries. In fact, family planners were merely following the only path known to them for inducing an industrial revolution and higher living standards by replicating the characteristics of industrialized countries. Small families were not as strongly advocated or assisted as changes in agriculture, education, and such public health programs as immunization.

The fatal misconceptions Connelly stresses were such undesirable programs as the vasectomy camps in Kerala, the Indian Emergency, the one-child family of China, and the Dalkon Shield. None of these events was guided by the mainline family planning movement, and most can be understood as a product of political authoritarianism. Even the small assistance given to China can be seen as an attempt to keep in touch with what was happening, in the hope that a kinder program might result.

Fatal Misconception is the result of an awesomely sustained research effort. But it remains a lawyer's argument, with a far greater effort given to making Connelly's case than to presenting a balanced treatment. Sexual activity and reproduction are matters that seem to excite much frenzy. That said, it should be added that the book is eminently readable and informative.

References

1. J. C. Caldwell, *Theory of Fertility Decline* (Academic Press, London, 1982).
2. J. C. Caldwell, P. H. Reddy, P. Caldwell, *The Causes of Demographic Change: Experimental Research in South India* (Univ. Wisconsin Press, Madison, 1988).
3. J. C. Caldwell, H. Ware, *Popul. Stud.* (London) **27**, 7 (1973).

10.1126/science.1159014

The reviewer is at the Demography and Sociology Program, Research School of Social Sciences, Australian National University, Canberra, ACT 0200, Australia. E-mail: jack.caldwell@anu.edu.au

ECOLOGY

Toward a Global Biodiversity Observing System

Tracking biodiversity change is increasingly important in sustaining ecosystems and ultimately human well-being.

R. J. Scholes,[1*] G. M. Mace,[2] W. Turner,[3] G. N. Geller,[4] N. Jürgens,[5] A. Larigauderie,[6] D. Muchoney,[7] B. A. Walther,[6] H. A. Mooney[8]

Biodiversity is a composite term used to embrace the variety of types, forms, spatial arrangements, processes, and interactions of biological systems at all scales and levels of organization, from genes to species and ecosystems (*1*), along with the evolutionary history that led to their existence (*2*). In part because of this complexity, universally applicable measures of biodiversity have proven elusive. Commonly used measures, such as the number of species present, are strongly scale-dependent and only reveal a change after species have been lost. Indices incorporating several proxy signals are potentially sensitive, but their arbitrariness obscures underlying trends and mechanisms. Integrated measures (*3*, *4*) are both sensitive and achievable, but more research is needed to construct the globally robust relations between population data, genetic variation, and ecosystem condition that they require.

The need for national to global-scale biodiversity measurements has been highlighted by the adoption of a target to "reduce the rate of loss of biodiversity by 2010" by the 190 countries that are parties to the Convention on Biological Diversity (CBD) (*5*, *6*). As we approach the target date, it is clear that this intention may suffer if we cannot effectively assess progress. The recent Conference of Parties to the CBD in Bonn, Germany, reinforced commitment to the goal, while acknowledging that much still needs to be done to reach it. Despite the absence of comprehensive data, there is little dispute that biodiversity continues to decline with uncertain, but potentially serious, consequences for society (*7*).

Unlike, for instance, the Framework Convention on Climate Change, there is no widely accepted and globally available set of measures to assess biodiversity. Consequently, the community has fallen back on a range of existing data sets gathered for other purposes. Currently, in the CBD process alone, there are ~40 measures reflecting 22 headline indicators in seven focal areas (see Biodiversity Indicator Partnership, www. twentyten.net). It seems unlikely that this set will provide clear messages to decision-makers (*8*).

There is no general shortage of biodiversity data, although it is uneven in its spatial, temporal, and topical coverage. The problem lies in the diversity of the data and the fact that it is physically dispersed and unorganized (*9*). The solution is to organize the information, to unblock the delivery pipeline between suppliers and users, and to create systems whereby data of different kinds, from many sources, can be combined. This will improve our understanding of biodiversity and will allow the development of fit-for-purpose measures of its condition over time. The proposed Group on Earth Observations Biodiversity Observation Network (GEO BON) is a new global partnership to help collect, manage, analyze, and report data relating to the status of the world's biodiversity.

The Group on Earth Observations (GEO) was launched in 2002 in response to the widely identified need for adequate information to support environmental decision-making. GEO is a voluntary partnership of 73 national governments and 46 participating organizations. It provides a framework within which these partners can coordinate their strategies and investments for Earth observation. The GEO members are establishing a Global Earth Observation System of Systems (GEOSS, www.earthobservations.org) that provides access to data, services, analytical tools, and modeling capabilities through a Web-based GEO Portal (www.geoportal.org). GEOSS has identified nine priority "societal benefit areas" in its first decade. Biodiversity is one of them. U.S. National Aeronautics and Space Administration (NASA) and DIVERSITAS, the international programme of biodiversity science, accepted the task of leading the planning phase of GEO BON, in collaboration with the GEO Secretariat.

No single organization could build a "system of systems" such as the one envisaged. Many local, national, and international activities exist to record various genes, species, and ecosystems, as well as the services they provide to society. GEO BON aims to create a global network from these efforts by linking and supporting them within a scientifically robust framework. For example, GEO BON will facilitate the combination of top-down measures of ecosystem integrity from satellite observations with a host of bottom-up measures of ecosystem processes, population trends of key organisms, and the genetic basis of biodiversity arising from the latest field-based and molecular survey methods. The role of GEO BON is to guide data collection, standardization, and information exchange. The participating organizations retain their mandates and data ownership, but agree to collaborate in making part of their information accessible to others.

The process to develop a GEO BON took shape in April 2008, when some 100 biodiver-

[1]Council of Scientific and Industrial Research (CSIR), Natural Resources and Environment, Post Office Box 395, Pretoria 0001, South Africa. [2]Centre for Population Biology, National Environment Research Council, Imperial College London, Silwood Park, Ascot, Berkshire, SL5 7PY, UK. [3]Earth Science Division, U.S. National Aeronautics and Space Administration (NASA) Headquarters, 300 E Street S.W., Washington, DC 20546–0001, USA. [4]NASA Ecological Forecasting Program, Jet Propulsion Laboratory, California Institute of Technology, MS171-264, 4800 Oak Grove Drive, Pasadena, CA 91109–8099, USA. [5]University of Hamburg, BioCentre Klein Flottbek and Botanical Garden, Ohnhorststrasse 18, 22609 Hamburg, Germany. [6]DIVERSITAS, Muséum National d'Histoire Naturelle, Maison Buffon, 57, rue Cuvier–Case Postale 41, 75231 Paris, Cedex 05, France. [7]Group on Earth Observations (GEO), 7 bis, avenue de la Paix, Case Postale 2300, CH-1211 Geneva 2, Switzerland. [8]Department of Biological Sciences, Stanford University, Stanford, CA 94305, USA.

*Author for correspondence. E-mail: bscholes@csir.co.za.

CREDITS (TOP TO BOTTOM): R. J. SCHOLES

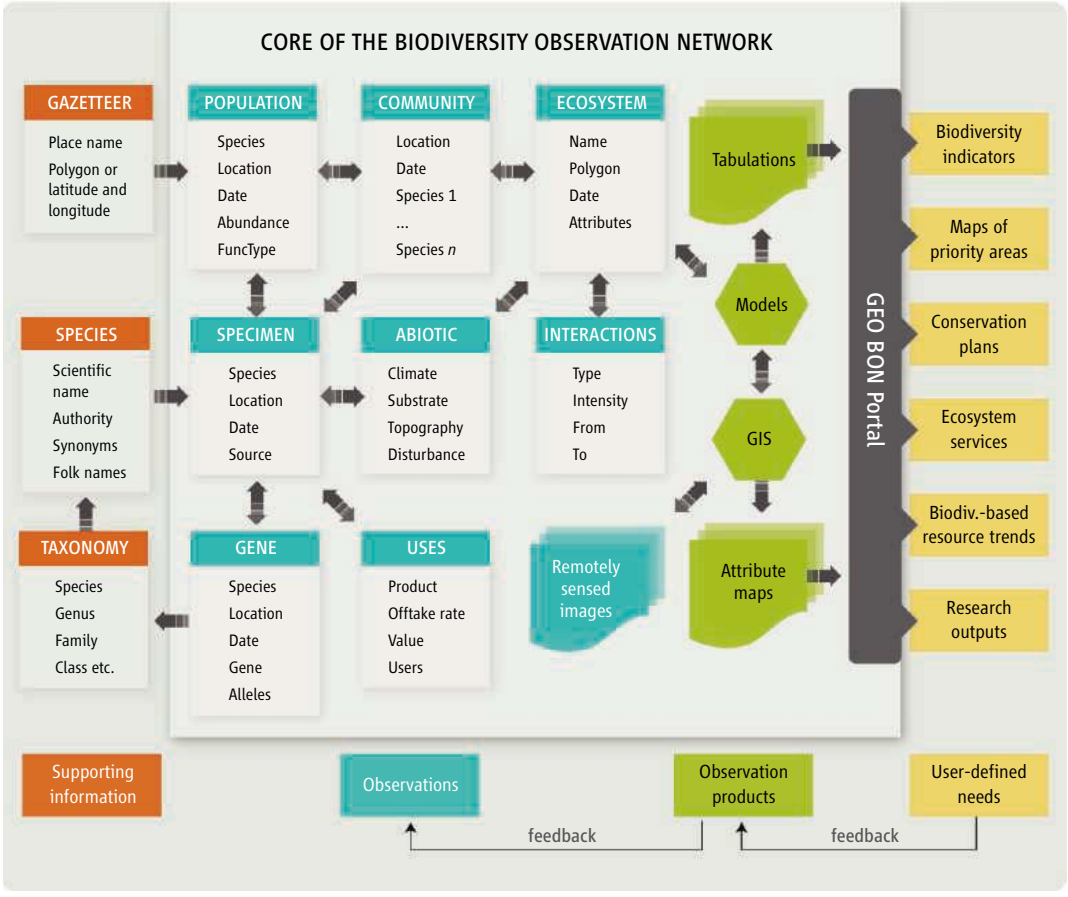

Integrated biodiversity observation system. The core data types, observation products, and end uses of an integrated biodiversity observation system are shown. Most of the elements already exist, but are incomplete or dispersed among a wide range of partners. The proposed implementation strategy involves linking them by using data-sharing protocols, followed by incremental, needs-led, and opportunistic growth. GIS, geographic information systems.

sity specialists representing over 60 scientific and intergovernmental organizations met at Potsdam, Germany, to complete the concept document. Seven working groups have been formed to draft an initial Implementation Plan by the end of the year. The key concept is a shared and interoperable system bringing data of different types and from many sources to bear on the information needs as defined by users (see figure, above). The primary data would include historical and future records from specimen collections in museums and herbaria, but also field observations by researchers, conservation and natural resource management agencies, and lay experts. A hierarchical sampling approach, involving millions of point observations of relatively simple data (e.g., the presence or absence of a species), thousands of records of abundance or community composition, and hundreds of detailed studies on individual ecosystems, bound together with models, remote sensing, and spatial analysis, would enable both global coverage and local relevance while remaining feasible and affordable. The supporting information and data-description protocols that allow this information to be shared among many independent sources are already relatively well-developed, thanks to the efforts, among others, of the Global Biodiversity Information Facility. They need to be expanded beyond collection records to include ecological observations. A biodiversity gateway on the GEO Portal, providing users easy access to data and the tools they need to understand it, will be an important part of the operational system.

The GEO BON initiative was noted by the Conference of Parties of the CBD at its May 2008 meeting, which requested the secretariat to "continue collaborating with the Biodiversity Observation Network with a view to promoting coherent biodiversity observation with regard to data architecture, scales and standards, observatory network planning, and strategic planning for its implementation" (*10*). Actions driven by the desire to adapt to and mitigate climate change, such as expansion of biofuel plantings and payments for avoided deforestation, emphasize the importance of reliable biodiversity information for other international conventions as well.

There are challenges ahead, including overcoming a tradition of data restriction within the biodiversity field. The initiative will require new kinds of cooperation among governments and nongovernmental organizations and between data providers and users of the information. The yardstick of success is not a cheaper global biodiversity observation system, but a more useful one and, thus, an improved cost-benefit relation. By analogy to the Global Climate Observing System (*11*), which is in more advanced implementation, it is estimated that the final total cost of a GEO BON could amount to €200 million to €500 million (U.S. $309 million to U.S. $772 million) per year. Because much of this is already committed in national agencies, the additional cost of global networking and gap-filling will be much more modest. The costs would be spread across many nations and organizations and phased in over a number of years, leveraging the existing expenditure in partial and stand-alone systems. The potential benefits are worth the extra effort.

References

1. R. F. Noss, *Conserv. Biol.* **4**, 355 (1990).
2. D. P. Faith, *Conserv. Biol.* **16**, 248 (2002).
3. R. J. Scholes, R. Biggs, *Nature* **434**, 45 (2005).
4. D. F. Hui, R. Biggs, R. J. Scholes, R. B. Jackson, *Biol. Conserv.* **141**, 1091 (April 2008).
5. A. Balmford *et al.*, *Science* **307**, 212 (2005).
6. H. M. Pereira, H. D. Cooper, *Trends Ecol. Evol.* **21**, 123 (2006).
7. "EU environment-related indicators 2008," www.energy.eu/publications/KH8107174END_002.pdf.
8. G. M. Mace, J. E. M. Baillie, *Conserv. Biol.* **21**, 1406 (2007).
9. The Royal Society, "Measuring biodiversity for conservation" (Policy doc. 11/03, The Royal Society, London, 2003).
10. CBD, *Monitoring, Assessment and Indicators: Follow up to the Millennium Ecosystem Assessment*: *Draft decisions for the 9th Conference of the Parties*, Bonn, Germany, 19 to 30 May 2008 (UNEP/CBD/COP/9/L.19, CBD, Montreal, Canada, 2008)
11. "Implementation plan for the Global Observing System for Climate in support of the UNFCCC" (GCOS-92) (Tech. doc. 1219, World Meteorological Organization, Geneva, October 2004).

10.1126/science.1162055

PSYCHOLOGY

The Unseen Mind

The human mind operates largely out of view, and yet people are unaware of their unawareness, confabulating reasons for their actions and preferences.

Timothy D. Wilson and Yoav Bar-Anan

Can people think they are undecided about a political issue after they have already made up their minds? The study by Galdi *et al.*, on page 1100 in this issue (*1*), suggests that they can, which raises intriguing questions about how well people know their own minds. The short answer, based on research in social psychology, is not very well.

Social psychologists have discovered an adaptive unconscious that allows people to size up the world extremely quickly, make decisions, and set goals—all while their conscious minds are otherwise occupied. The human mind operates largely out of view of its owners, possibly because that's the way it evolved to work initially, and because that's the way it works best, under many circumstances. Without such an efficient, powerful, and fast means of understanding and acting on the world, it would be difficult to survive. We would be stuck pondering every little decision, such as whether to put our left or right foot forward first, as the world sped by (*2*–*7*). But as a result, we are often strangers to ourselves, unable to observe directly the workings of our own minds.

Confabulation. As in this drawing by Saul Steinberg, people construct images of themselves. In real life, people do not realize that their self-knowledge is a construction, and fail to recognize that they possess a vast adaptive unconscious that operates out of their conscious awareness.

One way we know this is from computer-based measures that assess implicit attitudes and traits, such as the one used by Galdi *et al.* to measure people's automatic associations to a political issue. Typically, people perform a simple cognitive task (usually sorting words into groups), and their accuracy and speed of performance provide information about the associative strength between the different concepts used in the task. Automatic attitudes are measured by comparing people's associations between the attitude object and words with positive versus negative meaning. A common finding, using such implicit measures, is that people's automatic responses correspond poorly to their self-reported attitudes (*8*–*10*). For example, Galdi *et al.* found that the correlation between people's automatic associations and reported attitudes about a political issue were low and mostly nonsignificant. To be sure, there are many interpretations of such a lack of correspondence. Some argue that low correlations between automatic responses and self-reports reflect attempts to hide one's attitudes and not a lack of awareness of them (*11*). But there is widespread agreement that people lack access to a broad range of mental processes, and that attitudes can affect people's behavior (such as voting) without their awareness.

Curiously, people seem to be unaware of their own unawareness, rarely answering "I don't know" when asked to explain their decisions. People freely give reasons for their preferences, even when it is clear that these reasons are confabulations and not accurate reports. In one study, for example, researchers showed participants photographs of two women and asked them to choose the one they found more attractive (*12*). The experimenter then showed people the photograph they preferred and asked them to explain the reasons for their choice. On some trials, through sleight of hand, the experimenter actually showed people the photograph they found less attractive. It might seem that people would immediately see through this ruse, but surprisingly, they noticed the switch only about a quarter of the time. Even more surprisingly, in the 75% of the trials in which they did not notice the switch, participants had no problem coming up with plausible reasons for their choice. One participant, for example, said, "She's radiant. I would rather have approached her in a bar than the other one. I like earrings"—even though he initially found the other woman, who wasn't wearing earrings, more attractive. Perhaps most tellingly, the researchers could not find any differences in the kinds of reasons people gave for their real versus their false choices, suggesting that people were confabulating reasons in both cases.

Other studies have also found that people confabulate when asked to explain the reasons for their preferences (*2*, *13*, *14*), a message that has not been heeded by political pollsters. Exit polling, in which voters leaving the polling booth are asked about their voting decisions, is common in the United States and elsewhere, not only as a means of predicting the outcome of an election, but also as a way of uncovering why people voted the way they did. In the recent presidential primaries in the United States, for example, voters were asked which qualities of the candidates were most important when deciding how to vote (for example, "has the right experience" versus "has the best chance to win [the presidency] in November"), as well as to rate how much the candidates' campaign ads influenced their decision. Political operatives and pundits pore over the answers to questions such as these to try to gain insights about why people voted the way they did. But to social psychologists and academic political scientists, people's answers are highly suspect. Voters explain their reasons by relying on cultural and idiosyncratic causal theories that may bear little relation to the real reason for their preferences (*2*, *3*, *15*). The Galdi *et al.*

University of Virginia, Charlottesville, VA 22904–4400, USA. E-mail: twilson@virginia.edu

study suggests that pollsters should be equally skeptical of voters who say they are undecided, because they may have already made up their minds at an implicit level.

Why are people so unaware of their unawareness? One reason may be because we do have access to a good deal of information that is immediate, compelling, and privileged. The fact that we experience a rich mental life makes it hard to recognize that the vast majority of our mental processes are not directly observable. As an analogy, one of us was recently driving on a California coast highway when he saw a sign indicating that a nearby beach was a haven for elephant seals. He and his wife stopped and saw five gigantic seals sunbathing on the beach, and after observing them for a few minutes they turned to go, satisfied that they had had the prototypical elephant seal experience. It was only when they looked down the beach that they realized that they had gone to the wrong overlook—a mere 50 yards away there were hundreds of seals sleeping, playing, and snuggling. Unfortunately, when it comes to human introspection, there is no overlook from which one can see the vast contents of the adaptive unconscious. We are left with the illusion that the few "elephant seals" we can see—the feelings and thoughts that are conscious—are the entirety of our mental life.

Research psychology is helping to dispel this illusion. Studies such as that by Galdi *et al*. are documenting how the adaptive unconscious works and people's limited introspective access to it. As these studies become more widely known, people might realize that there are many more elephant seals than the few they can observe directly—that is, that their conscious thoughts and feelings are but a small part of the workings of their minds. And, political pollsters might learn that there are some questions better left unasked.

References and Notes

1. S. Galdi, L. Arcuri, B. Gawronski, *Science* **321**, 1100 (2008).
2. R. E. Nisbett, T. D. Wilson, *Psychol. Rev.* **84**, 231 (1977).
3. T. D. Wilson, *Strangers to Ourselves: Discovering the Adaptive Unconscious* (Harvard Univ. Press, Cambridge, MA, 2002).
4. J. A. Bargh, in *Advances in Social Cognition*, R. S. Wyer Jr., Ed. (Erlbaum, Mahwah, NJ, 1997), vol. 10, pp. 1–61.
5. D. M. Wegner, *The Illusion of Conscious Will* (MIT Press, Cambridge, MA, 2003).
6. R. R. Hassin, J. S. Uleman, J. A. Bargh, Eds., *The New Unconscious* (Oxford Univ. Press, New York, 2005).
7. A. Dijksterhuis, L. F. Nordgren, *Perspect. Psychol. Sci.* **1**, 95 (2006).
8. A. G. Greenwald, M. R. Banaji, *Psychol. Rev.* **102**, 4 (1995).
9. T. D. Wilson, S. Lindsey, T. Y. Schooler, *Psychol. Rev.* **107**, 101 (2000).
10. B. A. Nosek, *Curr. Dir. Psychol. Sci.* **16**, 65 (2007).
11. R. H. Fazio, M. A. Olson, *Annu. Rev. Psychol.* **54**, 297 (2003).
12. P. Johansson, L. Hall, S. Sikström, A. Olsson, *Science* **310**, 116 (2005).
13. M. S. Gazzaniga, J. E. LeDoux, *The Integrated Mind* (Plenum, New York, 1978).
14. J. St B. Evans, P. C. Wason, *Br. J. Psychol*. **67**, 479 (1976).
15. W. M. Rahn, J. A. Krosnick, M. Breuning, *Am. J. Pol. Sci.* **38**, 582 (1994).
16. T.D.W. acknowledges the support of research grant BCS-0722915 from the National Science Foundation.

10.1126/science.1163029

ASTRONOMY

Stars in the Making

The observation of stars close to the galactic center requires a rethink of the star formation process.

Philip J. Armitage

One of the remarkable properties of star formation is its apparent universality. Although stars form with masses that span three orders of magnitude, the distribution of masses among a population of newly formed stars—the initial mass function (IMF)—is the same across many different environments within the Milky Way. Theorists believe that this universality breaks down in extreme conditions, for example, when the first stars formed from the metal-free gas of the Big Bang. Observational tests of that theory, however, are lacking. Hence the excitement surrounding the suggestion, bolstered by simulations reported by Bonnell and Rice on page 1060 of this issue (*1*), that a new mode of star formation may be needed to explain stars observed in the immediate vicinity of the supermassive black hole at our own galactic center.

First of all, it is surprising to find any star formation close to a massive black hole. Stars customarily form from tenuous clouds of molecular gas, which would be ripped apart by the tidal gravitational field of the black hole out to a distance of several light-years.

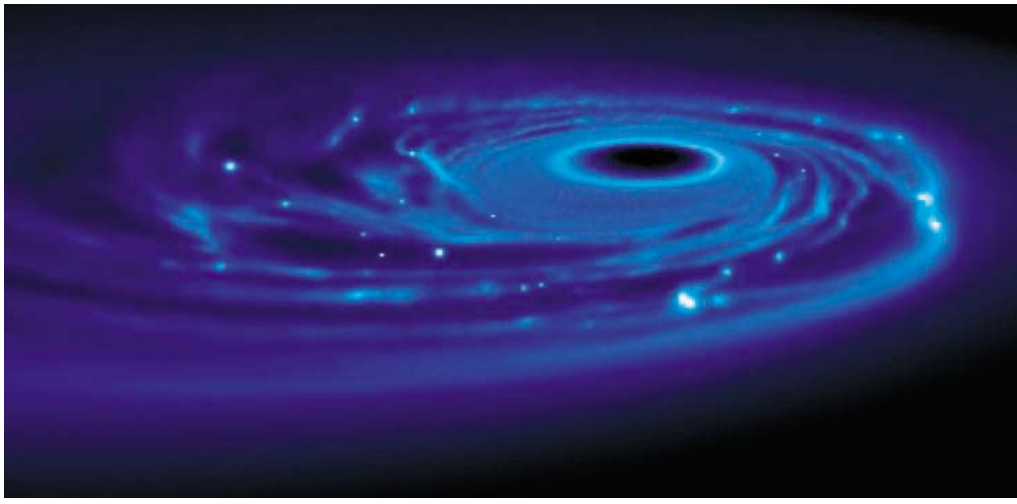

CREDIT: RICHARD ALEXANDER/LEIDEN UNIVERSITY

Unexpected stars. Computer simulation (*15*) of star formation from an eccentric gas disk around a supermassive black hole.

Observations of the galactic center, however, reveal two populations of massive stars whose short lifetimes mean that they must have formed relatively recently. Within this expected disruptive zone and closest (within a light-month) to the black hole are the S-stars, with orbital periods as short as a decade (*2*, *3*). Long-term monitoring of these stars' orbits has been used to measure the black hole mass, and higher precision should ultimately reveal departures from Newtonian orbits due to the effects of relativity and the predicted presence of a cluster of as-yet-unobserved stellar-mass black holes. Slightly farther out—but still within the zone where ordinary star formation is inhibited—is a second population of around 100 massive stars that formed just 6 million years ago. Many of

JILA, University of Colorado, Boulder, CO 80309, USA. E-mail: pja@jilau1.colorado.edu

these stars orbit the black hole within a single disk (*4*–*6*), and their IMF appears to contain many more massive stars than would be expected from normal star formation (*7*).

One idea proposed to explain why young stars are found so close to a black hole is that they initially formed in a normal environment before subsequently spiraling inward. The S-stars may have formed within binaries that were disrupted during black hole flybys, leaving one star in a short-period orbit while the other was ejected from the galactic center (*8*). Promisingly for this scenario, a handful of hypervelocity stars that may originate from the galactic center have recently been identified elsewhere in the Milky Way (*9*). To explain the disk stars, an analogous model suggests that an entire cluster of stars spiraled into the galactic center, losing stars along the way and finally depositing the massive stars of the cluster core in the disk (*10*). To date, though, no sign has been seen of the stellar trail that a dissolving cluster would leave in its wake.

A rival model postulates that a thin disk of gas once orbited the black hole before fragmenting into a stellar disk (*11*). It has long been known that gas disks orbiting black holes at these radii are unstable to star formation (*12*). The new aspect that Bonnell and Rice have addressed is how an unstable disk could form in the first place. Their numerical simulations show that an ordinary molecular cloud—formed at distances large enough to be immune from the black hole's dangerous tidal forces—could survive the inward plunge to deposit a fraction of its gas into an eccentric disk from which the stars subsequently form. Turbulent support within the gas cloud is the key ingredient in their model, sustaining it against premature collapse long enough to permit disk formation. During the infall, the gas is heated as it is compressed and torn apart by the black hole, promoting the top-heavy IMF observed for the disk stars.

As satisfying as the new results are, the case for disk fragmentation as the origin for the disk stars remains unproven. We do not know whether the initial conditions assumed by Bonnell and Rice are realized in the galactic center. Most of the molecular gas in the inner 100 light-years avoids the very center (*13*), and future work will need to assess whether a fraction of that gas can be occasionally diverted into a plunging trajectory. Another interesting avenue will be to explore the implications for other galactic nuclei. A rather older disk of massive stars is seen in the nucleus of Andromeda (*14*), the nearest galaxy comparable to the Milky Way, but the frequency of similar phenomena remains poorly constrained. There is an obvious potential trade-off with black hole growth, because star formation at these small radii consumes gas whose fate would otherwise be to feed the black hole. Black hole growth is known to be slowing over cosmic time, and it is tempting to speculate that the exquisite observations of the galactic center may be affording us a glimpse of one of the mechanisms responsible for that trend.

References

1. I. A. Bonnell, W. K. M. Rice, *Science* **321**, 1060 (2008).
2. R. Schödel *et al.*, *Nature* **419**, 694 (2002).
3. A. M. Ghez *et al.*, *Astrophys. J.* **586**, L127 (2003).
4. R. Genzel *et al.*, *Mon. Not. R. Astron. Soc.* **317**, 348 (2000).
5. T. Paumard *et al.*, *Astrophys. J.* **643**, 1011 (2006).
6. J. R. Lu *et al.*, *J. Phys. Conf. Ser.* **54**, 279 (2006).
7. S. Nayakshin, R. Sunyaev, *Mon. Not. R. Astron. Soc.* **364**, L23 (2005).
8. J. G. Hills, *Nature* **331**, 687 (1988).
9. W. R. Brown *et al.*, *Astrophys. J.* **647**, 303 (2006).
10. O. Gerhard, *Astrophys. J.* **546**, L39 (2001).
11. Y. Levin, A. M. Beloborodov, *Astrophys. J.* **590**, L33 (2003).
12. P. I. Kolykhalov, R. A. Sunyaev, *Sov. Astron. Lett.* **6**, 357 (1980).
13. M. Morris, E. Serabyn, *Annu. Rev. Astron. Astrophys.* **34**, 645 (1996).
14. R. Bender *et al.*, *Astrophys. J.* **631**, 280 (2005).
15. R. D. Alexander *et al.*, *Astrophys. J.* **674**, 927 (2008).

10.1126/science.1162876

DEVELOPMENTAL BIOLOGY

How Now, Brown Fat?

Brown adipose tissue is, surprisingly, more related to skeletal muscle than to white adipose tissue.

Mitchell A. Lazar

Obesity, the condition of excess fat storage in adipose tissue, is harmful to health and epidemic in modern society (*1*). Adipocytes, or "fat cells," are specialized cells that store this fat in triglyceride-containing droplets. Until recently, it was thought that all adipocytes are derived from a common precursor. It seemed almost obvious that different types of fat cells are closely related. However, this week, a study by Seale *et al*. (*2*) provides compelling evidence against this doctrine.

Not all adipocytes have the same physiological function. Those in white adipose tissue constitute the major energy storage depot in mammals. When nutritional sources of energy are scarce, triglyceride breakdown in white adipocytes generates fatty acids that are exported and used as fuel by other tissues, including muscle. In obesity, where energy expenditure is matched, and usually exceeded, by caloric consumption, both the size and the number of white adipocytes increase. White adipose tissue is often classified on the basis of its location as subcutaneous and abdominal (or visceral) fat. Secretions from visceral fat pass through the liver before entering the general circulation, and this has been implicated in the pathogenesis of type 2 diabetes and insulin resistance (*3*). Visceral adipocytes differ from subcutaneous adipocytes in their gene expression profiles (*4*), although there is no evidence that the precursors of white adipocytes in visceral and subcutaneous depots are fundamentally different.

In contrast to white adipose tissue, brown adipose tissue plays an active role in energy expenditure, oxidizing fatty acids produced by triglyceride hydrolysis to generate heat. As the name suggests, brown adipose tissue appears different from white adipose tissue, largely because of the increased number of mitochondria (cytochromes within the mitochondria account for the color) that function in oxidative metabolism. Also, brown adipocytes contain multiple small lipid droplets, whereas white adipocytes usually have a single large lipid droplet. The thermogenic oxidation of fatty acids is facilitated by uncoupling protein–1, which is expressed specifically in brown adipocytes. In rodents, brown fat is characteristically found in the interscapular region, and is critical for thermoregulation throughout life. By contrast, humans have proportionally more brown fat at birth than in adulthood, when it can be difficult to locate. Nevertheless, recent studies point to the existence and conserved function of brown adipose tissue in humans (*5*).

Although brown and white adipocytes look different and have different physiological

Institute for Diabetes, Obesity, and Metabolism, Department of Medicine, University of Pennsylvania, 415 Curie Boulevard, Philadelphia, PA 19104, USA. E-mail: lazar@mail.med.upenn.edu

functions, they are considered to have derived from a common precursor cell. One reason is that the transcription factor peroxisome proliferator-activated receptor γ (PPARγ), which is the master regulator of adipogenesis, is required for differentiation of both white and brown adipocytes (*6*). In addition, conversion of white to brown adipocytes is induced by β-adrenergic stimulation—that is, stimulation of white adipose with hormones (catecholamines) that are released in situations of stress or low blood sugar concentration (*7*).

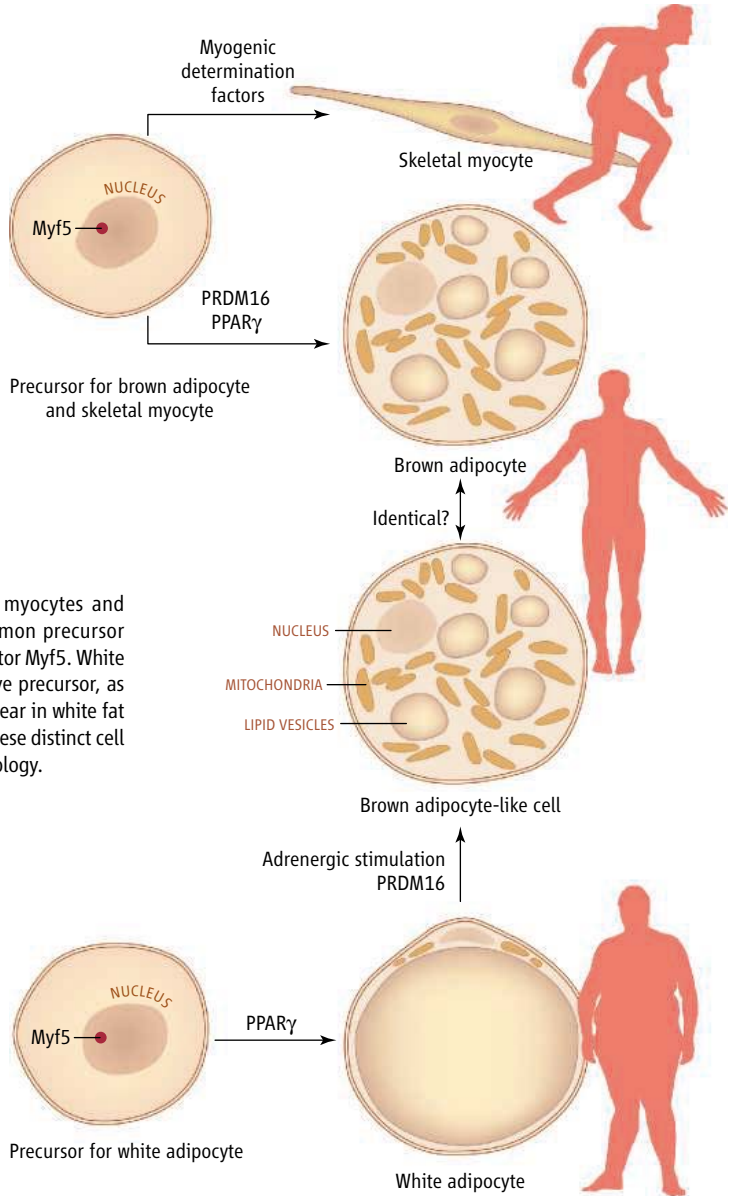

Paths to muscle and fat. Skeletal myocytes and brown adipocytes derive from a common precursor cell that expresses the transcription factor Myf5. White adipocytes derive from a Myf5-negative precursor, as do brown adipocyte–like cells that appear in white fat depots after adrenergic stimulation. These distinct cell types play very different roles in physiology.

The factors that mediate conversion of white to brown adipose tissue have been extensively investigated, motivated, in part, by the hope that expansion of the brown-fat compartment, leading to increased energy expenditure, would be a novel way to treat obesity (*8*). Ten years ago, PPARγ coactivator 1α (PGC-1α) was identified as a transcriptional coactivator that is enriched in brown adipocytes (*9*). Since then, PGC-1α has emerged as a major metabolic regulator in brown fat, as well as other tissues, although it is not required for the expression of other brown fat–specific genes, including uncoupling protein–1 (*10*). About a year ago, in a more systematic search for brown-fat transcription factors, Seale *et al*. found that a previously unsuspected protein, PRDM16, is required to maintain the brown-fat phenotype, including the expression of uncoupling protein–1 (*11*).

The implication that PRDM16 and PGC-1α are involved in the generation and function of brown adipocytes advanced the field, but did not alter the basic notion that brown and white adipocytes derive from a common precursor. Therefore, the new finding from Seale and colleagues is a real surprise: Brown adipocytes actually derive from a cell that otherwise gives rise to skeletal muscle but not to white adipocytes (*2*). This conclusion is supported by evidence that forced expression of PRDM16 leads cultured mouse skeletal muscle cells to differentiate into brown adipocytes and, conversely, that brown adipocytes depleted of PRDM16 take on the look and function of skeletal muscle cells. Independent of genetic manipulation of PRDM16, lineage-tracing studies indicate that brown adipocytes are derived from cells that express the transcription factor Myf5, a molecular marker of skeletal muscle precursors. Importantly, white adipocytes did not derive from these cells, demonstrating that the developmental pathways of white and brown adipocytes diverge before the switch between brown fat and skeletal muscle (see the figure).

The link between brown fat and skeletal muscle was presaged by the observation that gene-expression profiles of brown adipose tissue share features characteristic of skeletal muscle (*12*). Indeed, in retrospect, the oxidative metabolism of brown fat, as well as its color and mitochondrial content, is more similar to those of skeletal muscle than to those of white adipose tissue. The relationship between brown adipose tissue and skeletal muscle is likely to extend to humans, where brown adipocyte precursors have recently been identified in skeletal muscle (*13*).

The close connection between brown adipose tissue and skeletal muscle raises several questions. How does adrenergic stimulation convert white to brown adipose tissue? Seale *et al*. report that these brown adipocyte–like cells, although they express PRDM16, are not derived from Myf5-expressing precursors. Hence, there must be an alternative pathway to brown adipocyte formation that is more highly related to that of white adipogenesis. Are the brown adipocyte–like cells that emerge in white fat depots distinguishable, molecularly or functionally, from the adipocytes in brown fat depots? Will understanding the origin of brown adipocytes lead to novel therapeutic approaches to obesity? Confronted with a seemingly inexorable rise in obesity and its dire medical consequences, our society may well benefit from new developments.

References

1. M. A. Lazar, *Science* **307**, 373 (2005).
2. P. Seale *et al*., *Nature*, **454**, 961 (2008).
3. A. H. Kissebah, G. R. Krakower, *Physiol. Rev.* **74**, 761 (1994).
4. S. Gesta, Y. H. Tseng, C. R. Kahn, *Cell* **131**, 242 (2007).
5. J. Nedergaard, T. Bengtsson, B. Cannon, *Am. J. Physiol. Endocrinol. Metab.* **293**, E444 (2007).
6. M. Lehrke, M. A. Lazar, *Cell* **123**, 993 (2005).
7. S. R. Farmer, *Genes Dev.* **22**, 1269 (2008).
8. C. Tiraby, D. Langin, *Trends Endocrinol. Metab.* **14**, 439 (2003).
9. P. Puigserver *et al.*, *Cell* **92**, 829 (1998).
10. B. N. Finck, D. P. Kelly, *J. Clin. Invest.* **116**, 615 (2006).
11. P. Seale *et al*., *Cell Metab.* **6**, 38 (2007).
12. J. A. Timmons *et al*., *Proc. Natl. Acad. Sci. U.S.A.* **104**, 4401 (2007).
13. M. Crisan *et al*., *Stem Cells* 10.1634/stemcells.2008-0325 (2008).

10.1126/science.1164094

CHEMISTRY

Soluble Allotropes of Main-Group Elements

Small clusters of main-group elements can be stabilized in the highly active zero oxidation state and used for reactions in solution.

C. Adam Dyker and Guy Bertrand*

Elements can occur as allotropes, which differ in the number of atoms per structural unit, in their bonding, or both. For example, oxygen can exist as dioxygen (O_2) but also as ozone (O_3), and carbon exists in forms based on hexagonal lattices (such as graphite, fullerenes, and nanotubes) but also on a tetrahedral lattice (diamond). However, all allotropes are alike in that the atoms are in the zero oxidation state. Aside from allotropes, the zero oxidation state is classically found in metals, when stabilized by ligands that donate electron pairs into their empty orbitals. However, such a state has been difficult to realize for main-group elements such as silicon. On page 1069 of this issue, Wang *et al*. report the synthesis of a compound that can be regarded as a diatomic silicon allotrope, stabilized by two ligands (*1*) (see the figure).

The strategy used by the authors to stabilize diatomic silicon(0) is based on their recent discovery that diborene (H-B=B-H) can be stabilized and even isolated when the vacant orbital on each boron atom is coordinated by an N-heterocyclic carbene, which acts as a two-electron donor ligand and forms a dative bond (*2*, *3*). Wang *et al*. introduced the carbene ligand (L) by coordination to silicon tetrachloride, and the resulting hypervalent Si(IV) species [(L)$SiCl_4$] was reduced with potassium graphite in tetrahydrofuran to give product 1 (see the figure).

The oxidation state of silicon can be assessed on the basis of the bond angles and distances in compound 1. The x-ray crystal structure reveals a distinctly nonlinear C-Si-Si-C backbone (C-Si-Si angle of 93.37°) and long C-Si bonds (1.927 Å). If the Si atoms were in the oxidized Si^{2+} state, the expected geometry would be a perfectly planar skeleton with a linear C-Si-Si-C arrangement and short C-Si bonds (see compound 1′ in the figure). Thus, in compound 1, the carbene ligand does not withdraw electron density from silicon but leaves a nonbonding electron pair on each silicon center.

Compound 1 can thus be regarded as a diatomic silicon(0) unit stabilized by ligands that are Lewis bases, that is, a base-stabilized allotrope. It also represents a landmark in low-coordinate silicon chemistry, because each silicon center is involved in a multiple bond and, at the same time, features a lone pair of electrons; these two attributes are usually associated with extreme instability. We note that the isolation of compound 1 has been made possible by the use of carbenes, species that themselves have been historically considered as nonisolable (*4*, *5*).

Related to this discovery, there has recently been much interest in using Lewis bases to stabilize monoatomic carbon(0) (*6*). Detailed computational studies by Frenking and Tonner (*7*, *8*) showed that two N-heterocyclic carbene ligands could stabilize a carbon(0) center possessing two lone pairs of electrons. Experimental confirmation of this prediction came soon after with the isolation of derivative 2 (*9*, *10*). This compound has eight electrons that could be available for bonding between the three central carbon centers (as shown in its typical rigid and linear allene resonance structure 2′). However, the experimentally determined C-C-C bond angle of 134.8° was indicative of the predicted bonding situation.

Investigations on carbene-stabilized allotropes have not been limited to group-14 elements. The addition of carbenes to white phosphorus (compound 3; see the figure) leads to base-stabilized P_4 and P_{12} compounds 4 and 5, depending on the nature of the car-

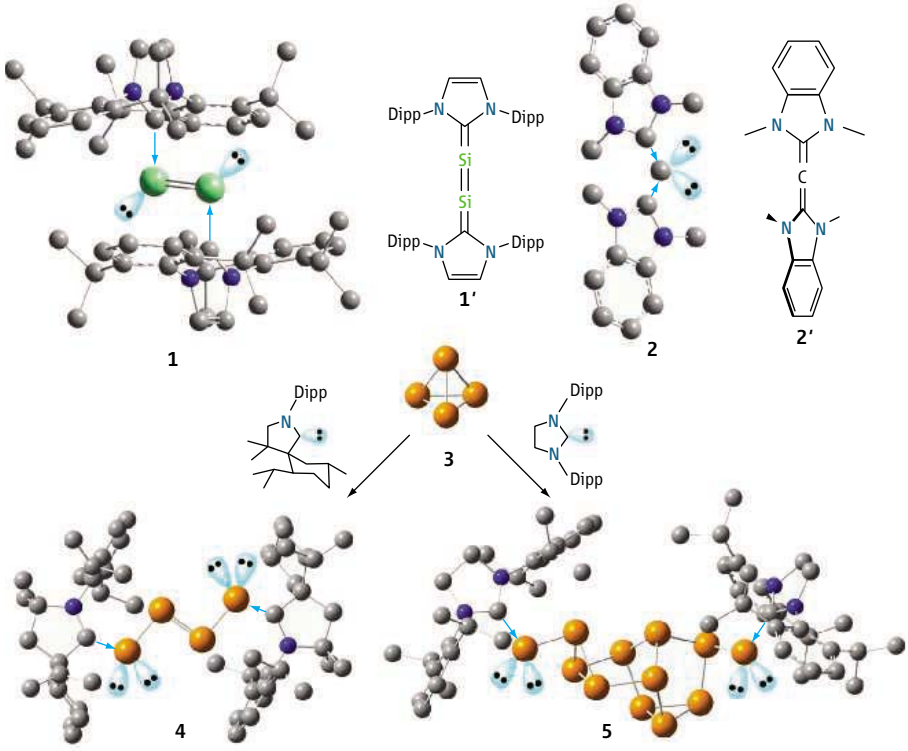

Stabilizing power. Carbenes with their nonbonding electrons in the same orbital (the spin-paired singlet state) act as nonoxidizing two-electron donors toward Si_2 and C_1 units, as indicated by the observed geometry of compounds **1** and **2**, versus more classical Lewis structures **1′** and **2′**, which are not observed. Both the silicon and central carbon centers of **1** and **2** possess one and two electron pairs, respectively, and are in the zero oxidation state. Carbene-induced transformations of white phosphorus (**3**) into novel P_4 (**4**) and P_{12} (**5**) clusters illustrate the broad applicability of carbenes in the stabilization of artificial main-group-element allotropes. (Dipp, 2,6-diisopropylphenyl; carbon, gray; silicon, green; nitrogen, blue; phosphorus, orange.)

UCR-CNRS Joint Research Chemistry Laboratory (UMI 2957), Department of Chemistry, University of California, Riverside, CA 92521–0403 USA. E-mail: cadamd@ucr.edu (C.A.D.); gbertran@mail.ucr.edu (G.B.)

bene ligand (*11*, *12*). These are examples of transformations of a well-known allotrope into unprecedented phosphorus(0) clusters.

These molecules are not just academic curiosities. One of the obvious advantages of base-stabilized element(0) compounds, versus their known allotropes, is their greater solubility, which facilitates further chemical transformations. As an illustration, soluble, ligand-coordinated metal(0) complexes undergo chemistry that is not possible using the insoluble elemental forms of the metal (homogeneous versus heterogeneous catalysis). Moreover, this stabilization technique is not limited to element(0) compounds, as shown already for diborene, and should allow for the solubilization and subsequent chemical transformation of elementary units of large frameworks, such as the basic unit of sand, SiO_2.

References and Notes

1. Y. Wang *et al.*, *Science* **321**, 1069 (2008).
2. Y. Wang *et al.*, *J. Am. Chem. Soc*. **129**, 12412 (2007).
3. Y. Wang *et al.*, *J. Am. Chem. Soc*. **130**, 3298 (2008).
4. A. Igau, A. Baceiredo, G. Trinquier, G. Bertrand, *Angew. Chem. Int. Ed. Engl.* **28**, 621 (1989)
5. A. J. Arduengo III, R. L. Harlow, M. Kline, *J. Am. Chem. Soc.* **113**, 361 (1991).
6. O. Kaufhold, F. E. Hahn, *Angew. Chem. Int. Ed.* **47**, 4057 (2008).
7. R. Tonner, G. Frenking, *Angew. Chem. Int. Ed.* **46**, 8695-(2007).
8. R. Tonner, G. Frenking, *Chem. Eur. J.* **14**, 3260 (2008).
9. C. A. Dyker, V. Lavallo, B. Donnadieu, G. Bertrand, *Angew. Chem. Int. Ed.* **47**, 3206 (2008).
10. A. Fürstner, M. Alcarazo, R. Goddard, C. W. Lehmann, *Angew. Chem. Int. Ed.* **47**, 3210 (2008).
11. J. D. Masuda *et al.*, *J. Am. Chem. Soc.* **129**, 14180 (2007).
12. J. D. Masuda *et al.*, *Angew. Chem. Int. Ed*. **46**, 7052 (2007).

13. We thank the NSF (CHE 0808825) for financial support.

10.1126/science.1162926

ECOLOGY

A Matter of Timing

The cues used by birds and other species to trigger reproduction determine how successfully they can respond to climate change.

Bruce E. Lyon,[1] Alexis S. Chaine,[2] David W. Winkler[3]

Climate change is causing shifts in the distribution and phenology of many plants and animals (*1*, *2*). Birds have played a key role in detecting these changes, because long-term data are available on the distribution, migration, and breeding of many species. Studies of the timing of egg laying—a key trait with extensive records dating back half a century for some species—are providing crucial insights into the mechanisms that underlie the response to climate change.

Response to climate change. A striking geographic difference in how two populations of great tits respond to climate change raises the question about the underlying mechanisms of this variation.

Egg laying is occurring earlier in the year in a wide variety of temperate-zone birds (*1*, *3*). Evidence that climate change is directly involved comes from geographic variation in well-studied taxa, such as European populations of flycatchers (*4*). Changes in laying date are consequential because birds must time reproduction to coincide with seasonal pulses in resources. If prey advance their emergence more rapidly than birds advance their laying (*5*), decreased reproductive success and population decline may result (*6*).

Which evolutionary and behavioral mechanisms underlie these responses to climate change (*5*, *7*–*9*)? Two mechanisms in particular have been investigated: phenotypic plasticity and evolutionary response to natural selection (*8*, *9*). With phenotypic plasticity, individual females show flexibility and alter their timing of breeding when environmental conditions change. With an evolutionary response, breeding date has a strong genetic component and change occurs by a shift in the genetic makeup of the population.

Evidence to date implicates phenotypic plasticity as the driver of most change in laying date in birds (*9*), but some populations seem to show much less plasticity than others. For example, two long-term studies of the great tit (*Parus major*; see the figure) reveal striking geographic variation in phenotypic plasticity for laying date (*5*, *7*). In a 32-year study, the mean laying date for a Dutch population shifted little in response to increasingly warm spring temperatures, leaving the birds' laying date increasingly out of step with the advancing emergence of their key caterpillar food source (*5*). However, phenotypic plasticity varied among females; some responded little to annual variation in temperature while others showed more extensive responses. Moreover, the variation in plasticity is heritable, and analyses suggest that the more plastic genotypes should eventually be favored by natural selection (*5*). In contrast, a 47-year study in England found a strong adaptive response to climate change; both the birds and their caterpillar prey have shifted in unison as warm spring temperatures arrive increasingly early (*7*). The shifts in the British population appear to be explained entirely by phenotypic plasticity, and there were no detectable differences in the degree of plasticity among females (*7*).

How do the Dutch and British tits differ? Might differences in their response mechanisms explain geographic variation in plasticity more generally?

One explanation is that the birds may use different cues to trigger egg laying. Timing of egg laying in temperate-zone birds is thought to involve many cues, integrated in a tiered fashion: Day length (photoperiod) begins the process, and then supplemental cues such as food, temperature, or the phenology of other organisms can be used to fine-tune the timing of laying to year-to-year variation in spring conditions (*10*, *11*). Variation in the relative importance of different cues could explain variation in plasticity with respect to temperature among populations or even among individuals in the same population (*12*, *13*).

For example, organisms that show little or no plasticity with respect to temperature variation—like many individuals in the Dutch great tit population—may use photoperiod as their sole cue. A bird that used only photoperiod would have a consistent breeding date unaffected by variation in environmental con-

[1]Department of Ecology and Evolutionary Biology, University of California, Santa Cruz, CA 95064, USA. [2]Station d'Ecologie Experimentale du CNRS à Moulis USR 2936, 09200 Moulis, France. [3]Museum of Vertebrates and Department of Ecology and Evolutionary Biology, Cornell University, Ithaca, NY 14853, USA. E-mail: lyon@biology.ucsc.edu

ditions. In contrast, complete plasticity with respect to temperature, as observed in the British great tits, would result if birds relied heavily on temperature (or some strong correlate of temperature, such as the phenology of another organism) as their sole or supplemental cue. Moreover, the apparent ability of the British birds to track changes in the timing of their prey could result if both birds and prey use the same cues.

Precisely how birds assess and compile temperature is not well understood. Nonetheless, a recent study of geographic variation in the relative importance of photoperiod and temperature-related supplemental cues in great tits provides some support for the idea that variation in plasticity can be explained by the types of cues used (*13*), and it would be fruitful to further explore these links.

Knowing which cues organisms use will be necessary for predicting the long-term impacts of climate change on the timing of breeding in birds and other organisms (*12*). Scientists typically study phenotypic plasticity by analyzing a norm of reaction—that is, a statistical measure of the response of a given genotype (or individual) to variation in some environmental variable, such as temperature, measured by the researcher. However, it is critical not to confuse a norm of reaction with the organismal traits under selection (*14*). The actual traits that produce plasticity in laying date include features of the neuroendocrine system that assess and integrate environmental cues and trigger egg laying (*11*, *14*). Without experiments, it is exceedingly difficult to verify which cues are used by the organism and how they are used. At best, our investigations examine close approximations of the actual cues; at worst, we may analyze proxies that are the wrong cues.

This inaccuracy may hamper our ability to understand variation in plasticity across populations and to make predictions about how plasticity might evolve in the future. For example, say we compare laying dates in relation to temperature, but the organism actually assesses another cue that is reasonably well correlated with temperature (for example, leaf bud break in a plant species). As spring temperatures increase over time, the correlation between what we measure (temperature) and what the birds assess (plants) may change, making extrapolations from current reaction norms problematic. Geographic variation among populations—such as the British and Dutch tits—might occur not because the populations use different cues, but because the cues they use vary geographically in their correlation with temperature.

Laying date can affect offspring production, Darwinian fitness, and population stability (*6*, *15*). The widespread observation that early breeders produce more offspring than late breeders implies that time in season is a direct cause of variation in reproductive success (*15*). However, experiments show that about half of the variation in reproductive success results from differences in individual quality, independent of season (*15*).

The fact that individuals within populations vary so much in their timing of breeding implies that factors other than external cues determine the timing of breeding, a detail that is often not fully explored. Thus, a clearer understanding of all factors—including cues and individual quality—that trigger breeding would improve our understanding of not only the potential for phenotypic plasticity to cope with climate change, but also the demographic consequences of such plasticity. Only by drawing direct links between the specific cues and mechanisms used to time egg laying, the potential for microevolution in these mechanisms, and the demographic consequences of this flexibility for exploiting ever-changing food sources will we be able to predict and mitigate the effects of climate change on regional population persistence.

References and Notes

1. H. Q. P. Crick, T. H. Sparks, *Nature* **399**, 423 (1999).
2. C. Rosenzweig *et al.*, *Nature* **453**, 353 (2008).
3. P. Dunn, *Adv. Ecol. Res.* **35**, 69 (2004).
4. C. Both *et al.*, *Proc. R. Soc. London Ser. B* **271**, 1657 (2004).
5. D. H. Nussey, E. Postma, P. Gienapp, M. E. Visser, *Science* **310**, 304 (2005).
6. C. Both, S. Bouwhuis, C. M. Lessells, M. E. Visser, *Nature* **441**, 81 (2006).
7. A. Charmantier *et al.*, *Science* **320**, 800 (2008).
8. M. E. Visser, *Proc. R. Soc. London Ser. B* **275**, 649 (2008).
9. P. Gienapp, C. Teplitsky, J. S. Alho, J. A. Mills, J. Merila, *Mol. Ecol.* **17**, 167 (2008).
10. J. C. Wingfield, T. P. Hahn, R. Levin, P. Honey, *J. Exp. Zool.* **261**, 214 (1992).
11. A. Dawson, *Philos. Trans. R. Soc. London Ser. B* **363**, 1621 (2008).
12. T. Coppack, *J. Ornithol.* **148**, S459 (2007).
13. B. Silverin *et al.*, *Hormones Behav.* **54**, 60 (2008).
14. C. M. Lessells, *Philos. Trans. R. Soc. London Ser. B* **363**, 1589 (2008).
15. S. Verhulst, J. A. Nilsson, *Philos. Trans. R. Soc. London Ser. B* **363**, 399 (2008).
16. We thank J. Eadie, D. Futuyma, P. Koch, G. Pogson, and especially D. Emlen and K. Wasson for discussion and comments. Supported by NSF grant IOS 0443807 (B.E.L.), an Agence Nationale de la Recherche EVO-INF-ECOL grant (A.S.C.), and NSF grant DEB 0717021 (D.W.W.).

10.1126/science.1159822

PLANT SCIENCE

Using Tobacco to Treat Cancer

Charles J. Arntzen

Plant biotechnology brings us closer to personalized therapies as tobacco plants are genetically reprogrammed to produce a vaccine to treat lymphoma.

Tobacco, which has a gained a reputation as a cause of cancer, may soon earn some praise rather than recrimination after being used by McCormick *et al.* to manufacture patient-specific vaccines against follicular B cell lymphoma (see the figure) (*1*).

Follicular lymphomas are a subtype of non-Hodgkin's lymphoma, the seventh leading cause of cancer-related deaths in the United States (*2*), and are a malignant disease of the lymphatic system that originates from cells of the immune system (lymphocytes). The administration of a tobacco-derived non-Hodgkin's lymphoma vaccine (a single-chain segment of an antibody protein) in a human clinical trial resulted in immune responses in more than 70% of the patients. A majority of patients showed a cellular immune response, suggesting that the vaccine specifically directs the immune system to attack cancer cells. The study not only demonstrates the safety and efficacy of the plant-made protein, but represents the first time that such responses have been observed using a subcutaneously administered antibody-based vaccine in the absence of a carrier protein (which typically boosts the immune response and has been used in all previous clinical studies). Bayer AG, a major pharmaceutical company, has acquired the supporting data from the new study, and very recently announced the opening of a production facility that will use tobacco to manufacture biopharmaceuticals, the first of which will be a candidate patient-specific antibody vaccine for non-Hodgkin's lymphoma therapy.

Although the report of McCormick *et al.* will undoubtedly be appreciated as an advance in immunotherapy for cancer patients, the results will likely generate even greater excitement in the plant biotechnology community. It has been almost two decades since genetically engineered plants were shown to produce monoclonal antibodies or vaccine subunits (the latter can be antigens that

School of Life Sciences and Arizona Biodesign Institute, Arizona State University, Tempe, AZ 85287, USA. E-mail: charles.arntzen@asu.edu

elicit protective antibodies) (*3*–*5*). To date, however, only small biotechnology companies have used plant biotechnology to produce protein pharmaceuticals, such as glucocerebrosidase to treat Gaucher disease, lipase to treat cystic fibrosis, α-interferon, lactoferrin, and others (*3*). Meanwhile, large pharmaceutical companies have watched from the sidelines.

To understand what technical or economic forces have enticed a major player in the pharmaceutical industry into the use of plant biotechnology, one need only look at the strategy for producing a patient-specific vaccine. In the case of non-Hodgkin's lymphoma, patients are diagnosed through symptomatology, followed by excision biopsies (from either a tumor mass or lymph node where the tumorous B cells predominate). Biopsy materials are used to characterize the specific type of non-Hodgkin's lymphoma. Because each B cell bears a unique surface immunoglobulin protein, and because a malignant B cell is of clonal origin, the immunoglobulin becomes a specific marker for the tumor of a specific patient (*6*). Once the specific gene sequences encoding the individual's tumor immunoglobulin have been determined, the challenge is to find a way to obtain a portion of this very specific immunoglobulin in sufficient quantity and conformation to use it as a vaccine that will trigger the body to attack the malignant B cells bearing this immunoglobulin (and not normal B cells).

Earlier studies had shown that immunization with a complete immunoglobulin protein (composed of four polypeptides, with regions that specify the class of antibody and specific antigen target) induced the desired immune response (*7*). From a technical standpoint, however, the time between identification of the immunoglobulin gene sequences in a tumor and manufacture of the corresponding protein is slow (many months) and complex. The time delay, in particular, is a severe hindrance to the use of vaccination as a therapy for non-Hodgkin's lymphoma patients who are newly diagnosed. Rather than wait for a vaccine, these patients are more likely to start conventional (immunosuppressive) chemotherapy even with its negative side effects and uncertainty of durable remissions.

Speed of manufacture turns out to be the key to plant biotechnology's contribution to non-Hodgkin's lymphoma vaccine development. The genomic sequences of many plant viruses are known, and molecular tools are available to quickly insert new genes into a viral genome in such a way that virus replication produces a new nonviral protein as a "by-product" to virus replication. As reported by McCormick *et al.*, a fragment of the tumor-specific immunoglobulin protein called the autologous single-chain variable domain was incorporated into a virus that infects tobacco. Because the single-chain variable domain must correspond uniquely to the immunoglobulin found on the surface of a patient's malignant B cell, a unique virus must be engineered for each patient. Once introduced into a tobacco plant, the engineered virus replicates and spreads rapidly throughout the plant, diverts normal cellular metabolism, and turns on production of the proteins encoded by the viral genome, including the single-chain variable domain gene. Even without optimizing or automating production, patient-specific single-chain variable domain protein fragments could be produced under good manufacturing practice (GMP) regulations within 12 to 16 weeks of receiving biopsy specimens (*8*). The high-risk arena of pharmaceutical development makes it difficult to predict when (or if) a plant-made non-Hodgkin's lymphoma vaccine will ultimately be marketed, but the production facility investment commitment by a large and experienced pharmaceutical company suggests probability of success.

Plant biopharmaceuticals. Shown is the species of tobacco plant (*Nicotiana benthamiana*) that McCormick *et al.* used to manufacture a non-Hodgkin's lymphoma vaccine. Each plant is an identical biomanufacturing unit, which allows for cost-effective vaccine production scale-up. Up to 1000 plants were used to manufacture the vaccine for each patient (*8*).

Academic scientists who have long promoted the use of plant biotechnology as a tool to attack global public health issues and achieve lower-cost protein drugs will learn a valuable lesson if the non-Hodgkin's lymphoma vaccine is successful: There is more to moving a pharmaceutical product into practical use than simple "cost of goods" arguments. For example, the speed by which useful proteins can be produced in plant systems (such as in patient-specific vaccine production) is also advantageous to companies that wish to rapidly obtain GMP samples for phase I clinical trials. And the fact that each individual tobacco plant is a manufacturing unit provides an infinitely scalable manufacturing platform, with low capital investment for the protein production component of biomanufacturing.

The value of plant biotechnology to global health should not be forgotten, however. Protein drugs are now widely used in the developed world, but economic barriers make most of these new biotechnology products inaccessible to all but the very wealthiest inhabitants of the developing world. It is likely that another opportunity for plant-made pharmaceuticals will come in the arena of "biosimilars" (new versions of biopharmaceutical products) or "generic" versions of existing protein drugs (the latter is often through reverse engineering, in which an existing product is produced in a redesigned manufacturing process), especially as patents on current drugs expire. Cancer therapeutics offer a major opportunity. For example, the monoclonal antibody Avastin (manufactured by Genentech) used to treat colorectal and lung cancer and approved earlier this year by the U.S. Food and Drug Administration for treating advanced breast cancer, costs $84,700 for an average 11-month course of breast cancer treatment (*9*). It is conceivable that Avastin and a related monoclonal antibody, Herceptin (also manufactured by Genentech), prescribed for women with breast cancers with high expression of the HER2 receptor, could be manufactured using plant biotechnology with considerable cost advantages. Protein-based therapeutics is still at an early stage, and the involvement of plant biotechnology in their production is at an even earlier stage. But the prospects are exciting.

References and Notes

1. A. A. McCormick *et al.*, *Proc. Natl. Acad. Sci. U.S.A.* **105**, 10131 (2008).
2. L. A. G. Ries *et al.*, *SEER Cancer Statistics Review, 1975–2005*, National Cancer Institute, Bethesda, MD (http://seer.cancer.gov/csr/1975_2005).
3. J. Kaiser, *Science* **320**, 473 (2008).
4. A. Hiatt, R. Cafferkey, K. Bowdish, *Nature* **342**, 76 (1989).
5. H. S. Mason, D. M. Lam, C. J. Arntzen, *Proc. Natl. Acad. Sci. U.S.A.* **89**, 11745 (1992).
6. W. L. Carroll *et al.*, *J. Exp. Med.* **164**, 1566 (1986).
7. P. A. Ruffini *et al.*, *Curr. Gene Ther.* **5**, 511 (2005).
8. D. Tusé, personal communication based on antigen production by Large Scale Biology Corporation.
9. M. Chase, A. W. Mathews, *Wall Street Journal*, 23–24 February 2008, p. A3.

10.1126/science.1163420

The Geological Evolution of the Tibetan Plateau

Leigh H. Royden,* B. Clark Burchfiel, Robert D. van der Hilst

The geological evolution of the Tibetan plateau is best viewed in a context broader than the India-Eurasia collision zone. After collision about 50 million years ago, crust was shortened in western and central Tibet, while large fragments of lithosphere moved from the collision zone toward areas of trench rollback in the western Pacific and Indonesia. Cessation of rapid Pacific trench migration (~15 to 20 million years ago) coincided with a slowing of fragment extrusion beyond the plateau and probably contributed to the onset of rapid surface uplift and crustal thickening in eastern Tibet. The latter appear to result from rapid eastward flow of the deep crust, probably within crustal channels imaged seismically beneath eastern Tibet. These events mark a transition to the modern structural system that currently accommodates deformation within Tibet.

Commonly referred to as the "Roof of the World," the Tibetan plateau stands 5 km high over a region of approximately 3 million km^2 (Fig. 1). As early as the 1920s, Argand (*1*) postulated that the plateau formed as the result of collision and postcollisional convergence of the Indian subcontinent with Eurasia, causing shortening and thickening of the crust to ~80 km and producing the magnificent mountain ranges of the Himalaya, Karakorum, and Tien Shan. This perspective remains widely accepted, but the development of the plateau can also be evaluated within the context of the large dynamic system related to subduction of oceanic lithosphere beneath eastern Eurasia and Indonesia.

Despite decades of study, controversy remains over basic aspects of Tibetan geology. For example, the mantle lithosphere beneath Tibet has been proposed to be cold, hot, thickened by shortening, or thinned by viscous instability. Other controversies include the degree of mechanical coupling between the crust and deeper lithosphere and the nature of large-scale deformation (*2*–*4*). The Tibetan lithosphere is complex, composed of fragments of different ages, compositions, temperatures, and rheology. Understanding the processes that have formed the plateau requires reconstruction of changing patterns of deformation and uplift across a wide range of temporal and spatial scales.

Precollisional Tectonics (Before ~50 Ma)

The development of high topography and thickened crust in the Tibetan region began before continental collision, during subduction of the Tethys oceans northward beneath Eurasia. Early Cretaceous thrust faulting, folding, and crustal thickening took place along the Bangong suture in what is now central Tibet. In Late Cretaceous to Early Eocene time, an Andean mountain range with abundant magmatic activity and a back-arc thrust belt developed along the southern margin of the Eurasian plate (*5*) (Fig. 2).

By Late Cretaceous time, the southern and central plateau was elevated above sea level, which suggests thickening of the continental crust, but northern and northeastern Tibet contained broad areas of nonmarine, and locally marine, deposition, which indicates little crustal thickening there. Plate reconstructions at the time of collision, ~50 million years ago (Ma) (*6*, *7*), place the Indian subcontinent ~2500 km south of its current position (Fig. 3). Estimates of subsequent shortening within the central Himalaya suggest that ~500 to 1000 km of Indian continental lithosphere existed northward of what is now north-central India (*8*).

Through much of Late Cretaceous time, the trenches of the western Pacific subduction boundaries rolled back slowly. This produced north-south trending extension in east China and adjacent offshore areas (*9*), but there is little evidence for eastward movement of continental lithosphere away from southeastern Tibet before collision.

Early Cenozoic Tectonics (~50 Ma to ~20 Ma)

After collision, intracontinental convergence and deformation continued across Tibet, reaching

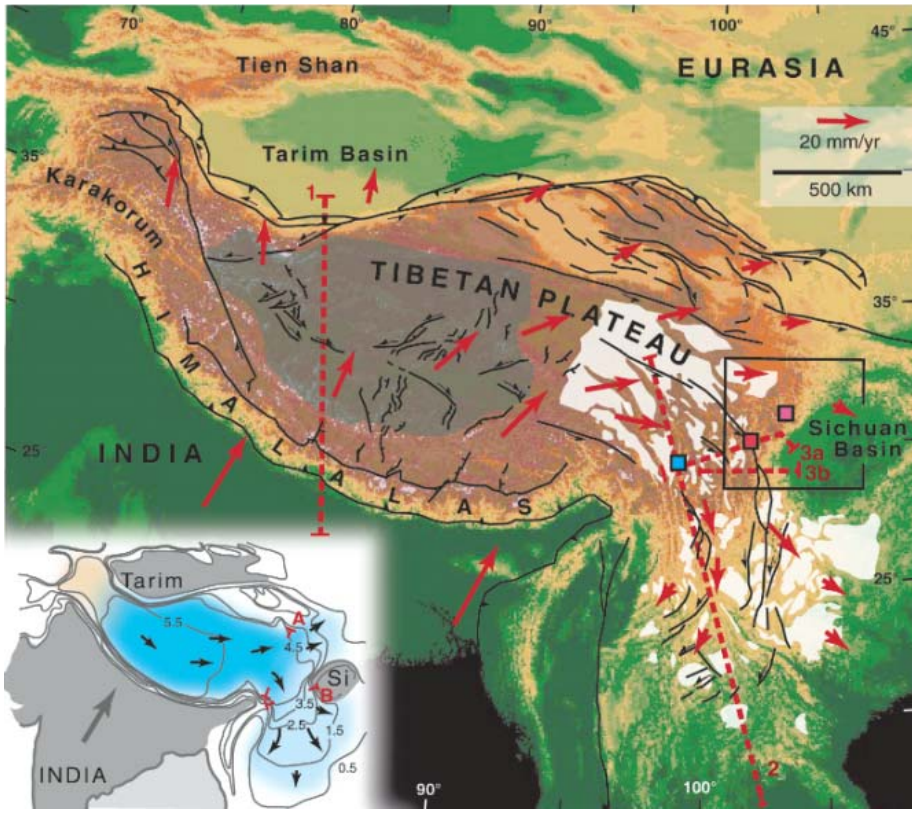

Fig. 1. Topography shade map for the Tibetan region showing the relict landscape of eastern Tibet (white shading) and internally drained region of central Tibet (gray-green shading). Red arrows are selected and slightly generalized GPS measurements (*22*, *24*). Red dashed lines are cross-section locations for Fig. 5; box outlined in black is location of Fig. 6; black lines are young geologic structures; colored squares are ages of initiation of rapid river incision (pink, 5 to 12 Ma; blue, 10 to 15 Ma; red, 8 to 10 Ma) (*34*–*36*). Inset shows the approximate area of deep crustal flow (blue shading) with topographic contours (1-km interval from 500 m) and section lines (A and B) used to constrain rates of deep crustal flow. Black arrows are inferred direction of lower crustal flow (*38*), Si, Sichuan Basin.

Department of Earth, Atmospheric, and Planetary Sciences, Massachusetts Institute of Technology, Cambridge, MA 01890, USA.

*To whom correspondence should be addressed. E-mail: lhroyden@mit.edu

northward to involve a larger area than previously (Fig. 2). In the central Himalaya, postcollisional deformation involved south-vergent thrusting and folding of rocks of the north Indian passive margin as it was subducted beneath Eurasia. Concurrently, crustal shortening formed mostly narrow basins in central and southern Tibet with thick nonmarine, syntectonic strata, bounded by thrust faults that dip south and, more commonly, north (*10*). The magnitude of this Early Cenozoic shortening is unknown; within the basins, shortening is small but locally may reach more than 50%. It has been suggested that this shortening reflects the beginning of southward underthrusting of Eurasia below Tibet (*11*, *12*). Oxygen isotope data suggest that as early as Eocene/Oligocene time the southern and central part of the Tibetan plateau had reached high elevations, whereas the northern part of the plateau remained low (*13*).

At this time, large fragments of Eurasian lithosphere were extruded eastward out of central Tibet, from the Bangong suture region toward southern China and northern Indochina (*2*, *14*) (Fig. 3). The similarity between Eocene folded strata in northern Indochina and central Tibet indicates that these continental fragments were deformed after collision but before or during extrusion. Deformation may have been facilitated by very high lithospheric temperatures, as expressed by a belt of alkali-rich magmatic rocks erupted between ~30 and ~50 Ma (more were erupted later) with melt temperatures of ~1300°C to 1400°C at depths of 80 to 100 km (*15*). In the east, the distribution of these magmatic rocks corresponds closely with that of the extruded fragments.

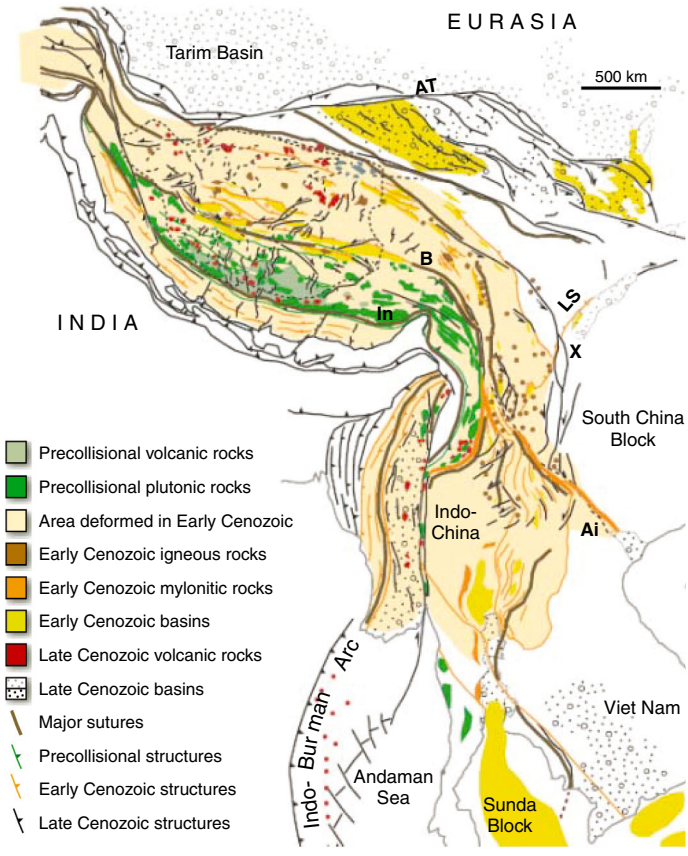

Fig. 2. Tectonic map of Tibet and adjacent regions showing distribution of major structures and rock units grouped approximately into precollisional (before ~50 Ma), Early Cenozoic (before ~20 Ma), and Late Cenozoic (after ~20 Ma). In, Indus suture; B, Bangong suture; LS, Longminshan thrust belt; X, Xianshuehe fault system; Ai, Ailao Shan; AT, Altyn Tagh fault.

The Ailao Shan shear zone (Fig. 2) probably formed the northern boundary of the east-moving fragments (*2*) until the Altyn Tagh fault became active in the late part of the Early Cenozoic. Left-slip on the Altyn Tagh fault was transferred into shortening in the northeastern plateau, probably beginning by Oligocene time when nonmarine rocks, previously deposited in broad basins connected with the Tarim Basin, began to be confined to local basins (*10*, *11*).

Eastward extrusion of lithosphere from central Tibet occurred during a time of rapid trench rollback along much of the Pacific, Philippine, and Indonesian oceanic subduction boundaries (*2*, *16*). This is documented by widespread Early Cenozoic extension within the upper plate lithosphere of Indonesia (*17*), Eocene-Oligocene extension in the South and East China Seas (*18*), and Early Miocene extension in the Sea of Japan (*19*). Rapid fragment extrusion did not continue past ~15 to 20 Ma, when slab rollback and upper plate extension slowed or ended in most places (*16*).

P-wave tomography reveals a seismically fast structure up to ~400-km depth beneath the southern plateau and northern India (*20*, *21*) (Figs. 4 and 5, profile 1). This broad structure differs from the narrow oceanic slabs imaged beneath the western Pacific; it probably represents subducted continental mantle lithosphere of India. West of ~85°E, its cross-sectional area is consistent with subduction and stacking of ~1000 km of Indian continental lithosphere. East of 85°E, the smaller cross-sectional area indicates that less continental lithosphere may have been subducted here.

Late Cenozoic Tectonics (After ~15 to 20 Ma)

As India-Eurasia convergence continued into Late Cenozoic time, southward thrusting continued in the middle and lesser Himalaya, in-

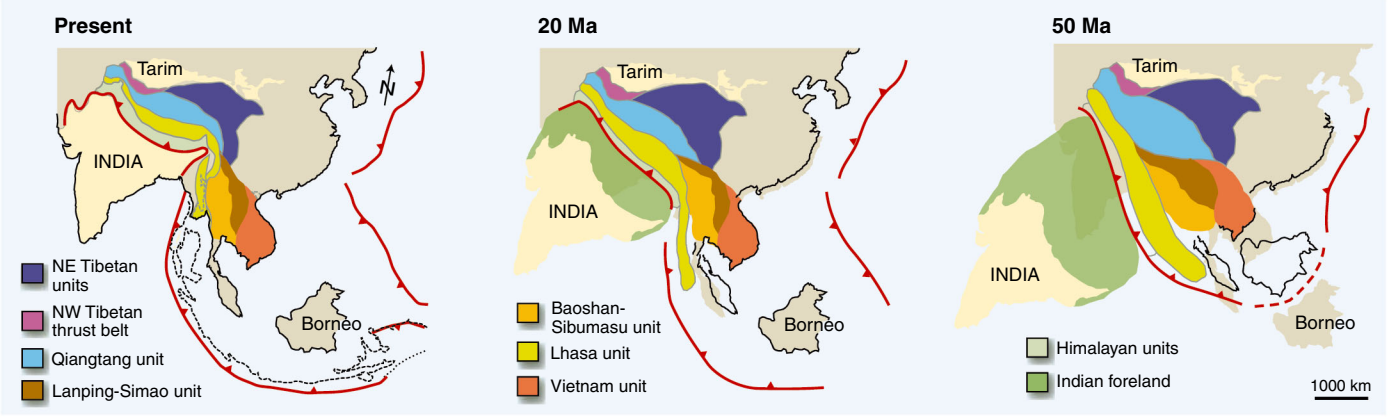

Fig. 3. Tectonic reconstructions around the time of collision (~50 Ma) and at 20 Ma, with India and Eurasia positions determined from sea-floor magnetic anomalies (*6*). Major tectonic units of Tibet and Indochina are generalized by color; their reconstructed shapes are estimates and are poorly known. Bold red lines are estimated positions of subduction zones. Light brown shows the present distribution of land areas.

volving deeper parts of the Indian crust (Fig. 2). North of the Himalaya, the pattern of large-scale deformation changed substantially after the Early Cenozoic, with rapid surface uplift of the eastern plateau and the onset of east-west extension in the central plateau. Some shortening still occurred within narrow basins of the central plateau (*13*), but most shortening relocated to northeastern Tibet and to the Tien Shan.

The timing and structural pattern of young faults and Global Positioning System (GPS) data indicate that the modern deformation regime was established by ~15 Ma in central Tibet and by ~8 to 10 Ma in eastern Tibet (*22*, *23*), with north-south shortening, east-west extension, and eastward motion occurring in the southern and central plateau region (*22*, *24*), and shortening in northeastern Tibet. Evidence for Late Cenozoic crustal shortening in eastern and southeastern Tibet is largely absent. Shortening structures of this age are found only along the Longmenshan thrust belt (*25*, *26*), with total displacements of tens of kilometers and active rates less than a few millimeters per year.

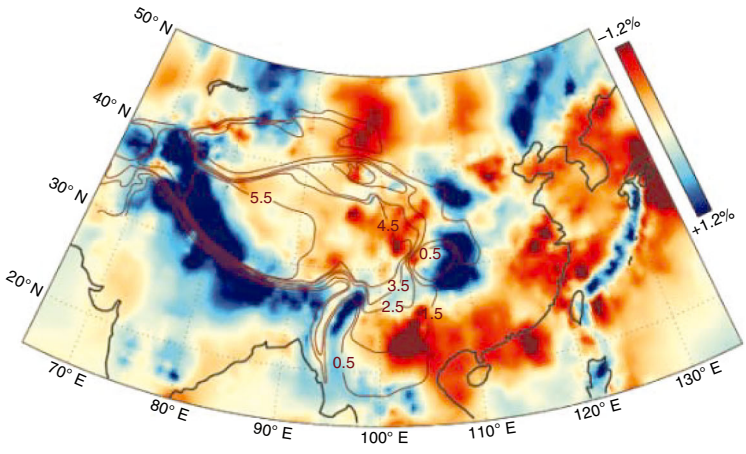

Fig. 4. Lateral variation in *P*-wave speed, at 200-km depth, relative to a laterally homogeneous reference Earth model. This image is part of a global model obtained through tomographic inversion of *P*-wave arrival time data from global, national, and regional seismograph networks (*20*, *21*). The topographic contours (dark red) outline the Tibetan plateau and adjacent areas at elevations from 0.5 to 5.5 km above sea level.

Through the Late Cenozoic, lithospheric fragments continued to be extruded outside the plateau and toward South China and Indochina (*22*). The rates of extrusion were slower than in the Early Cenozoic, but motion was still toward the location of coeval trench rollback along adjacent oceanic subduction boundaries. This is clearest for the Indo-Burman region where upper-plate extension documents westward trench migration beginning at ~20 Ma (*17*). Rapid eastward motions still occurred within the plateau, but most of this motion did not extend outside the plateau. For example, left-slip on the Altyn Tagh fault was transferred into thrust faulting and folding in northeastern Tibet (*27*). Here, narrow high mountain ranges formed and separated deep narrow basins with nonmarine deposition, possibly accompanied by southward subduction of Eurasian crust below central Tibet (*2*, *12*).

To the east, the eastward-moving upper crust of the central and eastern plateau is diverted northeast and southeast around the Sichuan Basin. Marked by fast *P*-wave propagation to at least 250-km depth, this basin appears to be a deeply rooted, mechanically strong unit underlain by craton-like lithosphere that has resisted the multiple deformations that affected the surrounding regions (Fig. 4). Slow seismic-wave propagation in the lithosphere beneath eastern

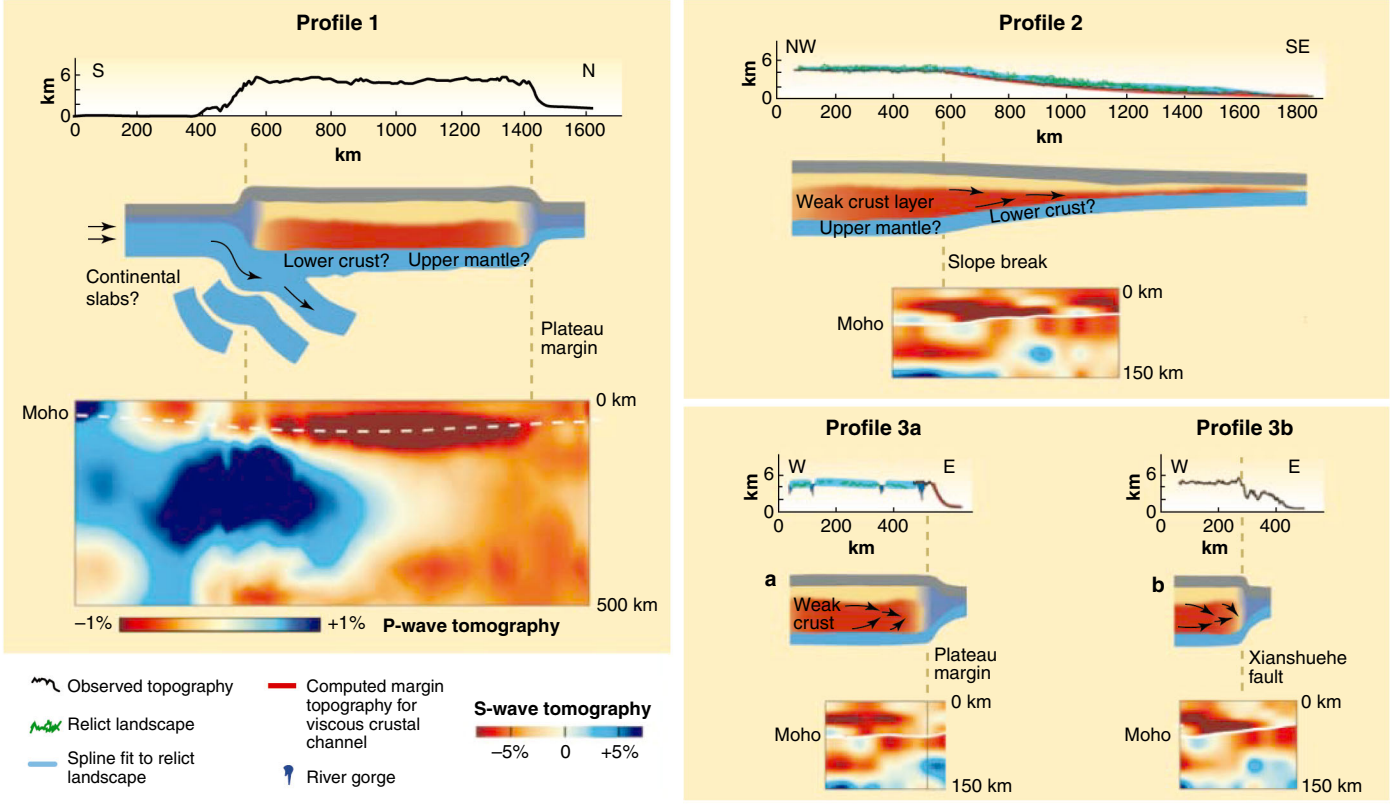

Fig. 5. Profiles through the Tibetan plateau region showing topography (top), conceptual crustal model (middle), and seismic section (bottom). Velocity anomalies are *P*-wave speed on profile 1 and *S*-wave speed on profiles 2, 3a, and 3b (*47*). Moho position is poorly constrained on profile 1, but well constrained from receiver function analysis (*42*) on profiles 2, 3a, and 3b. Profile locations are shown in Fig. 1.

Tibet suggests that its mechanical strength is much lower than beneath the Sichuan Basin.

West and southwest of the Sichuan Basin, southward motion of the upper crust is accommodated by clockwise rotation and by left-slip along the Xianshuihe fault system, which became active at ~8 to 10 Ma and has a net displacement of ~70 km and GPS-measured rates of ~10 to 12 mm/year (*22*–*24*). Southward, near the Ailao Shan, its displacement remains uniform but occurs across a zone 100 km wide without identifiable faults. Northwest of the Sichuan basin, Tibetan upper crust also deforms and moves relative to the basin across a wide area without identifiable faults (*28*). Both regions of active shear without recognized faulting are marked by low seismic-wave speeds, and presumably high temperatures, at ≤200-km depth (*20*) (Fig. 4).

One of the most conspicuous changes in Late Cenozoic deformation is the onset of east-west crustal extension in central Tibet. Extension occurs along north-south trending grabens, northeast-striking left-slip faults and northwest-striking right-slip faults, and reaches southward to include parts of the High Himalaya. Extension may have begun by 13 to 18 Ma and was well under way by 8 Ma (*29*, *30*). The initiation of extension has been proposed to result from rapid removal of Tibetan mantle lithosphere, with a consequent increase in surface elevation of the plateau (*31*), but in our view the initiation of extension is more likely tied to the uplift of eastern Tibet (*32*).

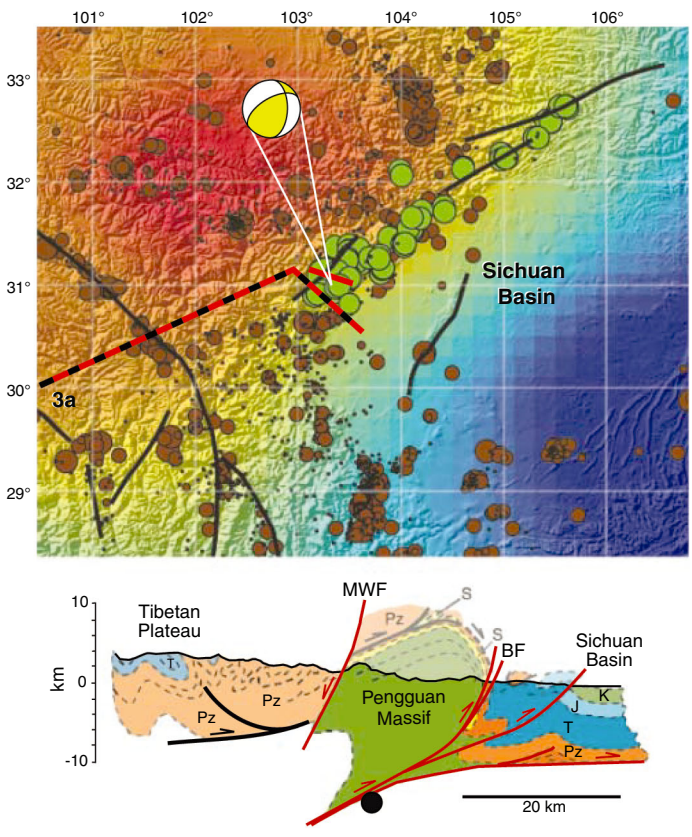

Fig. 6. (**Top**) Epicenters of 12 May 2008 Wenchuan earthquake and aftershocks (green circles), with focal mechanism for the main event (*48*). Events are superimposed on map of lateral variation in *P*-wave speed at 100-km depth relative to a laterally homogeneous reference Earth model (*47*), with color scale the same as in Fig. 4. Brown dots, regional seismicity (body wave magnitude larger than 3, symbol size scaled with magnitude, time interval 1964 to 2007) from EHB catalog (*49*). Map location given in Fig. 1. (**Bottom**) Geological structure along a profile through the hypocenter, modified after (*28*), with location shown by the red line on the map. Black lines, Jurassic faults; red lines, Late Cenozoic faults; S, Sinian (latest Proterozoic); MWF, Maowen-Wenchuan fault zone; BF, southern continuation of the Beichuan fault zone. Partially whited-out structures indicate geologic reconstruction above the modern topographic surface. Yellow circle depicts location of main Wenchuan earthquake with estimated uncertainty in depth of ±5 km.

Tibetan Landscape

The surface of the high central plateau is internally drained, differing considerably from eastern and southeastern Tibet, where a relict landscape is preserved between major rivers (*33*) (Fig. 1). This relict landscape, which extends from the 5-km-high eastern plateau to regions below 1-km elevation, may have been largely established by the end of the Cretaceous; areas deformed in the Early Cenozoic were rebeveled before the Late Cenozoic (*33*). Comparison with modern landscapes suggests that the east Tibetan landscape formed at regional slopes of not more than 10^{-3} to 10^{-4}. Because its downstream end has remained near sea level, where it merges with the modern coastal plain, its upstream portion probably formed at elevations less than ~1.5 km.

The east Tibetan landscape is currently undergoing rapid change as the major rivers that drain the plateau are incising at ~0.3 to 0.4 mm/year (*34*, *35*), carving gorges up to 3 km deep. U-Th/He dating on apatite shows that river incision started at ~8 to 15 Ma on major tributaries of the Yangtze River (*34*, *35*) and at ~5 to 12 Ma along the Longmenshan plateau margin (*36*) (Fig. 1). Thus, uplift of the eastern plateau, the onset of east-west extension in the central plateau, and the structural transition to the modern fault patterns all date to ~10 to 15 Ma, whereas uplift of central Tibet occurred much earlier (*13*).

Crustal Rheology and Dynamics

Much of the active deformation of Tibet results from its high topography. Surface strain rates, inferred from GPS and earthquake data, are consistent with gravitationally driven flow of a viscous lithosphere bounded by stronger converging blocks to the north and south (*4*, *37*, *38*) (Fig. 1). Whether this coherently deforming layer extends into the upper mantle or whether it ends within the crust, thereby allowing for some degree of mechanical decoupling between upper crust and mantle, is a topic of ongoing debate.

Magnetotelluric data from the eastern and south central plateau indicate a hot, fluid-rich middle crust (*39*). In a few localities, young magmatic rocks with melt temperatures of 1300 to 1400°C indicate high temperatures just below and probably within the deeper crust (*15*). Surface-wave tomography (*40*, *41*) and receiver function analysis (*42*) from regional seismic arrays in eastern and southeastern Tibet show a middle and lower crustal network with low shear-wave speed, and presumably low mechanical strength (Fig. 5). These low-velocity zones terminate against the steeply sloping plateau margin adjacent to the Sichuan Basin. These results support model predictions that plateau morphology correlates with the underlying crustal rheology (*38*, *43*, *44*): The high plateau and the gently sloping southeastern and northeastern margins overlie weak crustal zones, and steeply sloping margins overlie crust that is strong throughout.

Arguments for deep crustal flow beneath Tibet come largely from the history of the eastern plateau, which was uplifted without substantial shortening of the upper crust (*23*, *38*). Unless new crust is introduced from the mantle, crustal thickening and surface uplift require rapid eastward flow in the deep crust (Fig. 1), probably within the slow seismic zones imaged in the middle and lower crust, but this interpretation remains controversial. Deep crustal flow would have occurred over distances of hundreds to perhaps 1000 km. A rough volume balance for the past 15 million years suggests that deep crustal flow through profiles A and B (Fig. 1, inset) averaged a minimum of ~70 to 100 mm/year, approximately five times that of the upper crust, with the viscosity of the deep crust being several orders of magnitude smaller than that of the upper crust (*45*).

The cause, formation, and lateral interconnectivity of weak crustal zones beneath Tibet remain unclear. The weak crust is probably hot, an expected consequence of radiogenic heating in a thickened crust, but modeling and surface-wave tomography indicate that weak crust also

extends to low elevations beneath the southeastern margin where the crust has not been greatly thickened. Model studies suggest that the east Tibetan crust became weak before it became thick.

We speculate that until ~15 Ma, a zone of stronger crust supported the eastern margin of the plateau, separating an area of weak lower crust beneath what is now the central plateau from an area of weak lower crust beneath the lowland region that is now eastern Tibet. We further suggest that this plateau margin advanced into eastern Tibet at ~15 to 10 Ma, uniting the areas of weak crust. This enabled rapid eastward flow of deep crust from central Tibet into eastern and southeastern Tibet, along with slower flow in the upper crust and east-west surface extension. In our interpretation, the initiation of east-west extension in central Tibet, the uplift of eastern Tibet, and the establishment of the modern deformation field in central and eastern Tibet are all the result of this process originating in the deep crust.

Conclusions

The evolution of the Tibetan plateau involves subduction of Indian lithosphere, thickening of Tibetan crust, and eastward extrusion of Tibetan lithosphere. Data summarized here indicate that extrusion of lithospheric fragments beyond the borders of the plateau correlates with trench rollback in the western Pacific and around Indonesia. We suggest that both a source (area of thickening crust in central Tibet) and a sink (areas of trench rollback to the east and southeast) are needed to enable large-scale extrusion of lithospheric fragments beyond the borders of the plateau. As a corollary, the slowing and reorganization of oceanic trench rollback in the early part of Late Cenozoic time may have been responsible for the coeval slowing and reorientation of fragment extrusion and may have contributed to eastward growth of the plateau.

We propose that the transformation from the older structural regime that dominated Early Cenozoic deformation to the modern structural regime is related to eastward migration of the eastern plateau margin into an area of weak lower crust beneath eastern Tibet. This resulted in merging of two regions of weak crust and in rapid eastward flow within the deep crust.

Epilogue

On 12 May 2008, a magnitude 7.9 earthquake occurred near the town of Wenchuan, China (*46*) (Fig. 6). Rupture propagated for ~270 km along north-northeast striking, west-dipping fault(s) with up to ~10 m of thrust- and right-slip displacement. The hypocenter of the main event is estimated at ~10- to 20-km depth, but details of the surface rupture and slip distribution remain under investigation.

The main event and aftershocks occurred beneath the steep margin of the Tibetan plateau, adjacent to the mechanically strong Sichuan Basin and near profile 3a (Fig. 5), where GPS data reveal up to several millimeters per year convergence and right-slip. A geological section through the epicenter shows an imbricate thrust sequence, emplaced above the Pengguan massif in Jurassic time. These units were refolded and thrust eastward in Late Cenozoic time. The basal thrust fault roots westward into the basement beneath the Pengguan massif. Folded strata can be matched across the Cenozoic faults, which do not appear to have large displacement, perhaps several tens of kilometers in total. Initial rupture during the Wenchuan earthquake probably occurred along a ramp in the basal thrust or related faults (*46*) (Fig. 6).

From information currently available and from the arguments presented here, we propose that along the steep Longmen Shan margin (i) active thrust faulting serves mainly to accommodate vertical uplift of the plateau margin, with crustal thickening occurring by lateral injection of weak crust (Fig. 5), and (ii) the right-slip component of displacement serves to flux upper-crustal material northeastward around the strong lithosphere of the Sichuan Basin. Ongoing study of postseismic displacements related to the Wenchuan earthquake of 12 May 2008 should provide much data to test hypotheses of flow and deformation in the deep crust beneath eastern Tibet.

References and Notes

1. E. Argand, *Cong. Geol. Int.* **1922**, 171 (1922).
2. P. Tapponnier, G. Peltzer, R. Armijo, *Geol. Soc. London Spec. Publ.* **19**, 115 (1986).
3. P. Tapponnier *et al*., *Science* **294**, 1671 (2001).
4. G. A. Houseman, P. C. England, *J. Geophys. Res.* **91**, 3651 (1986).
5. P. Kapp, P. G. DeCelles, G. E. Gehrels, M. Heizler, L. King, *Geol. Soc. Am. Bull.* **119**, 917 (2007).
6. P. Molnar, P. C. England, J. Martinod, *Rev. Geophys.* **31**, 357 (1993).
7. D. B. Rowley, *J. Geol.* **106**, 229 (1998).
8. P. G. DeCelles, D. M. Robinson, G. Zandt, *Tectonics* **21**, 1062, 10.1029/2001TC001322 (2002).
9. L. Shu, X. Zhou, P. Deng, W. Zhu, *Acta Geol. Sin.* **81**, 573 (2007).
10. Z. Liu, C. Wang, H. Yi, *J. Sed. Res.* **71**, 971 (2001).
11. E. Cowgill, A. Yin, M. Harrison, *J. Geophys. Res.* **108**, 2346, 10.1029/2002JB002080 (2003).
12. B. Meyer *et al*., *Geophys. J. Int.* **135**, 1 (1998).
13. D. S. Rowley, B. S. Currie, *Nature* **439**, 677 (2006).
14. S. Akciz, B. C. Burchfiel, J. L. Crowley, J. Yin, L. Chen, *Geosphere* **4**, 292 (2008).
15. E. S. Holbig, T. L. Grove, *J. Geophys. Res.* **113**, B04210, 10.1029/2007JB005149 (2008).
16. R. van der Hilst, T. Seno, *Earth Planet. Sci. Lett.* **120**, 395 (1993).
17. R. Hall, C. K. Morley, in *Continental-Ocean Interactions Within East Asian Marginal Seas*, P. Clift, W. Kuhnt, P. Wang, D. Hayes, Eds., *AGU Geophys. Monogr.* **149**, pp. 55–85 (2004).
18. J.-C. Sibuet, S. K. Hsu, E. Debayle, in *Continental-Ocean Interactions Within East Asian Marginal Seas*, P. Clift, W. Kuhnt, P. Wang, D. Hayes, Eds., *AGU Geophys. Monogr.* **149**, pp. 127–158 (2004).
19. E. Honza, H. Tokuyama, S. Wonn, in *Continental-Ocean Interactions Within East Asian Marginal Seas*, P. Clift, W. Kuhnt, P. Wang, D. Hayes, Eds., *AGU Geophys. Monogr.* **149**, pp. 87–108 (2004).
20. C. Li, R. D. van der Hilst, A. S. Meltzer, E. R. Engdahl, *Earth Planet. Sci. Lett.*, 10.1016/j.epsl.2008.07.016 (2008).
21. C. Li, R. D. van der Hilst, E. R. Engdahl, S. Burdick, *Geochem. Geophys. Geosyst.*, 10.1029/2007GC001806 (2008).
22. P.-Z. Zhang *et al*., *Geology* **32**, 809 (2004).
23. E. Wang *et al*., *Geol. Soc. Am. Spec. Publ.* **327**, 108 (1998).
24. B. J. Meade, *Geology* **35**, 81 (2007).
25. R. Zhou *et al*., *Acta Geol. Sin.* **81**, 593 (2007).
26. B. C. Burchfiel, *GSA Today* **14**, 4 (2004).
27. B. C. Burchfiel *et al*., *Geology* **17**, 748 (1989).
28. B. C. Burchfiel, Z. Chen, Y. Liu, L. H. Royden, *Int. Geol. Rev.* **37**, 661 (1995).
29. H. Williams, S. Turner, S. Kelley, N. Harris, *Geology* **29**, 339 (2001).
30. P. M. Blisniuk *et al*., *Nature* **412**, 628 (2001).
31. P. C. England, G. A. Houseman, *J. Geophys. Res.* **94**, 17561 (1989).
32. K. L. Cook, L. H. Royden, *J. Geophys. Res.*, 10.1029/2007JB005457 (2008).
33. M. K. Clark *et al*., *J. Geophys. Res.* **111**, 10.1029/2005JF000294 (2006).
34. M. K. Clark *et al*., *Geology* **33**, 525 (2005).
35. W. Ouimet, thesis, Massachusetts Institute of Technology (2007).
36. E. Kirby *et al*., *Tectonics* **21**, 1001, 10.1029/2000TC001246 (2002).
37. L. M. Flesch, A. J. Haines, W. E. Holt, *J. Geophys. Res.* **106**, 16435 (2001).
38. M. K. Clark, L. H. Royden, *Geology* **28**, 703 (2000).
39. K. D. Nelson *et al*., *Science* **274**, 1684 (1996).
40. H. Yao, R. D. van der Hilst, M. V. de Hoop, *Geophys. J. Int.* **166**, 732 (2006).
41. H. Yao, C. Beghein, R. D. van der Hilst, *Geophys. J. Int.* **173**, 205 (2008).
42. L. Xu, S. Rondenay, R. D. van der Hilst, *Phys. Earth Planet. Inter.* **165**, 176 (2007).
43. L. H. Royden, *J. Geophys. Res.* **101**, 17679 (1996).
44. F. Shen, L. H. Royden, B. B. C. Burchfiel, *J. Geophys. Res.* **106**, 6793 (2001).
45. Profile A: Crust added east of the profile (after 15 Ma) is ~2.4×10^7 km^3. Profile B: Crust added south of the profile (after 15 Ma) is ~1.5×10^7 km^3. Upper-crustal viscosity (and whole-crust viscosity under steep plateau margins) is 10^{20} to 10^{21} Pa s; deep crustal channel thickness is assumed to be 20 km and its viscosity is 10^{16} to 10^{17} Pa s beneath the high plateau and 10^{18} Pa s beneath the southeastern and northeastern plateau margins.
46. B. C. Burchfiel *et al*., *GSA Today* **18**, 4 (2008).
47. The tomographic cross sections depict wave speed perturbations relative to a laterally homogeneous reference Earth model and show slow seismic-wave propagation in parts of the crust and mantle lithosphere. The *P*-wave speed model is obtained from travel-time tomography (*20*, *21*); the *S*-wave speed model is obtained from surface-wave array tomography (*40*, *41*).
48. U.S. Geological Survey Earthquake Center, http://earthquake.usgs.gov/eqcenter/eqinthenews/2008/us2008ryan.
49. E. R. Engdahl, R. D. van der Hilst, R. P. Buland, *Bull. Seismol. Soc. Am.* **88**, 722 (1998).

50. This project has been supported by NSF Earth Science, Continental Dynamics Program since 1986, most recently by grant EAR-0003571. This work would not have been possible without the collaboration and support of our colleagues at the Chendu Institute of Geology and Mineral Resources over many years, especially Chen Zhiliang, and at the Geological Institute of Yunnan, in Kunming.

10.1126/science.1155371

N_2O_5 Oxidizes Chloride to Cl_2 in Acidic Atmospheric Aerosol

James M. Roberts,[1]* Hans D. Osthoff,[1,2]† Steven S. Brown,[1] A. R. Ravishankara[1,3]

Molecular chlorine (Cl_2) has been observed in the mid-latitude marine boundary layer at mixing ratios ranging from a few tens to several hundred parts per trillion by volume (*1*–*3*). Cl_2 photolyzes readily to atomic chlorine, a highly reactive species that affects abundances of ozone (both production and destruction), aerosol formation, and important trace gases as varied as methane, mercury, and naturally occurring sulfur compounds. A number of possible mechanisms have been proposed for the conversion of chloride to Cl_2 (*4*, *5*); however, the detailed processes involved remain uncertain. We show that reaction of dinitrogen pentoxide (N_2O_5) with aerosol phase chloride yields Cl_2 at low pH (<2) and should constitute an important halogen activation pathway.

It has been known for some time that heterogeneous uptake of N_2O_5 to NaCl or sea salt aerosol results in the efficient production of nitryl chloride ($ClNO_2$) (*6*).

$$N_2O_5(g) + Cl^-(aq) \rightarrow ClNO_2(g) + NO_3^-(aq) \quad (1)$$

Such surfaces are highly hygroscopic such that their chemistry resembles that of concentrated aqueous solutions (*5*). Recently, we showed that the reaction in Eq. 1 occurs in the atmosphere on particles of moderate to low chloride content (*7*). This formation has also been observed in laboratory experiments (*8*, *9*), but those studies lacked detail in the Cl^- concentrations and pH ranges of potential interest. We report a series of laboratory experiments on the reactivity of N_2O_5 on a variety of halide-containing substrates, for example, ammonium sulfate, ammonium bisulfate, and oxalate (table S1). We used iodide ion chemical ionization mass spectrometry to simultaneously measure $ClNO_2$, Cl_2, and Br_2 (*10*). These studies confirmed that the N_2O_5 converts to $ClNO_2$ at low Cl^- concentrations on a range of substrates pertinent to atmospheric aerosol, but they also revealed the presence of an additional channel, the direct formation of Cl_2.

To confirm that $ClNO_2$ was an intermediate in this Cl_2 formation, we used a salt slurry to nearly quantitatively convert (94%) a flow of N_2O_5 in air to $ClNO_2$ and passed the resulting stream over a deliquesced mixture of oxalic acid and NaCl (pH ≈ 1.8). Figure 1 shows that $ClNO_2$ was efficiently converted to Cl_2 under these conditions. $ClNO_2$ is normally insoluble and relatively unreactive, as indicated by the low uptake coefficients ($\gamma = 0.3 \times 10^{-6}$ to 5×10^{-6}) on water or NaCl solutions, at neutral pH (*4*). The uptake coefficient estimated from our low pH experiment was much higher, $\gamma = 6 \times 10^{-3} \pm 2 \times 10^{-3}$. Coupled with a Henry's Law constant of 4×10^{-2} M atm^{-1}, this value implies a first-order loss coefficient in solution of 1.6×10^7 s^{-1} and rate coefficients for reaction of $ClNO_2$ with $Cl^- \geq 10^7$ M^{-1} s^{-1} at low pH. Moreover, our measurements of the $ClNO_2$-to-Cl_2 conversion of 60 to 100% [see (*10*) for detailed measurement precision] indicate that the overall conversion of N_2O_5 to Cl_2 is an efficient process on acidic aerosol particles in the atmosphere.

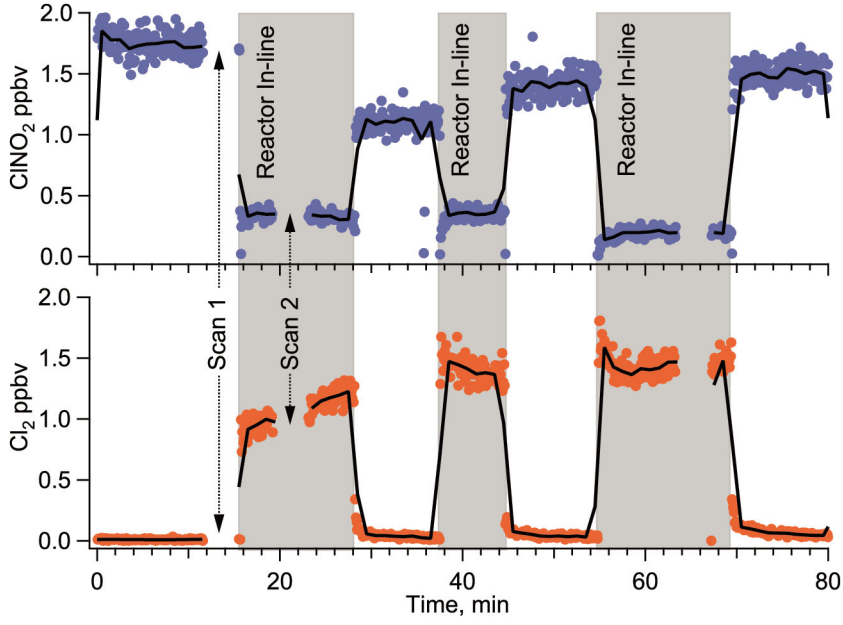

Fig. 1. Efficient reaction of $ClNO_2$ with Cl^- to form Cl_2 (60 to 100% conversion within measurement precision) on deliquesced oxalic acid and NaCl. Mixing ratios were in parts per billion by volume, ppbv. Mass scans 1 and 2 are shown in fig. S1.

Production of Cl_2 from either N_2O_5 or $ClNO_2$ was observed on aqueous solutions of NaCl, $(NH_4)HSO_4$, or oxalic acid, at pH less than or equal to 2 and at Cl^- concentrations as low as 0.05 M (*10*). The acid catalysis observed in our work implies that there are significant barriers to this chemistry at neutral pH and that a solution or quasi-liquid layer is needed for the reaction to proceed. A more detailed discussion of the proposed mechanism is included in (*10*).

This process of Cl_2 formation has not been previously considered in atmospheric chemistry. Low-pH aerosol particles have been observed in the lower troposphere (*2*), and thermodynamic models suggest that chloride concentrations above 0.05 M can exist on such particles (*11*). Moreover, low-temperature models predict that chloride-containing aerosol should exist in the upper troposphere and lower stratosphere (*12*). Therefore, implications for tropospheric and stratospheric chemistry should be further explored through future laboratory, field, and modeling studies.

References and Notes

1. C. W. Spicer *et al.*, *Nature* **394**, 353 (1998).
2. W. C. Keene *et al.*, *J. Geophys. Res.* **112**, D10S12 10.1029/2006JD007689 (2007).
3. B. D. Finley, E. S. Saltzman, *Geophys. Res. Lett.* **33**, 10.1029/2006GL025799 (2006).
4. M. J. Rossi, *Chem. Rev.* **103**, 4823 (2003).
5. B. J. Finlayson-Pitts, *Chem. Rev.* **103**, 4801 (2003).
6. B. J. Finlayson-Pitts, M. J. Ezell, J. N. Pitts Jr., *Nature* **337**, 241 (1989).
7. H. D. Osthoff *et al.*, *Nat. Geosci.* **1**, 324 (2008).
8. W. Behnke, C. George, V. Scheer, C. Zetzsch, *J. Geophys. Res.* **102**, 3795 (1997).
9. F. Schweitzer, P. Mirabel, C. George, *J. Phys. Chem. A* **102**, 3942 (1998).
10. Materials and methods are available on *Science* Online.
11. S. L. Clegg, P. W. Brimblecombe, A. S. Wexler, *J. Phys. Chem. A* **102**, 2155 (1998).
12. K. S. Carslaw, S. L. Clegg, P. Brimblecombe, *J. Phys. Chem.* **99**, 11557 (1995).
13. This work was supported in part by the NOAA's Health of the Atmosphere Program and NOAA's Climate Goal.

Supporting Online Material

www.sciencemag.org/cgi/content/full/1158777/DC1
Materials and Methods
Fig. S1
Table S1
References

7 April 2007; accepted 9 June 2008
Published online 3 July 2008;
10.1126/science.1158777
Include this information when citing this paper.

[1]Chemical Sciences Division, Earth System Research Laboratory, National Oceanic and Atmospheric Administration (NOAA), Boulder, CO 80305, USA. [2]Cooperative Institute for Research in the Environmental Sciences, NOAA, and the University of Colorado, Boulder, CO 80309, USA. [3]Department of Chemistry and Biochemistry, University of Colorado, Boulder, CO 80309, USA.

*To whom correspondence should be addressed. E-mail: James.M.Roberts@noaa.gov
†Present address: Department of Chemistry, University of Calgary, Calgary, Alberta T2N 1N4, Canada.

Star Formation Around Supermassive Black Holes

I. A. Bonnell[1]* and W. K. M. Rice[2]

The presence of young massive stars orbiting on eccentric rings within a few tenths of a parsec of the supermassive black hole in the galactic center is challenging for theories of star formation. The high tidal shear from the black hole should tear apart the molecular clouds that form stars elsewhere in the Galaxy, and transport of stars to the galactic center also appears unlikely during their lifetimes. We conducted numerical simulations of the infall of a giant molecular cloud that interacts with the black hole. The transfer of energy during closest approach allows part of the cloud to become bound to the black hole, forming an eccentric disk that quickly fragments to form stars. Compressional heating due to the black hole raises the temperature of the gas up to several hundred to several thousand kelvin, ensuring that the fragmentation produces relatively high stellar masses. These stars retain the eccentricity of the disk and, for a sufficiently massive initial cloud, produce an extremely top-heavy distribution of stellar masses. This potentially repetitive process may explain the presence of multiple eccentric rings of young stars in the presence of a supermassive black hole.

By tracking the motions of young massive stars, two teams of astronomers have uncovered the existence of a supermassive black hole, measured at 3.6×10^6 solar masses ($M_\odot$), in the center of our Galaxy (*1*–*3*). In addition, one, possibly two, eccentric rings of young massive stars orbit slightly farther out, near ~0.1 pc (*4*), whereas low-mass stars are sparse in the region (*5*), making our galactic center the best example of an atypical distribution of stellar masses (or stellar initial mass function, IMF).

The presence of young massive stars in the vicinity of the galactic center is difficult to reconcile with current models of star formation, in which turbulent molecular clouds produce a mostly clustered population of stars with a remarkably constant distribution of stellar masses ranging from $<0.1\ M_\odot$ to $>100\ M_\odot$ (*6*). The tidal pull from the supermassive back hole should disrupt anything as tenuous as a molecular cloud, thereby destroying it before it can even form and thus removing the necessary conditions for star formation (*7*). This leaves two possibilities: Either the stars formed elsewhere and migrated to the galactic center, or the stars formed in situ by an unusual mechanism, such as the fragmentation of a gaseous disk rotating around the supermassive black hole (*8*, *9*).

A stellar cluster could migrate to the galactic center by losing energy through its gravitational disturbance of the background stars in the Galaxy. However, this appears to take too long to explain the existence of the young stars found there (*10*). Star formation in an accretion disk around the supermassive black hole is possible if the disk is sufficiently massive (*11*) and if it is able to cool sufficiently rapidly (*12*, *13*). A priori, disk fragmentation should produce circular orbits, not the eccentric rings recently detected. Dynamical relaxation of a top-heavy IMF could increase the eccentricities of individual stars but is unlikely to reach the values observed, which suggests that the stars are likely to have formed from an initially eccentric disk (*14*, *15*). Here, we explore how the accretion disk formed around the black hole, and in particular how it could form with an initial eccentricity, by simulating the evolution of a giant molecular cloud falling toward a supermassive black hole (*16*). The cloud is presumed to be the result of a collision at a distance of several parsecs from the galactic center, sending it on a plunging orbit toward the black hole.

We carried out the simulations with the use of smoothed particle hydrodynamics, a Lagrangian hydrodynamics formalism (*17*). We considered two situations: a $10^4\ M_\odot$ molecular cloud falling toward a $10^6\ M_\odot$ black hole, and a $10^5\ M_\odot$ molecular cloud falling toward a $3 \times 10^6\ M_\odot$ black hole. The clouds were initially placed 3 pc from the black hole and on an orbit with an impact parameter of ~0.1 pc. The clouds were turbulently supported and had a minimum temperature of 100 K due to the background radiation field. We included an approximate radiative transfer formalism with compressional heating balanced by cooling rates derived from estimated optical depths (*18*). Dense protostellar fragments were replaced by sink-particles (*19*) that accreted all bound gas particles that fell within 200 AU (*20*). Our computations were performed at the UK Astrophysical Fluids Facility and at our local SUPA High-Performance Computing facility.

The early evolution of both clouds was broadly similar over the $\sim 2 \times 10^4$ years required to reach the galactic center. As the $10^4\ M_\odot$ molecular cloud fell toward the $10^6\ M_\odot$ black hole (Fig. 1), it became tidally distorted and unbound because of the strong gravitational field. The turbulence in the cloud formed local structures, some of which collapsed to form stars before the cloud reached the black hole. Stars that formed before closest approach remained unbound and escaped the system. In contrast, 10% of the gas cloud became bound as a result of the combination of gas dissipation and tidal torques at closest approach and remained in orbit within a few tenths of a parsec. The tidal disruption of the self-gravitating cloud formed coherent spiral structures that transferred orbital angular momentum outward while shocks from infalling streams, which passed either side of the black hole, also removed orbital angular momentum from the gas, allowing it to form an eccentric disk-like structure.

Structure in the infalling gas ensured that the disk of bound gas was very clumpy, forming spiral patterns that grew because of the disk's self-gravity and fragmented to form individual stars. The fragmentation occurred very quickly (on an orbital time scale) to form 498 stars with eccentricities between $e = 0.6$ and $e = 0.76$ and semimajor axes between $a = 0.11$ pc and $a = 0.19$ pc. The larger $10^5\ M_\odot$ cloud (the final state is shown in Fig. 2) formed 198 stars with semimajor axes between $a = 0.02$ pc and $a = 0.13$ pc and eccentricities between $e = 0$ and $e = 0.53$. The larger mass and size of the cloud resulted in more angular momentum being removed by the tidal torques and by direct shocks on the incoming streams, such that the eccentric disk and stars were formed closer to the black hole. The stellar disks were fairly thin, with an initial height-to-radius ratio (H/R) varying from 0.1 to 0.2. Dynamical relaxation of these disks would increase the H/R slightly over several million years.

The resulting masses of the stars formed depends crucially on the balance between compressional heating of the gas as it infalls toward the black hole and the radiative cooling given by the gas temperature and the local optical depth. Near the black hole, the heating dominated, increasing the gas temperature to between several hundred and several thousand kelvin. This resulted in a Jeans mass, the minimum fragment mass, on the order of $0.5\ M_\odot$ for the $10^4\ M_\odot$ cloud and up to 10 to 50 $M_\odot$ for the $10^5\ M_\odot$ cloud. The higher-mass cloud produced higher temperatures, and hence higher Jeans masses, as more gas was captured closer in to the black hole. This increased the compressional heating while the increased optical depths decreased the cooling rate. Stars that formed farther out, near 0.1 pc, had masses of several $M_\odot$ as in the lower-mass cloud.

The stellar mass functions from the two simulations are very different: The lower-mass cloud (Fig. 3) formed a typical stellar mass distribution peaking at $0.8\ M_\odot$ and following a Salpeter-type power law at higher masses [$dN(\log m) = m^{-\Gamma}\ d(\log m)$, where dN is the number of stars with masses between m and $m + dm$, and the exponent $\Gamma \sim 1.35$

[1]Scottish Universities Physics Alliance, School of Physics and Astronomy, University of St. Andrews, North Haugh, St. Andrews, Fife KY16 9SS, UK. [2]Scottish Universities Physics Alliance, Institute for Astronomy, University of Edinburgh, Blackford Hill, Edinburgh EH9 3HJ, UK.

*To whom correspondence should be addressed. E-mail: iab1@st-andrews.ac.uk

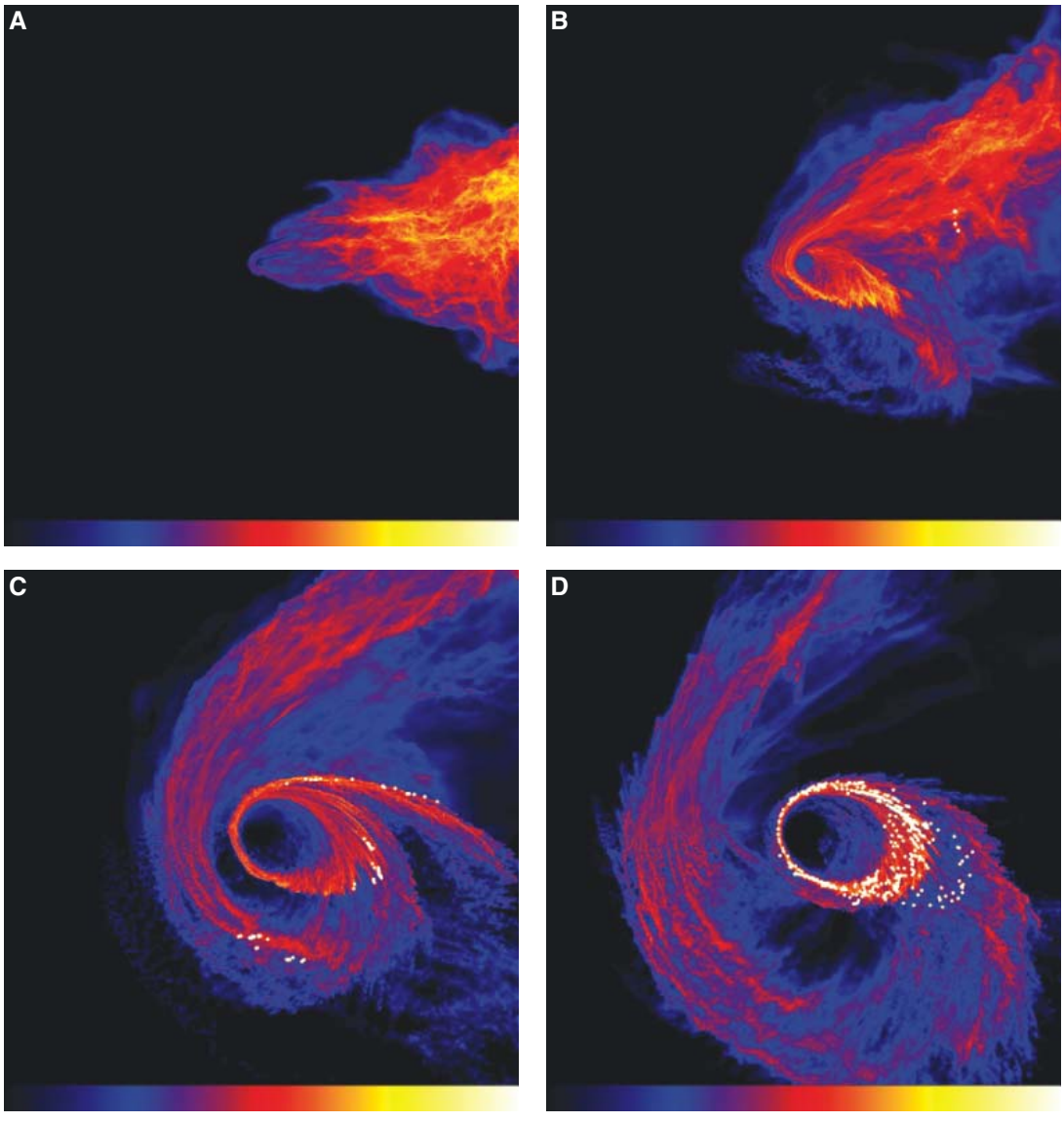

Fig. 1. The evolution of a $10^4\ M_\odot$ molecular cloud falling toward a $10^6\ M_\odot$ supermassive black hole. (**A**) The region within 1.5 pc of the black hole, ~32,000 years after start of evolution; colors denote the column density on a logarithmic scale from 0.01 g cm^{-2} to 100 g cm^{-2}. (**B**) Image at 42,000 years, showing the region within 1 pc of the black hole; color scale is from 0.025 g cm^{-2} to 250 g cm^{-2}. (**C** and **D**) Images at 47,000 and 51,000 years, showing the region within 0.5 pc of the black hole; color scale is from 0.1 g cm^{-2} to 1000 g cm^{-2}. Although the cloud is tidally disrupted by the black hole, some of the material is captured by the black hole to form an eccentric disk that quickly fragments to form stars. These are illustrated by the white dots and have eccentricities between $e = 0.6$ and $e = 0.76$ and semimajor axes between $a = 0.11$ pc and $a = 0.19$ pc. A small population of stars also forms quite early, becoming visible in (B) and being ejected from the system in (D).

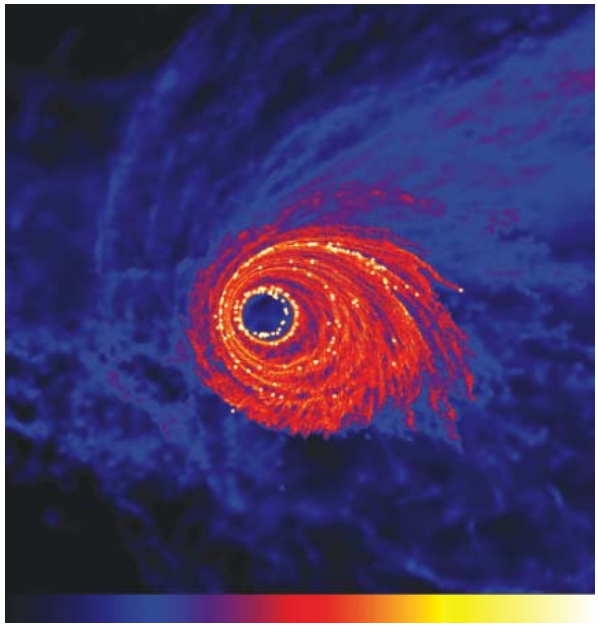

Fig. 2. The final state of the simulation of a $10^5\ M_\odot$ molecular cloud falling toward a $3 \times 10^6\ M_\odot$ supermassive black hole. The image shows the region within 0.25 pc of the black hole located at the center; colors denote column densities from 0.75 g cm^{-2} to 7500 g cm^{-2}. A portion of the cloud has formed a disk around the black hole, while—at the stage shown here—most of the mass is still outside the region shown. The disk fragments very quickly, producing 198 stars with semimajor axes between $a = 0.04$ pc and $a = 0.13$ pc and eccentricities between $e = 0$ and $e = 0.53$.

encodes the relative numbers of stars as a function of the stars' masses]. The higher-mass cloud (Fig. 4) produced a bimodal mass function: a population of very massive stars with masses between ~10 and ~100 $M_\odot$, and a population of lower-mass stars. The higher-mass stars formed in the inner ring ($a \sim 0.02$ pc) while the lower-mass stars formed farther out ($a \sim 0.05$ to 0.1 pc) because of the different gas temperatures produced (*20*). As additional gas remained bound at larger radii, it is possible that more lower-mass stars would eventually form if the simulation were followed further in time.

In addition to forming the stars, 10 to 30% of the infalling gas clouds were accreted onto the black hole. This accretion implies only that the material is bound within the size of the sink-particles' accretion radius of 4000 AU, and in fact this material had sufficient angular momentum to form a disk at radii of 1000 to 4000 AU around the black hole.

The actual size and evolution of this inner disk were not determined by our simulations and could

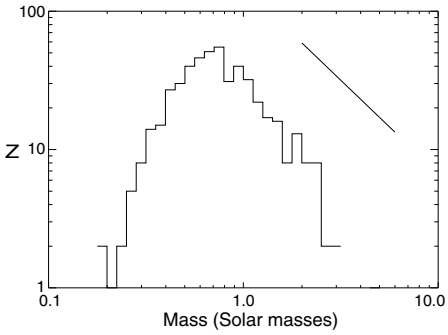

Fig. 3. Mass function of the stars formed in the simulation illustrated in Fig. 1. The stars form with masses close to 0.1 $M_\odot$ but grow quickly through gas accretion. The mass function therefore has a peak at ~0.8 $M_\odot$, above which it has a power-law form with a slope comparable to that of the Salpeter slope, illustrated by the diagonal line.

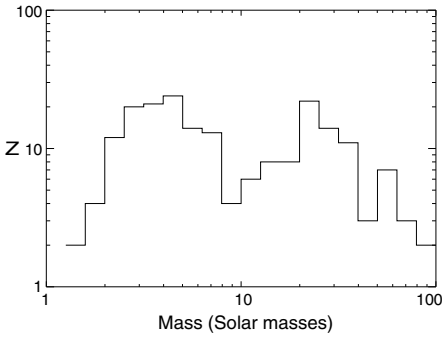

Fig. 4. Mass function of the stars formed in the simulation illustrated in Fig. 2. The mass function is extremely top-heavy and appears to have two populations of stars: one population of massive stars with masses from 10 $M_\odot$ to 100 $M_\odot$, and another with masses between 1 $M_\odot$ and 10 $M_\odot$.

involve further star formation or self-gravity–driven accretion. Assuming that all the gas would accrete directly onto the black hole on a viscous time scale (*21*) on the order of 10^7 years yields an average mass accretion rate on the order of 10^{-4} $M_\odot$/year for the 10^4 $M_\odot$ cloud and 10^{-3} $M_\odot$/year for the 10^5 $M_\odot$ cloud. This gives a maximum accretion luminosity on the order of 10^{43} ergs/s, or about 1% of the Eddington luminosity. This additional source of radiation, and that from the newly formed stars, could increase the gas temperature in the disk and thus increase the fragment masses.

Our simulations show that an infalling molecular cloud can indeed form an eccentric disk around a supermassive black hole, and that although the tidal force of the black hole will disrupt the cloud, it does not destroy the small-scale structures that seed the disk fragmentation. Furthermore, the compressional heating of the infalling gas results in the formation of a population of stars biased toward higher masses. The stellar masses depend crucially on the mass of the infalling cloud and on its impact parameter, allowing for a variety of final outcomes. The initial disk eccentricity also means that the stars can form with initial eccentricities and, if the molecular cloud is sufficiently massive, the stars that form may be extremely massive. This is therefore a viable mechanism for forming the rings of young, massive stars within ~0.1 pc of the galactic center. What is still unclear, however, is the origin of the infalling cloud and the probability of the small impact parameter that is required.

References and Notes

1. R. Genzel *et al.*, *Mon. Not. R. Astron. Soc.* **291**, 219 (1997).
2. R. Schödel *et al.*, *Nature* **419**, 694 (2002).
3. A. Ghez *et al.*, *Astrophys. J.* **620**, 744 (2005).
4. T. Paumard *et al.*, *Astrophys. J.* **643**, 1011 (2006).
5. S. Nayakshin, R. Sunyaev, *Mon. Not. R. Astron. Soc.* **364**, L23 (2005).
6. B. Elmegreen, *Astrophys. J.* **648**, 572 (2006).
7. E. S. Phinney, in *The Center of the Galaxy: Proceedings of the 136th Symposium of the IAU*, M. Morris, Ed. (Kluwer, Dordrecht, Netherlands, 1989), p. 543–553.
8. Y. Levin, A. M. Beloborodov, *Astrophys. J.* **590**, L33 (2003).
9. S. Nayakshin, J. Cuadra, *Astron. Astrophys.* **437**, 437 (2005).
10. M. A. Gürkan, F. A. Rasio, *Astrophys. J.* **628**, 236 (2005).
11. S. Nayakshin, J. Cuadra, V. Springel, *Mon. Not. R. Astron. Soc.* **379**, 21 (2007).
12. C. F. Gammie, *Astrophys. J.* **553**, 174 (2001).
13. W. K. M. Rice *et al.*, *Mon. Not. R. Astron. Soc.* **339**, 1025 (2003).
14. R. D. Alexander, M. C. Begelman, P. J. Armitage, *Astrophys. J.* **654**, 907 (2007).
15. R. D. Alexander, P. J. Armitage, J. Cuadra, M. C. Begelman, *Astrophys. J.* **674**, 927 (2008).
16. M. Wardle, F. Yusef-Zadeh, *Astrophys. J.* **683**, L37 (2008).
17. J. J. Monaghan, *Annu. Rev. Astron. Astrophys.* **30**, 543 (1992).
18. D. Stamatellos, A. P. Whitworth, T. Bisbas, S. Goodwin, *Astron. Astrophys.* **475**, 37 (2007).
19. M. R. Bate, I. A. Bonnell, N. M. Price, *Mon. Not. R. Astron. Soc.* **277**, 362 (1995).
20. See supporting material on *Science* Online.
21. The viscous time scale is the time for shearing interactions between adjacent annuli to transport mass to the central black hole.

Supporting Online Material

www.sciencemag.org/cgi/content/full/321/5892/1060/DC1
Materials and Methods
Figs. S1 to S3
References

19 May 2008; accepted 24 July 2008
10.1126/science.1160653

Quantum Gas of Deeply Bound Ground State Molecules

Johann G. Danzl,[1]* Elmar Haller,[1] Mattias Gustavsson,[1] Manfred J. Mark,[1] Russell Hart,[1] Nadia Bouloufa,[2] Olivier Dulieu,[2] Helmut Ritsch,[3] Hanns-Christoph Nägerl[1]

Molecular cooling techniques face the hurdle of dissipating translational as well as internal energy in the presence of a rich electronic, vibrational, and rotational energy spectrum. In our experiment, we create a translationally ultracold, dense quantum gas of molecules bound by more than 1000 wave numbers in the electronic ground state. Specifically, we stimulate with 80% efficiency, a two-photon transfer of molecules associated on a Feshbach resonance from a Bose-Einstein condensate of cesium atoms. In the process, the initial loose, long-range electrostatic bond of the Feshbach molecule is coherently transformed into a tight chemical bond. We demonstrate coherence of the transfer in a Ramsey-type experiment and show that the molecular sample is not heated during the transfer. Our results show that the preparation of a quantum gas of molecules in specific rovibrational states is possible and that the creation of a Bose-Einstein condensate of molecules in their rovibronic ground state is within reach.

Ultracold samples of molecules are ideally suited for fundamental studies in physics and chemistry, ranging from few-body collisional physics (*1*–*4*), ultracold chemistry (*5*), and high-resolution spectroscopy (*6*, *7*) to quantum gas preparation, molecular Bose-Einstein condensation (*8*), and quantum processing (*9*). For many of the proposed experiments, full control over the molecular wave function in specific deeply bound rovibrational states is needed. High densities are required for molecular quantum gas studies. Only in the rovibronic ground state (the lowest vibrational and rotational energy level of the electronic ground state) is collisional stability assured. However, direct molecular cooling toward high phase-space densities seems yet out of reach (*10*), whereas techniques such as Feshbach association (*11*) and photoassociation (*12*) either produce molecules exclusively in weakly bound rovibrational levels or suffer from low production rates and low state selectivity.

To produce a quantum gas of molecules in their absolute ground state, Jaksch *et al.* (*13*) proposed a scheme for homonuclear alkali molecules in which the technique of stimulated

[1]Institut für Experimentalphysik und Zentrum für Quantenphysik, Universität Innsbruck, Technikerstraße 25, 6020 Innsbruck, Austria. [2]Laboratoire Aimé Cotton, CNRS, Université Paris-Sud Bâtiment 505, 91405 Orsay Cedex, France. [3]Institut für Theoretische Physik und Zentrum für Quantenphysik, Universität Innsbruck, Technikerstraße 25, 6020 Innsbruck, Austria.

*To whom correspondence should be addressed. E-mail: johann.danzl@uibk.ac.at

two-photon transfer is repeatedly applied to molecules associated from a high-density sample of ultracold atoms. The initially very loosely bound molecules are transferred in successive steps to the rovibrational ground state of the singlet $X^1\Sigma_g^+$ molecular potential. The advantages of this scheme are that it is fully coherent, not relying on spontaneous processes, and that it involves only a very small number of intermediate levels. It promises that a ground state binding energy typically of 0.5 eV can be carried away without heating the molecular sample. It essentially preserves phase-space density, allowing the molecular sample to inherit the high initial phase-space density from the atomic sample. However, to realize this scheme, several challenges have to be met. First, there is a large difference in internuclear separation that has to be bridged: The overlap between the radial wave function of the least bound molecules and the radial wave functions of deeply bound molecular levels is extremely low, potentially leading to prohibitively low transition rates for the two-photon transitions. Second, the scheme requires the identification of suitable intermediate molecular levels while strictly avoiding parasitic excitations. Third, a large difference in binding energy has to be overcome. On a more technical side, the lasers driving the two-photon transitions at widely different wavelengths need to have extremely low relative short-term phase jitter and high long-term frequency stability to allow for coherence and reproducibility. In important experiments, Winkler *et al.* (*14*) and, recently, Ospelkaus *et al.* (*15*) demonstrated highly efficient two-photon transfer into lower-lying molecular levels starting from weakly bound dimer molecules, which were associated from ultracold atoms on a Feshbach resonance (*11*). However, the transferred molecules are still weakly bound. Their binding energy, on the order of the atomic hyperfine splitting, is $<10^{-4}$ of the binding energy of the rovibrational ground state, and wave function overlap with this state is still negligible.

In this experiment, we demonstrate the crucial step toward full control of the molecular wave function and toward the formation of a Bose-Einstein condensate (BEC) of molecules in their rovibronic ground state by linking weakly bound molecular states with deeply bound rovibrational states. We coherently transfer an ultracold quantum gas of weakly bound cesium Feshbach molecules to the rovibrational level $|v = 73, J = 2\rangle$ of the singlet $X^1\Sigma_g^+$ potential, bound by 1061 cm^{-1} (or $h \times 31.81$ THz, where h is Planck's constant), corresponding to more than one-fourth of the binding energy of the rovibrational ground state. To achieve this result, we overcome low wave function overlap by using a suitable intermediate excited molecular state while avoiding excitation into loss channels, and we reference the transfer lasers to a frequency comb, allowing us to flexibly bridge binding-energy differences of more than 1000 cm^{-1}.

Figure 1 shows the energy of the relevant molecular and atomic states. Our experiment starts with a cigar-shaped BEC of cesium atoms in the lowest hyperfine sublevel $F = 3$, $m_F = 3$ in an optical dipole trap. For BEC production, we essentially follow the procedure detailed in (*16*). For Feshbach molecule production out of the BEC, we ramp up the offset magnetic field from the initial value of 2.1 mT to ~5.0 mT in 10 ms. We then ramp down, sweeping across a *d*-wave Feshbach resonance at 4.8 mT after ~1 ms, as shown in Fig. 1B (*17*, *18*). Our procedure [see (*17*)] gives an ultracold and dense sample of up to 11,000 molecules every 10 s at densities above 1×10^{11} cm^{-3}. For the state-transfer experiments discussed here, we do not separate the molecules from the original BEC. Upon lowering the magnetic field, the molecules are transferred from the initial state $|d\rangle$ to a still weakly bound *s*-wave molecular state $|s\rangle$ of the lowest hyperfine channel ($F_1 = 3$, $F_2 = 3$) via an avoided crossing (*18*). The index $i = 1, 2$ denotes the ith atom.

Upon further lowering the magnetic field to about 2.2 mT, the molecules enter into a closed channel *s*-wave molecular state $|a\rangle$ via a second, broad avoided crossing (*18*). This state belongs to the uppermost hyperfine channel ($F_1 = 4$, $F_2 = 4$) and thus has an effective binding energy of more than $2 \times h\nu_{Cs}$. Here, $\nu_{Cs} \approx 9.19$ GHz is the Cs clock frequency. Similar to $|s\rangle$, this state is a mixture of the $X^1\Sigma_g^+$ ground state and the lowest triplet $a^3\Sigma_u^+$ state, coupled by hyperfine interaction, and it has zero rotational angular momentum. At a field of 1.9 mT, it has a binding energy of 5 MHz $\times$ h, with respect to the $F = 3$, $m_F = 3$ two-atom asymptote (*18*). As one might expect, we find that optical transition rates as measured below are improved when using this effectively more deeply bound state as the initial state for two-photon transfer instead of state $|s\rangle$. We shut off the trap and

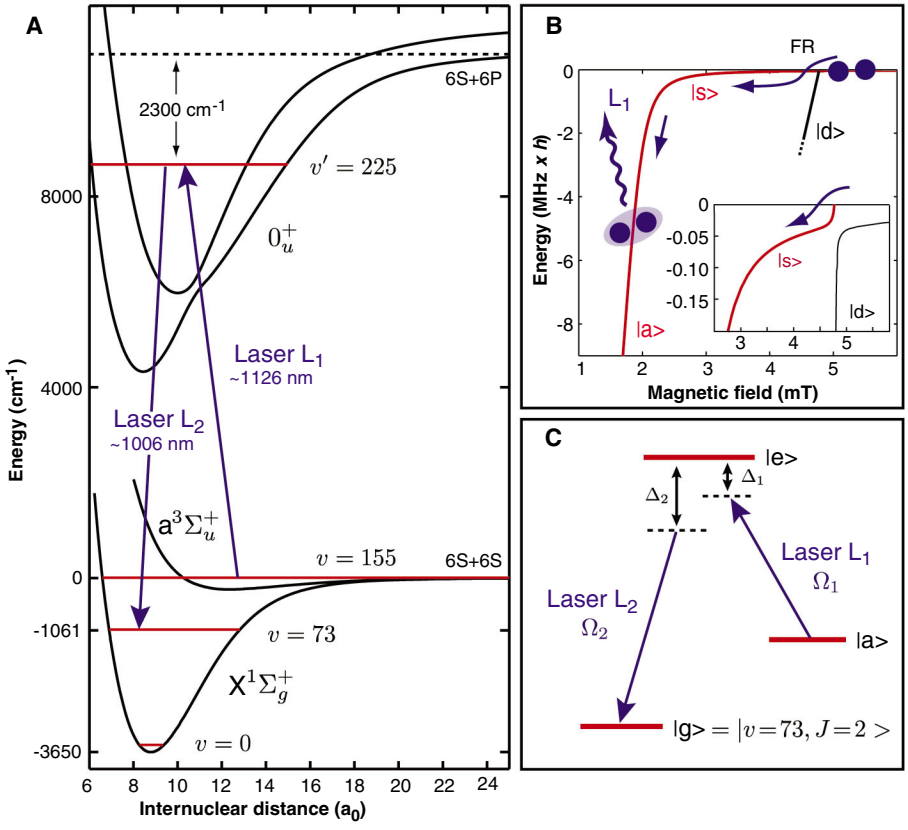

Fig. 1. (**A**) Molecular level scheme for Cs_2. Molecules in a weakly bound Feshbach level are transferred to rovibrational level $|v = 73, J = 2\rangle$ of the singlet $X^1\Sigma_g^+$ potential with a binding energy of 1061 cm^{-1} in a two-photon STIRAP process with wavelengths near 1126 and 1006 nm via the 225th level of the electronically excited $(A^1\Sigma_u^+ - b^3\Pi_u)0_u^+$ potentials. The $X^1\Sigma_g^+$ potential has about 155 vibrational levels. a_0 is the Bohr radius. (**B**) Zeeman diagram showing the energy of all relevant weakly bound molecular levels for initial Feshbach molecular state preparation (*18*). The binding energy is given with respect to the $F = 3$, $m_F = 3$ two-atom asymptote. The molecules are produced on a *d*-wave Feshbach resonance at 4.8 mT (inset) and then transferred to the weakly bound *s*-wave state $|s\rangle$ on an avoided state crossing. Further lowering of the magnetic offset field to 1.9 mT transfers the molecules from state $|s\rangle$ to state $|a\rangle$, the starting state for the STIRAP transfer. (**C**) STIRAP transfer scheme (*19*). The molecules are transferred from the initial state $|a\rangle$ to the final state $|g\rangle = |v = 73, J = 2\rangle$ by means of two overlapping laser pulses for which laser L_2 is pulsed on before L_1. The detunings and Rabi frequencies of L_i are Δ_i and Ω_i, $i = 1, 2$.

perform all subsequent experiments in free flight. This does not affect the particle density immediately but reduces it during the later detection procedure, which takes about 6 ms, to avoid collisions between atoms and weakly bound dimers and, hence, loss. We detect molecules in $|a\rangle$ via states $|s\rangle$ and $|d\rangle$ by first applying a magnetic field gradient for atom-molecule Stern-Gerlach separation, then reversing the magnetic field ramp, and finally dissociating them on the Feshbach resonance at 4.8 mT and imaging the resulting atoms (*17*).

Efficient two-photon transfer via the stimulated Raman adiabatic passage (STIRAP) technique (*14*, *19*) relies on a suitable choice for the excited state $|e\rangle$. In our case, this state must have singlet character so that it can be used as a transfer state to deeply bound levels of the $X^1\Sigma_g^+$ potential. In general, it must be well separated from other states, which otherwise could be off-resonantly excited. It should thus be situated far to the red of the excited $S_{1/2} + P_{1/2}$ potential asymptote to avoid the high density of excited molecular states near that asymptote. We have performed optical loss spectroscopy starting from state $|a\rangle$ in the wavelength range of 1120 to 1130 nm, ~2300 cm^{-1} to the red of the cesium D_1 line. For this measurement, we recorded the number of remaining molecules in $|a\rangle$ as a function of excitation wavelength and found two progressions of lines, which we assign to the potential curves of the mixed $(A^1\Sigma_u^+ - b^3\Pi_u)0_u^+$ excited states and to the $(1)^3\Sigma_g^+$ excited state, respectively. For the present experiments, we choose for $|e\rangle$ a level of the 0_u^+ progression that is 8879.63(1) cm^{-1} above the $F = 3$, $m_F = 3$ two-atom asymptote, corresponding to a transition wavelength of 1126.173(1) nm (Fig. 1A). We measure all wavelengths on a home-built wave meter. We identify this previously unknown level as the 225th one of the 0_u^+ system, with an uncertainty of two in the absolute numbering.

The ground state level $|g\rangle$ with vibrational quantum number $v = 73$ is well known from conventional molecular spectroscopy (*20*, *21*). However, its binding energy, as well as the binding energy of all deeply bound vibrational levels, has only been known with an uncertainty of ~±0.45 cm^{-1} before the present experiments (*21*). We search for $|g\rangle$ by simultaneously exciting the transition from $|a\rangle$ to $|e\rangle$ with laser L_1 and the one from $|e\rangle$ to $|g\rangle$ with laser L_2. The two light fields create a molecule-molecule dark state. The molecules initially in $|a\rangle$ are lost unless the second laser L_2 is on two-photon resonance, provided that the Rabi frequency Ω_2 on the second transition is $\geq\Omega_1$, the Rabi frequency on the first transition. For coherence, stability, and reproducibility, we lock both lasers to independent narrow-band optical resonators, which we reference to an optical frequency comb (*22*). The comb is not calibrated but it allows precise differential frequency measurements and provides long-term stability needed for systematic line searches (*23*). We find the resonance condition with vibrational level $v = 73$ at 1005.976(1) and 1005.982(1) nm, corresponding to rotational quantum numbers $J = 0$ and 2. Identification of J is possible because the rotational energy splitting is well known. Figure 2, A and B, shows typical molecular dark resonances when we set L_2 on resonance and step the detuning Δ_1 of L_1 near 1126.173 nm. Figure 2C shows a dark resonance involving $v = 73$, $J = 2$ using a different excited molecular state $|e'\rangle$, which is excited with L_1 near 1123.104 nm.

Figure 2, D to F, shows dark resonances involving the neighboring vibrational levels $v =$

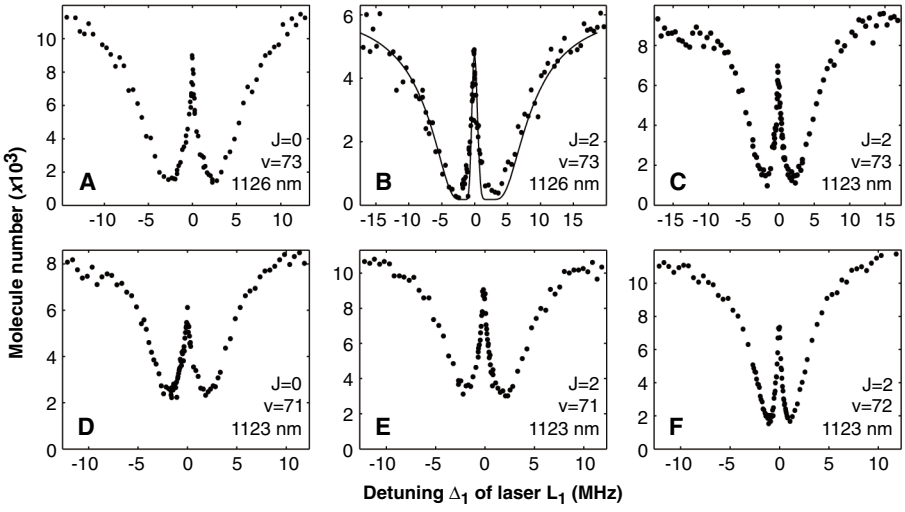

Fig. 2. Dark resonances for vibrational levels $v = 71$, 72, and 73. Laser L_2 is held on resonance while the detuning Δ_1 of L_1 is scanned. We record the number of molecules in $|a\rangle$ while both lasers are pulsed on simultaneously. (**A** to **C**) Dark resonances involving $v = 73$ for excitation with L_1 near 1126 nm into $J = 0$ and 2 and for excitation with L_1 near 1123 nm into $J = 2$, respectively. (**D** to **F**) Neighboring levels $v = 71$ and 72 for excitation near 1123 nm. The solid line in (B) is the result of a three-level model calculation matched to the data giving $\Omega_1 = 2\pi \times 2$ kHz $\sqrt{I_1/(\text{mW/cm}^2)}$ and $\Omega_2 = 2\pi \times 11$ kHz $\sqrt{I_2/(\text{mW/cm}^2)}$ for a pulse time of 5 μs at intensities of $I_1 = 4 \times 10^5$ mW/cm² for L_1 and $I_2 = 2 \times 10^5$ mW/cm² for L_2, assuming a laser linewidth of 2 kHz.

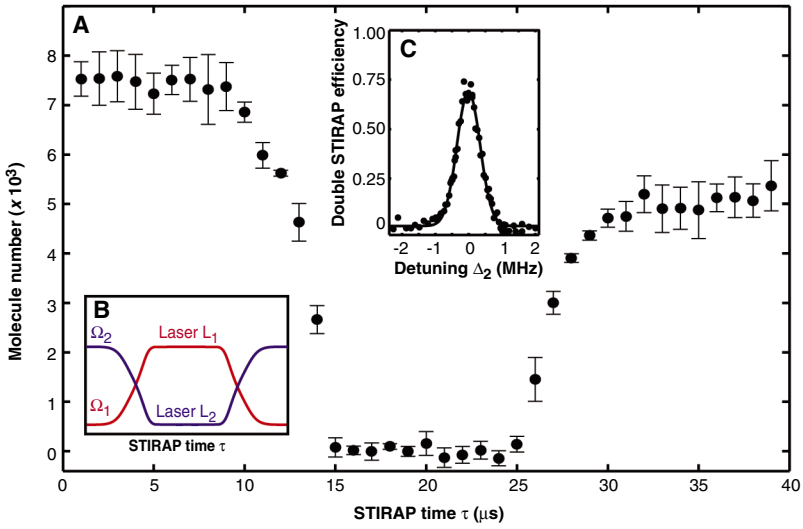

Fig. 3. STIRAP transfer from the weakly bound state $|a\rangle$ to the deeply bound state $|g\rangle = |v = 73, J = 2\rangle$ and back to $|a\rangle$. (**A**) Number of molecules in state $|a\rangle$ as a function of STIRAP time τ for $\Delta_1 \approx 0 \approx \Delta_2$. The measured pulse overlap begins at 5 μs and ends at ~15 μs. The second pulse overlap starts at 25 μs and ends at ~33 μs. (**B**) Schematic of the timing for the Rabi frequencies Ω_i, $i = 1$, 2, during the double STIRAP sequence. Laser L_1 is left on after the first STIRAP sequence to clear out any remaining population in $|a\rangle$. (**C**) Double STIRAP efficiency as a function of the detuning Δ_2 of laser L_2 for $\Delta_1 \approx 0$. The solid line is a Gaussian fit with a FWHM of 811 kHz. The peak Rabi frequencies are $\Omega_1 \approx 2\pi \times 3$ MHz and $\Omega_2 \approx 2\pi \times 6$ MHz. Error bars refer to the 1σ error in determining the particle number.

71 and 72. These $X^1\Sigma_g^+$ levels were easily found based on previously acquired Cs_2 spectra (*21*). We determine the binding energy of these levels, with respect to the atomic $F_1 = 3$, $F_2 = 3$ asymptote at zero magnetic field, to be 1060.9694(10), 1088.3101(10), and 1115.9148(10) cm^{-1} for $v = 73$, 72, and 71 with $J = 0$, respectively. The binding energy of the rovibrational ground state $v = 0$ is thus 3628.7053(14) cm^{-1}, which represents an improvement in precision of more than two orders of magnitude compared with the previous determination (*21*). Fitting the data for the dark resonances with a three-level model taking into account off-resonant excitations and laser linewidths, we determine the molecular transition strengths as given by the normalized Rabi frequencies for the transitions $|a\rangle$ to $|e\rangle$ and $|e\rangle$ to $|v = 73, J = 2\rangle$ to be $\Omega_1 = 2\pi \times 2$ kHz $\sqrt{I/(\mathrm{mW/cm^2})}$ and $\Omega_2 = 2\pi \times 11$ kHz $\sqrt{I/(\mathrm{mW/cm^2})}$, respectively. A comparison with a typical atomic transition strength of $\Omega_a = 2\pi \times 5$ MHz $\sqrt{I/(\mathrm{mW/cm^2})}$ giving $|\Omega_1/\Omega_a|^2 < 10^{-6}$ reflects the minuteness of the wave function overlap.

We are now in a position to carry out coherent transfer using the STIRAP technique. For $|g\rangle$ we choose the vibrational level with $v = 73$, $J = 2$. This level will allow us to reach the rovibrational ground state $v = 0$, $J = 0$ with a second STIRAP step in view of the selection rule $\Delta J = 0, \pm 2$. STIRAP uses a counterintuitive overlapping pulse sequence in which L_2 is pulsed on before L_1. As is well known (*19*), STIRAP relies on the existence of a dark state of the form $|D\rangle = \alpha(t)|a\rangle + \beta(t)|g\rangle$ (here, $\alpha(t)$ and $\beta(t)$ are time-dependent amplitudes with $|\alpha(t)|^2 + |\beta(t)|^2 = 1$). With sufficient adiabaticity, the function $|\alpha(t)|^2$ decreases smoothly from 1 to 0, while the function $|\beta(t)|^2$ increases smoothly from 0 to 1. The initial state $|a\rangle$ is thus rotated via $|D\rangle$ into the final state $|g\rangle$. The criterion for adiabaticity is $\tau_p\Omega^2 >> (2\pi)^2\Gamma$, where τ_p is the pulse overlap time, $\Omega \approx \Omega_1 \approx \Omega_2$ is the peak Rabi frequency during the pulse, and $\Gamma \approx 2\pi \times 4$ MHz is the (spontaneous) decay rate from the upper state $|e\rangle$, as determined from our loss measurements. This criterion is quite stringent, in particular, in view of the low wave function overlap that enters into Ω. An upper (experimental) limit for τ_p is given by the relative laser coherence time for L_1 and L_2. We choose τ_p to be ~10 μs. For detection, we apply the reverse STIRAP sequence after a waiting time $\tau_w \approx 10$ μs to transfer the molecules back into $|a\rangle$. During this time we leave laser L_1 on to assure that all possible residual population in state $|a\rangle$ is removed.

We perform double STIRAP ~3 ms after the production of the Feshbach molecules and 1 ms after shutting off the trap. Figure 3A shows the molecular population in $|a\rangle$ as a function of the STIRAP time τ, and Fig. 3B shows the timing sequence for the double-transfer scheme. For recording the time evolution of the population, we interrupt the transfer process after time τ and measure the remaining population in $|a\rangle$. The molecules in $|a\rangle$ initially disappear during the first STIRAP sequence. They are now in level $|v = 73, J = 2\rangle$ of the singlet $X^1\Sigma_g^+$ potential. Then a large fraction of them returns in the course of the reverse STIRAP sequence. For this particular measurement both lasers are on resonance. The peak Rabi frequencies are $\Omega_1 \approx 2\pi \times 3$ MHz and $\Omega_2 \approx 2\pi \times 6$ MHz. We typically obtain an overall efficiency >65% for the double-transfer process, corresponding to single-pass efficiencies >80%, assuming equal efficiencies for both passes. Figure 3C shows the double-pass efficiency as a function of detuning Δ_2 of laser L_2. Simulations for the three-level system show that the ~800-kHz full width at half maximum (FWHM) of the efficiency curve is compatible with a combination of laser power broadening and Fourier broadening. Our simulations also show that higher transfer efficiencies can be expected for an optimized STIRAP pulse sequence in which both peak Rabi frequencies are equal. Molecules not transferred by STIRAP are resonantly excited to $|e\rangle$ and then lost from our three-level system by spontaneous emission into a multitude of ground state levels.

We demonstrate coherence of the transfer process in a Ramsey-type experiment (*14*), halting the transfer process by simultaneously shutting off both lasers 12 μs into the first STIRAP sequence when a balanced superposition of $|a\rangle$ and $|g\rangle$ has been created with $|\alpha(\tau)|^2 \approx 1/2 \approx |\beta(\tau)|^2$. After a hold time τ_h we resume the STIRAP transfer, with the roles of lasers L_1 and L_2 reversed. Thus, for $\tau_h = 0$ the population will simply be rotated back into the initial state. A three-level calculation shows that the population in the initial state $|a\rangle$ is expected to oscillate at the rate of the two-photon detuning $|\Delta_2 - \Delta_1|/(2\pi)$. Figure 4A shows the initial state population for $\Delta_1 \approx 0$ and $\Delta_2 \approx 2\pi \times 113$ kHz as a function of τ_h. The population oscillates at a frequency of $|\Delta_2 - \Delta_1|/(2\pi)$, however with marked increase in phase jitter on the time scale of 30 μs. We attribute this apparent loss of phase coherence to a slow relative frequency drift of lasers L_1 and L_2, leading to a slightly different two-photon detuning from one experimental run to the next. In Fig. 4A, we have added a region indicating a frequency jitter of ±6 kHz. This value is compatible with the present long-term stability of our lasers. The frequency drift does not affect an individual STIRAP process because the transfer efficiency is very robust against laser detuning, as shown in Fig. 3C.

We now show that the molecular sample is not heated during the transfer process and is indeed in the quantum gas regime. Specifically, we measure and compare the rate of expansion of the molecular sample in state $|a\rangle$ with and without the double-transfer process. In our regime, the energy scale for expansion is usually set by the mean field of the BEC, resulting in typical expansion energies for the atoms in the range from $k_B \times 2$ nK to $k_B \times 10$ nK (where k_B is Boltzmann's constant), depending on the strength of the atomic interaction (*24*). We find that the initial magnetic field ramping excites collective motion of the BEC in the form of a breathing mode as a result of a change in the mean field potential due to a change in atomic interaction strength (*16*). The breathing is transformed into expansion of the sample when the trap is shut off. We follow the expansion by monitoring the change of the Thomas-Fermi radius r of the sample. Figure 4B shows this radius along the horizontal direction as a function of expansion time with and without STIRAP. Without STIRAP, we obtain from a linear fit an expansion rate of $dr/dt = 1.0(1)$ mm/s, corresponding to an energy of $k_B \times 14(4)$ nK. With STIRAP, the rate is $dr/dt = 0.7(1)$ mm/s, corresponding to an energy of $k_B \times 7(2)$ nK. Both values are compatible with a separate measurement of the expansion of the atomic BEC for the same magnetic field ramp. Interestingly, the rate for the case with STIRAP is lower. We speculate that STIRAP with the

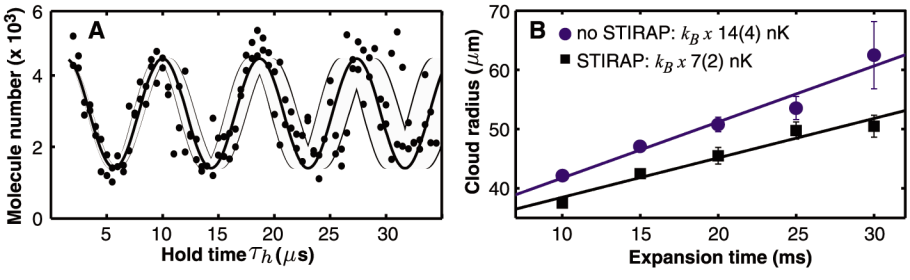

Fig. 4. (**A**) Ramsey-type experiment. The population in the initial state $|a\rangle$ oscillates as the hold time τ_h (during which both transfer lasers are off) is increased. The solid line is a sinusoidal fit to the data up to τ_h = 20 μs. Its frequency f is 115(2) kHz, in good agreement with the expected value of 113 kHz. The thin lines are borders to a region that is given by varying f by ±6 kHz, illustrating the estimated jitter in the two-photon detuning $|\Delta_2 - \Delta_1|$. (**B**) Comparison of the rate of expansion in the horizontal direction for the molecular sample without and with STIRAP transfer. The top curve (circles) shows the Thomas-Fermi radius r of the molecular sample as a function of expansion time without STIRAP. The linear fit gives a rate of expansion of dr/dt = 1.0(1) mm/s, corresponding to an energy of $k_B \times 14(4)$ nK. The bottom curve (squares) shows the expansion after double STIRAP with dr/dt = 0.7(1) mm/s, corresponding to $k_B \times 7(2)$ nK. Error bars indicate the 1σ error in the determination of the cloud radius.

tightly focused laser beams L_1 and L_2 preferentially transfers molecules in the center of the sample and is hence responsible for some selection in velocity space.

It should now be possible to add a second STIRAP step for transfer into the rovibrational ground state $v = 0$, $J = 0$. A suitable two-photon transition at readily available laser wavelengths is via the 68th excited state level of the 0_u^+ potential near 1329 nm (up) and 991 nm (down) with comparatively good wave function overlap at the level of $|\Omega/\Omega_a|^2 \approx 10^{-4}$. We expect that searching for dark resonances will be straightforward, as now all two-photon transition energies are known with an uncertainty of 10^{-3} cm^{-1}. Molecules in $v = 0$, $J = 0$ cannot further decay into a lower state upon a two-body collision, and they are thus expected to allow the formation of an intrinsically stable molecular BEC. The high speed of our STIRAP transfer will allow us to perform in situ as well as time-of-flight imaging for direct characterization of the spatial and momentum distribution of the molecular ensemble.

With our technique, any low-lying vibrational state can be coherently populated in a controlled fashion with full control over the rotational quantum number, allowing, for instance, state-specific collisional studies and high-precision molecular spectroscopy with possible implications for fundamental physics (*6*, *7*). Our procedure can be adapted to other species, in particular to heteronuclear alkali dimers such as RbCs (*25*) and KRb (*15*) for the creation of dipolar quantum gases (*26*). For heteronuclear alkali dimers, a single two-photon transfer step might suffice as a result of favorable wave function overlap (*27*). We expect that the combination of our technique with Feshbach molecule production out of a Mott-insulator state in a three-dimensional lattice (*28*) will increase the initial Feshbach molecule production efficiency, avoiding collective excitations as a result of magnetic field ramping and inhibiting collisional loss, and will provide full control over all internal and external quantum degrees of freedom of the ground state molecules.

References and Notes

1. C. Chin *et al.*, *Phys. Rev. Lett.* **94**, 123201 (2005).
2. T. Kraemer *et al.*, *Nature* **440**, 315 (2006).
3. P. Staanum, S. D. Kraft, J. Lange, R. Wester, M. Weidemüller, *Phys. Rev. Lett.* **96**, 023201 (2006).
4. N. Zahzam, T. Vogt, M. Mudrich, D. Comparat, P. Pillet, *Phys. Rev. Lett.* **96**, 023202 (2006).
5. R. V. Krems, *Int. Rev. Phys. Chem.* **24**, 99 (2005).
6. T. Zelevinsky, S. Kotochigova, J. Ye, *Phys. Rev. Lett.* **100**, 043201 (2008).
7. D. DeMille *et al.*, *Phys. Rev. Lett.* **100**, 043202 (2008).
8. M. Inguscio, W. Ketterle, C. Salomon, Eds., *Ultracold Fermi Gases, Proceedings of the International School of Physics "Enrico Fermi," Course CLXIV* (IOS Press, Amsterdam, 2008).
9. D. DeMille, *Phys. Rev. Lett.* **88**, 067901 (2002).
10. J. Doyle, B. Friedrich, R. V. Krems, F. Masnou-Seeuws, *Eur. Phys. J. D* **31**, 149 (2004).
11. T. Köhler, K. Góral, P. S. Julienne, *Rev. Mod. Phys.* **78**, 1311 (2006).
12. K. M. Jones, E. Tiesinga, P. D. Lett, P. S. Julienne, *Rev. Mod. Phys.* **78**, 483 (2006).
13. D. Jaksch, V. Venturi, J. I. Cirac, C. J. Williams, P. Zoller, *Phys. Rev. Lett.* **89**, 040402 (2002).
14. K. Winkler *et al.*, *Phys. Rev. Lett.* **98**, 043201 (2007).
15. S. Ospelkaus *et al.*, preprint available at http://arxiv.org/abs/0802.1093 (2008).
16. T. Weber, J. Herbig, M. Mark, H.-C. Nägerl, R. Grimm, *Science* **299**, 232 (2003), published online 5 December 2002; 10.1126/science.1079699.
17. J. Herbig *et al.*, *Science* **301**, 1510 (2003), published online 21 August 2003; 10.1126/science.1088876.
18. M. Mark *et al.*, *Phys. Rev. A* **76**, 042514 (2007).
19. K. Bergmann, H. Theuer, B. W. Shore, *Rev. Mod. Phys.* **70**, 1003 (1998).
20. W. Weickenmeier *et al.*, *J. Chem. Phys.* **82**, 5354 (1985).
21. C. Amiot, O. Dulieu, *J. Chem. Phys.* **117**, 5155 (2002).
22. Laser L_1 near 1126 nm and laser L_2 near 1006 nm are continuous-wave grating-stabilized tunable diode lasers with up to 26 mW and 5 mW of power at the sample position, respectively, both focused to a $1/e^2$ waist of ~25 μm for sufficiently high Rabi frequencies. We estimate the laser linewidth for both lasers to be on the order of 1 kHz. The laser beams propagate horizontally at an angle of 80° with the long axis of the BEC with vertical linear polarization. Copropagation assures that the imparted photon recoil during STIRAP is minimal, corresponding to an energy of $k_B \times 0.4$ nK, with Boltzmann's constant k_B. The beam intensity is controlled by acousto-optical modulators, allowing pulse lengths down to 1 μs.
23. The wave-meter calibration is currently not sufficient to allow absolute numbering of the frequency comb teeth.
24. T. Kraemer *et al.*, *Appl. Phys. B* **79**, 1013 (2004).
25. J. M. Sage, S. Sainis, T. Bergeman, D. DeMille, *Phys. Rev. Lett.* **94**, 203001 (2005).
26. K. Góral, L. Santos, M. Lewenstein, *Phys. Rev. Lett.* **88**, 170406 (2002).
27. W. C. Stwalley, *Eur. Phys. J. D* **31**, 221 (2004).
28. T. Volz *et al.*, *Nat. Phys.* **2**, 692 (2006).

29. We thank the team of J. Hecker Denschlag, the LevT team in our group, and T. Bergeman for very helpful discussions and M. Prevedelli for technical assistance. We are indebted to R. Grimm for generous support and gratefully acknowledge funding by the Austrian Ministry of Science and Research (Bundesministerium für Wissenschaft und Forschung) and the Austrian Science Fund (Fonds zur Förderung der wissenschaftlichen Forschung) in the form of a START prize grant and by the European Science Foundation in the framework of the EuroQUAM collective research project QuDipMol.

1 May 2008; accepted 1 July 2008
Published online 10 July 2008;
10.1126/science.1159909
Include this information when citing this paper.

Observation of Atomic Diffusion at Twin-Modified Grain Boundaries in Copper

Kuan-Chia Chen,[1]* Wen-Wei Wu,[2]* Chien-Neng Liao,[1]† Lih-Juann Chen,[1] K. N. Tu[3]

Grain boundaries affect the migration of atoms and electrons in polycrystalline solids, thus influencing many of the mechanical and electrical properties. By introducing nanometer-scale twin defects into copper grains, we show that we can change the grain-boundary structure and atomic-diffusion behavior along the boundary. Using in situ ultrahigh-vacuum and high-resolution transmission electron microscopy, we observed electromigration-induced atomic diffusion in the twin-modified grain boundaries. The triple point where a twin boundary meets a grain boundary was found to slow down grain-boundary and surface electromigration by one order of magnitude. We propose that this occurs because of the incubation time of nucleation of a new step at the triple points. The long incubation time slows down the overall rate of atomic transport.

Grain boundaries affect many physical properties of polycrystalline solids. For example, reduction of grain size is known to improve the mechanical strength of metals, governed by the Hall-Petch equation (*1*, *2*). A large-angle tilt-type grain boundary can short-circuit atomic diffusion, which has been the most serious reliability issue in Al interconnects in microelectronics technology. The atomic structure of a grain boundary is controlled by the misorientation between the two grains forming the grain boundary. Balluffi *et al.* have made bicrystals of Au thin films and varied systematically the tilt or twist angle in the bicrystals for studying the correlation between formation energy and atomic structure of grain boundaries (*3*, *4*). Generally speaking, the higher the grain-boundary misorientation angle, the higher the atomic diffusivity. Thus, by modifying the structure of a grain boundary, it should be possible to control the atomic diffusion along the grain boundary.

Lu *et al.* have synthesized a high density of nanotwins in pure Cu foils by pulsed electrodeposition (*5*). The average grain size in the Cu foils is ~400 nm, and the high-density twins have a peak at 15 nm in twin-lamella size distribution. The Cu foil shows a 10-fold improvement of the mechanical strength relative to a large-grained Cu, and the foil remains ductile but its electrical resistance did not significantly change. High mechanical strength and low electrical resistivity are desired properties for interconnecting wires in integrated circuits from the consideration of the resistive-capacitive delay, electromigration (EM), and stress migration (*6*–*8*). EM is enhanced

[1]Department of Materials Science and Engineering, National Tsing Hua University, Hsinchu 30013, Taiwan, Republic of China. [2]Department of Materials Science and Engineering, National Chiao Tung University, Hsinchu 30010, Taiwan, Republic of China. [3]Department of Materials Science and Engineering, University of California, Los Angeles, CA 90095, USA.

*These authors contributed equally to this work.
†To whom correspondence should be addressed. E-mail: cnliao@mx.nthu.edu.tw

atomic diffusion under a high-density electric current. Stress migration is creep and is atomic diffusion driven by a normal stress-potential gradient. With the increase in density of electric current in integrated circuits, EM-induced voids and hillocks in conductors can lead to circuit reliability failure (*9*). EM-induced mass transport, in principle, can take place along different diffusion paths such as lattices, grain boundaries, surfaces, and interfaces (*10*, *11*). It is now generally accepted that free surfaces or interfaces are principal EM paths in Cu interconnects at the device operation temperature ~100°C, and grain boundaries become preferential EM paths at high temperatures (*12*). Conventional EM investigations of interconnects were conducted by measuring the changes in electrical resistance or monitoring morphological changes due to void or hillock formation in the current-stressed metal lines (*13*, *14*). The mass transport can be observed indirectly by marker displacement (*15*). However, no direct observations of EM-induced atomic-scale mass transport have been conducted.

To study atomic-scale EM in the nanotwin modified grain boundaries requires in situ high-resolution transmission electron microscopy (HRTEM) and ultrahigh vacuum to prevent oxidation of the Cu under high temperature and high current. Our previous studies of Cu have revealed that the EM-induced mass transport occurs preferentially on the {111} surface planes and along the <110> directions, leading to a unique stepped atomic-surface structure in crystalline Cu (*16*, *17*). In the present study, we introduced nanotwins into the test samples of Cu (*18*). The specimens for in situ TEM observation were prepared through conventional thin-film deposition and patterning processes (fig. S1, A to E). A scanning electron micrograph of the test specimen around the observation window is shown in fig. S1F.

Figure 1 shows a set of HRTEM images of a twin-modified grain boundary at different stages during electric current stressing. A twin lamella has two twinning planes, so it will intersect a grain boundary with two triple points. Because a grain boundary is formed by two grains, we should have twins to intersect the grain boundary from both sides. We inspected only one of the two grains forming the grain boundary: the grain in the lower part of the image, which is $(01\bar{1})$-oriented or has $[01\bar{1}]$ as the surface normal. This grain has several {111}/<112>–type coherent twin boundaries that appear to have an angle of 70.5° with respect to the (111) lattice planes. Under the influence of EM, the edge of this $(01\bar{1})$-oriented grain in the grain-boundary plane has evolved into a zigzag shape. The zigzag edges in the grain boundary were found to be $(1\bar{1}\,\bar{1})$ and $(4\bar{2}\bar{2})$ atomic planes that are separated by the thickness of the twin lamellae, as shown in Fig. 1, A to D.

The direction of electron flux is from the right to the left of the inspected grain. We observed that an atomic step appeared at the triple point of the twin boundary (TB1) in Fig. 1 and moved rather rapidly on the $(1\bar{1}\,\bar{1})$ plane toward the other triple point of the twin boundary (TB2). The results indicate that the Cu atoms move on the $(1\bar{1}\,\bar{1})$ surface along the direction of electron flux (from right to left), resulting in the atomic step moving in the opposite direction. Once the atomic step reached TB2, we observed that it was trapped for a while before moving out onto the $(4\bar{2}\bar{2})$ plane. Movie S1 shows the atomic-step movement and the effect of the twin boundary on slowing down EM (*18*). By tracing the atomic steps moving along the $(1\bar{1}\,\bar{1})$ and $(4\bar{2}\bar{2})$ facet surfaces, we can plot the distances of different atomic steps from TB1 and TB2, with respect to time, as shown in Fig. 2. We found that there exists a time lag of ~5 s for the atomic steps to cross the triple points under electric current stressing with an average current density of 2.5×10^6 A/cm^2. The moving speeds of the atomic steps on the $(1\bar{1}\,\bar{1})$ and $(4\bar{2}\bar{2})$ surfaces were calculated to be 5.7 ± 0.4 and 3.4 ± 0.3 nm/s, respectively, based on the plots in Fig. 2, A and B. Because the {111} crystal planes have the lowest atomic-migration energies among the major low-index planes in Cu, it would not be surprising to find that the moving speed of atomic steps on the $(1\bar{1}\,\bar{1})$ surface is faster than that on the $(4\bar{2}\bar{2})$ surface (*19*). Nevertheless, the most important finding is that the triple points can slow down or block the EM-induced atomic migration in the twin-modified grain boundaries of Cu.

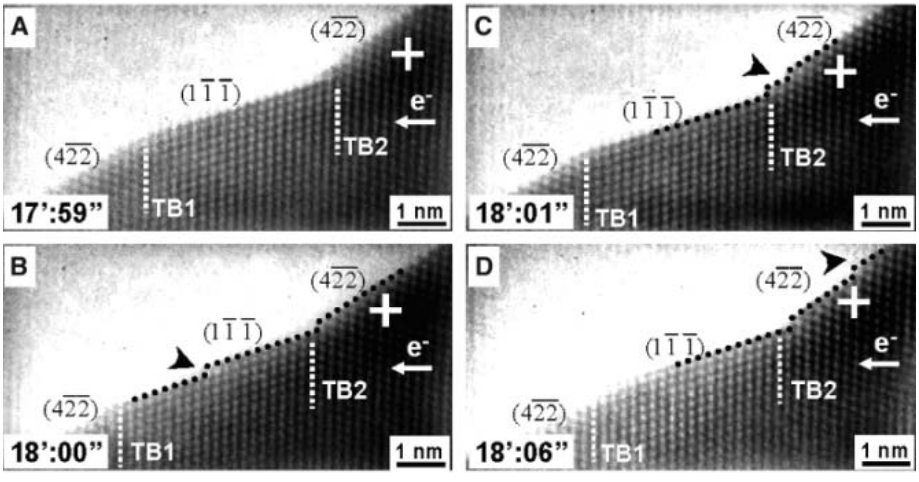

Fig. 1. (**A** to **D**) HRTEM images of the $(01\bar{1})$-oriented Cu grain under electric current stressing as a function of time. The time of the image capture (in minutes and seconds) is given in the rectangular box at the lower left corner. The direction of electron flow is from right to left. The arrowheads indicate the atomic steps on the lattice planes. The cross in each panel refers to a fixed point for ease of inspection. The HRTEM image was analyzed by fast Fourier transform technique.

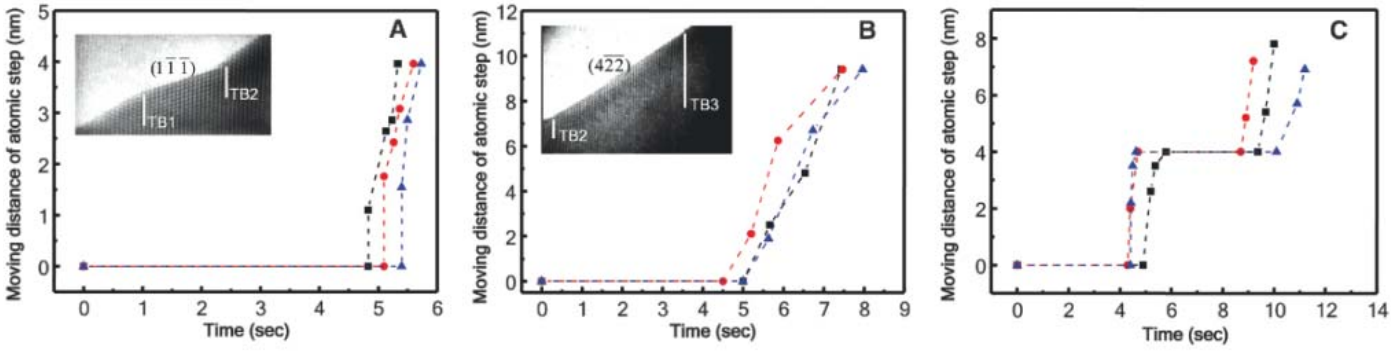

Fig. 2. Movement of different atomic steps on (**A**) the $(1\bar{1}\,\bar{1})$ surface, (**B**) the $(4\bar{2}\bar{2})$ surface, and (**C**) the surface between TB1 and TB3 as a function of time. Insets in (A) and (B) show the moving trace of the atomic steps. Black squares, atomic step 1; red circles, atomic step 2; blue triangles, atomic step 3.

Now the question is why can the triple points of twin boundaries block the EM-induced atomic diffusion? In general, atoms are released from a kink site on a stepped surface of $(1\bar{1}\,\bar{1})$ and $(4\bar{2}\bar{2})$ planes. At a triple point, if we assume that the atomic arrangement is close to a coincidence site, it is energetically less favorable to form a step and kink site at the triple points. More importantly, in a transition from a $(1\bar{1}\,\bar{1})$ to a $(4\bar{2}\bar{2})$ surface, for example, the nucleation of a new step and a kink site on the $(4\bar{2}\bar{2})$ surface is required, so an incubation time is also needed. Overall, the nucleation of steps from the triple points would be the rate-limiting step, resulting in a time lag for the atomic diffusion across the triple points, as shown in Fig. 2, A and B. When we recorded the atomic step moving along the facet surfaces and plotted the moving distance of an atomic step as a function of time, we found a stair-type curve, as shown in Fig. 2C. We interpret that the horizontal part of a step is the incubation time spent to nucleate a new step on the $(1\bar{1}\,\bar{1})$ or $(4\bar{2}\bar{2})$ surface, and the vertical part of a step is the propagation or growth of the step across the $(1\bar{1}\,\bar{1})$ or $(4\bar{2}\bar{2})$ surface. We obtained similar stair-type curves when we followed EM along the grain boundary over several triple points.

With the Cu atoms continuously drifting away under electric current stressing, the atomic steps in the $(01\bar{1})$-oriented grain were found to disappear gradually, and a void eventually formed along the entire grain boundary. This is because EM-induced grain-boundary diffusion is nonconservative (*20*). As it is an irreversible process, we cannot assume vacancy to be at equilibrium everywhere in the sample. Figure 3 shows a set of schematic diagrams of the grain boundary and twin boundaries of one of the Cu grains with $(01\bar{1})$ crystal planes parallel to the surface of the Cu line sample at different stages during electric current stressing. The HRTEM images were obtained from a local spot of the inspected Cu grain to highlight the evolution of the atomic-scale EM-induced voiding along the grain boundary. We found that the atomic steps gradually vanished from the upper left corner of the grain in Fig. 3A. With time, the void grows to the right against the electron-flow direction and also grows downward. The upper free surface of the void is the original grain-boundary plane on the top side, and the lower free surface of the void becomes a zigzag type of free surface consisting of $(1\bar{1}\,\bar{1})$ and $(4\bar{2}\bar{2})$ edges of twins, as shown in Fig. 3, B and C. The size of the void was ~10 to 20 nm wide. Finally, the whole grain almost completely disappeared after electrically stressing the specimen for 30 min, as revealed in Fig. 3D.

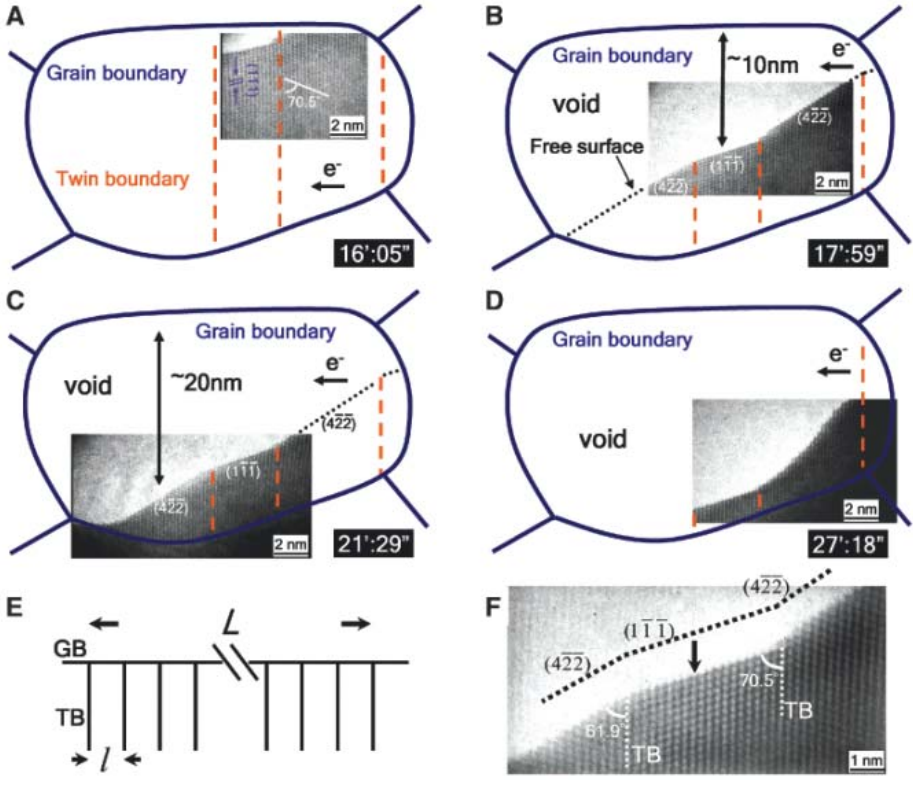

Fig. 3. Schematic diagrams of the grain boundary and twin boundaries of a $(01\bar{1})$-oriented Cu grain at different stages during electric current stressing. (**A** to **D**) Time of the HRTEM image capture is given (in minutes and seconds) in the rectangular box at the lower right corner. The direction of electron flow is from right to left. (**E**) Cartoon of a twin-structured Cu grain of dimension *L* with an average twin-lamella width of *l*. GB, grain boundary; TB, twin boundary. Arrows indicate the span of the Cu grain and twin lamella. (**F**) HRTEM image of the grain edge revealing the direction of EM-induced voiding (indicated by the downward arrow).

In dual-damascene Cu interconnect technology, surface and interfaces have been found to be the dominant kinetic paths of EM in device operation temperature. It is generally accepted that grain boundaries become the more active EM paths for copper when the surface and interfacial paths are blocked or if the temperature reaches above 300°C (*12*). However, as a void is formed (Fig. 3), surface diffusion occurs. We have performed an independent experiment to measure the heating of the Cu specimen induced by the transmission electron beam with the use of a thermocouple attached to the TEM specimen holder, and we found no significant temperature rise for the specimen exposed to the electron beam for 3 hours. One may argue that the local temperature of the specimen due to electron-beam heating might be much higher than the overall temperature measured. In fact, we also found lots of EM-induced grain-boundary voids elsewhere in the specimen without direct electron-beam exposure. This observation indicates that the observed EM-induced voiding is not directly affected by the electron-beam heating. If the electron-beam heating is not severe, it seems that grain-boundary diffusion in large-angle grain boundaries can still be active EM paths at low temperatures.

The measured speed of a moving atomic step and the triple point–induced incubation time lag can be used to evaluate the kinetics of EM-induced voiding in the twin-modified Cu. Figure 3, E and F, shows a schematic of a twin-modified Cu grain of dimension L with an average twin-lamella width of l and a HRTEM image of the grain edge with a zigzag feature. Surface diffusion becomes the active EM path once the void is formed in the upper part of the image, as shown in Fig. 3F. We can calculate the time (t_{tw}) required to remove a layer of Cu atoms from the edge of the twin-modified grain as follows

$$t_{tw} = \frac{L}{l} \times 5 + \frac{(L/2)\csc(70.5^\circ)}{v_{\{111\}}} + \frac{(L/2)\csc(61.9^\circ)}{v_{\{422\}}} \quad (1)$$

where $v_{\{111\}}$ and $v_{\{422\}}$ are the moving speeds of atomic step on the {111} and {422} crystal planes, respectively, and L and l are the grain size and twin-lamellar thickness, respectively. In the right-hand side of the equation, the 5 in the first term reflects the delay time of 5 s associated with each triple point of the twin boundaries, whereas the second and third terms account for the time of the atomic step moving along the {111} and {422} facets, respectively. Equation 1 is established with the reasonable assumption that the twinned region is approximately equal in extent to the untwinned region in the grain. On the other hand, the time required to remove an atomic layer from a twin-free Cu grain of dimension L will be $t_0 = [L\csc(70.5^\circ)]/v_{\{111\}}$, because the {111} planes are the most favorable EM surfaces. The EM-induced void is expected to grow in the direction normal to the facets with a rate that is inversely

proportional to the above estimated time (t_{tw} and t_0). With the measured $v_{\{111\}}$ and $v_{\{422\}}$ values, the EM-induced void growth rate for the twin-modified Cu grain (l = 5 nm) is calculated to be approximately one order of magnitude lower than that for the twin-free Cu grain. The effect of twin boundaries on slowing down the EM-induced voiding is expected to decrease with an increase of the twin-lamella width (that is, a decrease in the twin density). The twin boundary–induced atomic-migration delay may also decrease with rising temperature because the EM-induced atomic diffusion is a thermally activated process. However, typical integrated circuit devices usually operate at temperatures ~100°C.

We have observed the atomic-scale EM process in twin-modified Cu grains near room temperature with the use of ultrahigh-vacuum and high-resolution TEM technique. The EM-induced atomic migration along a twin-modified grain boundary was observed, and the presence of the triple point of a coherent twin boundary meeting a grain boundary was found to retard the EM-induced atomic transport.

References and Notes

1. E. O. Hall, *Proc. Phys. Soc. London Sect. B* **64**, 747 (1951).
2. N. J. Petch, *J. Iron Steel Inst. London* **174**, 25 (1953).
3. R. W. Balluffi, R. F. Mehl, *Metall. Mater. Trans. A* **13**, 2069 (1982).
4. S. W. Chan, R. W. Balluffi, *Acta Metall.* **33**, 1113 (1985).
5. L. Lu, Y. Shen, X. Chen, L. Qian, K. Lu, *Science* **304**, 422 (2004), published online 18 March 2004; 10.1126/science.1092905.
6. C. K. Hu, J. M. E. Harper, *Mater. Chem. Phys.* **52**, 5 (1998).
7. R. Frankovic, G. H. Bernstein, *IEEE Trans. Electron. Dev.* **43**, 2233 (1996).
8. P. Børgesen, J. K. Lee, R. Gleixner, C. Y. Li, *Appl. Phys. Lett.* **60**, 1706 (1992).
9. I. A. Blech, *J. Appl. Phys.* **47**, 1203 (1976).
10. C. K. Hu, R. Rosenberg, K. Y. Lee, *Appl. Phys. Lett.* **74**, 2945 (1999).
11. C. S. Hau-Riege, *Microelectron. Reliab.* **44**, 195 (2004).
12. K. N. Tu, *J. Appl. Phys.* **94**, 5451 (2003).
13. J. S. Huang, T. L. Shofner, J. Zhao, *J. Appl. Phys.* **89**, 2130 (2001).
14. E. Liniger, L. Gignac, C. K. Hu, S. Kaldor, *J. Appl. Phys.* **92**, 1803 (2002).
15. C. K. Hu, K. Y. Lee, L. Gignac, R. Carruthers, *Thin Solid Films* **308-309**, 443 (1997).
16. C. N. Liao, K. C. Chen, W. W. Wu, L. J. Chen, *Appl. Phys. Lett.* **87**, 141903 (2005).
17. K. C. Chen, C. N. Liao, W. W. Wu, L. J. Chen, *Appl. Phys. Lett.* **90**, 203101 (2007).
18. See supporting material on *Science* Online.
19. M. Karimi, T. Tomkowski, *Phys. Rev. B* **52**, 5364 (1995).
20. A. P. Sutton, R. W. Balluffi, in *Interfaces in Crystalline Materials* (Clarendon Press, Oxford, 1995), chap. 10, p. 598.

21. The work was supported by the National Science Council through grants NSC 96-2120-M-007-006 and 96-2628-E-007-018-MY3. K.N.T. acknowledges the support of NSF–Nanoscale Interdisciplinary Research Team contract CMS-0506841.

Supporting Online Material

www.sciencemag.org/cgi/content/full/321/5892/1066/DC1
Materials and Methods
Fig. S1
Movie S1

21 May 2008; accepted 10 July 2008
10.1126/science.1160777

A Stable Silicon(0) Compound with a Si=Si Double Bond

Yuzhong Wang, Yaoming Xie, Pingrong Wei, R. Bruce King, Henry F. Schaefer III, Paul von R. Schleyer,* Gregory H. Robinson*

Dative, or nonoxidative, ligand coordination is common in transition metal complexes; however, this bonding motif is rare in compounds of main group elements in the formal oxidation state of zero. Here, we report that the potassium graphite reduction of the neutral hypervalent silicon-carbene complex L:$SiCl_4$ {where L: is :C[N(2,6-Pr^i_2-C_6H_3)CH]$_2$ and Pr^i is isopropyl} produces L:(Cl)Si–Si(Cl):L, a carbene-stabilized bis-silylene, and L:Si=Si:L, a carbene-stabilized diatomic silicon molecule with the Si atoms in the formal oxidation state of zero. The Si-Si bond distance of 2.2294 ± 0.0011 (standard deviation) angstroms in L:Si=Si:L is consistent with a Si=Si double bond. Complementary computational studies confirm the nature of the bonding in L:(Cl)Si–Si(Cl):L and L:Si=Si:L.

Although silicon is predominantly associated with semiconductors, integrated circuits, and advanced electronic devices, its structures and bonding motifs intrigue chemists because they are often substantially different from those of silicon's lighter congener carbon. For example, the chemical and physical properties of CO_2 are totally unlike those of SiO_2, and hypervalent species such as $[SiF_5]^-$ are unknown for carbon (*1*). Even though molecules containing C-C multiple bonds are ubiquitous and have been studied for more than two centuries, it was not until 1981 that a disilene, a compound containing a Si-Si double bond ($R_2Si{=}SiR_2$, where R is $Me_3C_6H_2$) was prepared by West *et al.* (*2*); a disilyne (RSi≡SiR, where R is an extremely bulky ligand), a compound containing a Si-Si triple bond (albeit with a decidedly nonlinear, transbent geometry), was ultimately achieved by Sekiguchi *et al.* in 2004 (*3*). In addition to disilenes and disilynes, a number of other interesting stable low-coordinate Si compounds have been reported (*4*–*7*). Regarding the oxidation state of Si in low-coordinate compounds, the central Si atoms in disilenes and disilynes are in the formal oxidation states of two (+2) and one (+1), respectively. It is well known for transition metals to assume the formal oxidation state of zero in organometallic compounds [for example, $Ni(CO)_4$, $(C_6H_6)_2Cr$, etc.]; however, the formal oxidation state of zero is rare for main group elements in their compounds (apart from those in Zintl phases) (*8*, *9*).

The study of highly reactive Si(0) intermediates may prove critical in the development of new synthetic strategies in Si chemistry. Such experimental studies, however, require sophisticated instruments and elaborate techniques (*10*). For example, the diatomic Si_2 molecule, having a triplet ground state ($X^3\Sigma_g^-$), has been studied only in the gas phase and in argon matrices (*11*). Recently, the CO complex of the Si_2 molecule, OC:Si=Si:CO, was examined with argon matrix isolation absorption infrared spectroscopy and computed to have an unusual transbent structure

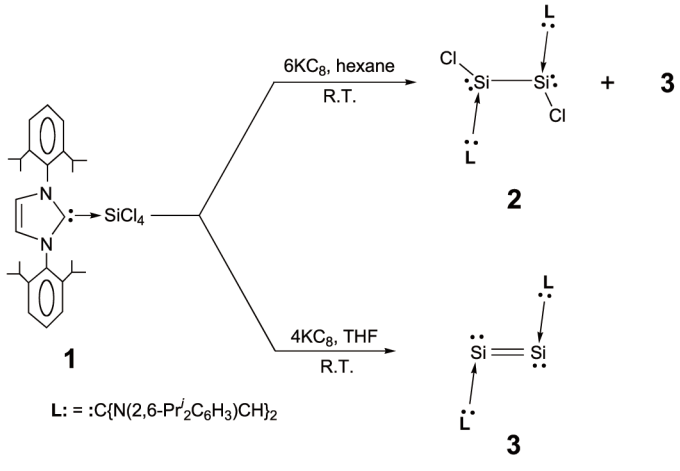

Fig. 1. Synthetic scheme for compounds **2** and **3**.

Department of Chemistry and Center for Computational Chemistry, The University of Georgia, Athens, GA 30602–2556, USA.

*To whom correspondence should be addressed. E-mail: schleyer@chem.uga.edu (P.v.R.S.); robinson@chem.uga.edu (G.H.R.)

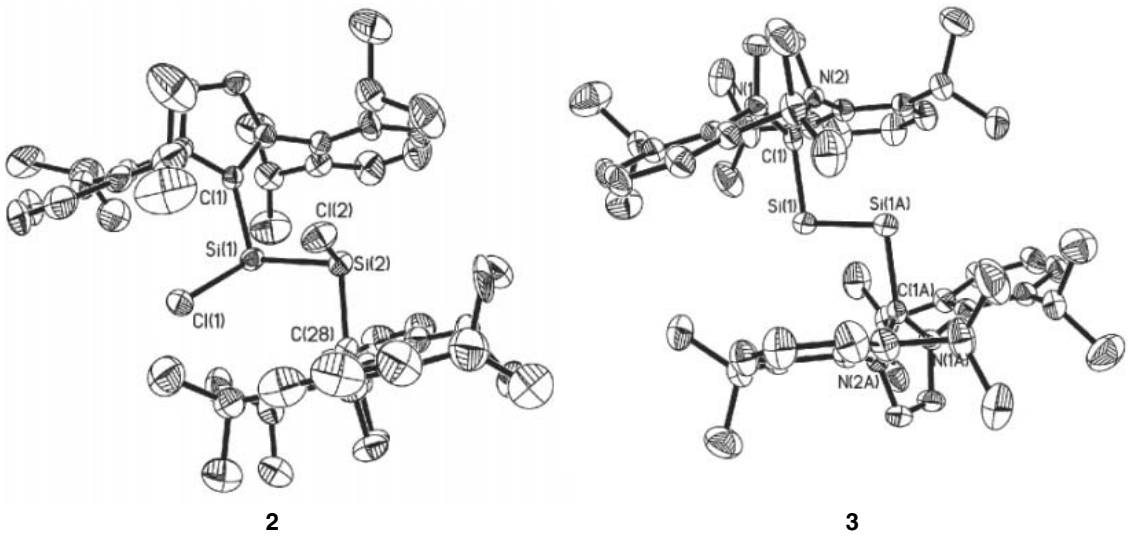

2 **3**

Fig. 2. Molecular structures of L:(Cl)Si–Si(Cl):L, (**2**), and L:Si=Si:L, (**3**). L: is :C{N(2,6-$Pr^i_2C_6H_3$)CH}$_2$. Thermal ellipsoids represent 30% probability. Hydrogen atoms were omitted for clarity. Selected bond distances (Å) and angles (deg) for (**2**) are Si(1)–Si(2), 2.393(3); Si(1)–C(1), 1.939(6); Si(1)–Cl(1), 2.161(3); Si(2)–C(28), 1.929(7); Si(2)–Cl(2), 2.168(3); C(1)–Si(1)–Si(2), 98.76(19); Cl(1)–Si(1)–Si(2), 108.75(11); C(1)–Si(1)–Cl(1), 101.2(2); C(28)–Si(2)–Si(1), 98.7(2); Cl(2)–Si(2)–Si(1), 107.96(11); and C(28)–Si(2)–Cl(2), 100.7(2). Selected bond distances (Å) and angles (deg) for (**3**) are Si(1)–Si(1A), 2.2294(11); Si(1)–C(1), 1.9271(15); and C(1)–Si(1)–Si(1A), 93.37(5).

with Si-Si-C angles approaching 90° (*12*). How might the fleeting diatomic Si_2 molecule be sufficiently stabilized for routine laboratory inquiry? We recently produced neutral diborenes, L:(H)B=B(H):L, by employing N-heterocyclic carbene ligands, L:, to complex the highly reactive and electron-deficient diborene(2) parent H-B=B-H (*13*, *14*). Extending this strategy, we now report the syntheses (Fig. 1) (*15*), molecular structures (Fig. 2) (*15*), and computational analyses (*16*) of L:$SiCl_4$, **1**; L:(Cl)Si–Si(Cl):L, **2**, a carbene-stabilized bis-silylene; and L:Si=Si:L, **3**, a carbene-stabilized :Si=Si: compound {where L: is :C[N(2,6-$Pr^i_2C_6H_3$)CH]$_2$ and Pr^i is isopropyl}. Both Si atoms in compound **3** are in the formal oxidation state of zero.

Kuhn *et al.* synthesized hypervalent L′:$SiCl_4$ {where L′: is :C[N(R)C(CH_3)]$_2$ and R is alkyl} complexes (*17*), which are neutral equivalents of $[SiCl_5]^-$. Consistently, we found that room-temperature reaction of a sterically demanding N-heterocyclic carbene ligand, L:, with $SiCl_4$ in hexane, gives L:$SiCl_4$, **1**, in an essentially quantitative yield. The potassium graphite reduction of **1** (in a **1**:KC_8 ratio of 1:6) in hexane produced air-sensitive, orange-red, sheetlike crystals of **2** (6.1% yield) and air-sensitive, dark red, block crystals of **3** (as a minor product) (Fig. 1). However, when the potassium graphite reduction of **1** is performed (with a **1**:KC_8 ratio of 1:4) in tetrahydrofuran (THF) (Fig. 1), compound **3** can be exclusively isolated and in higher yield (23.2%). In the ^{1}H nuclear magnetic resonance (NMR) spectra, the imidazole resonances (in C_6D_6) of compounds **1**, **2**, and **3** appear at 6.40, 6.31, and 6.58 parts per million (ppm), respectively. The ^{1}H-decoupled ^{29}Si NMR spectra of compounds **1** to **3** were also determined. The ^{29}Si NMR chemical shift of **1** (in CD_2Cl_2), –108.9 ppm, is comparable to reported values (–104.7 to –105.9 ppm) of hypervalent Si compounds L′:$SiCl_4$ {where L′: is :C[N(R)C(CH_3)]$_2$ and R is alkyl} (*17*). The ^{29}Si NMR resonance of **2** (in C_6D_6), 38.4 ppm, compares with 78.3 ppm of [C(H)N(*t*Bu)]$_2$Si: (*18*) and 14.6 ppm of [PhC(N*t*Bu)$_2$]SiCl (*19*), but is at a considerably lower field than the –48.6- to –57.4-ppm range of silylene-isocyanide complexes (*20*). The ^{29}Si chemical shift of **3** (in C_6D_6), 224.5 ppm, resides at an even lower field than typical disilene resonances (50 to 155 ppm) (*5*).

The x-ray structural analysis of **2** (Fig. 2) reveals that the (Cl)Si–Si(Cl) core is sterically well-shielded by the two L: ligands. The central Si–Si bond distance, 2.393(3) Å, is only about 0.05 Å longer than the sum of Si covalent radii (2.34 Å) (*21*) and about 0.03 Å longer than the Si–Si single-bond distance in α-silicon (2.36 Å) (*22*). Each Si atom in **2**, in the formal +1 oxidation state, is three-coordinate in a trigonal pyramidal geometry. The sum of the bond angles of the Si atoms in **2**, 308.0° (mean), compares very well with that in (*t*Bu$_2$MeSi)$_2$Si(F)Li•(THF)$_3$ (307.6°) (*23*) as well as with the computed value for Ph_2Si:CNPh (306.8°) (*20*). The pyramidal geometry at each Si atom in **2** results from substantial lone electron-pair character on both Si atoms. The two L:(Cl)Si moieties of **2** adopt a gauche conformation [the Cl(1)–Si(1)–Si(2)–Cl(2) torsion angle is –46.5°]. These structural features of **2** are akin to those of its isolobal equivalent H_2P–PH_2, which also favors a gauche conformation (*24*). Although a Lewis base–stabilized silylene was reported a decade ago (*20*), **2** is noteworthy as a Lewis base–stabilized bis-silylene—namely, two silylene units bridged by a Si–Si bond. The Si–C bond distances [1.934(6) Å, mean] of **2** are comparable to that of **1** [1.928(2) Å] (fig. S1) whereas the mean Si–Cl bond distance [2.164(3) Å] of **2** matches the sum of the Si and Cl covalent radii (2.16 Å) (*21*). The visible absorption maximum of **2** (λ_{max} = 510 nm, in hexane) is similar to that of an intramolecularly base-stabilized three-coordinate silylene (λ_{max} = 478 nm) (*25*).

The nature of the bonding in **2** was delineated by density functional theory (DFT) computations at the B3LYP/6-311+G** level on the simplified L:(Cl)Si–Si(Cl):L [where L: is :C(NHCH)$_2$] model, **2-H**. The computed Si–Si (2.405 Å) and Si–C (1.926 Å) bond distances of **2-H** compare well with the experimental values [2.393(3) and 1.934(6) (mean) Å, respectively] of **2**. The computed Si–Cl bond distance of 2.238 Å in **2-H** is about 0.07 Å longer than that in **2** [2.164 (3) Å, mean]. The fact that the sum of the bond angles around the Si atoms in **2-H** (298.2°) is smaller than that of **2** (308.0°) may be attributed to the substantially lower steric crowding of the model ligands used in **2-H**. The theoretical analysis of **2-H** included both localized molecular orbitals (LMOs) (fig. S2) and canonical molecular orbitals (fig. S3). The LMOs reveal a Si–Si σ bonding orbital and two nonbonding lone-pair orbitals, one at each Si atom. Natural bonding orbital (NBO) analysis shows that the Si-Si σ single bond [Wiberg bond index (WBI) = 0.94] has 12.1% s-, 87.4% p-, and 0.5% d-character, whereas the nonbonding Si lone-pair orbitals have 68.3% s-, 31.6% p-, and 0.1% d-character. The Si-Cl bond has 8.5% s-, 89.9% p-, and 1.6% d-character.

We also examined the structure of the uncomplexed Si_2Cl_2 parent molecule. Unlike acetylenes and Sekiguchi's disilyne (*3*), a doubly-bridged (C_{2v}) Si(μ-Cl)$_2$Si geometry with a 102.1° dihedral angle between the two Si_2Cl rings is preferred in the B3LYP/6-311+G* (*16*) optimization, which compares with the doubly-bridged (C_{2v}) global minimum of Si_2H_2 (*26*). The Si–Si bond distance, 2.361 Å, corresponds to a single Si–Si bond. The symmetrical Cl-bridged bonding elongates the Cl–Si distance (2.387 Å) and involves Cl lone pairs. However, in **2** these Cl-bridging interactions are replaced by the complexation of two-electron donor carbene ligands to the Si atoms.

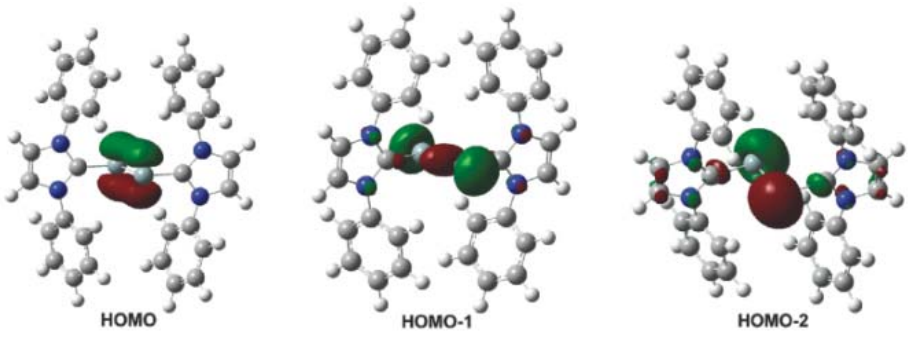

Fig. 3. The HOMO (π), HOMO-1 (σ), and HOMO-2 (lone pair) of **3-Ph**.

One structural feature of **3**, of C_i symmetry, is the :Si=Si: core (Fig. 2). The Si=Si bond distance in **3**, 2.2294(11) Å, is within the reported range of disilene bond distances (2.14 to 2.29 Å) (*5*) and compares well with the computed [2.249 Å, BHLYP (*27*); 2.281 Å, B3LYP (*16*)] and experimental (2.246 Å) (*28*) bond distances of Si_2. Both OC:Si=Si:CO (2.310 Å, B3LYP) (*12*) and singlet $Si_2H_2^{2-}$ (2.288 Å, B3LYP) (*29*) suggest further comparisons. The Si-Si double-bond character of **3** is further supported by the $\pi_{Si=Si}$–$\pi^*_{Si=Si}$ absorption (λ_{max} = 466 nm, in THF), which is comparable to the reported ultraviolet/visible absorption maxima (390 to 480 nm) of stable disilenes (*5*). However, in contrast to previously reported disilenes, in which three-coordinate Si atoms (in the +2 formal oxidation state) reside in trigonal planar environments, the Si atoms in **3**—in the formal oxidation state of zero—are only two-coordinate and have transbent geometries with C–Si–Si angles of 93.37(5)°. The two parallel carbene ligands are bound almost perpendicularly to the central Si=Si double bond. Generally, Si does not hybridize extensively. The almost-90° transbent skeletal conformation is consistent with the predominantly 3p-character of the Si-Si bonding orbitals in **3** and the predominantly 3s-character of the Si lone-pair molecular orbitals (see the NBO analysis below). Indeed, the nearly orthogonal transbent conformation of **3** is shared by the OC:Si=Si:CO complex, the dianionic $Si_2H_2^{2-}$, and the simple valence isoelectronic HP=PH model of the dipnictene family, RË=ËR (E = P, As, Sb, Bi) (*30*), all of which possess an electron lone pair on the central core (E) atoms. The Si–C bonds [1.9271(15) Å] of **3** are only marginally shorter than those of **1** and **2**. The fact that no ^{29}Si-^{1}H coupling was observed in the ^{1}H-coupled ^{29}Si NMR spectrum further supports the formulation of **3**.

DFT computations at the B3LYP/6-311+G** level on the simplified L:Si=Si:L {where L: is :C[N(C$_6$H$_5$)CH]$_2$} model, **3-Ph**, support the bonding analysis. The computed Si=Si bond distance (2.2407 Å), the Si–Si–C bond angle (99.2°), and the C–Si–Si–C torsion angle (180.0°) are very close to the experimental values of **3** [$d_{Si=Si}$ = 2.2294(11) Å; Si–Si–C bond angle = 93.37(5)°, C–Si–Si–C torsion angle = 180.0°]. The highest occupied molecular orbital (HOMO) corresponds to the Si-Si π bond, whereas the HOMO-1 is dominated by the Si-Si σ bond. The HOMO-2 is one of the two nonbonding lone-pair molecular orbitals (Fig. 3).

The molecular orbital (MO) profile of **3-Ph** differs from that of the triplet ($X^3\Sigma_g^-$) ground state of the isolated Si_2 species, in which each of the two degenerate $1\pi_\mu$ MOs are occupied by one electron with the same spin (*31*). Complexation of Si_2 by two carbene ligands (as electron-pair donors) results in the occupancy of all valence orbitals of Si. Indeed, the WBI, 1.73, is supportive of a Si=Si double bond in **3-Ph**. NBO analysis characterizes the occupancies of the Si-Si σ bond as 17.3% s, 82.2% p, and 0.5% d, the Si-Si π bond as 0.0% s, 99.6% p, and 0.4% d, and the Si lone-pair nonbonding orbitals as 72.8% s, 27.2% p, and 0.0% d.

The B3LYP/6-311+G** computed (*16*) binding energies [zero point energy–corrected based on data in the supporting online material (SOM)] of the carbene ligand models {where L: is :C[N(Me)CH]$_2$} to the Si-based cores are particularly noteworthy (Eqs. 1 to 3)

$$SiCl_4 + L: \rightarrow L{:}SiCl_4\ (\mathbf{1\text{-}Me}) \quad -10.6\ \text{kcal/mol} \qquad (1)$$

$$Si_2Cl_2\ (C_{2v}) + 2L: \rightarrow L{:}(Cl)Si\text{-}Si(Cl){:}L\ (\mathbf{2\text{-}Me}) \quad -69.4\ \text{kcal/mol} \qquad (2)$$

$$Si_2\ (X^3\Sigma_g^-) + 2L: \rightarrow L{:}Si{=}Si{:}L\ (\mathbf{3\text{-}Me}) \quad -80.9\ \text{kcal/mol} \qquad (3)$$

The very large binding energies of **2-Me** and **3-Me** reflect the coordinatively unsaturated character of Si_2 ($X^3\Sigma_g^-$) and of Si_2Cl_2 (C_{2v}), respectively, as well as the remarkable complexation proclivity of the carbene ligand (*32*). Bulky N-heterocyclic carbene ligands are further demonstrated to be effective lone-pair donors capable of stabilizing—both thermodynamically and kinetically—unusual molecules.

References and Notes

1. K. Akiba, *Chemistry of Hypervalent Compounds* (Wiley-VCH, New York, 1999).
2. R. West, M. J. Fink, J. Michl, *Science* **214**, 1343 (1981).
3. A. Sekiguchi, R. Kinjo, M. Ichinohe, *Science* **305**, 1755 (2004).
4. P. P. Gaspar, R. West, in *The Chemistry of Organic Silicon Compounds, Volume 2*, Z. Rappoport, Y. Apeloig, Eds. (Wiley, Chichester, UK, 1998), chap. 43.
5. M. Weidenbruch, in *The Chemistry of Organic Silicon Compounds, Volume 3*, Z. Rappoport, Y. Apeloig, Eds. (Wiley, Chichester, UK, 2001), chap. 5.
6. H. Ottosson, P. G. Steel, *Chem. Eur. J.* **12**, 1576 (2006).
7. M. Weidenbruch, *Angew. Chem. Int. Ed.* **45**, 4241 (2006).
8. C. L. B. Macdonald, B. D. Ellis, in *Encyclopedia of Inorganic Chemistry, Volume V*, R. B. King, Ed. (Wiley, Hoboken, NJ, 2005), pp. 2718–2729.
9. C. A. Dyker, V. Lavallo, B. Donnadieu, G. Bertrand, *Angew. Chem. Int. Ed.* **47**, 3206 (2008).
10. P. Jutzi, U. Schubert, Eds., *Silicon Chemistry: From the Atom to Extended Systems* (Wiley-VCH, Weinheim, Germany, 2003).
11. R. J. Van Zee, R. F. Ferrante, W. Weltner Jr., *J. Chem. Phys.* **83**, 6181 (1985).
12. M. Zhou, L. Jiang, Q. Xu, *J. Chem. Phys.* **121**, 10474 (2004).
13. Y. Wang *et al.*, *J. Am. Chem. Soc.* **129**, 12412 (2007).
14. Y. Wang *et al.*, *J. Am. Chem. Soc.* **130**, 3298 (2008).
15. Materials and methods are available as supporting material on *Science* Online.
16. Computations: The structures of **2-H** and **3-Ph** were optimized at the B3LYP/6-311+G** DFT level with the Gaussian 94 program (*33*) and Gaussian 03 program (*34*). Computational details can be found in the SOM.
17. N. Kuhn, T. Kratz, D. Bläser, R. Boese, *Chem. Ber.* **128**, 245 (1995).
18. M. Denk *et al.*, *J. Am. Chem. Soc.* **116**, 2691 (1994).
19. C.-W. So, H. W. Roesky, J. Magull, R. B. Oswald, *Angew. Chem. Int. Ed.* **45**, 3948 (2006).
20. N. Takeda, H. Suzuki, N. Tokitoh, R. Okazaki, S. Nagase, *J. Am. Chem. Soc.* **119**, 1456 (1997).
21. J. Y. Corey, in *The Chemistry of Organic Silicon Compounds, Volume 1*, S. Patai, Z. Rappoport, Eds. (Wiley, Chichester, UK, 1989), chap. 1.
22. R. Nesper, A. Currao, S. Wengert, in *Organosilicon Chemistry II: From Molecules to Materials,* N. Auner, J. Weis, Eds. (VCH, Weinheim, Germany, 1996), p. 469.
23. G. Molev *et al.*, *J. Am. Chem. Soc.* **128**, 2784 (2006).
24. A. H. Cowley, W. D. White, M. C. Damasco, *J. Am. Chem. Soc.* **91**, 1922 (1969).
25. R. Corriu *et al.*, *J. Organomet. Chem.* **466**, 55 (1994).
26. B. T. Colegrove, H. F. Schaefer III, *J. Phys. Chem.* **94**, 5593 (1990).
27. C. Pak, J. C. Rienstra-Kiracofe, H. F. Schaefer III, *J. Phys. Chem. A* **104**, 11232 (2000).
28. M. R. Nimlos, L. B. Harding, G. B. Ellison, *J. Chem. Phys.* **87**, 5116 (1987).
29. M. Takahashi, Y. Kawazoe, *Organometallics* **24**, 2433 (2005).
30. P. P. Power, *Chem. Rev.* **99**, 3463 (1999).
31. A. Krapp, F. M. Bickelhaupt, G. Frenking, *Chem. Eur. J.* **12**, 9196 (2006).
32. D. Bourissou, O. Guerret, F. P. Gabbaï, G. Bertrand, *Chem. Rev.* **100**, 39 (2000).
33. M. J. Frisch *et al.*, Gaussian 94, revision B.3 (Gaussian, Pittsburgh, PA, 1995).
34. M. J. Frisch *et al.*, Gaussian 03, revision C.02 (Gaussian, Wallingford, CT, 2004).

35. We thank NSF for support of this work through grants CHE-0608142 (G.H.R.) and CHE-0716718 (P.v.R.S. and R.B.K.). Coordinates and other crystallographic information for compounds **1, 2,** and **3** have been deposited in the Cambridge Crystallographic Database Center with deposition numbers 686707, 686708, and 687305, respectively.

Supporting Online Material

www.sciencemag.org/cgi/content/full/321/5892/1069/DC1
Materials and Methods
SOM Text
Figs. S1 to S13
Tables S1 to S3
References

21 May 2008; accepted 8 July 2008
10.1126/science.1160768

In Situ Formation of an Oxygen-Evolving Catalyst in Neutral Water Containing Phosphate and Co^{2+}

Matthew W. Kanan and Daniel G. Nocera*

The utilization of solar energy on a large scale requires its storage. In natural photosynthesis, energy from sunlight is used to rearrange the bonds of water to oxygen and hydrogen equivalents. The realization of artificial systems that perform "water splitting" requires catalysts that produce oxygen from water without the need for excessive driving potentials.
Here we report such a catalyst that forms upon the oxidative polarization of an inert indium tin oxide electrode in phosphate-buffered water containing cobalt (II) ions. A variety of analytical techniques indicates the presence of phosphate in an approximate 1:2 ratio with cobalt in this material. The pH dependence of the catalytic activity also implicates the hydrogen phosphate ion as the proton acceptor in the oxygen-producing reaction. This catalyst not only forms in situ from earth-abundant materials but also operates in neutral water under ambient conditions.

Sunlight is the only renewable and carbon-neutral energy source of sufficient scale to replace fossil fuels and meet rising global energy demand (*1*). The diurnal variation in local insolation, however, demands a cost-effective storage of solar energy for its large-scale utilization. Of the possible storage methods, nature provides the blueprint for storing sunlight in the form of chemical fuels (*1*, *2*). The primary steps of natural photosynthesis involve the absorption of sunlight and its conversion into spatially separated electron/hole pairs. The holes of this wireless current are then captured by the oxygen-evolving complex (OEC) to oxidize water to oxygen and the electrons are captured by photosystem I to reduce $NADP^+$ (nicotinamide adenine dinucleotide phosphate) to NADPH (the reduced form of $NADP^+$), nature's form of hydrogen (*3*). Thus, the overall primary events of photosynthesis store solar energy in a fuel by rearranging the chemical bonds of water to form H_2 (i.e., NADPH) and O_2.

An approach to duplicating photosynthesis outside of a photosynthetic membrane is to convert sunlight into spatially separated electron/hole pairs within a photovoltaic cell and then capture the charges with catalysts that mediate "water splitting" (*1*, *4*). The four holes are captured by a catalyst at the anode to produce oxygen, and the four electrons are captured by a separate catalyst at the cathode to produce hydrogen. The net result is the storage of solar energy in the chemical bonds of H_2 and O_2.

A key determinant of energy storage in artificial photosynthesis is the efficiency of the water-splitting catalysts. Electrocatalysts that are efficient for solar-to-fuels conversion must operate close to the Nernstian potentials (E) for the H_2O/O_2 and H_2O/H_2 half-cell reactions shown in Scheme 1 (half-cell potentials given in the convention of reduction potentials).

The voltage in addition to E that is required to attain a given catalytic activity—referred to as overpotential—limits the efficiency of converting light into catalytic current. Of the two reactions, the H_2O/O_2 reaction is considerably more complex (*5*). This reaction requires a four-electron oxidation of two water molecules coupled to the removal of four protons to form a relatively weak oxygen-oxygen bond. In addition to controlling this proton-coupled electron transfer (PCET) (*6*, *7*), a catalyst must tolerate prolonged exposure to oxidizing conditions. Even at the thermodynamic limit, water oxidation requires an oxidizing power that causes most chemical functional groups to degrade. Accordingly, the generation of oxygen from water presents a substantial challenge toward realizing artificial photosynthesis (*8*).

The fine-tuned molecular machinery of the OEC oxidizes water at a low overpotential using a Mn_4O_4Ca cluster (*9*–*12*). Outside the OEC, examples of water oxidation catalysts include first-row spinel and perovskite metal oxides, which require concentrated basic solutions (pH > 13) and moderate overpotentials (<400 mV), and precious metals and precious metal oxides, which operate with similar efficiencies under acidic conditions (pH < 1) (*13*–*15*). However, few catalysts operate in neutral water under ambient conditions. Neutral water is oxidized at Pt electrodes, and some precious metal oxides have been reported to operate electrocatalytically in neutral or weakly acidic solutions (*16*). The development of an earth-abundant, first-row catalyst that operates at pH 7 at low overpotential remains a fundamental chemical challenge. Here, we report an oxygen-evolving catalyst that forms in situ upon anodic polarization of an inert electrode in neutral aqueous phosphate solutions containing Co^{2+}. Oxygen generation occurs under benign conditions: pH = 7, 1 atm, and room temperature.

Cobalt ions in the presence of chemical oxidants such as $Ru(bpy)_3^{3+}$ (bpy, bipyridine; E^o = 1.26, where E^o is the standard potential) catalyze the oxidation of water to O_2 in neutral phosphate solutions (*17*, *18*). Oxygen yields drop in these reactions when oxidized Co species precipitate from solution because the catalytically active species is removed from the solution-phase reaction. However, an oxidation-induced precipita-

$$O_2 + 4H^+ + 4e^- \rightleftharpoons 2H_2O \qquad E_{anodic} = 1.23\,V - 0.059\,(pH)\,V \text{ vs NHE}$$

$$4H^+ + 4e^- \rightleftharpoons 2H_2 \qquad E_{cathodic} = 0\,V - 0.059\,(pH)\,V \text{ vs NHE}$$

$$2H_2O \longrightarrow 2H_2 + O_2 \qquad E_{rxn} = -1.23\,V$$

Scheme 1.

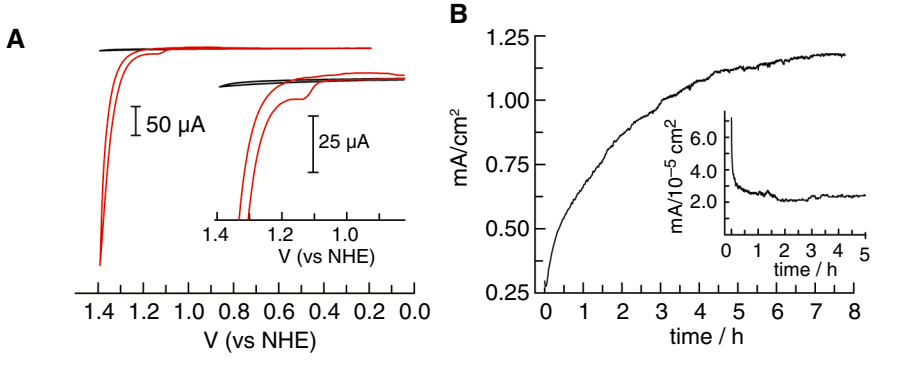

Fig. 1. (**A**) Cyclic voltammagram in 0.1 M KPi electrolyte at pH 7.0 with no Co^{2+} ion present (black line) and with 0.5 mM Co^{2+} present (red line). The potential was measured against a Ag/AgCl reference and converted to NHE potentials by using E(NHE) = E(Ag/AgCl) + 0.197 V. (**B**) Current density profile for bulk electrolysis at 1.29 V (versus NHE) in 0.1 M KPi electrolyte at pH 7.0 containing 0.5 mM Co^{2+}. (Inset) Profile in the absence of Co^{2+}.

Department of Chemistry, 6-335, Massachusetts Institute of Technology, Cambridge, MA 02139–4307, USA.

*To whom correspondence should be addressed. E-mail: nocera@mit.edu

tion may be exploited to prepare electrocatalysts in situ if the precipitated material remains catalytically active and can be oxidized at an electrode surface. To explore this possibility for Co-catalyzed water oxidation, we examined electrochemical oxidations of aqueous solutions containing phosphate and Co^{2+}. Cyclic voltammetry of a 0.5 mM solution of $Co(NO_3)_2$ in 0.1 M potassium phosphate pH 7.0 (KPi electrolyte) exhibits an oxidation wave at $E_p = 1.13$ V (where E_p is the peak potential) versus the normal hydrogen electrode (NHE), followed by the onset of a strong catalytic wave at 1.23 V (Fig. 1A). A broad, relatively weak reduction wave is observed on the cathodic scan. The presence of a catalytic wave prompted us to examine the electrode activity during controlled-potential electrolysis.

Indium tin oxide (ITO) was used as the electrode for bulk electrolysis to ensure a minimal background activity for O_2 production. An electrolysis at 1.29 V without stirring in neutral KPi electrolyte containing 0.5 mM Co^{2+} exhibits a rising current density that reaches a peak value >1 mA/cm^2 after 7 to 8 hours (Fig. 1B). During this time, a dark coating forms on the ITO surface, and effervescence from this coating becomes increasingly vigorous (*19*).The same results are observed with either $CoSO_4$, $Co(NO_3)_2$, or $Co(OTf)_2$ (where OTf = triflate) as the Co^{2+} source, which indicates that the original Co^{2+} counterion is unimportant and that this activity does not depend on an impurity found in a specific source. The amount of charge passed during the course of an 8-hour electrolysis far exceeds what could be accounted for by stoichiometric oxidation of the Co^{2+} in solution (*20*). These observations are indicative of the in situ formation of an oxygen-evolving catalyst. Catalyst formation also proceeds on a fluorine tin oxide electrode and if KPi is replaced by NaPi electrolyte. In a control experiment, the current density during bulk electrolysis under identical conditions in the absence of Co^{2+} rapidly drops to a baseline level of ~25 nA/cm^2 (inset in Fig. 1B).

The morphology of the electrode coating formed during electrolysis in the presence of Co^{2+} was examined by scanning electron microscopy (SEM). The electrodeposited material consists of particles that have coalesced into a thin film and individual micrometer-sized particles on top of the film (Fig. 2A). The ITO substrate can be seen through cracks in the film that form upon drying, as evidenced by particles that are split into complementary pieces. The film thickness gradually increases over the course of the electrodeposition (see fig. S4 for additional images). At maximum activity under these electrolysis conditions, the film is >2 μm thick. The x-ray powder diffraction pattern of an electrodeposited catalyst shows broad amorphous features and no peaks indicative of crystalline phases other than the peaks associated with the ITO layer (fig. S1).

In the absence of detectable crystallites, the composition of the electrodeposited material was analyzed by three complementary techniques. Energy-dispersive x-ray analysis (EDX) spectra were obtained from multiple 100-to-300–m^2 regions of several independently prepared samples. These spectra identify Co, P, K, and O as the principal elemental components of the material (Fig. 2B). Although the material's morphology is not ideally suited for quantitative EDX, the analyses consistently indicate a Co:P:K ratio between ~2:1:1 and 3:1:1. To obtain an independent determination of elemental composition, electrolysis was performed with several larger ITO electrodes; the deposited material was scraped off and combined for a total yield of ~3 mg. Microanalytical elemental analysis of the combined material indicates 31.1% Co, 7.70% P, and 7.71% K, corresponding to a 2.1:1.0:0.8 Co:P:K ratio. Finally, the surface of an electrodeposited catalyst on the ITO substrate was analyzed by x-ray photoelectron spectroscopy (XPS). All peaks in the XPS spectra are accounted for by the elements detected above, in addition to In and Sn from the ITO substrate. The high-resolution P 2p peak at 133.1 eV is consistent with phosphate. The Co 2p peaks at 780.7 and 795.7 eV are in a range typical of Co^{2+} or Co^{3+} bound to oxygen (fig. S2) (*21*). Together, the x-ray diffraction and analytical results indicate that electrolysis of a Co^{2+} solution in neutral KPi electrolyte results in the electrodeposition of an amorphous Co oxide or hydroxide incorporating a substantial amount of phosphate anion at a stoichiometric ratio of roughly 2:1:1 for Co:P:K.

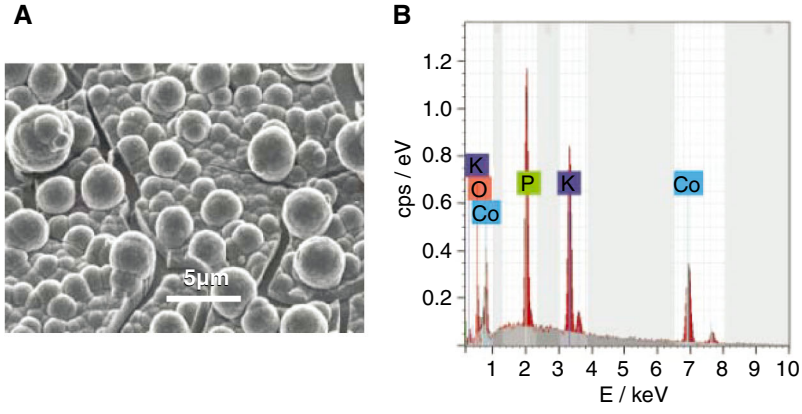

Fig. 2. (**A**) SEM image (30° tilt) of the electrodeposited catalyst after 30 C/cm^2 were passed in 0.1 M KPi electrolyte at pH 7.0, containing 0.5 mM Co^{2+}. The ITO substrate can be seen through cracks in the dried film. (**B**) Typical EDX histogram acquired at 12 kV. cps, counts per second.

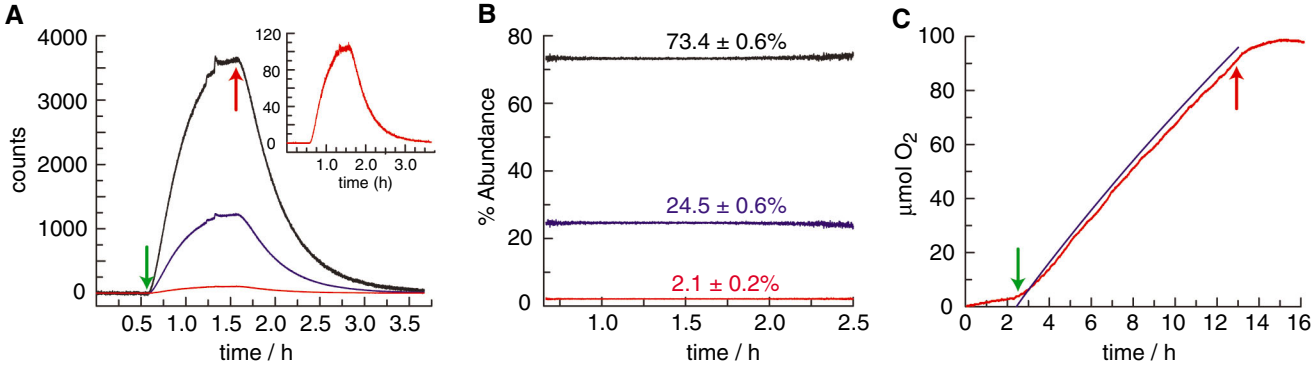

Fig. 3. (**A**) Mass spectrometric detection of isotopically labeled $^{16,16}O_2$ (black line), $^{16,18}O_2$ (blue line), and $^{18,18}O_2$ (red line) during electrolysis of a catalyst film on ITO in a KPi electrolyte containing 14.6% $^{18}OH_2$. The green arrow indicates the initiation of electrolysis at 1.29 V (NHE), and the red arrow indicates the termination of electrolysis. (Inset) Expansion of the $^{18,18}O_2$ signal. (**B**) Percent abundance of each isotope over the course of the experiment. Average observed abundance of ±2σ is indicated above each line. Statistical abundances are 72.9, 24.9, and 2.1%. (**C**) O_2 production measured by fluorescent sensor (red line) and theoretical amount of O_2 produced (blue line), assuming a Faradic efficiency of 100%. The green arrow indicates the initiation of electrolysis at 1.29 V, and the red arrow indicates the termination of electrolysis.

Three experiments were performed to establish that the catalytic activity observed with this material corresponds to authentic water oxidation. Each of these experiments was performed in neutral KPi electrolyte in the absence of Co^{2+}. Catalyst coatings (~1.3 cm^2) were prepared in a preliminary step as described above and stored under ambient laboratory conditions until they were used.

To confirm that water is the source of the O_2 produced, electrolysis was performed in helium-saturated electrolyte containing 14.6% $^{18}OH_2$ in a gas-tight electrochemical cell in line with a mass spectrometer. The helium carrier gas was continuously flowed through the headspace of the anodic compartment into the mass spectrometer, and the relative abundances of $^{32}O_2$, $^{34}O_2$, and $^{36}O_2$ were monitored at 2-s intervals. Within minutes of initiating electrolysis at 1.29 V, the signals for the three isotopes began to rise above their background levels as the O_2 produced by the catalyst escaped into the headspace. Upon terminating the electrolysis 1 hour later, these signals slowly returned to their background levels (Fig. 3A). The $^{32}O_2$, $^{34}O_2$, and $^{36}O_2$ isotopes were detected in the statistical ratio (72.9, 24.9, and 2.1% relative abundances, respectively) (Fig. 3B).

The Faradaic efficiency of the catalyst was measured with a fluorescence-based O_2 sensor. Electrolysis was performed in KPi electrolyte in a gas-tight electrochemical cell under an N_2 atmosphere with the sensor placed in the headspace. After initiating electrolysis at 1.29 V, the percentage of O_2 detected in the headspace rose in accord with what was predicted by assuming that all of the current was caused by $4e^-$ oxidation of water to produce O_2 (Fig. 3C). The amount of O_2 produced (95 μmol, 3.0 mg) greatly exceeds the amount of catalyst (~0.2 mg), which shows no perceptible decomposition during the course of the experiment.

The stability of phosphate under catalytic conditions was assayed by ^{31}P nuclear magnetic resonance (NMR). Electrolysis in a two-compartment cell with 10 mL of KPi electrolyte (1 mmol phosphate) on each side was allowed to proceed until 45 C had been passed through the cell (0.46 mmol electrons). Electrolysis solutions from both chambers show single, clean ^{31}P resonances, which indicate that the electrolyte is robust under these conditions (fig. S3). Together, the mass spectrometry, Faradaic efficiency, and ^{31}P NMR results demonstrate that the electrodeposited catalyst cleanly oxidizes H_2O to O_2 in neutral KPi solutions.

The current density of a catalyst on ITO was measured as a function of the overpotential (η) in KPi electrolyte without Co^{2+} (black circles in Fig. 4A). At pH 7.0, appreciable catalytic current is observed beginning at η = 0.28 V, and a current density of 1 mA/cm^2 (corresponding to 9 μmol O_2 cm^{-2} h^{-1}) requires η = 0.41 V. The Tafel plot deviates slightly from linearity, possibly reflecting an uncompensated iR drop caused by the surface resistivity of the ITO (8 to 12 ohms per square). Substantial improvements in the activity profile may be attainable without changing the catalyst composition by depositing on alternative substrates or improving ohmic contact to the ITO.

The catalyst used to obtain the Tafel plot at pH 7 was subsequently transferred to KPi electrolyte at pH 4.6, and the current density was measured at a constant applied potential (1.24 V) while the pH was increased incrementally to 9.4 by adding aliquots of concentrated KOH. A plot of the log of current density versus pH exhibits a steep initial rise that levels off in the high-pH range such that increasing the pH from 8 to 9.4 at this applied potential has little effect (Fig. 4B). These data can be converted to a Tafel plot by using Eq. 1 (Scheme 1) and accounting for iR drop (see Fig. 4 legend). A comparison to the Tafel plot obtained at pH 7 indicates that the catalyst exhibits approximately Nernstian behavior from pH 5 to 8: Increasing the pH by one unit at constant applied potential (1.24 V) has nearly the same effect as increasing the overpotential by 0.059 V at pH 7 (red circles in Fig. 4A). This result implicates a reversible ne^-, nH^+ removal before the rate-determining step for O_2 evolution in this pH range (here, n is the number of equivalents). Thus, an important component of the activity at pH 7 with this catalyst is the existence of one or more intermediates preceding O_2 formation that are deprotonated reversibly by HPO_4^{2-} in a PCET event (*22*). The pH-independent behavior above pH 8 at the applied potential may indicate a change in mechanism, most likely involving a deprotonated intermediate.

In addition to mediating the deprotonation required for catalysis, the KPi electrolyte provides a medium for in situ catalyst formation. Given that phosphate is a structural element and that the catalyst forms under oxidizing conditions, it is plausible that deposition is driven by the interaction of phosphate and Co^{3+}. By judicious choice of other metal-anion pairs or combinations of multiple metals and anions, it may be possible to access other oxygen-evolving catalysts that form in situ and operate in neutral solutions. In situ formation is advantageous because, in principle, it enables catalyst deposition on a variety of substrates, including those that are too delicate to tolerate traditional catalyst preparation techniques. This attribute is important for interfacing a catalyst with a variety of electrochemical or photoelectrochemical cell designs.

In situ formation also implies a self-repair mechanism. Proposed molecular mechanisms involving O_2/H_2O cycles at Co centers suggest that catalytic reactions cycle among Co^{2+}-, Co^{3+}-, and Co^{4+}-oxo oxidation states (*18*, *23*). The propensity of metal ion dissolution has been shown to correlate with ligand substitution (*24*). Given that Co^{3+} is substitutionally inert relative to Co^{2+}, a dynamic equilibrium between Co^{2+}-HPO_4^{2-} in solution and Co^{3+}-HPO_4^{2-} on the anodically poised electrode may be established. More generally, if a catalytic cycle involves an oxidation state that is prone to dissolution, this process can be countered by continual catalyst formation by establishing an equilibrium with the judicious choice of an anion.

The results reported herein highlight a new area of exploration for the development of easily prepared, earth-abundant catalysts that oxidize water. If artificial photosynthesis is to enable the storage of solar energy commensurate with global demand, water-splitting chemistry will need to be performed at a daunting scale. Storing the equivalent of the current energy demand would require splitting more than 10^{15} mol/year of water, which is roughly 100 times the scale of nitrogen fixation by the Haber-Bosch process. The conditions under which water splitting is performed will determine how solar energy is deployed. The catalyst reported here has many elements of natural photosynthesis, including (i) its formation from earth-abundant metal ions in aqueous solution, (ii) a plausible pathway for self-repair, (iii) a carrier for protons in neutral water, and (iv) the generation of O_2 at low overpotential, neutral pH, 1 atm, and room temperature.

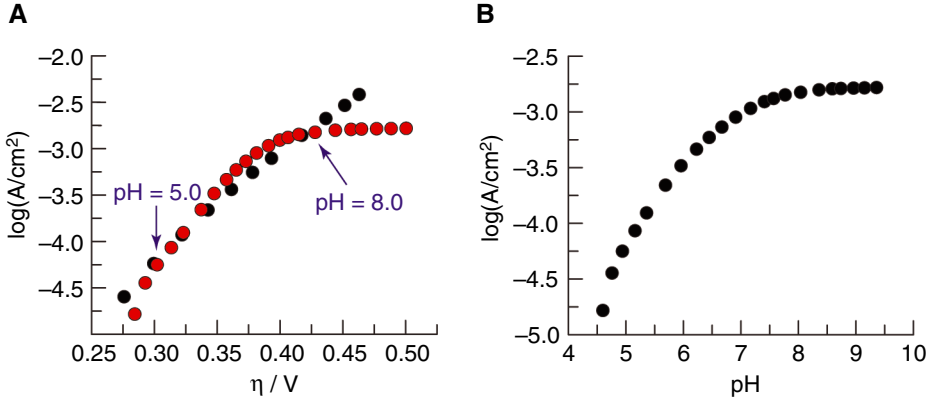

Fig. 4. (**A**) Tafel plot (black circles), $\eta = (V_{appl} - iR) - E(pH\ 7)$ (where V_{appl} is the applied potential), of a catalyst film on ITO in 0.1 M KPi electrolyte pH 7.0, corrected for the iR drop of the solution. pH data were converted into a Tafel plot (red circles), $\eta = (V_{appl} + 0.059\Delta pH - iR) - E(pH\ 7)$, assuming Nernstian behavior and correcting for the iR drop of the solution. The pH = 5 and pH = 8 data points are indicated by arrows. (**B**) Current density dependence on pH in 0.1 M KPi electrolyte. The potential was set at 1.24 V (versus NHE) with no iR compensation.

References and Notes

1. N. S. Lewis, D. G. Nocera, *Proc. Natl. Acad. Sci. U.S.A.* **103**, 15729 (2006).
2. N. Nelson, A. Ben-Shem, *Nat. Rev. Mol. Cell Biol.* **5**, 971 (2004).
3. J. Barber, *Philos. Trans. R. Soc. London Ser. A* **365**, 1007 (2007).
4. A. J. Bard, M. A. Fox, *Acc. Chem. Res.* **28**, 141 (1995).
5. T. A. Betley, Q. Wu, T. Van Voorhis, D. G. Nocera, *Inorg. Chem.* **47**, 1849 (2008).
6. R. I. Cukier, D. G. Nocera, *Annu. Rev. Phys. Chem.* **49**, 337 (1998).
7. M. H. V. Huynh, T. J. Meyer, *Chem. Rev.* **107**, 5004 (2007).
8. R. Eisenberg, H. B. Gray, *Inorg. Chem.* **47**, 1697 (2008).
9. K. N. Ferreira, T. M. Iverson, K. Maghlaoui, J. Barber, S. Iwata, *Science* **303**, 1831 (2004), published online 5 February 2004; 10.1126/science.1093087.
10. S. Iwata, J. Barber, *Curr. Opin. Struct. Biol.* **14**, 447 (2004).
11. J. Yano *et al.*, *Science* **314**, 821 (2006).
12. B. Loll, J. Kern, W. Saenger, A. Zouni, J. Biesiadka, *Nature* **438**, 1040 (2005).
13. S. Trassati, in *Electrochemistry of Novel Materials*, J. Lipkowski, P. N. Ross, Eds. (VCH, New York, 1994), chap. 5.
14. J. O. Bockris, T. J. Otagawa, *J. Electrochem. Soc.* **131**, 290 (1984).
15. M. R. Tarasevich, B. N. Efremov, in *Electrodes of Conductive Metal Oxides*, S. Trasatti, Ed. (Elsevier, Amsterdam, 1980), chap. 5.
16. M. Yagi, E. Tomita, S. Sakita, T. Kuwabara, K. Nagai, *J. Phys. Chem. B* **109**, 21489 (2005).
17. V. Y. Shafirovich, N. K. Khannanov, V. V. Strelets, *Nouv. J. Chim.* **4**, 81 (1980).
18. B. S. Brunschwig, M. H. Chou, C. Creutz, P. Ghosh, N. Sutin, *J. Am. Chem. Soc.* **105**, 4832 (1983).
19. Materials and methods, videos of an active electrode, and figs. S1 to S4 are available as supporting material on *Science* Online.
20. In a typical experiment, >40 C are passed over 8 hours, whereas oxidation of all the Co^{2+} in solution requires 1.9 C per oxidation-state change.
21. K. D. Bomben, J. F. Moulder, P. E. Sobol, W. F. Stickel, in *Handbook of X-Ray Photoelectron Spectra: A Reference Book of Standard Spectra for Identification*, J. Chastain, Ed. (Perkin Elmer, Eden Prairie, MN, 1992).
22. T. Irebo, S. Y. Reece, M. Sjödin, D. G. Nocera, L. Hammarström, *J. Am. Chem. Soc.* **129**, 15462 (2007).
23. C. J. Chang, Z.-H. Loh, C. Shi, F. C. Anson, D. G. Nocera, *J. Am. Chem. Soc.* **126**, 10013 (2004).
24. W. H. Casey, *J. Colloid Interface Sci.* **146**, 586 (1991).

25. This work was supported by a grant from the NSF Chemical Bonding Center (CHE-0802907). M.W.K. is supported by a Ruth L. Kirchenstein National Research Service Award postdoctoral fellowship provided by NIH (F32GM07782903). We thank E. Shaw for obtaining XPS spectra, G. Henoch for providing the videos in the supporting online material, and Y. Surendranath for many productive discussions.

Supporting Online Material

www.sciencemag.org/cgi/content/full/1162018/DC1
Materials and Methods
Figs. S1 to S4
Movies S1 and S2

19 June 2008; accepted 18 July 2008
Published online 31 July 2008;
10.1126/science.1162018
Include this information when citing this paper.

The Global Atmospheric Circulation on Moist Isentropes

Olivier Pauluis,[1]* Arnaud Czaja,[2] Robert Korty[3]

The global atmospheric circulation transports energy from the equatorial regions to higher latitudes through a poleward flow of high-energy and -entropy parcels and an equatorward flow of air with lower energy and entropy content. Because of its turbulent nature, this circulation can only be described in some averaged sense. Here, we show that the total mass transport by the circulation is twice as large when averaged on moist isentropes than when averaged on dry isentropes. The additional mass transport on moist isentropes corresponds to a poleward flow of warm moist air near Earth's surface that rises into the upper troposphere within mid-latitudes and accounts for up to half of the air in the upper troposphere in polar regions.

Earth absorbs shortwave radiation from the Sun and emits back longwave radiation to space. Although the total amounts of energy received and emitted are about equal, Earth absorbs more energy than it emits in the equatorial regions and emits more energy than it absorbs at high latitudes (*1*). Such imbalance requires an energy transport by the atmosphere and the oceans, with the former responsible for the bulk of the transport in mid-latitudes (*2*). Determining the relationship between the atmospheric energy transport and the global distribution of temperature and humidity is a central question for our understanding of the Earth's climate.

Averaging the global atmospheric circulation usually implies computing a zonal and temporal mean over a sufficiently long period. One of the most common descriptions is the Eulerian mean circulation (*1*), obtained by averaging the flow at constant pressure or geopotential height. The Eulerian mean stream function Ψ_p is defined as

$$\Psi_p(p,\phi) = \frac{1}{\tau}\int_0^\tau \int_0^{2\pi} \int_p^{p_{\mathrm{surf}}} va\cos\phi \frac{dp}{g} d\lambda dt \qquad (1)$$

Here, p is pressure, ϕ is latitude, τ is the time period over which the average is computed, p_{surf} is surface pressure, λ is longitude, a is Earth's radius, v is the meridional velocity, and g is the gravitational acceleration. Figure 1A shows the annual mean stream function on pressure surfaces based on the National Centers for Environmental Prediction–National Center for Atmospheric Research (NCEP-NCAR) Reanalysis monthly data (*3*) from January 1970 to December 2004. The Eulerian-mean circulation exhibits a three-cell structure in each hemisphere: the Hadley cell in the tropics, the Ferrel cell in mid-latitudes, and a polar cell at high latitudes. The Hadley and polar cells, with air parcels moving poleward at high altitude and equatorward at low altitude, are direct circulations that transport energy toward the poles. In the Ferrel cell, the flow is poleward near the surface and equatorward at high altitude. This corresponds to an energy transport toward the equator. Nonetheless, in mid-latitudes, synoptic-scale (~1000 km) eddies transport more energy toward the poles than is brought equatorward by the Ferrel cell, so that the total energy transport in the atmosphere remains poleward.

An alternative to the Eulerian mean circulation is to average the circulation on isentropic surfaces (*4*–*6*). In atmospheric sciences, it is common to use the potential temperature θ instead of entropy. The potential temperature is given by $\theta = \left(\frac{p_0}{p}\right)^{\frac{R}{C_p}} T$, with p the pressure, R the ideal gas constant, C_p the specific heat, T the temperature, and p_0 = 1000 mbar an arbitrary reference pressure. Potential temperature is conserved for reversible adiabatic transformations in the absence of a phase transition, and a surface of constant potential temperature corresponds to isentropic surfaces. The stream function $\Psi_\theta(\theta,\phi)$ on potential temperature surfaces is defined by

$$\Psi_\theta(\theta_0,\phi) = \frac{1}{\tau}\int_0^\tau \int_0^{2\pi} \int_0^{p_{\mathrm{surf}}} H(\theta_0-\theta) va\cos\phi \frac{dp}{g} d\lambda dt \qquad (2)$$

Here, $H(x)$ is the Heavyside function, with $H(x) = 1$ for $x \geq 0$ and $H(x) = 0$ for $x < 0$. Figure 1B shows the annual mean stream function on potential temperature surfaces based on the NCEP-NCAR Reanalysis daily data from January 1970 to December 2004.

In contrast to the Eulerian mean circulation, the circulation in isentropic coordinates exhibits a single overturning cell in each hemisphere. Because the atmosphere is stratified in potential temperature ($\partial_z\theta > 0$), the isentropic circulation corresponds to a poleward flow at upper levels balanced by a return flow near Earth's surface—in the direction opposite to the Eulerian mean circulation (*4*). The meridional mass transport on an isentrope can be written as

$$\overline{\rho_\theta v} = \overline{\rho}_\theta \overline{v} + \overline{\rho_\theta' v'} \qquad (3)$$

[1]Courant Institute of Mathematical Sciences, New York University, 251 Mercer Street, New York, NY 10012, USA. [2]Space and Atmospheric Physics Group, Department of Physics, Imperial College, Huxley Building, Room 726, London SW7 2AZ, UK. [3]Department of Atmospheric Sciences, Texas A&M University, 3150 TAMU, College Station, TX 77843–3150, USA.

*To whom correspondence should be addressed. E-mail: pauluis@cims.nyu.edu

where $\rho_\theta = -g^{-1}\frac{\partial p}{\partial \theta}$ is the isentropic density, the overline indicates a time and zonal average, and the prime a departure from such a temporal and zonal average (i.e., $f' = f - \overline{f}$). The first term on the right-hand side is the mass transport by the zonal and time mean circulation and is in the same direction as the Eulerian mean circulation. The second term is the mass transport by the eddies and dominates the isentropic mass transport in mid-latitudes. This eddy mass transport is similar to the Stoke's drift in shallow water waves (*7*). The circulation on isentropic surfaces is similar to the transformed Eulerian mean circulation in which a residual circulation is computed by accounting for the eddy mass transport (*8*–*10*). Because the potential temperature of an air parcel is approximately conserved in the free troposphere in the absence of condensation, the isentropic circulation is more indicative of the parcel trajectories than the circulation obtained through Eulerian averaging.

A key issue when discussing the isentropic circulation lies in that the entropy of moist air is not uniquely defined (*11*). Indeed, the specific entropy of water vapor can be specified only to within an additive constant. As a consequence, the entropy of moist air can be known only up to this constant multiplied by the water concentration. To test whether this has an impact on the averaged circulation, we computed the circulation by using the equivalent potential temperature, θ_e, to define isentropic surfaces (*11*). The equivalent potential temperature is conserved for reversible adiabatic transformations, including phase transitions. In contrast to the potential temperature, it includes a contribution from the latent heat content of water vapor and can be roughly approximated by $\theta_e \sim \theta + \frac{L_v}{C_p} q$, with L_v the latent heat of vaporization and q the water vapor concentration. Both θ and θ_e define two distinct sets of isentropic surfaces, and correspond to a correct definition of the thermodynamic entropy. We refer here loosely to "dry" isentropes as surfaces of constant potential temperature and to "moist" isentropes as surfaces of constant equivalent potential temperature. The stream function on moist isentropes, $\Psi_{\theta_e}(\theta_e, \phi)$, is defined by

$$\Psi_{\theta_e}(\theta_{e0}, \phi) = \frac{1}{\tau}\int_0^{\tau}\int_0^{2\pi}\int_0^{p_{surf}} H(\theta_{e0} - \theta_e) va \cos\phi \frac{dp}{g} d\lambda dt \quad (4)$$

Figure 1, B and C, compares the stream functions on dry and moist isentropes. Although qualitatively similar, the two circulations differ substantially in that the total mass transport on moist isentropes is approximately twice that on dry isentropes. This difference is present in both hemispheres and throughout the entire year.

The discrepancy between the two circulations can be understood by looking at the joint distribution, $M(\theta_e, \theta)$, of the meridional mass transport at a given latitude ϕ. To obtain this distribution, we sorted the meridional mass flux $a \cos\phi v d\lambda \frac{\delta p}{g}$ by the value of θ and θ_e and integrated over time. Figure 2 shows the joint distribution obtained from the NCEP-NCAR Reanalysis at 40°N during December, January, and February, averaged between 1970 and 2004. By definition, the equivalent potential temperature is larger than the potential temperature, $\theta_e > \theta$, so the distribution is 0 below the diagonal $\theta_e = \theta$. In addition, the water content is roughly proportional to the difference $q \approx \frac{C_p}{L}(\theta_e - \theta)$, so that the further a parcel is above the diagonal, the higher its water content. The maximum amount of water vapor in an air parcel rapidly decreases with temperature due to the Clausius-Clapeyron relationship. The mass transport distribution becomes narrower in the upper-right corner of Fig. 2: This portion of the graph corresponds to upper tropospheric air parcels with low temperature and therefore low water vapor. The stream function at a given latitude Ψ_θ and Ψ_{θ_e} can be obtained by integrating the joint distribution $M(\theta_e, \theta)$ over selected portions of the domain. The mass transport between two dry isentropes θ_1 and θ_2 is given by the integral

$$\Delta\Psi_\theta = \Psi_\theta(\theta_2, \phi) - \Psi_\theta(\theta_1, \phi) = \int_{\theta_1}^{\theta_2}\int_0^{\infty} M(\theta_e, \theta) d\theta_e d\theta \quad (5)$$

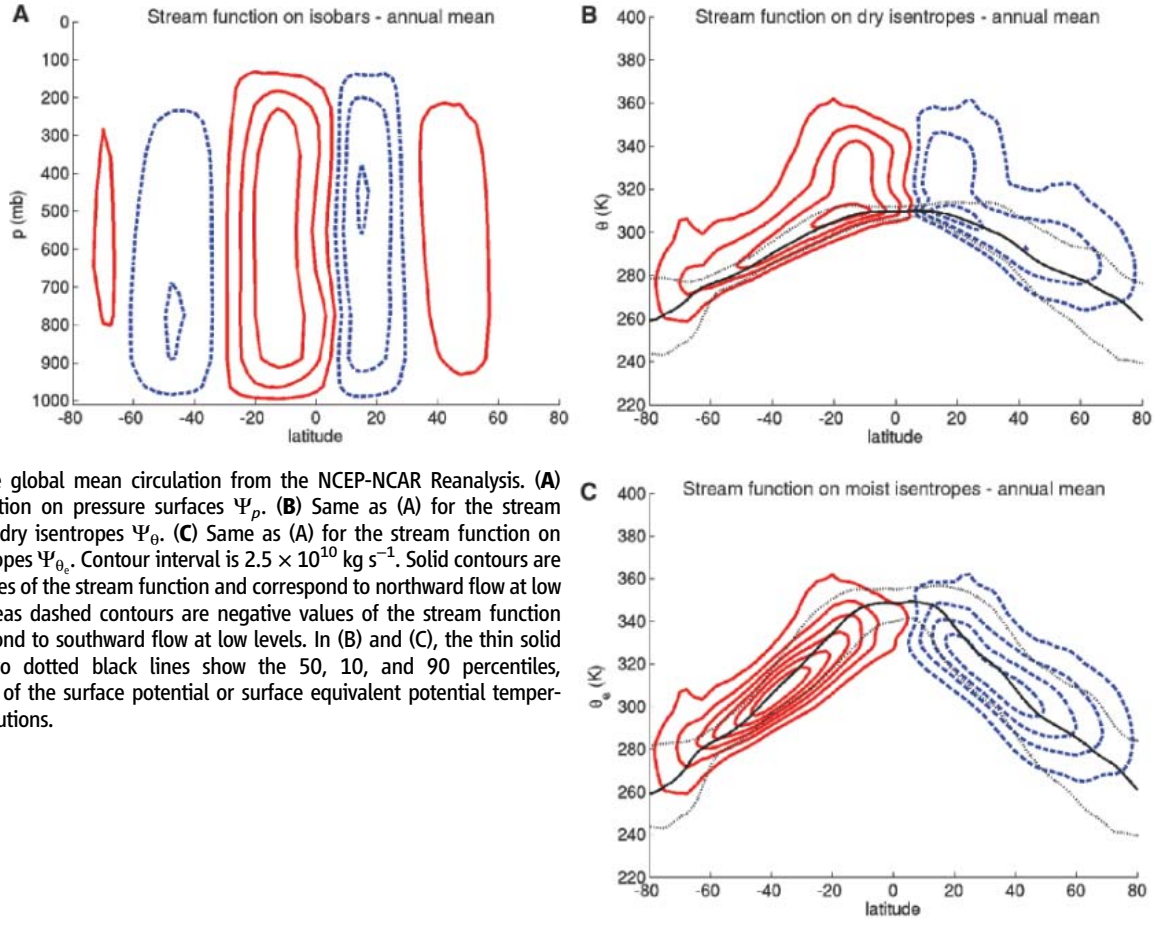

Fig. 1. The global mean circulation from the NCEP-NCAR Reanalysis. (**A**) Stream function on pressure surfaces Ψ_p. (**B**) Same as (A) for the stream function on dry isentropes Ψ_θ. (**C**) Same as (A) for the stream function on moist isentropes Ψ_{θ_e}. Contour interval is 2.5×10^{10} kg s^{-1}. Solid contours are positive values of the stream function and correspond to northward flow at low levels, whereas dashed contours are negative values of the stream function and correspond to southward flow at low levels. In (B) and (C), the thin solid line and two dotted black lines show the 50, 10, and 90 percentiles, respectively, of the surface potential or surface equivalent potential temperature distributions.

Similarly, the mass transport between two moist isentropes θ_{e1} and θ_{e2} is given by the integral

$$\Delta\Psi_{\theta_e} = \Psi_{\theta_e}(\theta_{e2}, \phi) - \Psi_{\theta_e}(\theta_{e1}, \phi) = \int_{\theta_{e1}}^{\theta_{e2}} \int_0^{\infty} M(\theta_e, \theta) d\theta d\theta_e \quad (6)$$

The integral in Eq. 5 is taken between two vertical lines in Fig. 2, whereas the integral in Eq. 6 is taken between two horizontal lines. It is apparent from Fig. 2 that the flow on moist isentropes (corresponding to horizontal lines in the figure) tends to point uniformly either toward the pole (at high values of θ_e) or toward the equator (at low values of θ_e). In contrast, the flow on dry isentropes (corresponding vertical lines) has contributions in both the equatorward and poleward directions. There is thus less cancellation between equatorward and poleward components of the flow when the circulation is integrated on moist isentropes than on dry isentropes, and the mass transport (Eqs. 5 and 6) is larger on moist isentropes than on dry isentropes. Because the equivalent potential temperature better separates poleward and equatorward flows, averaging on moist isentropes includes a larger portion of eddy mass transport into the global circulation.

The difference between the mass transports on dry and moist isentropes can be attributed to the contribution from the upper left quadrant of the distribution shown in Fig. 2. This corresponds to poleward moving air parcels with high θ_e and low θ. The poleward mass transport from this upper left quadrant cancels out with the equatorward flow at low θ and low θ_e when computing the mass transport on dry isentropes but is added to the poleward flow at high θ_e and high θ when computing the circulation on moist isentropes. The low potential temperature of these parcels is typical of the lower troposphere. In Fig. 2, the black contour line shows the values of θ and θ_e found at Earth's surface: This additional mass transport on moist isentropes corresponds to a low-level poleward flow of warm moist air. Its high equivalent potential temperature is indicative of air parcels that are nearly convectively unstable.

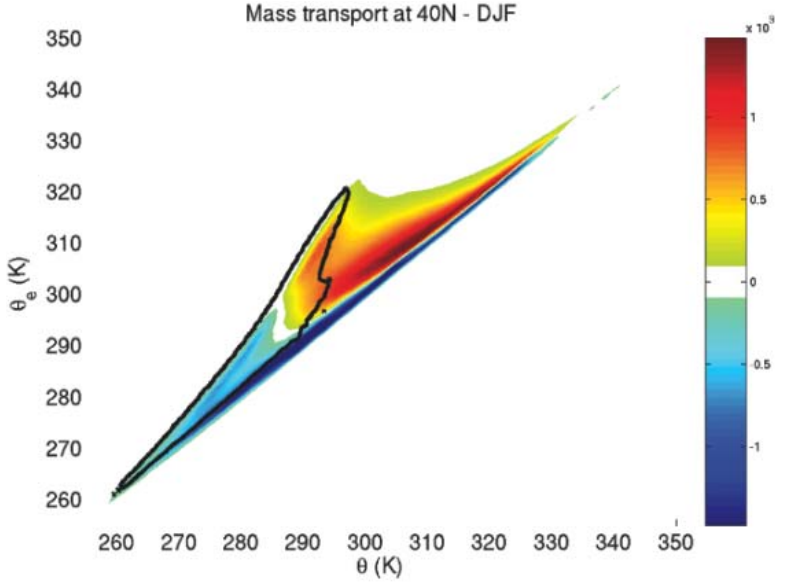

Fig. 2. Joint distribution of the mass transport as a function of θ and θ_e at 40°N during December, January, and February, averaged between 1970 and 2004. The combinations of (θ, θ_e) found within the black contour line have a high probability to be found at Earth's surface at 40°N, defined as having a probability density function larger than 0.001 K^{-2}.

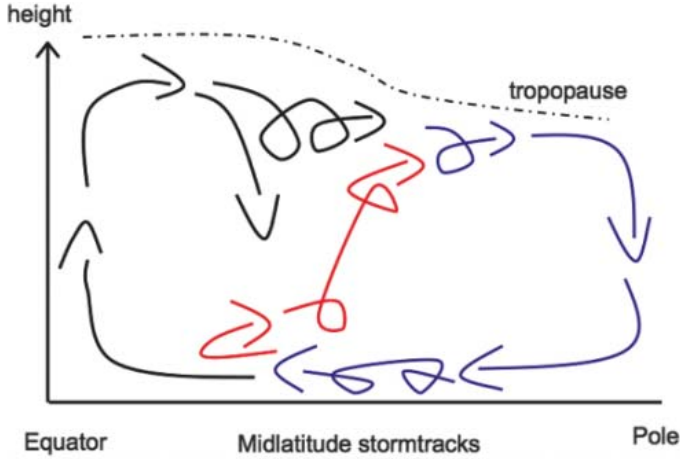

Fig. 3. Schematic representation of the global atmospheric circulation. Black and blue arrows indicate isentropic circulation on dry isentropes, with air rising at the equator, moving poleward in the upper troposphere, and returning equatorward near the surface. Red and blue arrows show the moist branch of the circulation corresponding to the additional mass transport on moist isentropes, with warm moist air moving toward the mid-latitudes at low levels, rising into the upper troposphere within the storm tracks, and subsiding over the pole and dry cold air moving toward the equator near the surface.

On the basis of these findings, we propose a revised description of the global atmospheric circulation in Fig. 3. It includes the previously identified global circulation on dry isentropes (black and blue arrows): Air rises to the upper troposphere within the precipitation zones of the equatorial regions and moves poleward; although some air subsides in the subtropics, the rest is advected poleward across the storm tracks by synoptic eddies, subsides over the poles, and returns equatorward near the surface (*4*, *5*). The additional mass transport found in the moist isentropes is associated with a "moist" branch of the circulation (red and blue arrows) in which low-level warm moist air in the subtropics is advected poleward by synoptic-scale eddies and rises within the storm tracks before subsiding over the poles and returning equatorward near Earth's surface. This moist branch is reminiscent of the Palmén-Newton circulation (*12*, *13*), which stresses the role of ascending warm air in mid-latitude eddies. These two branches of the circulation transport roughly the same amount of air: Half of the air parcels in the polar upper troposphere have risen within the storm tracks, whereas the other half rose within the equatorial regions.

This revised circulation emphasizes the importance of moist processes in mid-latitude dynamics. Although previous studies have noted some impacts of the moist processes on the isentropic circulation (*5*) and the transformed Eulerian mean circulation (*10*) in the mid-latitudes, we have shown that an analysis based on a dry framework systematically underestimates the atmospheric circulation by averaging out the moist branch of the circulation from the total mass transport. The moist branch is closely tied to the latent heat transport, which accounts for roughly half of the poleward energy transports (*2*). Ascent of warm, moist air within the storm tracks occurs through a combination of deep and slantwise convection (*14*, *15*) and results in enhanced precipitation. A key question is to what extent moist processes play an active role in setting the atmospheric lapse rate in mid-latitudes, as has been suggested recently (*16*, *17*). Without fully answering this question, our findings confirm that the circulation provides an ample supply of warm, moist air that should have a direct impact on the temperature structure in the mid-latitudes. As Earth's temperature rises, the amount of water vapor present in the atmosphere is extremely likely to increase as well (*18*). Understanding how changes in temperature and humidity affect the dynamics of the storm tracks and, in particular, the mass transport in the two branches of the cir-

culation is a critical issue for better predicting mid-latitude climate in a warmer world.

References and Notes

1. J. P. Peixoto, A. H. Oort, *Physics of Climate* (AIP Press, Melville, NY, 1992).
2. A. Czaja, J. Marshall, *J. Atmos. Sci.* **63**, 1498 (2006).
3. E. M. Kalnay *et al.*, *Bull. Am. Meteorol. Soc.* **75**, 437 (1996).
4. I. M. Held, T. Schneider, *J. Atmos. Sci.* **56**, 1688 (1999).
5. R. D. Townsend, D. R. Johnson, *J. Atmos. Sci.* **42**, 1565 (1985).
6. D. R. Johnson, *Adv. Geophys.* **31**, 43 (1989).
7. G. Stokes, *Trans. Cambr. Philos. Soc.* **8**, 441 (1847).
8. D. G. Andrews, M. E. McIntyre, *J. Atmos. Sci.* **33**, 2031 (1976).
9. T. Dunkerton, *J. Atmos. Sci.* **35**, 2325 (1978).
10. H. J. Edmon, B. J. Hoskins, M. E. McIntyre, *J. Atmos. Sci.* **37**, 2600 (1980).
11. K. A. Emanuel, *Atmospheric Convection* (Oxford Univ. Press, Oxford, 1994).
12. E. Palmén, *Q. J. R. Meteorol. Soc.* **77**, 337 (1951).
13. E. Palmén, C. W. Newton, *Atmospheric Circulation Systems* (Academic Press, New York, 1969).
14. K. A. Emanuel, *Mon. Weather Rev.* **116**, 1805 (1988).
15. R. L. Korty, T. Schneider, *J. Clim.* **20**, 5977 (2007).
16. M. N. Juckes, *J. Atmos. Sci.* **57**, 3050 (2000).
17. D. M. W. Frierson, I. Held, P. Zurita-Gotor, *J. Atmos. Sci.* **63**, 2548 (2006).
18. I. Held, B. Soden, *J. Clim.* **19**, 5686 (2006).

19. This work was supported by NSF under grant no. ATM-0545047 and grant no. PHY05-51164.

25 April 2008; accepted 8 July 2008
10.1126/science.1159649

Targeting QseC Signaling and Virulence for Antibiotic Development

David A. Rasko,[1]* Cristiano G. Moreira,[1] De Run Li,[2] Nicola C. Reading,[1] Jennifer M. Ritchie,[3] Matthew K. Waldor,[3] Noelle Williams,[2] Ron Taussig,[4] Shuguang Wei,[2] Michael Roth,[2] David T. Hughes,[1] Jason F. Huntley,[1] Maggy W. Fina,[4] John R. Falck,[2,4] Vanessa Sperandio[1,2]†

Many bacterial pathogens rely on a conserved membrane histidine sensor kinase, QseC, to respond to host adrenergic signaling molecules and bacterial signals in order to promote the expression of virulence factors. Using a high-throughput screen, we identified a small molecule, LED209, that inhibits the binding of signals to QseC, preventing its autophosphorylation and consequently inhibiting QseC-mediated activation of virulence gene expression. LED209 is not toxic and does not inhibit pathogen growth; however, this compound markedly inhibits the virulence of several pathogens in vitro and in vivo in animals. Inhibition of signaling offers a strategy for the development of broad-spectrum antimicrobial drugs.

A key challenge for medicine is to develop new drugs against pathogens that are resistant to current antimicrobial agents (*1*, *2*). A promising strategy is to identify agents that inhibit microbial virulence without inhibiting growth, because these present less selective pressure for the generation of resistance (*3*–*5*). Many bacterial pathogens recognize the host environment by sensing and responding to the host adrenergic signaling molecules epinephrine and norepinephrine (NE) in order to promote the expression of virulence factors (*6*, *7*). These pathogens appear to use the same membrane-embedded sensor histidine kinase, QseC (*7*), to recognize both host-derived adrenergic signals and the bacterial aromatic signal autoinducer-3 (AI-3) to activate their virulence genes (*5*, *6*). Upon sensing any of these signaling molecules, QseC autophosphorylates and subsequently phosphorylates a transcription factor, QseB (Fig. 1A) (*7*), which initiates a relay to a complex regulatory cascade and leads to the transcription of key virulence genes (Fig. 1B) (*5*–*8*).

QseC homologs are present in at least 25 important human and plant pathogens (table S1), and *qseC* mutants of enterohemorrhagic *Escherichia coli* (EHEC) (Fig. 1C and fig. S1) (*7*), *Salmonella typhimurium* (Fig. 2A) (*8*), and *Francisella tularensis* (*9*) are attenuated in infected animals. Because of the central role of the AI-3/epinephrine/NE QseC receptor in promoting the virulence of several important pathogens, we tested the effectiveness of inhibitors of this receptor as broad-spectrum antimicrobial agents.

A library of 150,000 small organic molecules from the University of Texas (UT) Southwestern was screened at a 5 μM concentration in a high-throughput assay to identify inhibitors of QseC-dependent virulence gene activation in EHEC (fig. S2) (*10*). The first round of positive hits, which represented a diverse range of molecular architecture, was subjected to additional rounds of screening followed by preliminary evaluations for toxicity against bacterial cells in vitro. This yielded a pool of 75 potential inhibitors with median inhibitory concentration (IC_{50}) values at or below 10^{-5} M. One compound was selected based on its potency as compared with other lead molecules, minimal toxicity toward bacterial and human cell lines, and potential for chemical modification. This molecule was subjected to structure-activity studies to identify ways to improve its potency. The result, LED209 [*N*-phenyl-4-{[(phenylamino) thioxomethyl]amino}-benzenesulfonamide] (Fig. 1D), was prepared in three steps (fig. S3).

New types of antimicrobial agents are needed to treat EHEC infections because treatments based on conventional antibiotics have been associated with worse clinical outcomes (*11*), probably because antibiotics induce an SOS response that enhances EHEC virulence (*12*). The genes encoding Shiga toxin are located within the late genes of a λ bacteriophage (a bacteriaphage that infects bacteria) and are transcribed when the phage enters its lytic cycle upon induction of an SOS response in EHEC (*13*). Shiga toxins are responsible for the morbidity and mortality of these infections. Transcription of EHEC virulence genes is induced by AI-3 and epinephrine. Neither AI-3 nor epinephrine had any effect on promoting virulence in a *qseC* mutant (Fig. 1B).

It was reported (*7*) and we confirmed that purified QseC in a liposome binds to tritiated NE and that phentolamine (an alpha-adrenergic antagonist) antagonizes this binding to block QseC autophosphorylation. In contrast, propranolol (a β-adrenergic antagonist) has no effect on QseC (Fig. 1E). We found that NE binding can be directly antagonized by 5 pM, but not 5 fM, LED209. Autophosphorylation of QseC in response to 50 μM epinephrine is also inhibited in the presence of 5 pM LED209 (Fig. 1F).

Consequently, QseC-dependent virulence gene expression in response to epinephrine (Fig. 1G) and AI-3 (Fig. 1H) was inhibited in the presence of 5 pM LED209. LED209-mediated inhibition of virulence gene expression also inhibited the secretion of EspA and EspB, two proteins encoded within the locus of enterocyte effacement (LEE) that are required for EHEC to translocate bacterial proteins into host cells and cause attaching-effacing (AE) lesions (Fig. 1I). At 5 pM, LED209 abolished EHEC AE lesion formation on cultured epithelial cells (Fig. 1J). Unlike conventional antibiotics, LED209 does not kill or hinder EHEC growth (fig. S4) or trigger the EHEC SOS response. Consequently, it does not promote the expression of Shiga toxin; indeed, it decreases the expression of the *stxAB* genes that encode this toxin (Fig. 1H).

However, administration of LED209 to infant rabbits before, after, or along with EHEC resulted in only a modest (and statistically nonsignificant) reduction in EHEC colonization of the intestine (fig S5). The failure of LED209 to reduce EHEC colonization in this animal may be attributable to rapid absorption from the gastrointestinal (GI) tract (see below and fig. S6). A nonabsorbable formulation may be required for noninvasive human pathogens such as EHEC.

S. typhimurium encodes a homolog of the EHEC QseC (87% similarity) sensor kinase that also controls virulence gene expression (*14*) (Fig. 2C). EHEC and *S. typhimurium* QseC are functionally interchangeable (*14*), and a *S. typhimurium*

[1]Department of Microbiology, University of Texas (UT) Southwestern Medical Center, Dallas, TX 75390, USA. [2]Department of Biochemistry, University of Texas (UT) Southwestern Medical Center, Dallas, TX 75390, USA. [3]Channing Laboratory, Brigham and Women's Hospital, Harvard Medical School, Boston, MA 02115, USA. [4]Department of Pharmacology, University of Texas (UT) Southwestern Medical Center, Dallas, TX 75390, USA.

*Present address: Department of Microbiology and Immunology, University of Maryland School of Medicine, Baltimore, MD 21201, USA.

†To whom correspondence should be addressed. E-mail: vanessa.sperandio@utsouthwestern.edu

qseC mutant was found to be defective for colonization of the swine GI tract (*8*) and attenuated for systemic disease in mice (Fig. 2A). LED209 [20 mg per kilogram of body weight (mg/kg)] was given orally to mice 3 hours before and 3 hours after intraperitoneal injection of a lethal dose of *S. typhimurium.* Twenty-four hours after infection, only 30% of untreated mice remained alive, whereas 80% of the LED209-treated mice were still alive (Fig. 2A). All the *S. typhimurium*–infected mice died within 72 hours of infection, and 20% of LED209-treated mice survived up to 12 days (Fig. 2A and fig. S7). Even though LED209 did not influence *S. typhimurium* growth in vitro (fig. S4), ~10 times fewer *S. typhimurium* colony-forming units (CFUs) were recovered from the spleens and livers of treated animals (Fig. 2B). Addition of LED209 to cultures in vitro diminished expression of the *sifA* virulence gene (Fig. 2D), which is important for the development of systemic disease by *S. typhimurium* (*15*). Transcription of *sifA* is activated by NE in a QseC-dependent manner (Fig. 2C). Together, these observations suggest that LED209 inhibition of *S. typhimurium* virulence gene expression in vivo compromises the survival of the pathogen in the host.

F. tularensis has one histidine sensor kinase, QseC (57% similarity), encoded in its genome, and a *qseC* mutant is attenuated for mouse infection (*9*). The *F. tularensis* and EHEC QseC proteins are also functionally interchangeable, and the *F. tularensis* QseC can rescue expression of a QseC-dependent gene in an *E. coli qseC* mutant (Fig. 2E). LED209 reduced 10-fold the amount of *F. tularensis* strain SCHU-S4 recovered from macrophages (Fig. 2F). Furthermore, LED209 decreased the expression of several *F. tularensis* virulence genes in vitro (Fig. 2G), including *qseC* itself. Quantitative real-time fluorescence polymerase chain reaction (QPCR) assays demonstrated that *qseC* expression is up-regulated during infection of mice by SCHU-S4 (Fig. 2H). LED209 was administered orally in a single dose 3 hours after infection with SCHU-S4. Although 80% of LED209-treated mice remained alive 9 days after infection, only 10% of the untreated mice survived to this point (Fig. 2I). Thus, a single oral dose of LED209 can protect mice already exposed to aerosolized *F. tularensis.* There was no overt toxicity of the LED209, and none of the mice treated with LED209 alone died (Fig. 2I).

Because LED209 blocks epinephrine- and NE-triggering of QseC-mediated activation of virulence gene expression, we were concerned that this compound might also interfere with adrenergic signaling systems in the host. Using

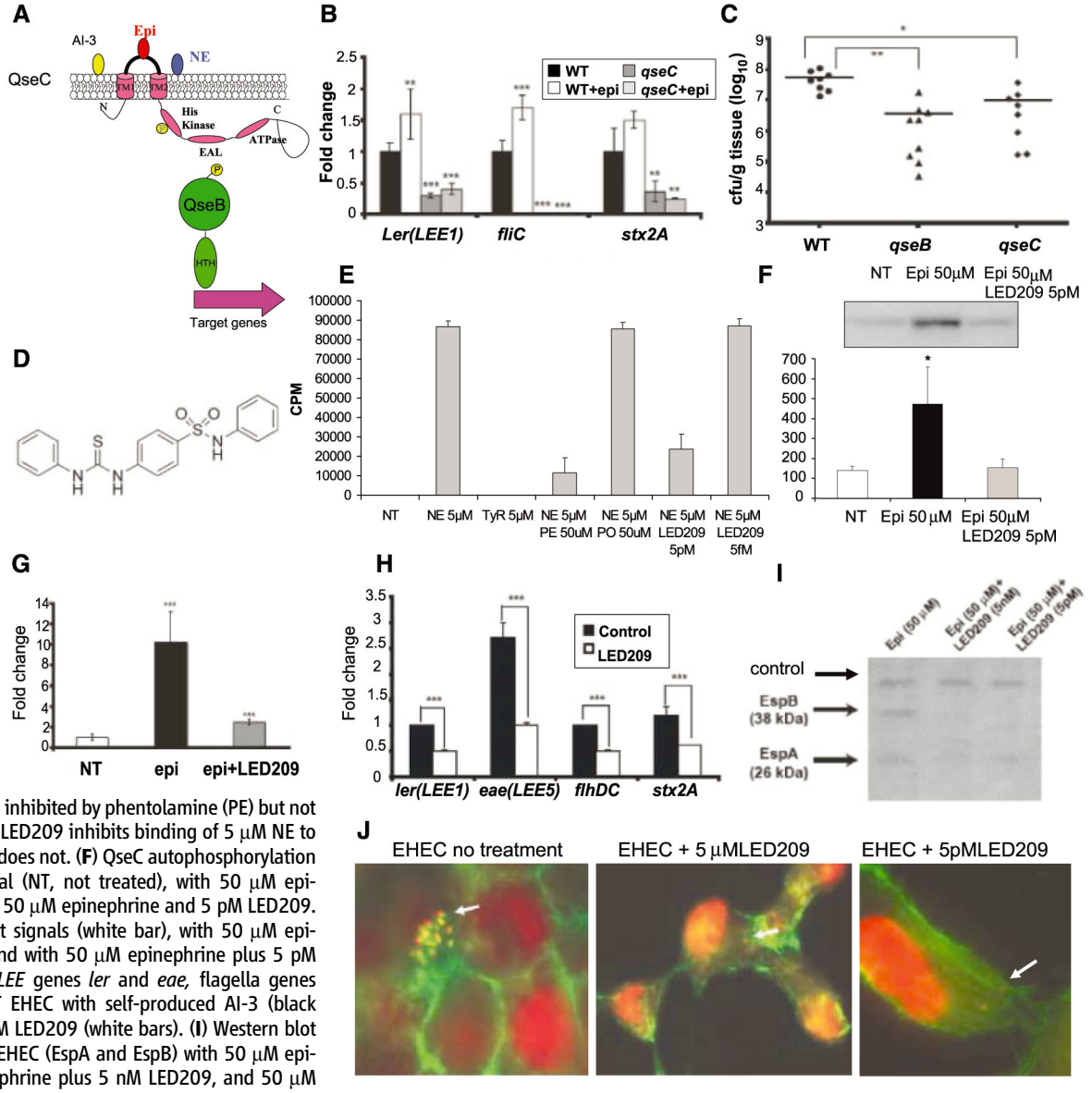

Fig. 1. LED209 inhibits EHEC virulence traits in vitro. (**A**) Schematic of the autophosphorylation of QseC in response to signals and phosphotransfer to QseB. (**B**) QPCR of *LEE1* gene *ler*, *fliC*, and *stx2A* in wild-type (WT) EHEC with self-produced AI-3 (black bars) and AI-3 plus 50 μM epinephrine (white bars), and the *qseC* mutant with self-produced AI-3 (dark gray bars) and AI-3 plus 50 μM epinephrine (light gray bars). (**C**) Colonization of the colon of infant rabbits by WT EHEC, the *qseC* and *qseB* mutants (CFUs/gram of tissue). (**D**) Chemical structure of LED209. (**E**) Binding of QseC to 5 μM tritiated NE and to 5 μM tyrosine (tyrosine is a negative control, not a signal to QseC). Binding of NE to QseC is inhibited by phentolamine (PE) but not propranolol (PO); 5 pM LED209 inhibits binding of 5 μM NE to QseC, but 5 fM LED209 does not. (**F**) QseC autophosphorylation in the absence of signal (NT, not treated), with 50 μM epinephrine (Epi) and with 50 μM epinephrine and 5 pM LED209. (**G**) QPCR of *ler* without signals (white bar), with 50 μM epinephrine (black bar), and with 50 μM epinephrine plus 5 pM LED209. (**H**) QPCR of *LEE* genes *ler* and *eae,* flagella genes *flhDC* and *stx2A* in WT EHEC with self-produced AI-3 (black bars) and AI-3 plus 5 pM LED209 (white bars). (**I**) Western blot of secreted proteins of EHEC (EspA and EspB) with 50 μM epinephrine, 50 μM epinephrine plus 5 nM LED209, and 50 μM epinephrine plus 5 pM LED209 (cross-reactive band as loading control). (**J**) Inhibition of the AE lesions by LED209 (5 μM and 5 pM). Cell nuclei and bacterial cells are stained red (propidium iodide) and the cytoskeleton is stained green (fluorescein isothiocyanate–phalloidin). EHEC forms AE lesions atop the green-stained pedestals. There are no pedestals with LED209. * $P < 0.05$; ** $P < 0.001$; *** $P < 0.0001$.

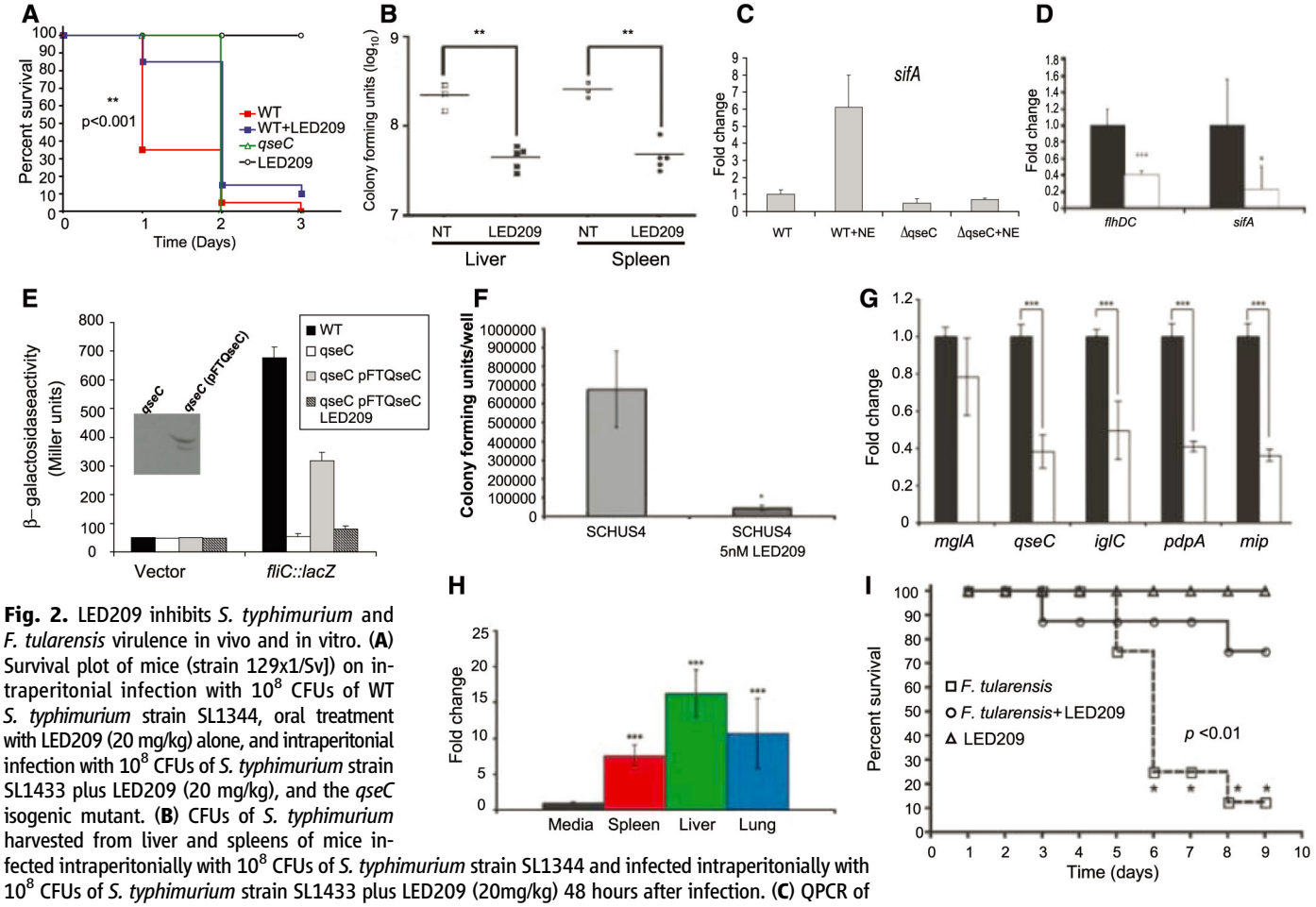

Fig. 2. LED209 inhibits *S. typhimurium* and *F. tularensis* virulence in vivo and in vitro. (**A**) Survival plot of mice (strain 129x1/Sv]) on intraperitonial infection with 10^8 CFUs of WT *S. typhimurium* strain SL1344, oral treatment with LED209 (20 mg/kg) alone, and intraperitonial infection with 10^8 CFUs of *S. typhimurium* strain SL1433 plus LED209 (20 mg/kg), and the *qseC* isogenic mutant. (**B**) CFUs of *S. typhimurium* harvested from liver and spleens of mice infected intraperitonially with 10^8 CFUs of *S. typhimurium* strain SL1344 and infected intraperitonially with 10^8 CFUs of *S. typhimurium* strain SL1433 plus LED209 (20mg/kg) 48 hours after infection. (**C**) QPCR of *sifA* in vitro in WT and a *qseC* mutant (Δ*qseC*) of *S. typhimurium* in the absence and presence of NE (50 μM). (**D**) QPCR of expression of the flagella regulator (*flhDC*) and *sifA* in vitro in the absence (black bars) and presence (5 pM) of LED209 (white bars). (**E**) The *E. coli fliC::lacZ* fusion was introduced into WT *E. coli*, the *qseC E. coli* mutant, and the *qseC E. coli* mutant complemented with *F. tularensis qseC* (*qseC* pFTQseC) in the absence and presence (5 pM) of LED209. The *F. tularensis* QseC was his-tagged and the inset shows that the *F. tularensis* QseC is expressed in the *E. coli qseC* mutant. (**F**) Infection of J774 murine macrophages with *F. tularensis* SCHU S4 in the absence and presence (5 nM) of LED209. (**G**) QPCR of *F. tularensis* virulence genes in the absence (gray bars) and presence (white bars) of LED209 (5 pM). (**H**) QPCR measuring expression of *qseC* in SCHU S4 during growth in vitro and in vivo (spleen, liver, and lungs). These data were collected from five C3H HeN mice intranasally infected with 30 CFUs of SCHU S4. QPCR of *qseC* was normalized against *rpoA*. (**I**) Survival plot of mice (C3H HeN) upon oral treatment with LED209 (20 mg/kg) alone, intranasal infection with 30 CFUs of SCHU S4, and intranasal infection with 30 CFUs of SCHU S4 plus LED209 (20 mg/kg). * $P < 0.01$; ** $P < 0.001$; *** $P < 0.0001$.

live cell-based assays (*16*), we showed that LED209 did not influence signaling through human β-adrenergic receptor isoforms (fig. S6). Pharmacokinetic studies suggested that there are no inherent structural features that might limit its bioavailability or biocompatibility and revealed that LED209 is approximately 70% bioavailable when administered orally to mice (fig. S6). Moreover, studies of LED209 in mice did not reveal any evidence of toxicity (figs. S8 to S10).

Bacterial histidine sensor kinases, such as QseC, should make attractive drug targets because mammals lack this class of signal-transduction molecules (*17*, *18*). Because *qseC* is present in many important animal and plant pathogens, drugs that target this sensor kinase have the potential to have a broad spectrum. Because the QseC-dependent interkingdom-signaling system does not directly influence bacterial growth, inhibition of this signaling pathway may not exert a strong selective pressure for the development of resistance.

References and Notes

1. S. B. Levy, B. Marshall, *Nat. Med.* **10**, S122 (2004).
2. S. R. Palumbi, *Science* **293**, 1786 (2001).
3. D. T. Hung, E. A. Shakhnovich, E. Pierson, J. J. Mekalanos, *Science* **310**, 670 (2005).
4. L. Cegelski, G. R. Marshall, G. R. Eldridge, S. J. Hultgren, *Nat. Rev. Microbiol.* **6**, 17 (2008).
5. D. T. Hughes, V. Sperandio, *Nat. Rev. Microbiol.* **6**, 111 (2008).
6. V. Sperandio, A. G. Torres, B. Jarvis, J. P. Nataro, J. B. Kaper, *Proc. Natl. Acad. Sci. U.S.A.* **100**, 8951 (2003).
7. M. B. Clarke, D. T. Hughes, C. Zhu, E. C. Boedeker, V. Sperandio, *Proc. Natl. Acad. Sci. U.S.A.* **103** (27), 10420 (2006).
8. B. L. Bearson, S. M. Bearson, *Microb. Pathog.* **44**, 271 (2008).
9. D. S. Weiss *et al.*, *Proc. Natl. Acad. Sci. U.S.A.* **104**, 6037 (2007).
10. Materials and methods are available as supporting material on *Science* Online.
11. P. I. Tarr, H. M. Tsai, W. L. Chandler, *N. Engl. J. Med.* **347**, 2171 (2002).
12. X. Zhang *et al.*, *J. Infect. Dis.* **181**, 664 (2000).
13. P. L. Wagner *et al.*, *J. Bacteriol.* **183**, 2081 (2001).
14. M. Merighi, A. Carroll-Portillo, A. N. Septer, A. Bhatiya, J. S. Gunn, *J. Bacteriol.* **188**, 141 (2006).
15. C. R. Beuzon *et al.*, *EMBO J.* **19**, 3235 (2000).
16. L. I. Jiang *et al.*, *J. Biol. Chem.* **282**, 10576 (2007).
17. G. J. Lyon, T. W. Muir, *Chem. Biol.* **10**, 1007 (2003).
18. S. Roychoudhury *et al.*, *Proc. Natl. Acad. Sci. U.S.A.* **90**, 965 (1993).

19. We thank M. V. Norgard, E. Vitetta, V. Miller, and S. L. McKnight for comments and J. Richardson for pathological review of tissues from LED209-treated mice. This work was supported by NIH grants RO3 NS053582, RO1 AI053067, RO1 GM31278, PO1-AI055637-03, UO1-AI77853, and R21 AI067827; the Ellison Medical Foundation; the Burroughs Wellcome Fund; the Robert A. Welch Foundation; and a High Impact High Risk grant from UT Southwestern Medical Center. M.K.W. is a Howard Hughes Medical Institute investigator. This work yielded the provisional patent application UTSD:1854USP1.

Supporting Online Material

www.sciencemag.org/cgi/content/full/321/5892/1078/DC1
Materials and Methods
Figs. S1 to S11
Tables S1 and S2
References

12 May 2008; accepted 26 June 2008
10.1126/science.1160354

Variability and Robustness in T Cell Activation from Regulated Heterogeneity in Protein Levels

Ofer Feinerman,[1]* Joël Veiga,[1]* Jeffrey R. Dorfman,[1]†
Ronald N. Germain,[2] Grégoire Altan-Bonnet[1]‡

In T cells, the stochasticity of protein expression could contribute to the useful diversification of biological functions within a clonal population or interfere with accurate antigen discrimination. Combining computer modeling and single-cell measurements, we examined how endogenous variation in the expression levels of signaling proteins might affect antigen responsiveness during T cell activation. We found that the CD8 co-receptor fine-tunes activation thresholds, whereas the soluble hematopoietic phosphatase 1 (SHP-1) digitally regulates cell responsiveness. Stochastic variation in the expression of these proteins generates substantial diversity of activation within a clonal population of T cells, but co-regulation of CD8 and SHP-1 levels ultimately limits this very diversity. These findings reveal how eukaryotic cells can draw on regulated variation in gene expression to achieve phenotypic variability in a controlled manner.

In biological systems, the stochasticity of protein expression can contribute to useful phenotypic variability within a clonal population (*1*), yet it also may compromise the reliability of a cellular response. How cells achieve robust physiological performance while experiencing substantial variation in the expression of molecules that control their functional activities has yet to be fully explained (*2*). Theoretical and experimental studies at the single-cell level have described the nature and origin of fluctuations in gene and protein expression (*3*–*7*) and have identified key molecular components controlling phenotypic variability. Most of these have been conducted on single-celled organisms, focusing on bacterial chemotaxis and competence (*8*–*10*).

Understanding the consequences of variation in protein expression is especially relevant for T lymphocyte activation in the immune system. Confrontation of these cells with foreign and self-ligands that bind their receptors initiates a signaling-based decision between productive activation and tolerance (*11*). Reliability of this process is critical for the proper functioning of the immune system and avoidance of autoimmunity (*12*). Nevertheless, ligand discrimination must also be flexible during T cell development (*13*) and diverse to allow differentiation between short-lived effector cells and long-lived memory cells during antigen-induced signaling responses (*14*, *15*). We examined how differences in protein expression within a clonal population might affect these dual features of robust and yet adaptable T cell responses to antigenic ligands.

We first theoretically tested how the natural variability in signaling-components expression within T cells might affect their response. To this end, a previously established computer model of T cell activation (*16*–*19*) was used, in which kinetic proofreading, enforced by two competing signaling feedback loops, accounts for sharp ligand discrimination (Fig. 1A). Signal transduction by the T cell receptor (TCR) of cytotoxic T cells is initiated when the co-receptor CD8 co-associates with TCRs engaged with their ligands [peptide-bound major histocompatability complex class I (pMHC) molecules]. Negative feedback, associated with the soluble hematopoietic phosphatase 1 (SHP-1), limits spurious stimulation by ligands that have weak affinity to the TCR (*20*). Positive feedback, involving the activation of the extracellular signal–regulated kinase 1 (ERK-1), maintains strong signaling if the cell is confronted with more strongly binding ligands (*20*). Because ERK-1 activation is digital ("all or none") in T cells (*19*), we defined the half-maximal effective concentration EC_{50} as the minimal number of ligands able to trigger phosphorylation of ERK-1 into ERK-pTpY (ppERK) in 50% of the cells. Our model predicts that EC_{50} is sharply dependent on the lifetime of the TCR-pMHC complex (Fig. 1B).

This model was then probed to examine how variability in the expression of signaling components might affect the T cell's response to antigen

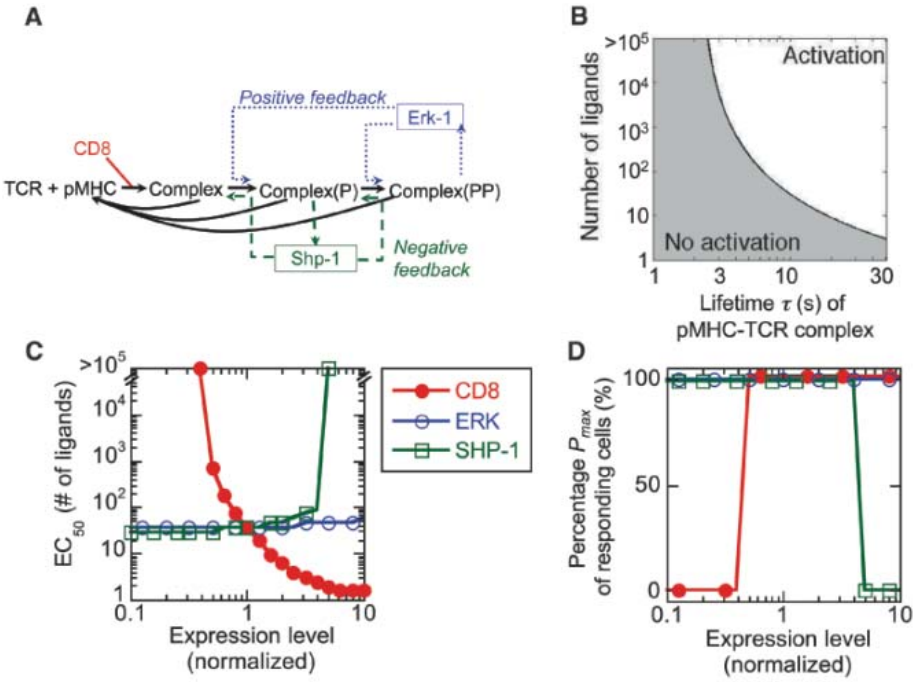

Fig. 1. Computational model of T cell activation links heterogeneity in protein expression with variability in cell response. (**A**) Model of proximal T cell signaling involved in ligand discrimination. (**B**) Predictions of digital ERK activation by different numbers of pMHC ligands, with varied lifetimes τ of interaction with TCR. We define activation as 100% of ERK becoming doubly phosphorylated and inactivation as no doubly phosphorylated ERK. The dependence of EC_{50} on τ is delineated by the black curve. (**C** and **D**) Predictions for the effect of varied expression of proteins on EC_{50} and on the percentage P_{max} of cells responding with $EC_{50} < 10^5$ (for an agonist ligand with $\tau = 10$ s; see fig. S8 for other ligands). Expression levels of proteins are normalized to the average wild-type level.

[1]ImmunoDynamics Group, Program in Computational Biology and Immunology, Memorial Sloan-Kettering Cancer Center, 1275 York Avenue, Box 460, New York, NY 10065, USA. [2]Lymphocyte Biology Section, Laboratory of Immunology, Program in Systems Immunology and Infectious Disease Modeling, National Institute of Allergy and Infectious Diseases, National Institutes of Health, Department of Health and Human Services, Building 10, Room 11N311, 10 Center Drive, MSC-1892, Bethesda, MD 20892-1892, USA.

*These authors contributed equally to this work.
†Present address: Seattle Biomedical Research Institute, 307 Westlake Avenue N, Suite 500, Seattle, WA 98109-5219, USA.
‡To whom correspondence should be addressed. E-mail: altanbonnet@cbio.mskcc.org

(*21*), revealing that signaling components would fall into three categories: noncritical components, defined as signaling proteins whose variation in expression within the observed range does not measurably affect ligand response; analog regulators, which are signaling proteins whose level of expression fine-tunes EC_{50}; and digital regulators, whose level of expression switches a cell between responsive and unresponsive states (among responsive cells, the level of digital regulator does not affect the EC_{50}).

Despite its key role in regulating ligand discrimination, our model predicted ERK-1 to be a noncritical regulator because its average expression is in excess, so that variation within the physiological range would not affect the T cell's response (Fig. 1C). The CD8 co-receptor was predicted by the model to be an analog regulator (Fig. 1C): Higher levels of expression of CD8 considerably decrease the minimum number of ligands required for effective activation, without affecting the percentage of cells that can respond to the maximum dose of ligands (P_{max}). In contrast, the model predicted that SHP-1 would be a digital regulator. Thus, below a critical level (four times above the average level of SHP-1), the TCR signaling network responds consistently to strong agonists, with little variation in activation threshold EC_{50} (Fig. 1C). However, in cases where SHP-1 exceeds the critical level, the EC_{50} for the signaling network becomes infinite, and P_{max} becomes null (Fig. 1D). This means that, as SHP-1 levels increase, an increasing fraction of T cells becomes unresponsive to any physiologically relevant amount of ligands, whereas the other cells remain as sensitive as cells expressing low levels of SHP-1.

Simple mechanisms can explain how CD8 and SHP-1 differently regulate TCR signaling. Because Lck, a kinase associated with the CD8 co-receptor, directly phosphorylates antigen-engaged TCRs, lower levels of CD8 may be compensated for by increased ligand availability, leading to analog regulation. In contrast, at a low level of SHP-1, ligands fail to activate enough of that phosphatase to prevent an early digital ERK response that, in turn, protects TCRs from dephosphorylation by SHP-1. This makes the precise level of SHP-1 irrelevant under these conditions. At higher levels of SHP-1, negative feedback associated with phosphatase activity rapidly affects enough TCRs to prevent ERK activation and suppress effective signaling: The cells become unresponsive to any level of ligand. In combination, these latter effects lead to digital regulation within the T cell population.

To test these predictions, we used a quantitative assessment of protein expression in individual cells, based on antibody staining and flow cytometry (figs. S1 to S4). We studied OT-1 TCR-transgenic Rag1 knockout $CD8^+$ T cell clones, which are cells that express only a single TCR specific for the ovalbumin peptide (residues 257 to 264) bound to the class I molecule K^b (K^b/OVA) pMHC (*13*). For these cells, the distributions of expression for CD8, ERK-1, and SHP-1 were log-normal, with coefficients of variations equal to 0.32, 0.56, and 0.62, respectively (Fig. 2A). Thus, 99% of cells express CD8 within a threefold range of one another, and ERK-1 and SHP-1 within a sixfold range. The large range in expression levels of these key signaling components, in conjunction with our computer predictions of response variability (Fig. 1, C and D), raised the possibility that a clonal population of T cells would not respond homogeneously to antigen stimulation.

To examine this, multiparameter flow cytometry was used to simultaneously analyze individual cells for both endogenous protein expression and the TCR signaling response to antigen. Ligand response was measured by intracellular antibody staining for ppERK (*22*) 5 min after stimulation by peptide-pulsed antigen-presenting cells (*4*–*7*, *21*). Consistent with our model's predictions, variations in the levels of CD8, ERK-1, and SHP-1 were found to have substantially different effects on T cell responsiveness (Fig. 2B and fig. S6). CD8 functioned as a positive analog regulator, such that subpopulations with varied CD8 levels displayed different EC_{50} but had nearly equal P_{max} (Fig. 2B). A sixfold difference in membrane CD8 expression was associated with a 100-fold change in EC_{50} (Fig. 2C and fig. S5). Our model predicted that very low CD8 levels would reduce P_{max}, although this would occur only beyond the normal physiological range of CD8 expression (Figs. 1C and 2A). SHP-1 acted as a negative digital regulator, again consistently with the predictions of the model: Subpopulations with varied levels of SHP-1 expression had different P_{max}, whereas the responsive fractions had the same EC_{50} (Fig. 2C). A twofold increase in SHP-1 levels was associated with a 2.5-fold decrease in P_{max} (Fig. 2D). In contrast to CD8 and SHP-1, and also in agreement with the simulations, variation in ERK-1 expression only marginally affected the T cell

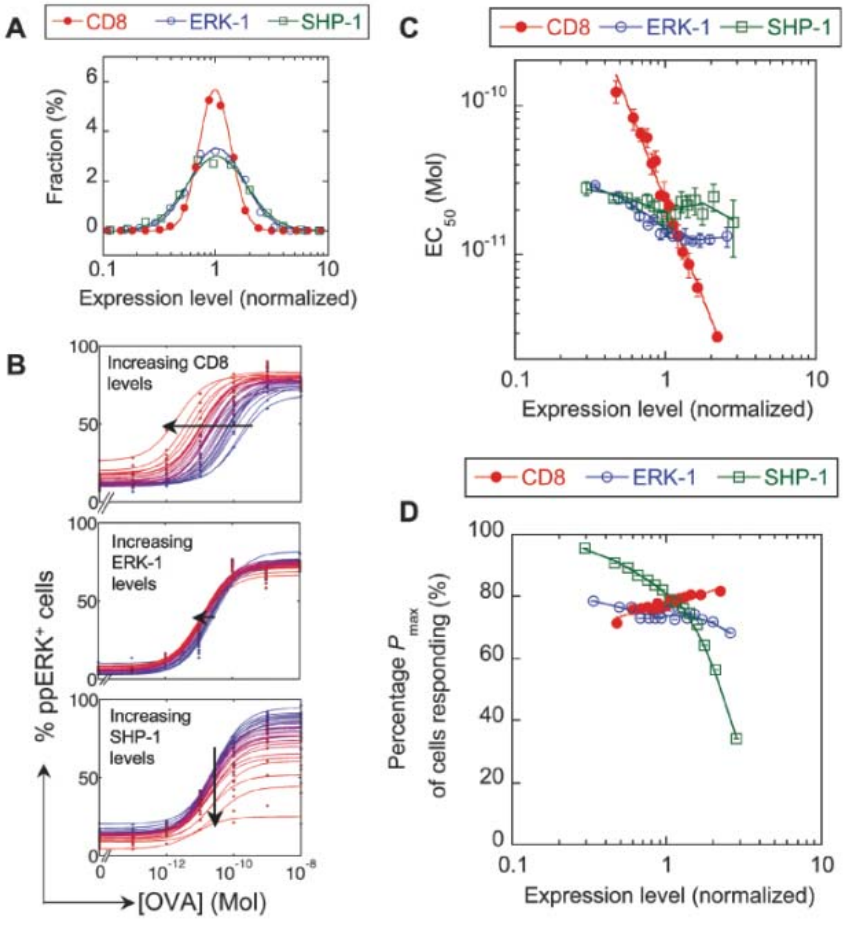

Fig. 2. Experimental single-cell analysis classifies CD8, ERK-1, and SHP-1 as analog, noncritical, and digital regulators of the T cell response, respectively. (**A**) Distribution of endogenous levels of these signaling proteins in OT-1 T lymphocytes. (**B**) Single-cell analysis of OT-1 T cell responses to varying concentrations of OVA peptide at different levels of expressions of CD8, ERK-1, and SHP-1 (blue, low levels; red, high levels). (**C**) EC_{50} and (**D**) P_{max} of different levels of signaling proteins, obtained by fitting the curves in (B). The solid lines are eye guides. Error bars are SEs for triplicate samples.

response in terms of either EC_{50} or P_{max} (Fig. 2, C and D).

These observations demonstrate that a clonal population of T cells can display substantial phenotypic variability based on stochastic variation in the expression of signaling proteins (here, CD8 and SHP-1). In contrast, experimental measurements of interferon-γ (*23*), calcium (*24*), or ppERK (*19*) responses suggest that the T cell antigen response can in some circumstances be highly uniform (robust) within a clonal population. We then identified two different mechanisms, associated with the different categories of signaling components, which enforce such robustness despite stochasticity in protein expression. Digital regulators such as SHP-1 maintain constant EC_{50} but at the expense of a fraction of cells made unresponsive (Fig. 2D), a parameter not often examined in published studies. Analog regulators modulate the cell's responsiveness in a sensitive manner, so their variability in expression levels must be constrained to limit variability in response (*6*, *7*), and this is seen for CD8 (Fig. 2, A and C).

We also considered a third, less obvious, constraint mechanism, based on recent evidence for covariation in gene expression among components in functional networks (*7*, *9*). The contradictory effects of positive and negative modulators might cancel out if their expression levels were co-regulated, reducing response variation in the population. To examine this hypothesis, we examined computer-modeled responses for the effects of varying levels of both CD8 and SHP-1 (Fig. 3A). These analyses revealed that, for any increase of SHP-1 level, there is a corresponding increased CD8 level that maintains a constant EC_{50} (Fig. 3A), which implies that co-regulation of SHP-1 and CD8 expression would limit the diversity of T cell activation.

To explore this prediction experimentally, we analyzed the ppERK dose-response for different CD8 and SHP-1 levels in individual OT-1 T cell blasts and found a good match with our computer simulations (Fig. 3B). Moreover, our analyses revealed that T cell blasts co-regulate their CD8 and SHP-1 levels (Fig. 3C). To quantify how this correlation might limit response functional diversity, we estimated the distribution of EC_{50} by integrating over the distribution of CD8 and SHP-1 levels (Fig. 3, B and C) (*21*). For the natural distribution of signaling proteins (Fig. 3D, left), we found that the resulting distribution of EC_{50} was log-normal with a coefficient of variation of 5.0 (fig. S9). For a hypothetical distribution of CD8 and SHP-1, with the same individual distributions but without co-regulation (Fig. 3D, right), the distribution of EC_{50} would also be log-normal but with a larger coefficient of variation of 18 (fig. S9). In other words, the actual fraction of hyperresponsive OT-1 T cell blasts whose EC_{50} is below 0.1 pM is 0.03%, but this fraction would be predicted to be 10-fold higher (0.3%) without co-regulation of CD8 and SHP-1 levels (Fig. 3D, arrows). Thus, co-regulation decreases the number of hyperresponsive cells and potentially limits the risk of self-responsiveness and autoimmune activation among T cells. Several nonexclusive mechanisms—including gene locus colocalization (*4*), control of transcription by shared factors, and the targeting of transcripts by the same microRNA—may account for this co-regulated expression and will require further analysis to elucidate.

This study predicted theoretically and confirmed experimentally that signaling molecules within a network can have qualitatively distinct effects on cell responsiveness. It also revealed that intraclonal differences in protein expression generate dispersion in responsiveness among individual cells, and demonstrated how co-regulation of expression among these proteins limits this phenotypic variability. For T lymphocytes, these insights help explain how ligand discrimination can be tuned through the regulation of signaling components (*13*, *24*) and diversified (*14*) so that pathogen reactivity is preserved without encouraging autoimmunity. More generally, these observations suggest how cells may leverage regulated stochasticity of intracellular processes to generate controlled variability in physiological performance.

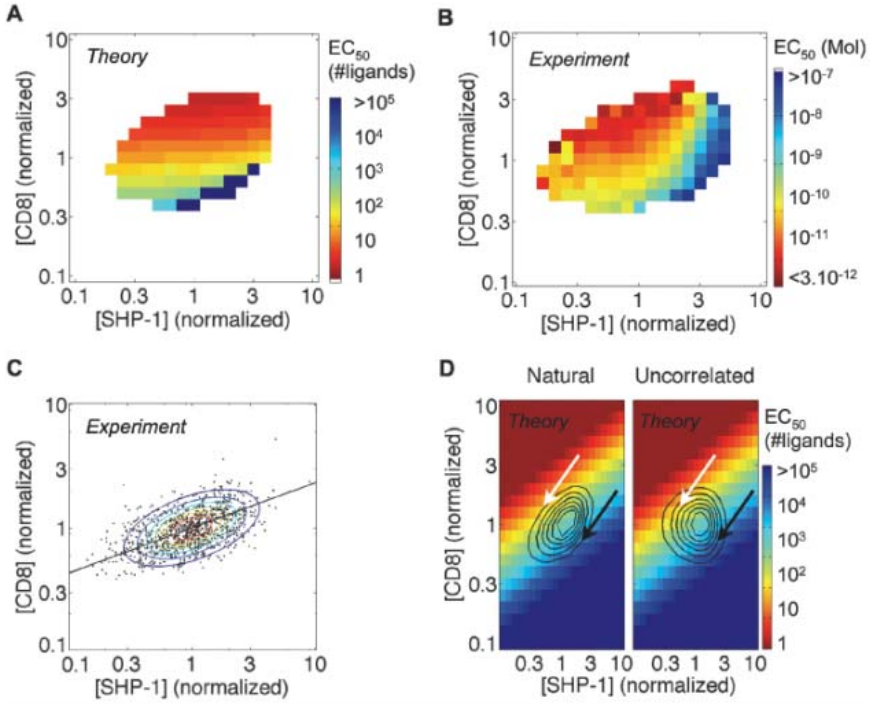

Fig. 3. Covariation of CD8 and SHP-1 levels limits the frequencies of hypo- and hyperresponsive cells. Computer model (**A**) and single-cell experimental measurements (**B**) for T cell activation demonstrate how the EC_{50} for ppERK responsiveness is determined by both CD8 and SHP-1 levels. (**C**) Single-cell analysis of OT-1 T cell blasts shows a correlation between the expression of SHP-1 and CD8. The line is the fit log([CD8]) = 0.4 × log([SHP-1]). (**D**) Overlay of a fitted color map of EC_{50} with the contour plot of the distribution of the levels of CD8 and SHP-1 (left, the endogenous/co-regulated population; right, a theoretical population with uncorrelated levels of CD8 and SHP-1 keeping their individual measured distributions). CD8/SHP-1 co-regulation limits the number of hypo- and hyperresponsive cells (indicated by black and white arrows, respectively).

References and Notes

1. M. Kaern, T. C. Elston, W. J. Blake, J. J. Collins, *Nat. Rev. Genet.* **6**, 451 (2005).
2. N. Barkai, S. Leibler, *Nature* **387**, 913 (1997).
3. M. B. Elowitz, A. J. Levine, E. D. Siggia, P. S. Swain, *Science* **297**, 1183 (2002).
4. A. Becskei, B. B. Kaufmann, A. van Oudenaarden, *Nat. Genet.* **37**, 937 (2005).
5. J. R. Newman *et al.*, *Nature* **441**, 840 (2006).
6. A. Bar-Even *et al.*, *Nat. Genet.* **38**, 636 (2006).
7. A. Sigal *et al.*, *Nature* **444**, 643 (2006).
8. E. Korobkova, T. Emonet, J. M. Vilar, T. S. Shimizu, P. Cluzel, *Nature* **428**, 574 (2004).
9. M. Kollmann, L. Lovdok, K. Bartholome, J. Timmer, V. Sourjik, *Nature* **438**, 504 (2005).
10. G. M. Suel, R. P. Kulkarni, J. Dworkin, J. Garcia-Ojalvo, M. B. Elowitz, *Science* **315**, 1716 (2007).
11. M. M. Davis *et al.*, *Annu. Rev. Immunol.* **25**, 681 (2007).
12. R. N. Germain, *Science* **293**, 240 (2001).
13. K. A. Hogquist *et al.*, *Cell* **76**, 17 (1994).
14. J. T. Chang *et al.*, *Science* **315**, 1687 (2007).
15. C. Stemberger *et al.*, *Immunity* **27**, 985 (2007).
16. R. N. Germain, I. Stefanova, *Annu. Rev. Immunol.* **17**, 467 (1999).
17. S. Y. Qi, J. T. Groves, A. K. Chakraborty, *Proc. Natl. Acad. Sci. U.S.A.* **98**, 6548 (2001).
18. I. Stefanova *et al.*, *Nat. Immunol.* **4**, 248 (2003).
19. G. Altan-Bonnet, R. N. Germain, *PLoS Biol.* **3**, e356 (2005).
20. O. Feinerman, R. N. Germain, G. Altan-Bonnet, *Mol. Immunol.* **45**, 619 (2008).
21. Materials and methods are available as supporting material on *Science* Online.

22. J. M. Irish *et al.*, *Cell* **118**, 217 (2004).
23. A. Viola, A. Lanzavecchia, *Science* **273**, 104 (1996).
24. Q. J. Li *et al.*, *Cell* **129**, 147 (2007).
25. We thank M. Van der Brink for the generous use of the flow cytometer and J. Allison, N. Altan-Bonnet, P. Cluzel, L. Denzin, M. Huse, E. O'Shea, N. Socchi, and D. Sant'Angelo for comments and discussion.

Supporting Online Material
www.sciencemag.org/cgi/content/full/321/5892/1081/DC1
Materials and Methods
Figs. S1 to S10
References

19 March 2008; accepted 3 July 2008
10.1126/science.1158013

Adenovirus Small e1a Alters Global Patterns of Histone Modification

Gregory A. Horwitz,[1] Kangling Zhang,[2] Matthew A. McBrian,[3] Michael Grunstein,[3] Siavash K. Kurdistani,[3] Arnold J. Berk[1,4]*

Adenovirus small early region 1a (e1a) protein drives cells into S phase by binding RB family proteins and the closely related histone acetyl transferases p300 and CBP. The interaction with RB proteins displaces them from DNA-bound E2F transcription factors, reversing their repression of cell cycle genes. However, it has been unclear how the e1a interaction with p300 and CBP promotes passage through the cell cycle. We show that this interaction causes a threefold reduction in total cellular histone H3 lysine 18 acetylation (H3K18ac). CBP and p300 are required for acetylation at this site because their knockdown causes specific hypoacetylation at H3K18. SV40 T antigen also induces H3K18 hypoacetylation. Because global hypoacetylation at this site is observed in prostate carcinomas with poor prognosis, this suggests that processes resulting in global H3K18 hypoacetylation may be linked to oncogenic transformation.

The adenovirus small e1a protein drives contact-inhibited primary cells through the cell cycle dependent on three conserved regions (CRs) in e1a (fig. S1) (*1*). e1a is not a DNA binding protein, but it binds several other proteins. e1a CR2 binds the retinoblastoma protein (RB) and its paralogs p107 (RBL1) and p130 (RBL2) with high affinity and, together with a lower affinity binding region within CR1, displaces RB proteins from E2F family transcription factors (heterodimers of E2F1 through E2F5 with DP1 or DP2) (*1*–*3*). Release of RB family proteins and their associated repressing chromatin modifying activities (*4*) results in de-repression of cell cycle genes (*1*). Although the N terminus of e1a is not as extensively conserved among primate adenoviruses as CR1 and CR2, it is nonetheless well conserved among these viruses (*5*) and is required to drive cells into the cell cycle (*1*). The N terminus and residues in CR1 that are required for e1a transforming activity bind to several cellular proteins involved in the regulation of chromatin structure, including p300 and CBP, PCAF, GCN5, and p400 (*1*). However, the interaction with p300/CBP is the most important for transformation (*5*) and inhibits p300/CBP-dependent co-activator activity in transient transfection assays (*6*). It is not understood how the e1a interaction with p300/CBP contributes to cell cycling.

In studies potentially related to this question, Seligson *et al.* (*7*) reported that the risk of tumor recurrence in patients with low-grade prostate cancer (tumors with well-formed glandular structures) is related to the global cellular levels of H3K18 acetylation and H3K4 methylation observed by the intensity of nuclear staining with antibodies specific for these histone modifications. Global H3K18 hypoacetylation plus H3K4 hypomethylation strongly correlate with increased risk of tumor recurrence (*7*). Because the e1a interaction with p300/CBP is required for transformation by e1a, and because all the p300 and CBP in a nuclear extract of adenoviros type 5 (Ad5)–transformed 293 cells co-elutes with e1a on a gel filtration column in a complex of ~600 kD (*8*), we asked whether e1a induces a global decrease in histone acetylation and whether such an activity might contribute to e1a's transforming activity.

[1]Molecular Biology Institute, University of California, Los Angeles, CA 90095, USA. [2]Mass Spectrometry Facility, Department of Biochemistry, School of Medicine, Loma Linda University, Loma Linda, CA 92350, USA. [3]Department of Biological Chemistry, David Geffen School of Medicine, University of California, Los Angeles, CA 90095, USA. [4]Department of Microbiology, Immunology, and Molecular Genetics, University of California, Los Angeles, CA 90095, USA.

*To whom correspondence should be addressed. E-mail: berk@mbi.ucla.edu

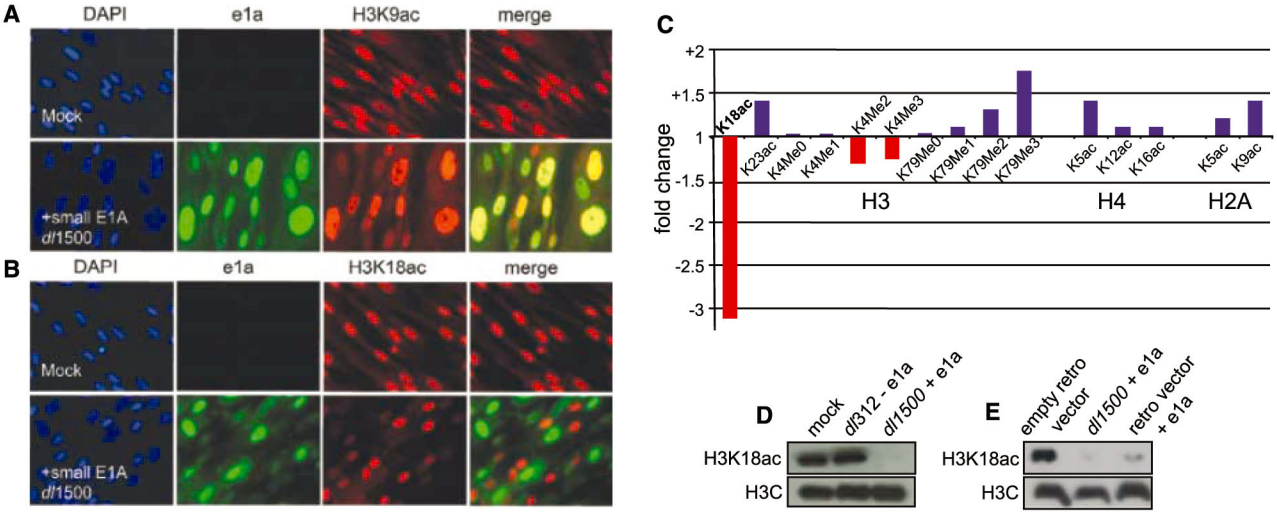

Fig. 1. e1a induces hypoacetylation of H3K18. Contact inhibited human primary IMR90 fibroblasts were mock-infected or infected with Ad5 *dl*1500 (e1a only). 24 hours p.i., cells were fixed and immunostained with antibodies to e1a (green), either (**A**) H3K9ac (red) or (**B**) K3K18ac (red), and 4′,6′-diamidino-2-phenylindole (DAPI) to stain nuclei. Merges of green and red signals are also shown. (**C**) Fold change in histone modifications after *dl*1500-infection of IMR90 cells determined by mass spectrometry (fig. S2). Western blots of histones from (**D**) IMR90 cells infected with *dl*312 (no e1a) or *dl*1500 (e1a only) and (**E**) HeLa cells transduced with the indicated retrovirus vectors or *dl*1500-infected.

To address these questions, we infected human primary IMR90 embryo lung fibroblasts with Ad5 *dl*1500 that expresses only e1a (*9*) or Ad5 *dl*312 with a deletion of the E1A region (*10*). At 24 hours postinfection (p.i.), cells were immunostained with highly specific antibodies for acetylated lysines on histones H3 (K9, K14, K18, K23, and K27) and H4 (K5, K8, K12, and K16) (*11*), di- and trimethylation at H3K4, and dimethylation at H3K9. Nuclei containing e1a had very low H3K18ac (Fig. 1B), with no detectable changes in H3K9ac (Fig. 1A) or any of the other 10 modifications examined (fig. S2). The immunofluorescence data were confirmed by mass spectrometry, which also revealed slight H3K4 hypomethylation (Fig. 1C, fig. S3, and table S1), and Western blot of acid-extracted histones (Fig. 1D and fig. S4). Similar results were observed in HeLa cells (table S2 and figs. S3 and S5) and after retrovirus vector expression of e1a (Fig. 1e), ruling out the possible influence of other adenovirus proteins expressed at a very low level in the absence of large E1A. Thus, e1a induces hypoacetylation of H3K18 and to a lesser extent hypomethylation of H3K4, similar to chromatin changes observed in primary prostate cancers with poor prognosis (*7*). Global H3K18 hypoacetylation requires e1a's interaction with p300/CBP because hypoacetylation was not induced by e1a mutants Δ4-25, R2G, and I5G, which interfere with p300/CBP binding, but was induced by H7A, which does not (*5*), and by e1a deletion mutants in its high-affinity binding site for RB proteins Δ111-123 (ΔCR2) (*3*), CtBP (Δ233-237) (*11*), and p400 (Δ25-36) (*12*) (figs. S6 and S7). The same e1a N-terminal mutations that prevented e1a-induced H3K18 hypoacetylation (Δ4-25, R2G, and I5G) were unable to induce S phase in quiescent human cells (*13*) or transformation of rodent cells (*5*).

In vitro, CBP and p300 acetylate several histone lysines, including H3K18 (*14*). However, small interfering RNA (siRNA) knockdown of both CBP and p300 (but not individually) resulted in specific H3K18 hypoacetylation in vivo in IMR90 and HeLa cells (Fig. 2A and fig. S8). Dual knockdown did not affect five other sites of histone modification assayed. Consequently, p300/CBP, and possibly PCAF which associates with them (*15*), are the major histone acetyltransferases (HATs) required for maintenance of global H3K18ac in vivo. e1a-induced H3K18 hypoacetylation was not due to inhibition of p300/CBP HAT enzymatic activities generally, or specifically for H3K18, even though they were quantitatively bound by e1a when isolated from infected cells (Fig. 2, B and C).

Simian virus 40 (SV40) large T antigen, like e1a, is a DNA tumor virus transforming protein that stimulates cell cycling through interactions with RB family proteins (*16*) as well as other cellular proteins, possibly including p300/CBP (*16*). Consequently, we examined H3K18ac in IMR90 cells expressing SV40 large T antigen and primary murine embryo fibroblasts (MEFs) transformed with an SV40 T antigen–expressing retrovirus vector (*17*) (fig. S9). Western blotting revealed decreased H3K18ac in both cell types expressing SV40 large T antigen (Fig. 2D). Induction of global H3K18 hypoacetylation by both e1a and SV40 large T antigen suggests that hypoacetylation at this site may be a general consequence of DNA tumor virus oncoprotein activity.

The accompanying report (*13*) shows that e1a causes a massive, genomewide relocalization of p300, CBP, and PCAF, targeting them to the promoter regions of a limited, but biologically related, set of genes that promote cell growth and division, causing H3K18 hyperacetylation in their promoter regions and strong induction. e1a also causes the redistribution of RB family proteins to promoter regions of genes involved in antiviral responses and differentiation, inducing their hypoacetylation at H3K18 and repression (*13*). This redistribution of p300/CBP/PCAF and RB family members may explain the observed global H3K18 hypoacetylation by restricting these HATs to the ~one-third of all genes involved in cell growth and replication that are activated by e1a (*13*).

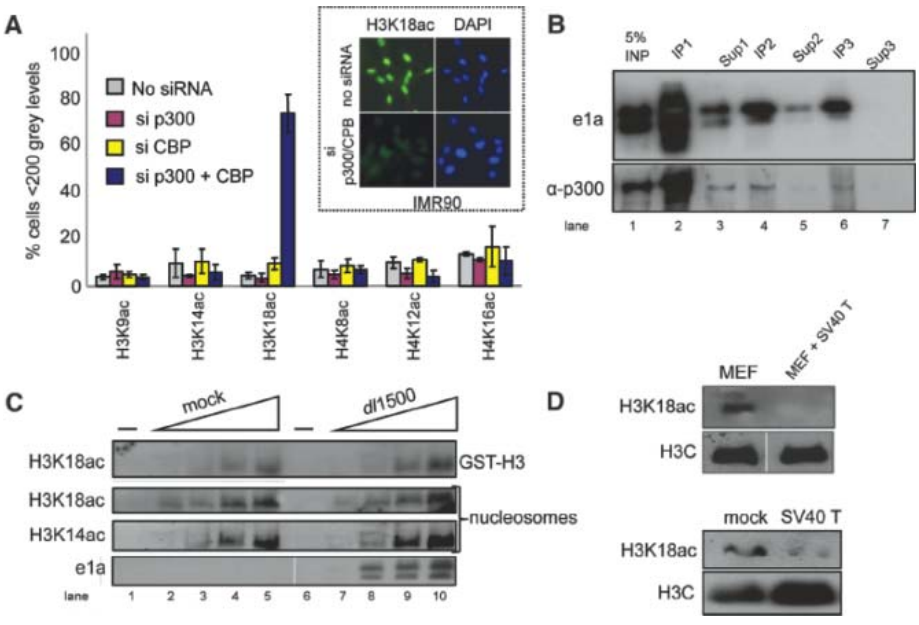

Fig. 2. CBP or p300 is required for acetylating H3K18. (**A**) Computational image analysis of immunofluorescent micrographs after IMR90 siRNA transfections against p300 and CBP (*18*) (fig. S7). The fraction ± SD of nonstaining nuclei is plotted, $n = 4$. (Inset) Typical micrographs. (**B**) Nuclear extract from *dl*1500-infected HeLa cells 24 hours p.i. was subjected to three successive immunoprecipitations (IP1 to IP3) with equal amounts of monoclonal antibody (mAb) M73 against e1a. One-tenth of the total IP and supernatant (Sup1 to Sup3) after each IP were subjected to Western blotting. Differences in post-translational modifications caused e1a to appear as a doublet. (**C**) Twofold increasing amounts of p300/CBP IPed from mock- or *dl*1500-infected HeLa cells were incubated with glutathione *S*-transferase (GST)–H3 N terminus or hypoacetylated nucleosomes plus acetyl-coenzyme A (*18*), and products were assayed by Western blotting with anti-H3K18ac or anti-H3K14ac. (**D**) Histones from MEFs transformed with a retrovirus vector expressing SV40 large T antigen or the parental MEFs (top) and from IMR90 fibroblasts mock-infected or infected with an Ad expression vector for SV40 large T antigen 24 hours p.i. (bottom) were subjected to Western blotting.

References and Notes

1. A. J. Berk, *Oncogene* **24**, 7673 (2005).
2. J. R. Nevins, *Curr. Opin. Genet. Dev.* **4**, 130 (1994).
3. X. Liu, R. Marmorstein, *Genes Dev.* **21**, 2711 (2007).
4. A. Blais, B. D. Dynlacht, *Curr. Opin. Cell Biol.* **19**, 658 (2007).
5. M. Rasti, R. J. Grand, J. S. Mymryk, P. H. Gallimore, A. S. Turnell, *J. Virol.* **79**, 5594 (2005).
6. C. Rochette-Egly, C. Fromental, P. Chambon, *Genes Dev.* **4**, 137 (1990).
7. D. B. Seligson *et al.*, *Nature* **435**, 1262 (2005).
8. G. Wang, A. J. Berk, *J. Virol.* **76**, 9186 (2002).
9. C. Montell, G. Courtois, C. Eng, A. Berk, *Cell* **36**, 951 (1984).
10. N. Jones, T. Shenk, *Proc. Natl. Acad. Sci. U.S.A.* **76**, 3665 (1979).
11. G. Chinnadurai, *Mol. Cell* **9**, 213 (2002).
12. M. Fuchs *et al.*, *Cell* **106**, 297 (2001).
13. R. Ferrari *et al.*, *Science* **321**, 1086 (2008).
14. T. Kouzarides, *Cell* **128**, 693 (2007).
15. X. J. Yang, V. V. Ogryzko, J. Nishikawa, B. H. Howard, Y. Nakatani, *Nature* **382**, 319 (1996).
16. D. Ahuja, M. T. Saenz-Robles, J. M. Pipas, *Oncogene* **24**, 7729 (2005).
17. M. J. O'Hare *et al.*, *Proc. Natl. Acad. Sci. U.S.A.* **98**, 646 (2001).
18. Materials and methods are available on *Science* Online.

19. Supported by NIH grant CA25235 to A.J.B. and a Beckman Young Investigator Award to S.K.K. We thank C. Eng for technical assistance.

Supporting Online Material

www.sciencemag.org/cgi/content/full/321/5892/1084/DC1
Materials and Methods
Figs. S1 to S9
Tables S1 and S2
References and Notes

22 January 2008; accepted 18 July 2008
10.1126/science.1155544

Epigenetic Reprogramming by Adenovirus e1a

Roberto Ferrari,[1] Matteo Pellegrini,[2] Gregory A. Horwitz,[3] Wei Xie,[1] Arnold J. Berk,[3,4] Siavash K. Kurdistani[1,5,6]*

Adenovirus e1a induces quiescent human cells to replicate. We found that e1a causes global relocalization of the RB (retinoblastoma) proteins (RB, p130, and p107) and p300/CBP histone acetyltransferases on promoters, the effect of which is to restrict the acetylation of histone 3 lysine-18 (H3K18ac) to a limited set of genes, thereby stimulating cell cycling and inhibiting antiviral responses and cellular differentiation. Soon after expression, e1a binds transiently to promoters of cell cycle and growth genes, causing enrichment of p300/CBP, PCAF (p300/CBP-associated factor), and H3K18ac; depletion of RB proteins; and transcriptional activation. e1a also associates transiently with promoters of antiviral genes, causing enrichment for RB, p130, and H4K16ac; increased nucleosome density; and transcriptional repression. At later times, e1a and p107 bind mainly to promoters of development and differentiation genes, repressing transcription. The temporal order of e1a binding requires its interactions with p300/CBP and RB proteins. Our data uncover a defined epigenetic reprogramming leading to cellular transformation.

The adenovirus small e1a oncoprotein interacts with multiple cellular factors to induce cell cycling in G_0-arrested cells to favor viral replication. Mutations of e1a regions that interact with the RB proteins or p300/CBP [cyclic adenosine monophosphate response element–binding protein (CREB)–binding protein] result in loss of e1a-transforming and mitogenic activities (*1*–*3*) (figs. S1 and S2). Binding of e1a to p300/CBP inhibits transcriptional activation by certain enhancers (*4*); however, it is unclear how this interaction promotes cell cycling and why it is required for e1a oncogenicity. The e1a-p300/CBP interaction causes a factor of ~3 reduction in total cellular histone 3 Lys^{18} acetylation (H3K18ac) specifically (*5*). Therefore, we sought to determine how e1a affects the genome-wide distributions of its interacting cellular factors as well as histone modifications (including H3K18ac) to establish an oncogenic gene expression program.

Using chromatin immunoprecipitation (ChIP) combined with microarrays (*6*), we examined the genome-wide binding of e1a at 2, 6, 12, and 24 hours (here and below, all times are post-infection) of confluent, contact-inhibited human IMR90 primary fibroblasts (ATCC CCL-186) in which e1a induces entry into S phase between 18 and 24 hours (fig. S2). We used an Agilent microarray containing probes for ~17,000 promoters, tiling an 8-kb region, which we divided computationally into 16 fragments of 500 base pairs (bp) each, spanning –5.5 to +2.5 kb of the transcription start site (TSS). Cells were infected with Ad5 mutant *dl*1500, which expresses only the small e1a protein (*7*). Using unbiased partitional clustering, we grouped the genes primarily into three clusters that captured the main trends in the data. We calculated a Z score to indicate the degree of enrichment for a given factor in each cluster.

During the 24-hour period after expression, at a cutoff of $Z \geq 2$, e1a bound to ~70% (9753) of the examined promoters in a temporal manner (Fig. 1A and fig. S3). Both cluster 1 (2414 genes) and cluster 2 (4052 genes) were enriched for e1a binding at 2 and 6 hours but became progressively depleted for e1a by 24 hours. Such transient e1a binding was observed earlier for the *Cdc6* gene (cluster 2) (*8*). Cluster 3 (7326 genes) showed relative lack of e1a binding at 2 and 6 hours but significant enrichment at 24 hours. The e1a-binding patterns at 6 and 24 hours were essentially opposite to each other (Pearson correlation r for average e1a binding = –0.46). Small e1a binding at 12 hours exhibited a transition-like state between early and late times, correlating at –0.28 and +0.21 with binding at 6 and 24 hours, respectively. Cluster 1 was enriched for genes involved in responses to pathogens and inflammation; cluster 2 for genes involved in cell growth, division, and DNA synthesis; and cluster 3 for development/differentiation, including homeobox domain–containing genes and cell-cell signaling (figs. S3 and S4).

Because e1a directly displaces the RB proteins from E2F transcription factors (*1*), we determined the average levels of e1a binding across promoter regions bound by E2Fs as determined in other cell lines (*9*). E2F-target genes were greatly enriched in cluster 2 (fig. S5), as were consensus E2F binding sites (*10*) (fig. S6), and were bound by e1a predominantly within 2 kb of the TSS at 6 hours but not at 24 hours (fig. S5, A to C). Thus, E2F–RB protein complexes may help e1a target the promoters of cell cycle genes early after infection.

To determine how e1a affects gene expression, we compared the expression profile of *dl*1500-infected to mock-infected confluent cells at 6, 12, and 24 hours. Cluster 1 genes were activated at 6 hours, consistent with a cellular response to viral infection, but were considerably

[1]Department of Biological Chemistry, University of California, Los Angeles, CA 90095, USA. [2]Department of Molecular, Cell and Developmental Biology, University of California, Los Angeles, CA 90095, USA. [3]Molecular Biology Institute, University of California, Los Angeles, CA 90095, USA. [4]Department of Microbiology, Immunology and Molecular Genetics, University of California, Los Angeles, CA 90095, USA. [5]Department of Pathology and Laboratory Medicine, University of California, Los Angeles, CA 90095, USA. [6]Eli and Edythe Broad Center of Regenerative Medicine and Stem Cell Research, David Geffen School of Medicine, University of California, Los Angeles, CA 90095, USA.

*To whom correspondence should be addressed. E-mail: skurdistani@mednet.ucla.edu

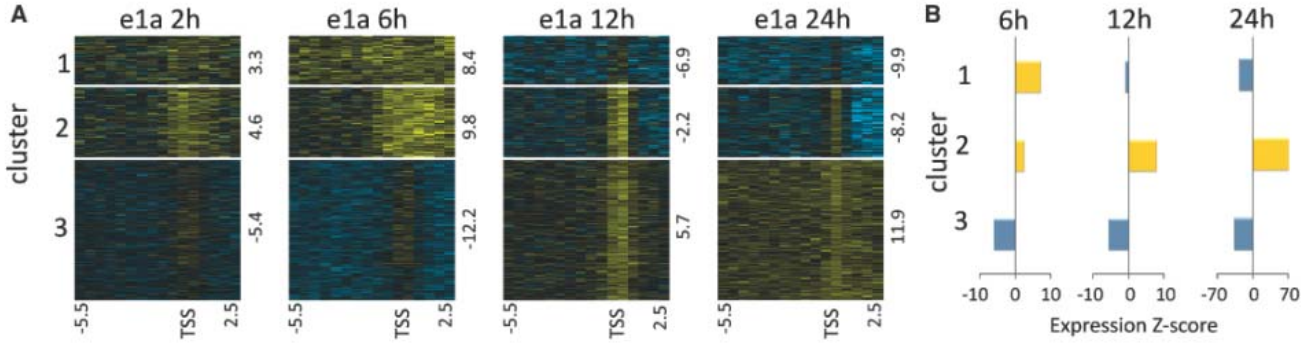

Fig. 1. Temporally ordered pattern of e1a binding reprograms host cell gene expression profile. (**A**) Time course of e1a genome-wide localization in IMR90 fibroblasts. Each row represents the promoter of a gene in 500-bp intervals from –5.5 to +2.5 kb of the transcription start site (TSS). Enrichment Z scores are indicated to the right of each cluster. (**B**) Relative gene expression changes of the three clusters at 6, 12, and 24 hours after e1a expression (note the scale).

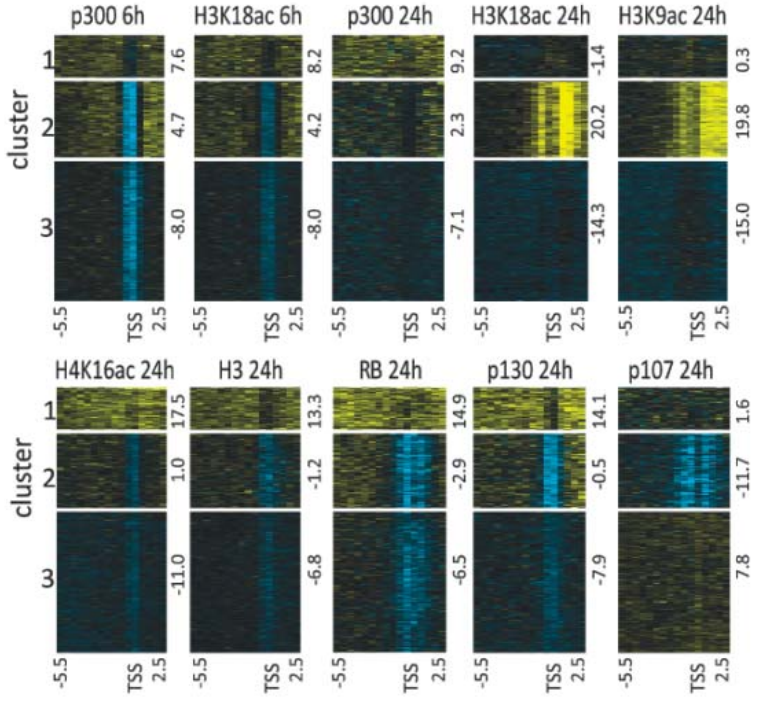

Fig. 2. Redistribution of transcriptional co-regulators and epigenetic reprogramming by e1a. The genome-wide distributions of p300, H3K18ac, H3K9ac, H4K16ac, histone H3, RB, p130, and p107 in the three e1a-binding clusters at the indicated times after e1a expression are shown.

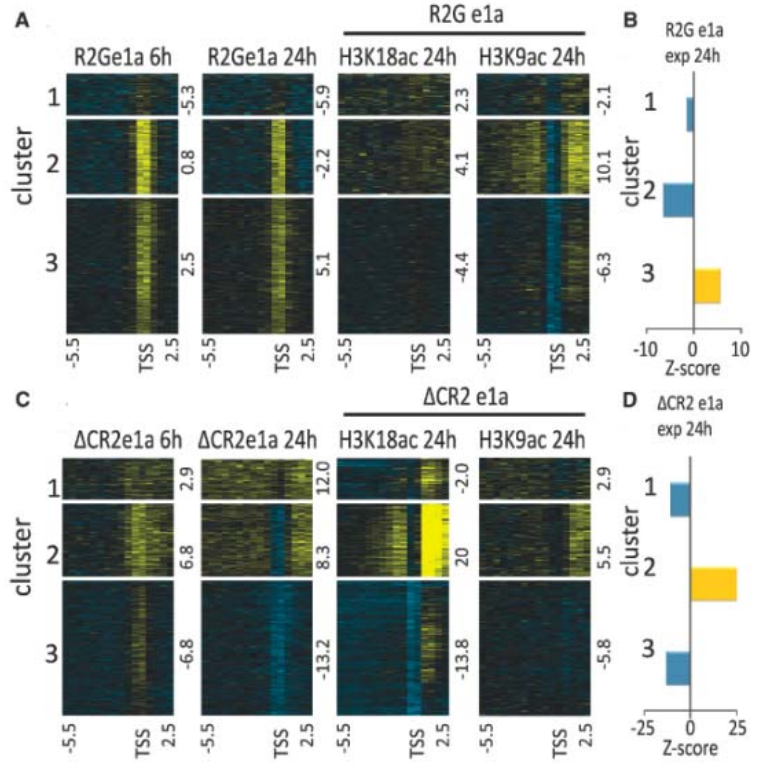

Fig. 3. Temporally ordered target gene selection and proper binding by e1a requires interactions with p300/CBP and the RB proteins. (**A** and **C**) Time course of R2Ge1a and ΔCR2e1a genome-wide localization in IMR90 fibroblasts in the three WTe1a-binding clusters (Fig. 1A). Also shown are the distribution and enrichment *Z* scores of H3K9ac and H3K18ac in R2Ge1a- or ΔCR2e1a-infected versus mock-infected cells. (**B** and **D**) Relative expression levels of the three clusters in each mutant 24 hours after e1a expression.

repressed by 24 hours (Fig. 1B; note the scales). Cluster 2 and 3 genes were progressively induced and repressed by 24 hours, respectively. The 24-hour expression profile was very similar to that induced by wild-type Ad5 (*11*), which suggests that small e1a induces most of the changes in host cell gene expression. Therefore, our data indicate that early e1a binding leads to activation of genes involved in cell cycling and proliferation and repression of antiviral response genes by 24 hours. Late e1a binding results in repression of development, differentiation, and cell-cell signaling genes.

We next analyzed H3K18ac. Relative to results from mock-infected cells, H3K18ac antibody ChIP yielded about one-third as much DNA from *dl*1500-infected cells, consistent with e1a-induced global H3K18 hypoacetylation (*5*) (fig. S7); we used equal amounts of ChIPed DNA for microarray analyses. Clusters 1 and 2 were enriched for H3K18ac at 6 hours mainly in regions away from the TSS, but only cluster 2 genes retained significant H3K18ac by 24 hours (Fig. 2). Cluster 3 genes were depleted or showed little enrichment for H3K18ac at 6 and 24 hours (Fig. 2). Therefore, e1a induces global H3K18 hypoacetylation, whereas the remaining H3K18ac at the molecular level is associated with a limited but biologically related set of genes with subsequent activation of their expression. The distribution of H3K9ac was similar to that of H3K18ac; by contrast, H4K16ac and histone H3 (irrespective of modifications) were enriched in cluster 1 at 24 hours and were specifically depleted around the TSS of cluster 2 and 3 genes (Fig. 2).

The e1a N terminus and conserved region 1 (CR1) directly bind p300/CBP (*2*); therefore, we asked whether these histone acetyltransferases and PCAF (p300/CBP-associated factor) were present at the e1a-target genes. p300 associated with genes in clusters 1 and 2, but at 6 and 24 hours p300 was significantly depleted from cluster 3 (Fig. 2). PCAF, and to lesser extent CBP, were also enriched in clusters 1 and 2 at 24 hours (fig. S8). The binding of p300 showed significant overlaps with H3K18ac at 6 hours in clusters 1 and 2, but only cluster 2 genes maintained high levels of H3K18ac at 24 hours (Fig. 2). In cluster 1, despite binding of p300/CBP/PCAF, H3K18ac was reduced and the genes were repressed at 24 hours. Repression of cluster 1 may be due to association of RB and p130 repressive complexes (see below) and/or e1a inhibition of p300/CBP activity at these genes (*4*). Note that both e1a and p300 bound to cluster 1 and 2 genes at 6 hours, whereas p300 remained at these promoters at 24 hours when e1a was depleted from them. This may involve continued recruitment of p300 by other transcription factors and/or direct binding to acetylated histones through the p300/CBP bromodomains (*12*).

In wild-type e1a (WTe1a)–expressing cells, p107 mRNA and protein increased at 24 hours, whereas expression of RB and p130 remained

unchanged (fig. S9). To determine whether the RB proteins contribute to e1a-mediated gene repression, we mapped genome-wide binding patterns of the three RB proteins at 24 hours in *dl*1500-infected versus mock-infected cells. RB and p130 were significantly enriched in cluster 1, consistent with repression of these genes at 24 hours (Fig. 2). RB, p130, and especially p107 were significantly depleted from the TSS regions of genes in cluster 2, perhaps because of WTe1a's ability to displace the RB proteins from E2Fs (*1*, *13*). p107 bound significantly to promoter regions of cluster 3 genes that were also bound by e1a at 24 hours and repressed. Thus, e1a probably uses RB and p130 to repress transcription of antiviral response genes, and uses p107 for repression of genes that would otherwise promote cellular differentiation and inhibit cell cycling.

Next, we analyzed gene expression, histone modifications, and e1a binding after expression of two e1a mutants. The $Arg^2 \rightarrow$ Gly (R2Ge1a) mutation disrupts the e1a-p300/CBP interaction, whereas deletion of CR2 (ΔCR2e1a) abolishes the high-affinity e1a interaction with RB proteins, but not the weaker e1a CR1–RB interactions (*1*). The R2G mutation greatly reduced binding of e1a to cluster 1 and to regions of cluster 2 genes away from the TSS (Fig. 3A), regions bound by p300 at 6 hours in WTe1a-expressing cells. In contrast to WTe1a, R2Ge1a also bound to development and differentiation genes at 6 hours (mainly around the TSS), and the binding patterns at 6 and 24 hours were similar to each other ($r = 0.44$; Fig. 3A). At E2F-target genes, R2Ge1a binding also remained unchanged between the time points (fig. S5). R2Ge1a induced only very slight enrichment of p300 or H3K18ac at the cluster 1 and 2 genes (Fig. 3A and fig. S10), but the H3K9ac pattern was similar to that induced by WTe1a, except that there was deacetylation at the TSS (Fig. 3A). R2Ge1a did not induce the gene expression changes observed with WTe1a and could not significantly suppress expression of antiviral genes (cluster 1, Fig. 3B and fig. S11). Thus, the e1a-p300/CBP interaction is required for the proper targeting and temporal order of e1a binding, the redistribution of p300 and H3K18ac, and e1a-regulated gene induction and repression.

ΔCR2e1a bound significantly to cluster 1 and 2 genes, including E2F-target genes at 6 hours, despite the CR2 deletion (Fig. 3C and fig. S5). However, in contrast to WTe1a, at 24 hours, ΔCR2e1a remained broadly associated with the cluster 1 and 2 promoter regions, except around the TSS of cluster 2 and 3 genes. ΔCR2e1a did not exhibit a temporally ordered pattern of binding; 6-hour and 24-hour binding patterns were similar ($r = 0.63$). These results suggest that e1a regions other than CR2 contribute to initial targeting of e1a to cell cycle and growth genes, but that CR2 is required for retention of WTe1a at the TSS of cluster 2 and 3 genes and its redistribution from clusters 1 and 2 to cluster 3 genes. In ΔCR2e1a-expressing cells, H3K18ac distribution was similar to that induced by WTe1a, but H3K9 showed much less hyperacetylation in cluster 2 and less hypoacetylation in cluster 1 relative to WTe1a or R2Ge1a (Fig. 3C). Because ΔCR2e1a cannot displace RB proteins from E2Fs (*1*), these results suggest that displacement of RB proteins and their associated histone deacetylases (*2*) from cluster 2 genes, and their transfer to cluster 1 genes, may contribute to changes in H3K9ac. The expression profile induced by ΔCR2e1a at 24 hours was similar to WTe1a ($r = 0.69$; fig. S11), except that the amplitude of gene induction and repression in the three clusters was decreased (Fig. 3D), particularly for certain critical genes (fig. S12); this probably explains ΔCR2e1a's lack of mitogenic activity. The data from the R2G and ΔCR2 mutants indicate that hyperacetylation of H3K18ac is required for transcriptional induction and relies on e1a regions necessary for interaction with p300/CBP, whereas changes in H3K9ac induced by both WTe1a and R2Ge1a are insufficient to induce transcriptional changes and depend on the high-affinity e1a–RB protein interactions.

By binding to the promoters of a large number of genes in a precise, time-dependent manner, e1a orchestrates redistribution of specific transcriptional co-regulators with associated epigenetic activities to promote S-phase entry and active repression of differentiation (fig. S13). Transcriptional reprogramming through use of epigenetic modifiers may have parallels in nonviral mechanisms of oncogenesis (*3*).

References and Notes

1. X. Liu, R. Marmorstein, *Genes Dev.* **21**, 2711 (2007).
2. A. J. Berk, *Oncogene* **24**, 7673 (2005).
3. See supporting material on *Science* Online.
4. D. Chakravarti *et al.*, *Cell* **96**, 393 (1999).
5. G. A. Horwitz *et al.*, *Science* **321**, 1084 (2008).
6. B. Ren *et al.*, *Science* **290**, 2306 (2000).
7. C. Montell, G. Courtois, C. Eng, A. Berk, *Cell* **36**, 951 (1984).
8. M. K. Ghosh, M. L. Harter, *Mol. Cell* **12**, 255 (2003).
9. X. Xu *et al.*, *Genome Res.* **17**, 1550 (2007).
10. O. Elemento, N. Slonim, S. Tavazoie, *Mol. Cell* **28**, 337 (2007).
11. D. L. Miller, C. L. Myers, B. Rickards, H. A. Coller, S. J. Flint, *Genome Biol.* **8**, R58 (2007).
12. S. Mujtaba, L. Zeng, M. M. Zhou, *Oncogene* **26**, 5521 (2007).
13. J. R. Nevins, *Curr. Opin. Genet. Dev.* **4**, 130 (1994).

14. We thank M. Carey for critical comments, M. Grunstein for providing the histone acetylation antibodies, and C. Millar and A. Sperling and for help with microarrays. Supported by U.S. Public Health Service grant CA25235 (A.J.B.), an HHMI Early Career Award, a UCLA Specialized Program of Research Excellence in Prostate Cancer grant, and an American Cancer Society grant (S.K.K.). Microarray data have been deposited in the Gene Expression Omnibus under accession numbers GSE12045, GSE12046, and GSE12047.

Supporting Online Material

www.sciencemag.org/cgi/content/full/321/5892/1086/DC1
Materials and Methods
SOM Text
Figs. S1 to S13
Table S1
References

22 January 2008; accepted 18 July 2008
10.1126/science.1155546

Heterochromatin Integrity Affects Chromosome Reorganization After Centromere Dysfunction

Kojiro Ishii,[1]* Yuki Ogiyama,[1]* Yuji Chikashige,[2] Saeko Soejima,[1] Fumie Masuda,[1] Tatsuyuki Kakuma,[3] Yasushi Hiraoka,[2,4] Kohta Takahashi[1]†

The centromere is essential for the inheritance of genetic information on eukaryotic chromosomes. Epigenetic regulation of centromere identity has been implicated in genome stability, karyotype evolution, and speciation. However, little is known regarding the manner in which centromere dysfunction affects the chromosomal architectures. Here we show that in the fission yeast *Schizosaccharomyces pombe*, the conditional deletion of the centromere produces survivors that carry either a neocentromere-acquired chromosome at the subtelomeric region or an acentric chromosome rescued by intertelomere fusion with either of the remaining chromosomes. The ratio of neocentromere formation to telomere fusion is considerably decreased by the inactivation of genes involved in RNA interference–dependent heterochromatin formation. By affecting the modes of chromosomal reorganization, the genomic distribution of heterochromatin may influence the fate of karyotype evolution.

The stable maintenance and propagation of linear eukaryotic chromosomes during cell division requires two specialized chromosomal structures: telomeres and centromeres. Telomeres protect the ends of linear chromosomes and prevent their fusion (*1*), whereas centromeres are essential for equal chromosome separation during M phase (*2*). The centromeric DNA sequence by itself cannot specify centromere identity, and instead epigenetic regulation plays a dominant role in most eukaryotes (*2*–*5*). However, when an epigenetically marked authentic centromere becomes unavailable, the type of molecular components that contribute to recruit kinetochore proteins such as CENP-A (a centromeric histone H3 variant) onto a new position (the neocentromere locus) remains

obscure. In the present study, we developed a conditional centromere disruption assay in *Schizosaccharomyces pombe*. The *S. pombe* haploid has three chromosomes whose centromeres are organized in a symmetrical fashion, so that the ~10- to 15-kb Cnp1/CENP-A–accumulated kinetochore region (*6*) is flanked by ~10- to 60-kb pericentromeric heterochromatin regions (*7*) (fig. S1).

We developed a haploid strain carrying chromosome I on which the centromere (*cen1*) DNA was bracketed by *loxP* sites (*loxP-cen1*) and then conditionally expressed Cre recombinase to excise *cen1* from chromosome I (fig. S1). After Cre induction, the cells carrying *loxP-cen1* showed reduced cell growth and viability (Fig. 1A). Eighteen hours after induction, most of the cells in early mitosis produced lagging chromosomes, many of which resulted in asymmetric nuclear division in late mitosis (Fig. 1B). Visualization of the *cen1*-adjacent *lys1* locus and ribosomal DNA (rDNA) loci on chromosome III revealed that our *cen1*-disruption assay can induce Cre recombinase–dependent segregation defects of chromosome I but presumably not of other chromosomes (Fig. 1C).

Cre recombinase is expected to excise the entire *cen1*, including the outer heterochromatic regions, and to generate an extra ring chromosome labeled with a *ura4*$^+$ marker (fig. S1). To anticipate neocentromere formation on chromosome I, *cen1* disruptants were selected from a fraction of excision-failed cells by their resistance to G418, because the *cen1* deletion re-forms the G418-resistant *kanR* gene at the *loxP* site. In addition, *ura4*$^+$-expressing survivors in which the *cen1* ring chromosome had recombined with the acentric chromosome I were eliminated by selection using 5-fluoroorotic acid (5-FOA). The double drug–resistant survivors were isolated at a mean frequency of 8.7×10^{-4} under the test conditions.

The chromosomes of the survivors showed no hybridization signal for the *cen1*-specific probe in Southern blots after pulse-field gel electrophoresis (PFGE), indicating that *cen1* was completely lost (Fig. 2 and fig. S2). Although some survivors (designated type I) possessed three chromosomes whose apparent sizes were identical to those in wild-type cells, other survivors (designated type II) lacked the bands corresponding to chromosome I and one of the two remaining chromosomes and had an additional more slowly migrating band, which presumably represents a fused chromosome (Fig. 2). In type I, the lengths of *Not* I fragments, excluding the fragment with lost *cen1*, were identical to those in the mother strain; whereas in type II, typically two *Not* I fragments containing the telomere end of chromosome I and the other end of either chromosome II or III were lost, and a new fusion fragment appeared (fig. S2). Consistently, mitotically arrested cells of type I and II survivors exhibited three and two condensed chromosomes, respectively, on which the *cen1*-adjacent *lys1* locus was located distantly from signals of Mis12 centromere protein (*8*) (fig. S3A). Type II survivors commonly exhibit streaked sister nuclei with *lys1* loci at their lagging tails during anaphase (fig. S3B), suggesting that the fused acentric chromosome I segregates into daughter cells by using the centromere on the connected chromosome. Thus, type I cells survived the loss of the centromere through neocentromere formation, whereas type II cells survived by intertelomere fusion. Neither growth retardation nor reduced cell viability was apparently observed in either type I or type II survivors (fig. S4).

To determine the location of the neocentromeres in type I survivors, we performed chromatin immunoprecipitation (ChIP)–chip analysis using green fluorescent protein (GFP)–tagged Mis6 centromere protein (*8*). Microarray data from type I survivors (*cd39* and *cd60*) indicated that Mis6 associates with the left and right telomere-proximal regions, respectively (Fig. 3A). The

[1]Division of Cell Biology, Institute of Life Science, Kurume University, Japan. [2]Kobe Advanced Information and Communications Technology Research Center, National Institute of Information and Communications Technology, Japan. [3]The Biostatistics Center, Kurume University, Japan. [4]Graduate School of Frontier Biosciences, Osaka University, Japan.

*These authors contributed equally to this work.
†To whom correspondence should be addressed. E-mail: takahash@lsi.kurume-u.ac.jp

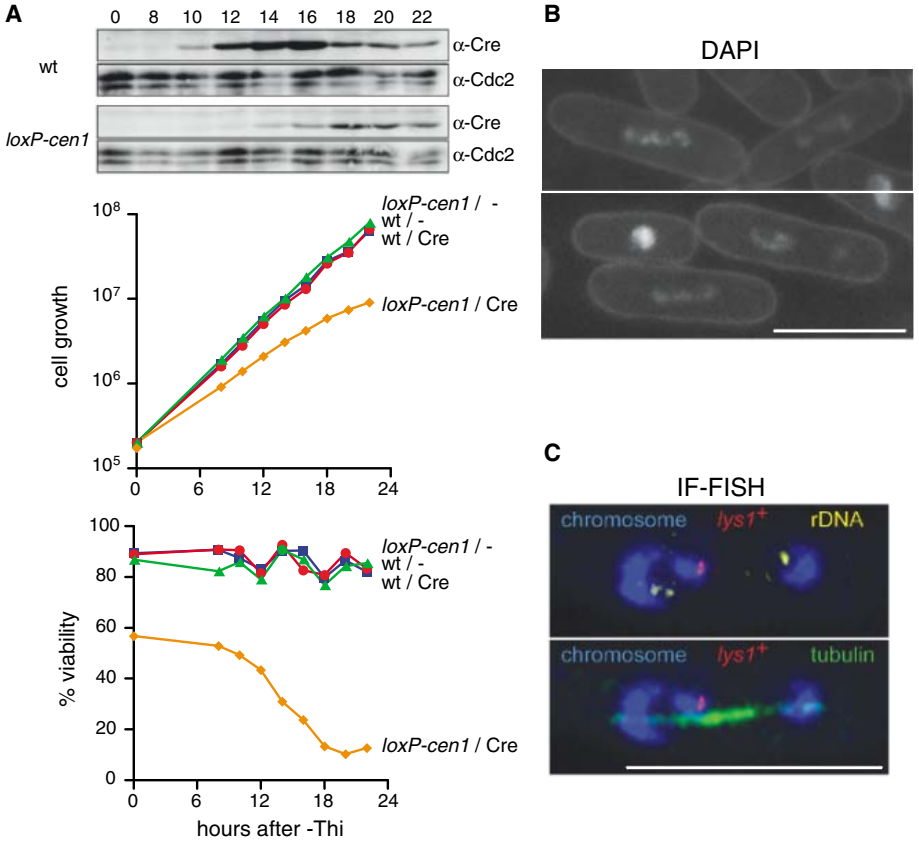

Fig. 1. Conditional centromere disruption causes mitotic cell death with frequent aneuploid formation. **(A)** The protein induction profile of Cre recombinase and Cdc2 (a loading control) in wild-type (wt) strain SP37 and *loxP-cen1* strain SP1376 (top), the cell number increase (middle), and the cell viability (bottom) of the indicated strains after Cre induction by thiamine depletion (–Thi). **(B** and **C)** The representative lagging chromosome images of the *loxP-cen1* cells at 18 hours after Cre induction; the cells were visualized by DAPI stain **(B)** and immunofluorescence–fluorescence in situ hybridization (IF-FISH) with an indicated set of probes **(C)**. Scale bars, 10 μm.

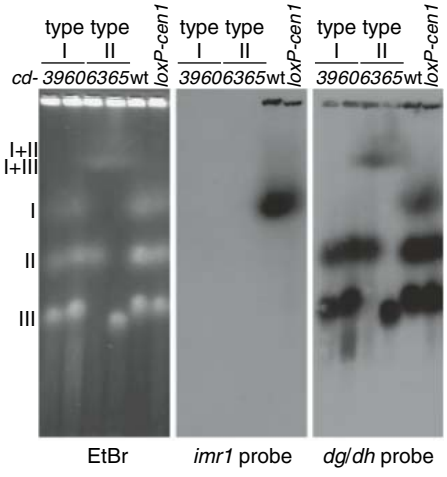

Fig. 2. Karyotype analysis of *cen1*-deleted survivors. The undigested chromosomes were subjected to pulsed-field gel electrophoresis (PFGE), followed by ethidium bromide (EtBr) staining and Southern blotting using a *cen1*-specific central probe (*imr1*) or an outer repeat probe common to all the centromeres (*dg*/*dh*) (*6*).

neocentromeric loci of 18 other type I survivors investigated thus far were classified into one of these two telomere-proximal regions (fig. S5). Several open reading frames (ORFs) but no obvious repetitive elements were present in the released genome DNA sequence corresponding to the neocentromeres (table S2). These neocentromeric ORFs largely overlapped with the clusters of genes, which were up-regulated after the removal of nitrogen from the media but are normally expressed at a low level (*9*, *10*) (table S2 and fig. S6); however, in cells that acquired neocentromeres, in particular, their expression level remained low even after nitrogen starvation (fig. S7). This suggests the incompatibility of neocentromere location with actively transcribed regions, a property that may influence the initial neocentromere site selection. However, a continuous region of repressed genes may not be sufficient to recruit neocentromeres, because none formed at another gene cluster on chromosome I

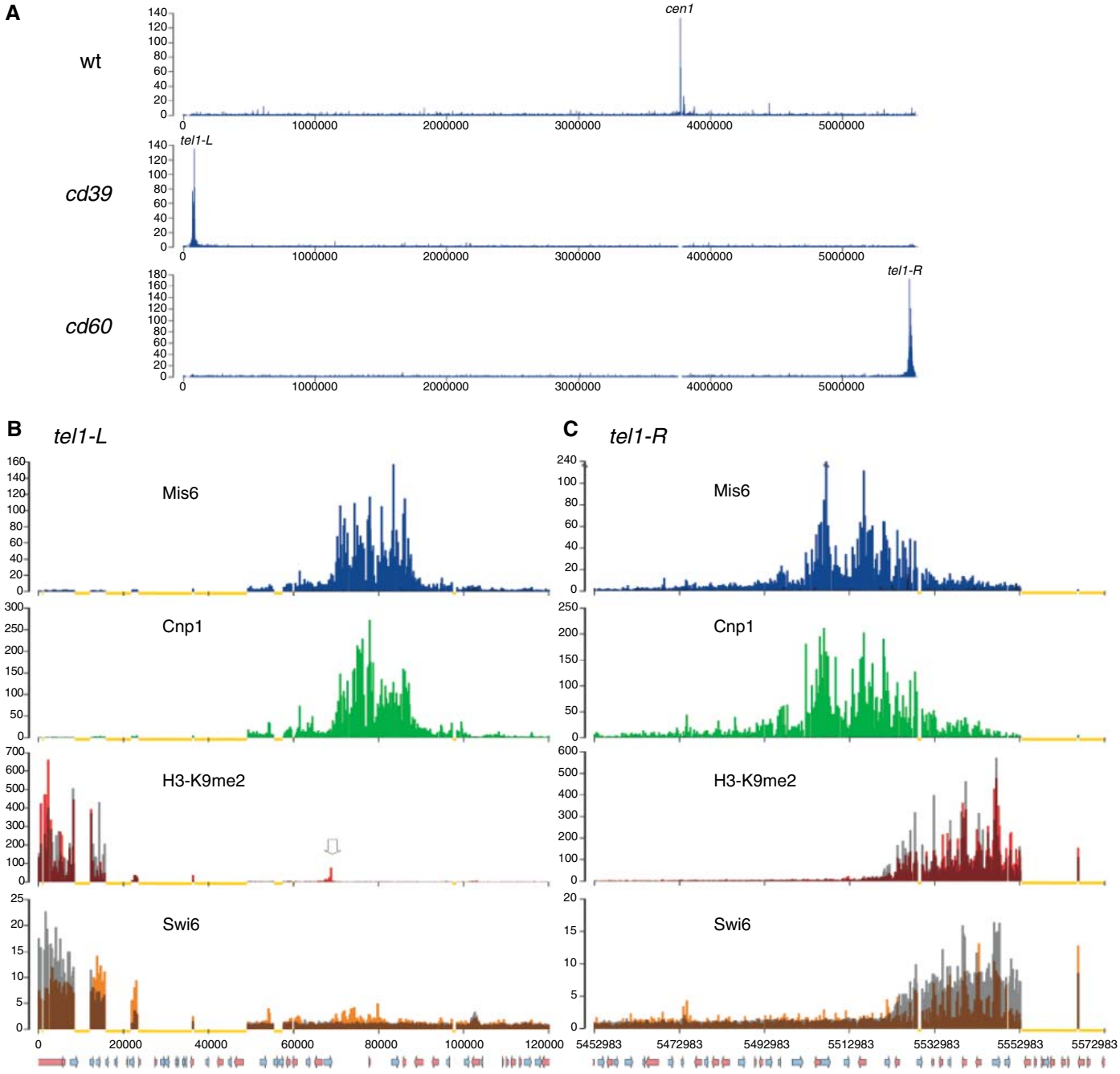

Fig. 3. Neocentromere formation on telomere-proximal regions. ChIP-chip analyses using an *S. pombe* genome tiling microarray devoid of repeated sequences are shown. The enrichment ratios of ChIP signals were plotted in alignment with the second sequence release of *S. pombe* chromosome I (NC_003424.2). **(A)** Distribution profiles of Mis6-GFP across the entire chromosome I in wild-type and type I survivors, *cd39* and *cd60* (SP2884, SP2867, and SP2881, respectively). **(B)** Genomic distributions of Mis6-GFP, Cnp1, Swi6, and di-methylated histone H3-K9 along the neocentromeric locus of the left subtelomeric region of chromosome I in *cd39*. The wild-type distribution of each protein along the same region was superimposed as transparent gray bars. The annotated genes in this region are indicated at the bottom. Yellow lines indicate probe-free regions in this array due to the repetitiveness in the genome. A white arrow indicates the enrichment of the heterochromatin hallmark (H3-K9me2) specific to *cd39*. **(C)** Genomic distributions of the same factors along the right subtelomeric regions in *cd60*, together with those in the wild type, as shown in **(B)**.

that shows a similar expression profile but is located far from the telomere (SPAC1002.18 to SPAC1399.01c) (*10*) (fig. S5).

We investigated the chromosomal distribution of the kinetochore and heterochromatin proteins Cnp1/CENP-A (*6*), Mis12 (*8*), Cnp3/Mif2/CENP-C (*8*), Swi6/HP1 (*11*), and methylated histone H3-K9 (*11*) in the neocentromeres by ChIP-chip analyses (Fig. 3, B and C). In both subtelomeric neocentromeres of *cd39* and *cd60*, Cnp1 newly localized to a region identical to that of Mis6 (Fig. 3, B and C), with Cnp3 or Mis12 showing similar behavior in *cd60* (fig. S6). Their association in the neocentromere extended over 20 kb, which is comparable to those of authentic centromeres (*6*, *7*). This kinetochore-assembling region borders a heterochromatin domain specified by Swi6 and K9-methylated histone H3 (Fig. 3, B and C). In contrast to *cd60*, the kinetochore-assembling region in the *cd39* neocentromere is close to but not in contact with the original subtelomeric heterochromatin, and a K9-methylated histone H3 peak appears adjacent to the region (Fig. 3B, arrow, and fig. S8); this implies a positive role of heterochromatin in neocentromere formation and/or maintenance. Heterochromatin is located at the distal but not the proximal side of the neocentromeric locus, in contrast to the distal and proximal heterochromatin found in authentic centromeres (*7*). The neocentromeres in both *cd39* and *cd60* strains are responsible for segregating the acentric chromosome I (fig. S9, A and B). Both strains have no obvious delay in mitotic progression (fig. S9C) and DNA replication (fig. S7C, time = 0). The drug sensitivities of *cd39* and *cd60* to carbendazim (a spindle poison) and hydroxyurea (an inhibitor of DNA replication) were also comparable to that of the wild-type (fig. S10). Thus, these telocentric neocentromeres appear to perform regular functions in both M and S phases during the vegetative growth cycle.

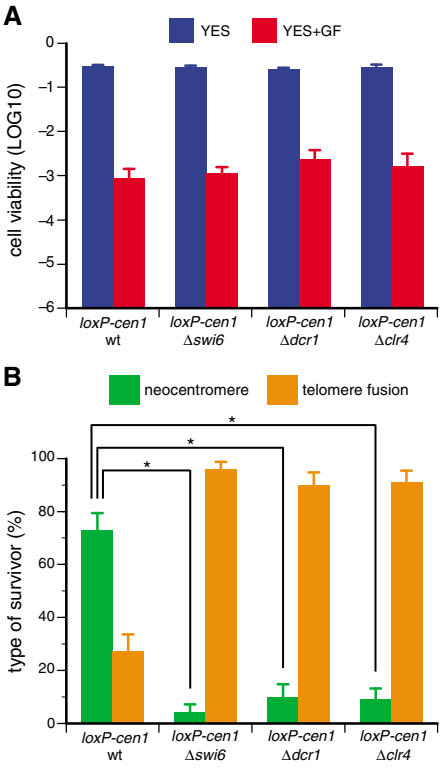

Fig. 4. Heterochromatin affects the modes of survival from centromere disruption. **(A)** The cell viability of 10^6 indicated cells (SP1376, SP2759, SP2404, and SP2754) with Cre induction for 18 hours was determined on a YES plate and a YES plate containing G418 and 5-FOA (YES+GF) at 33°C. Error bars indicate SEM from >20 experiments. **(B)** The summary of the ratio of karyotypes of *cen1*-deleted survivors determined by PFGE analyses. Error bars indicate SEM. *$P < 0.0001$ compared with the wild-type, based on the mixed logistic regression.

The kinetochores of many eukaryotes, including fission yeast (fig. S1), are known to be embedded in the pericentromeric heterochromatin (*3*, *11*), the epigenetic nature of which may contribute to centromere identity and function (*2*–*5*). Thus, the subtelomeric heterochromatin regions adjacent to the two neocentromeric loci (Fig. 3, B and C) may be a prerequisite for de novo kinetochore formation. To assess this possibility, we isolated *cen1*-deleted survivors from heterochromatin-deficient mutant strains and determined whether neocentromere formation occurred in these mutants. Figure 4 summarizes the karyotype classification of the survivor isolated from the mutants of Swi6/HP1, Dcr1 (involved in RNA interference–mediated heterochromatin silencing), and Clr4 methyltransferase (which methylates histone H3-K9) (*11*). Under 5-FOA/G418 double selection, no substantial difference was observed in the frequencies of survivor appearance among the wild-type and mutants (Fig. 4A). However, in the mutants, a statistically significant ($P < 0.0001$) decrease in neocentromere formation against telomere fusion was observed (Fig. 4B). Functional neocentromeres can be formed in the heterochromatin-deficient mutants, suggesting that the neighboring heterochromatin is not essential for, although it may assist in, de novo kinetochore formation at the noncentromeric locus. In 15 type I survivors with deficiency in heterochromatin (Δ*clr4*, Δ*swi6*, and Δ*dcr1*), we found Mis6 and Cnp1 enrichment at the same telomere-proximal regions as in *cd39* and *cd60* (fig. S5).

Centromere-deficient chromosomes in fission yeast can be transmitted to daughter cells by forming a neocentromere on the telomere-proximal region or by fusing to other chromosomes via telomere-telomere end fusion. Both modes reinforce the idea that telomere regions may have a role in karyotype evolution (*12*), which may be affected by the state of heterochromatin in the genome. Flanking heterochromatin may promote de novo kinetochore formation; for example, by ensuring a structural environment suitable for the recruitment of centromere proteins (*13*) and/or acting to maintain centromere size by creating a barrier against the expansion of centromere chromatin (*14*). Telomeric heterochromatin is not severely compromised in Δ*dcr1*, but the ordered arrangement of telomeres in the interphase nucleus is (*15*), suggesting that the higher-order architectural features of heterochromatin may play a role in the survival response of chromosomes after centromere dysfunction. Centromere-specific states of histone modifications have been reported in humans and *Drosophila* (*16*), and nucleosomes in the neocentromere-competent regions were reported to be hypoacetylated but not heterochromatic in *S. pombe* (*17*–*19*). In humans, partial histone hyperacetylation causes a reversible shift of the CENP-A–binding region in the neocentromere (*20*). Further studies will be needed to clarify whether such epigenetic modifications contribute to neocentromere formation in *S. pombe*. We found that two subtelomeric regions are the preferential sites for neocentromere formation, supporting the idea that centromeres were derived from telomeres during the evolution of the eukaryotic chromosome (*12*).

References and Notes

1. J. P. Murnane, L. Sabatier, *Bioessays* **26**, 1164 (2004).
2. D. W. Cleveland, Y. Mao, K. F. Sullivan, *Cell* **112**, 407 (2003).
3. G. H. Karpen, R. C. Allshire, *Trends Genet.* **13**, 489 (1997).
4. S. Henikoff, K. Ahmad, H. S. Malik, *Science* **293**, 1098 (2001).
5. D. J. Amor, K. H. Choo, *Am. J. Hum. Genet.* **71**, 695 (2002).
6. K. Takahashi, E. S. Chen, M. Yanagida, *Science* **288**, 2215 (2000).
7. J. F. Partridge, B. Borgstrom, R. C. Allshire, *Genes Dev.* **14**, 783 (2000).
8. S. Saitoh, K. Ishii, Y. Kobayashi, K. Takahashi, *Mol. Biol. Cell* **16**, 3666 (2005).
9. Y. Chikashige *et al.*, *Cell* **125**, 59 (2006).
10. J. Mata, R. Lyne, G. Burns, J. Bahler, *Nat. Genet.* **32**, 143 (2002).
11. S. I. Grewal, S. Jia, *Nat. Rev. Genet.* **8**, 35 (2007).
12. A. Villasante, M. Mendez-Lago, J. P. Abad, E. Montejo de Garcini, *Cell Cycle* **6**, 2872 (2007).
13. H. D. Folco, A. L. Pidoux, T. Urano, R. C. Allshire, *Science* **319**, 94 (2008).
14. K. A. Maggert, G. H. Karpen, *Genetics* **158**, 1615 (2001).
15. I. M. Hall, K. Noma, S. I. Grewal, *Proc. Natl. Acad. Sci. U.S.A.* **100**, 193 (2003).
16. B. A. Sullivan, G. H. Karpen, *Nat. Struct. Mol. Biol.* **11**, 1076 (2004).
17. H. P. Cam *et al.*, *Nat. Genet.* **37**, 809 (2005).
18. K. R. Hansen *et al.*, *Mol. Cell. Biol.* **25**, 590 (2005).
19. M. Wiren *et al.*, *EMBO J.* **24**, 2906 (2005).
20. J. M. Craig *et al.*, *Hum. Mol. Genet.* **12**, 3109 (2003).

21. We thank K. Nagao, S. Saitoh, and H. Kimura for their technical expertise and discussion and M. Yanagida, A. Carr, J. Nakayama, and K. Gull for providing experimental materials. This work was supported by Grants-in-Aid for Exploratory Research and Scientific Research on Priority Areas (Nuclear Dynamics, Chromosome Cycle, Decode Systems) from the Ministry of Education, Culture, Sports, Science, and Technology, Japan; and a grant from Time's Arrow and Biosignaling, Precursory Research for Embryonic Science and Technology, Japan Science and Technology Agency.

Supporting Online Material

www.sciencemag.org/cgi/content/full/321/5892/1088/DC1
Materials and Methods
Figs. S1 to S10
Tables S1 to S4
References

4 April 2008; accepted 16 July 2008
10.1126/science.1158699

Grueneberg Ganglion Cells Mediate Alarm Pheromone Detection in Mice

Julien Brechbühl, Magali Klaey, Marie-Christine Broillet*

Alarm pheromones (APs) are widely used throughout the plant and animal kingdoms. Species such as fish, insects, and mammals signal danger to conspecifics by releasing volatile alarm molecules. Thus far, neither the chemicals, their bodily source, nor the sensory system involved in their detection have been isolated or identified in mammals. We found that APs are recognized by the Grueneberg ganglion (GG), a recently discovered olfactory subsystem. We showed with electron microscopy that GG neurons bear primary cilia, with cell bodies ensheathed by glial cells. APs evoked calcium responses in GG neurons in vitro and induced freezing behavior in vivo, which completely disappeared when the GG degenerated after axotomy. We conclude that mice detect APs through the activation of olfactory GG neurons.

In a threatening situation, plants and animals warn conspecifics by secreting alarm pheromones (APs) (*1*–*4*). These substances signal injury, distress, or the presence of predators. In animals, the response of conspecifics to these signals is usually to freeze, attack, or disperse (*5*–*7*). Mammalian APs have not been identified yet; they may be low-molecular-weight volatile substances (*8*, *9*), and it remains unknown whether their detection by conspecifics is mediated by a specialized olfactory subsystem.

In mammals, the most recently discovered olfactory subsystem (*10*–*14*), the so-called Grueneberg ganglion (GG) (*15*), is present at the tip of the nose, close to the opening of the naris, and is easy to observe in one particular gene-targeted mouse strain called OMP-GFP (olfactory marker protein–green fluorescent protein) (Fig. 1A). In these mice, a GFP-positive, arrow-shaped neuronal structure 750 to 1000 μm in length lines both sides of the nasal septum and comprises 300 to 500 cells (Fig. 1B). Each cell sends out a single axon, and axons fasciculate immediately (Fig. 1C) as they project caudally along the dorsal roof of the nasal cavity to the necklace complex in the olfactory bulb (*10*–*12*). The GG starts developing around embryonic day 16 and appears to be complete at birth (*10*–*14*).

Olfactory neurons sense the external chemical environment through the presence, at the end of their single dendrite, of cilia or microvilli in direct contact with the airspace of the nasal cavity. In contrast, under light or confocal microscopy, the mouse GG looks like a densely packed population of round cell bodies lacking these typical olfactory neuronal features or supporting glial cells (Fig. 1D) (*11*–*14*). GG cells express, in addition to OMP, molecular olfactory components. Indeed, extensive reverse transcription polymerase chain reaction and in situ hybridization analyses identified one vomeronasal organ (VNO) receptor, a distinct subtype of the V2R class, V2R83; and heterotrimeric GTP-binding proteins (G proteins) $G_{\alpha o}$ and $G_{\alpha i2}$ (*16*, *17*). This suggests that the GG is in fact an olfactory subsystem with specific chemosensory functions.

To resolve the apparent contradiction between the lack of cilia or dendrites and a possible olfactory function of GG cells, we looked at the structure and cellular organization of the mouse GG by performing scanning electron microscopy (SEM) on coronal slices (Fig. 1, E to G). We found clusters of round GG cells in a fibroblast meshwork between the nasal septum and a keratinized epithelium (KE) (Fig. 1, E and F) (*13*). With this technical approach, four to eight ciliary processes were observed per GG cell (Fig. 1G). They were further characterized by transmission electron microscopy (TEM) (figs. S1 to S3) to be nonmotile primary cilia according to their microtubular characteristics (fig. S1, B and C) (*18*, *19*). Thirty to forty primary cilia were present per GG cell, profoundly invaginated into the cytoplasm (5 μm) (fig. S1B) and grouped into three to four packs of 8 to 12 per cell (figs. S1C and S3). Analyzing serial ultrathin sections, we estimated both their length (15 μm) and their diameter (0.2 μm). Primary cilia were observed in the extracellular matrix (fig. S1, E to G) but not within the leaky KE, and they did not cross the keratin layers to

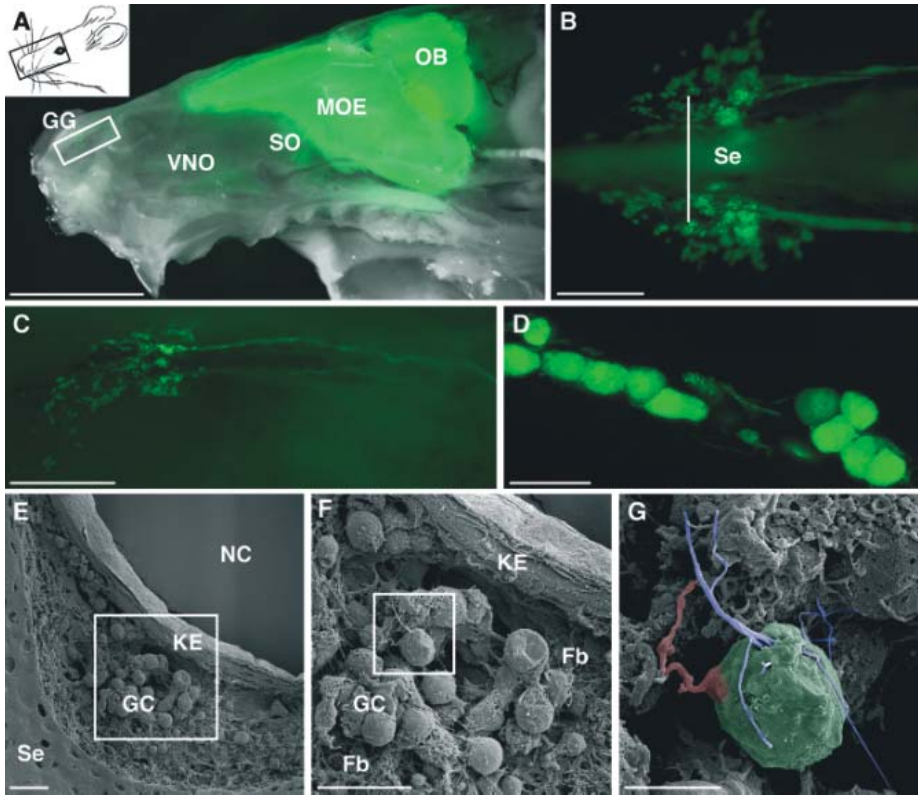

Fig. 1. Ciliary processes are present on the mouse GG cells. (**A**) Sagittal section through the nasal cavity of an OMP-GFP mouse: Neurons from the main olfactory epithelium (MOE), septal organ (SO), VNO, and GG (white rectangle) project to the olfactory bulb (OB). (**B**) Dorsal view of the GG, an arrow-shaped parallel organ on both sides of the nasal septum (Se). (**C**) High-power view from one GG [rectangle in (A)]. (**D**) Maximum-intensity projection (12 μm) of a GG cell cluster by confocal microscopy. (**E**) SEM micrograph of a GG coronal section [line in (B)]. Clusters of GG cells (GC) are shown, located along the Se underneath the KE lining the nasal cavity (NC) [square detailed in (F)]. (**F**) Close-up view of the GG cells in a fibroblast meshwork (Fb) [square detailed in (G)]. (**G**) GG cell (false color green) with its axon (false color red) and thin ciliary processes (false color blue). Scale bars, 1 mm in (A); 0.1 mm in (B); 0.25 mm in (C); 25 μm in (D); 20 μm in (E) and (F); and 5 μm in (G).

Department of Pharmacology and Toxicology, University of Lausanne, Bugnon 27, CH-1005 Lausanne, Switzerland.

*To whom correspondence should be addressed. E-mail: mbroille@unil.ch

reach the nasal cavity. Immunostaining experiments confirmed the presence of multiple cilia on GG cells (fig. S1, H to K).

We tried to resolve the difference between the number of cilia observed with SEM versus TEM (4 to 8 versus 30 to 40) and found another cell population that trapped most cilia inside the ganglion structure (fig. S1, D and K). These cells have a triangular shape with thin cytoplasmic extensions (Fig. 2A). Immunostaining experiments demonstrated the glial origin of the wrapping cells by positive staining for S100β (Fig. 2, B to D) and glial fibrillary acidic protein (fig. S4, A to C). The GFP-positive cells expressed the olfactory marker $G_{\alpha i2}$ (Fig. 2, E to G) and the neuronal marker βIII-tubulin (fig. S4, D to F). Thus, a GG comprises two different cell populations: glial cells and neurons (GFP-positive cells), which bear multiple primary cilia, putative sites of chemosensory transduction.

By systematic scanning of the nasal cavity (fig. S5), we found that the KE covering the GG was already present at birth (mice aged 30 min); no cilia were found protruding into the airspace of the nasal cavity. The aspect of KE did not

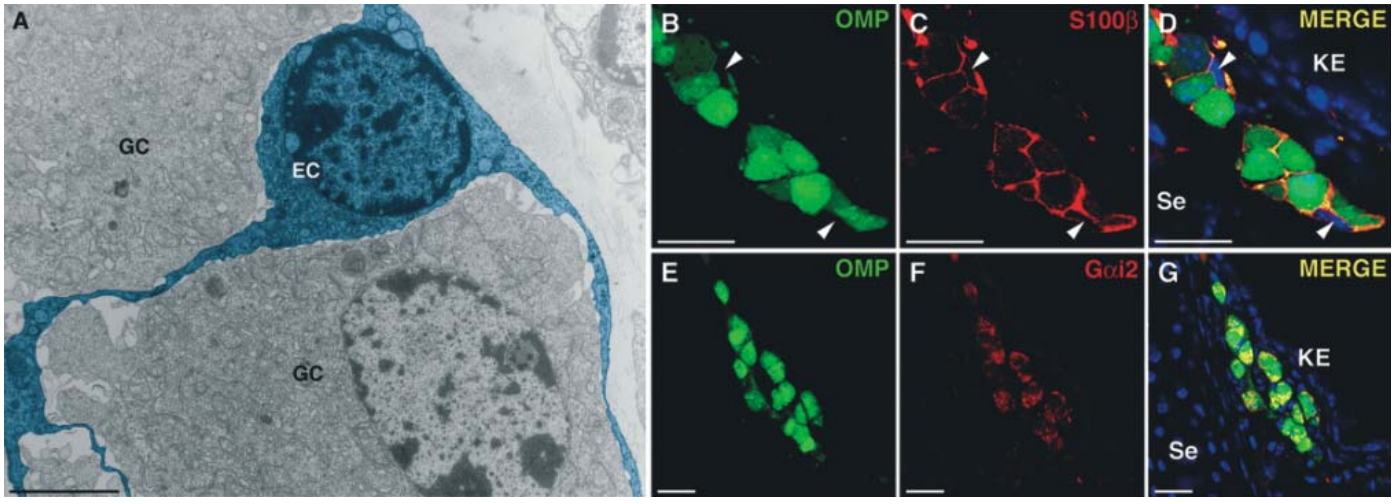

Fig. 2. The GG is composed of cells of different origins. (**A**) TEM micrograph confirming the presence of ensheathing cells (EC, false color blue) individually packaging GG cells (GC). An EC had a triangular cell body, a round nucleus, and long arms circling GG cells. (**B** to **G**) High-power views of glial or neuronal protein immunoreactivity. GG cells were recognized by their OMP-GFP expression [(B) and (E)]. (C) Glial marker S100β expressed in cells surrounding the GG cells. (D) Merge of (B) and (C). White arrowheads indicate GFP-negative glial cells [(B) to (D)]. (F) $G_{\alpha i2}$ staining in GG cells. (G) Merge of (E) and (F), where colocalization appears in yellow. Scale bars, 2 μm in (A) and 20 μm in (B) to (G).

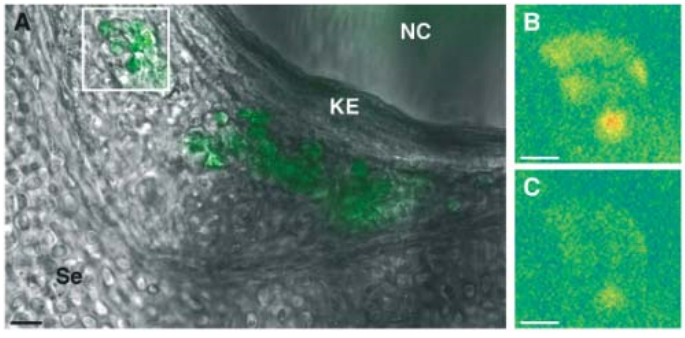

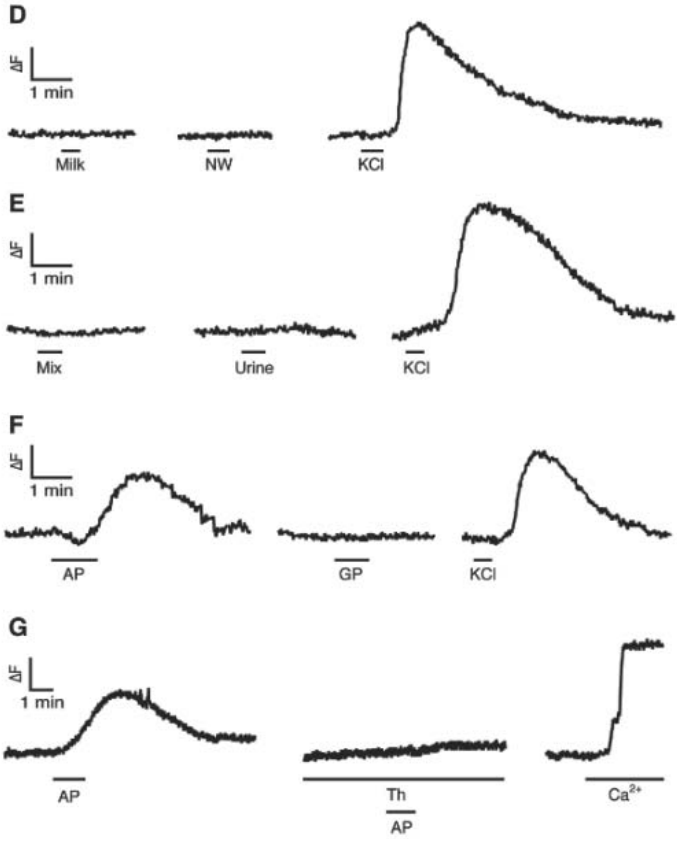

Fig. 3. APs activate GG cells. (**A**) Coronal slice from the GG region. (**B**) Uptake of Fura-2AM into GG cells within the white rectangle from (A), measured at 380 nm before (B) and at the peak of the intracellular calcium increase induced by a control pulse of KCl (**C**). (**D** to **E**) Lack of calcium transients after the perfusion of mouse milk (Milk), nipple wash (NW), a mix of odors and known mouse pheromones (Mix), or mouse urine. (**F**) APs but not general pheromones (GP) induced a reversible calcium transient. (**G**) AP response was abolished only after depletion of intracellular calcium stores by thapsigargin (Th, 20 mM) in divalent-free medium. Fluorescence intensity ratio (ΔF) = $F340/F380$. Perfusion times are indicated by horizontal bars in (D) to (G). Scale bars, 20 μm in (A) and 10 μm in (B) and (C).

change with aging (fig. S5, B to D). To assess how potential chemosensory stimuli could reach and activate GG cells, we performed standard skin permeability assays using Toluidine blue (fig. S6, A to C) and Lucifer yellow (fig. S6, D and E). In contrast to the control (the back skin of the same animal) (fig. S6D), the KE covering the GG cells was found to be permeable by hydrophilic substances, suggesting that water-soluble chemostimuli have access to the outside zone of the GG cell clusters, where primary cilia are located (fig. S6E). A similar morphological situation is observed in *Caenorhabditis elegans*, in which the cilia of the amphid chemosensory neurons (AWA, AWB, and AWC), located under the cuticle, sense volatile and hydrophilic odors via direct diffusion (*20*).

Focusing on its potential water-soluble quality, we used calcium imaging on coronal slices to identify the GG chemostimulus (Fig. 3). Tissue slices were incubated in Fura-2 acetoxymethyl ester (AM), a calcium-sensitive dye. GG cells were identified by the intrinsic green fluorescence of GFP in their cell bodies (Fig. 3A), and the uptake of the dye was confirmed by fluorescence measurements (Fig. 3B). Chemical stimuli were delivered in oxycarbonated artificial cerebrospinal fluid (ACSF) continuously perfused on the tissue slices in the imaging chamber. Cell viability was assessed by pulses of KCl (Fig. 3, C to F). Various hypotheses have been made concerning the possible GG function, the most favorite being its role in mother-pup recognition (*10*, *11*, *14*) because of its presence at birth (*11*) and axonal wiring to the necklace glomeruli of the olfactory bulb implicated in newborn suckling behavior (*21*). However, we did not record any calcium increase with mouse milk (n = 24 cells, 4 mice) or mammary secretions (n = 29 cells, 5 mice) from lactating female mice (Fig. 3D). A mix of odors and known isolated mouse pheromones (*22*) (n = 43 cells, 15 mice) or mouse urine as the major source of pheromones (n = 29 cells, 9 mice) did not enhance fluorescence (Fig. 3E). Looking for other volatile and water-soluble stimuli to test on GG cells, we noticed that the intraspecies danger signals, the so-called APs, released by stressed animals are known to have these physical characteristics (*8*, *9*). We collected APs during killing of mice with CO_2, which is known to be a major stress factor (*23*). The perfusion of APs induced a reversible fluorescence enhancement in almost all tested GG cells from newborn and adult mice (n = 39 out of 41 cells, 7 mice; Fig. 3F). As a control, general pheromones (GPs) collected from mice freely behaving and communicating, when no stress was applied, did not induce any calcium increase (n = 25 cells, 5 mice; Fig. 3F) and neither did CO_2 itself (*24*) (n = 26 cells, 5 mice) or other hypothesized stimuli (*10*–*14*) such as acidification (pH = 6) (n = 19 cells, 3 mice) or temperature changes (from 37° to 4°C) (n = 5 cells, 2 mice) (fig. S7).

We investigated the origin of the calcium increase observed in the presence of APs and found that it could be recorded in divalent-free ACSF solution (n = 26 cells, 6 mice; Fig. 3G), indicating that it was generated preferentially by Ca^{2+} released from intracellular stores and not only by external calcium influx. Depletion of Ca^{2+} stores by thapsigargin (20 mM), an inhibitor of the microsomal Ca^{2+}-ATPases (*25*), abolished the response to APs (n = 8 cells, 2 mice; Fig. 3G). At the end of these experiments, perfusion of ACSF containing calcium (2 mM) induced an overshoot of the intracellular calcium concentration, confirming the previous opening of store-operated calcium channels. Thus, contrary to olfactory neurons, GG cells, with their primary cilia localized in an extracellular matrix made of type IV collagen and not in a mucus layer (fig. S1), can act independently from the calcium concentration present in their environment.

We next addressed the question of the behavioral relevance of AP sensing by GG cells. The isolated nature of the GG makes it suitable for lesion experiments, allowing axonal projection bundles of GG cells to be sectioned (axotomy) (*11*). After surgery, pups were given back to their mothers and mother-pup recognition was not affected by the procedure. Thirty days after the lesion, we tested whether APs able to activate a calcium increase in GG cells (ACSF + AP) also modified mice behavior in vivo (Fig. 4). APs induce a typical freezing reaction in rodents (*26*). Such a reaction was observed in control mice (n = 6) placed in a closed Plexiglas container in the presence of ACSF + AP (Fig. 4, A and B, and movie S1). After axonal lesions (Axo mice, n = 5; Fig. 4C), this behavior was replaced by exploring activity. These Axo mice were not affected anymore by the presence of APs in their environment (Fig. 4D and movie S2). Control and lesioned mice were equally efficient at finding a buried cookie in the bedding (Fig. 4E).

Pheromonal communication plays an important role in social interactions among individuals of the same species, affecting, in particular, sexual, territorial, and maternal behaviors (*27*). We morphologically characterized the GG and identified it as the olfactory subsystem mediating AP detection in neonate and adult mice. To perform this primordial function, the GG has a specialized and basic morphology: a ganglion protected from the external world by water-permeable keratin. The GG acts as a warning system dedicated to the recognition of short-lived molecules encoding danger. These molecules require immediate attention. The unusual location of the GG at the tip of the nose, far from the main olfactory system,

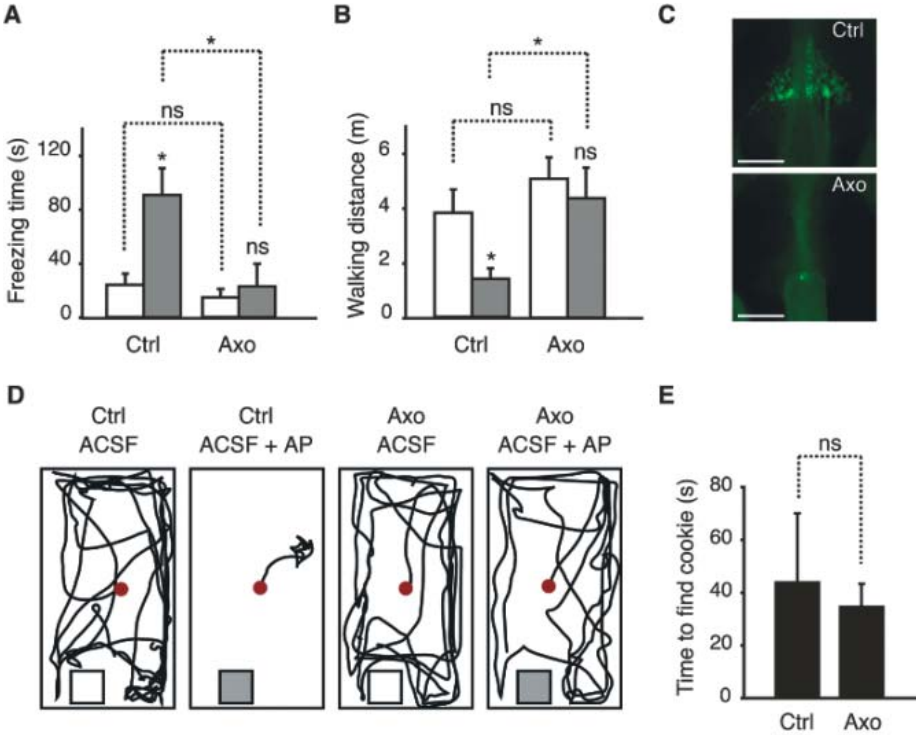

Fig. 4. AP sensing depends on a functional GG. (**A** and **B**) APs in ACSF solution (white bars, ACSF; gray bars, ACSF + AP) induced a significant increase in freezing behavior and a decrease in walking distance in control (Ctrl) but not in axotomized (Axo) OMP-GFP mice. (**C**) Whole-mount dorsal views of the GG region from Ctrl and Axo mice. (**D**) Representative tracking of the walking distance covered by mice in the test chamber in the absence (white square) or presence (gray square) of APs in the ACSF container (square). Red dots indicate the position of the mice at the beginning of the 3-min test. (**E**) Olfactory function in finding the cookie was similar in both experimental groups. In (A), (B), and (E), error bars indicate the SEM of n = 5 to 6 observations, $*P < 0.05$; ns, not significant. Scale bars, 500 μm in (C).

allows the stimuli to be rapidly detected. AP sensing is a conserved modality that is present from primitive organisms such as worms (*28*) to humans (*29*). The presence of a GG has been identified in all mammalian species looked at so far, including humans (*15*, *30*). When produced by a conspecific, APs play an important role in increasing overall species fitness (*31*).

References and Notes

1. M. H. Beale *et al*., *Proc. Natl. Acad. Sci. U.S.A.* **103**, 10509 (2006).
2. M. K. Stowe, T. C. Turlings, J. H. Loughrin, W. J. Lewis, J. H. Tumlinson, *Proc. Natl. Acad. Sci. U.S.A.* **92**, 23 (1995).
3. M. Ono, H. Terabe, H. Hori, M. Sasaki, *Nature* **424**, 637 (2003).
4. R. S. Mirza, D. P. Chivers, *J. Chem. Ecol.* **27**, 1641 (2001).
5. A. G. Gutierrez-Garcia, C. M. Contreras, M. R. Mendoza-Lopez, O. Garcia-Barradas, J. S. Cruz-Sanchez, *Physiol. Behav.* **91**, 166 (2007).
6. A. Boissy, C. Terlouw, P. Le Neindre, *Physiol. Behav.* **63**, 489 (1998).
7. C. Zalaquett, D. Thiessen, *Physiol. Behav.* **50**, 221 (1991).
8. Y. Kiyokawa, T. Kikusui, Y. Takeuchi, Y. Mori, *Chem. Senses* **30**, 513 (2005).
9. E. L. Abel, *Physiol. Behav.* **50**, 723 (1991).
10. D. S. Koos, S. E. Fraser, *Neuroreport* **16**, 1929 (2005).
11. D. Roppolo, V. Ribaud, V. P. Jungo, C. Luscher, I. Rodriguez, *Eur. J. Neurosci.* **23**, 2887 (2006).
12. S. H. Fuss, M. Omura, P. Mombaerts, *Eur. J. Neurosci.* **22**, 2649 (2005).
13. M. J. Storan, B. Key, *J. Comp. Neurol.* **494**, 834 (2006).
14. J. Fleischer, N. Hass, K. Schwarzenbacher, S. Besser, H. Breer, *Histochem. Cell Biol.* **125**, 337 (2006).
15. H. Grueneberg, *Z. Anat. Entwicklungsgesch.* **140**, 39 (1973).
16. J. Fleischer, K. Schwarzenbacher, H. Breer, *Chem. Senses* **32**, 623 (2007).
17. J. Fleischer, K. Schwarzenbacher, S. Besser, N. Hass, H. Breer, *J. Neurochem.* **98**, 543 (2006).
18. H. A. Praetorius, K. R. Spring, *Annu. Rev. Physiol.* **67**, 515 (2005).
19. V. Singla, J. F. Reiter, *Science* **313**, 629 (2006).
20. C. I. Bargmann, H. R. Horvitz, *Cell* **74**, 515 (1993).
21. K. Shinoda, Y. Shiotani, Y. Osawa, *J. Comp. Neurol.* **284**, 362 (1989).
22. T. Leinders-Zufall *et al*., *Nature* **405**, 792 (2000).
23. M. C. Leach, V. A. Bowell, T. F. Allan, D. B. Morton, *Comp. Med.* **52**, 249 (2002).
24. J. Hu *et al*., *Science* **317**, 953 (2007).
25. C. Mathes, S. H. Thompson, *J. Gen. Physiol.* **106**, 975 (1995).
26. T. Kikusui, S. Takigami, Y. Takeuchi, Y. Mori, *Physiol. Behav.* **72**, 45 (2001).
27. P. A. Brennan, F. Zufall, *Nature* **444**, 308 (2006).
28. B. D. Wisenden, M. C. Millard, *Anim. Behav.* **62**, 761 (2001).
29. R. Hauser *et al*., *Forensic Sci. Int.* **155**, 226 (2005).
30. T. Tachibana, N. Fujiwara, T. Nawa, *Arch. Histol. Cytol.* **53**, 147 (1990).
31. E. B. Mondor, B. D. Roitberg, *Proc. R. Soc. London Ser. B* **271**, S341 (2004).

32. We thank I. Rodriguez for the OMP-GFP mice; J. and S. Fakan for their enthusiastic help with EM techniques and for analyzing EM micrographs; G. Knott, A. Mucciolo, and S. Rosset for preparing EM tissue samples; the Cellular Imaging Facility of the University of Lausanne and its coordinator J.-Y. Chatton for valuable advice; C. Lebrand for providing antibodies; N. Rosenblatt-Velin for help with animal handling; and K. Geering and R. Stoop for fruitful discussions on the manuscript. Supported by the Department of Pharmacology and Toxicology, the Swiss National Science Foundation, and the Leenaards Foundation.

Supporting Online Material

www.sciencemag.org/cgi/content/full/321/5892/1092/DC1
Materials and Methods
Figs. S1 to S8
References
Movies S1 and S2

21 May 2008; accepted 21 July 2008
10.1126/science.1160770

Control of the Reversibility of Cellular Quiescence by the Transcriptional Repressor HES1

Liyun Sang,[1,2] Hilary A. Coller,[3] James M. Roberts[1,4]*

The mechanisms by which quiescent cells, including adult stem cells, preserve their ability to resume proliferation after weeks or even years of cell cycle arrest are not known. We report that reversibility is not a passive property of nondividing cells, because enforced cell cycle arrest for a period as brief as 4 days initiates spontaneous, premature, and irreversible senescence. Increased expression of the gene encoding the basic helix-loop-helix protein HES1 was required for quiescence to be reversible, because HES1 prevented both premature senescence and inappropriate differentiation in quiescent fibroblasts. In some human tumors, the HES1 pathway was activated, which allowed these cells to evade differentiation and irreversible cell cycle arrest. We conclude that HES1 safeguards against irreversible cell cycle exit both during normal cellular quiescence and pathologically in the setting of tumorigenesis.

Reversibility is a defining characteristic of cellular quiescence: In contrast to cells in other nonproliferating states, including terminal differentiation and senescence, only quiescent cells normally retain the ability to resume proliferation. Cells entering each of these arrested states stop the cell division cycle by increasing the abundance of cell cycle inhibitory proteins, such as cyclin-dependent kinase (CDK) inhibitors (*1*–*5*), yet it is only in quiescent cells that this block to proliferation can be reversed. Expression of CDK inhibitors is sufficient to enforce a nondividing state (*1*), and depletion of these proteins can disrupt quiescence in many cells, including hematopoietic stem cells (*6*, *7*). However, ectopic expression of CDK inhibitors does not recapitulate the transcriptional signature of quiescent cells (*8*), which suggested that cell cycle arrest and cellular quiescence are not functionally equivalent.

The amount of the CDK inhibitor $p21^{Cip1}$ (p21) is increased in fibroblasts that become quiescent in response to serum starvation or cell-cell contact (fig. S1A). To determine whether regulated expression of p21 would induce a reversible, quiescent-like cell cycle arrest, we used retroviral-mediated gene transduction to introduce into proliferating early-passage human lung fibroblasts a p21 expression cassette flanked by loxP sites (loxp-p21) (fig. S2A). Expression of p21 from this cassette efficiently blocked S-phase entry (Fig. 1A). Four days later, we reversed the increase in p21 abundance by infecting the cells with a vector expressing a cre recombinase–green fluorescent fusion protein (cre-GFP). Six days later, more than 95% of the cells showed fluorescence from GFP, and the expression of p21 had returned to the baseline level found in proliferating cells (Fig. 1B). Nevertheless, these cells failed to reenter the cell cycle (Fig. 1A), expressed increased amounts of the senescence-associated enzyme β-galactosidase (Fig. 1C), and formed senescence-associated heterochromatin foci (SAHF) (Fig. 1J). As a control, we also transduced cells with an empty loxp vector and arrested them by contact inhibition for 4 days. After infection with cre-GFP, more than 95% of the cells showed fluorescence from GFP. These cells resumed proliferation efficiently after release from contact inhibition (Fig. 1D) and did not display a senescent-like morphology. These experiments showed that sustained (4 days or longer) expression of p21 induced an irreversible senescent-like state. We thus explored the mechanism by which quiescent cells avoid this fate despite their constitutive expression of p21.

We previously used gene expression profiling to observe that the transcriptional repressor Hairy and Enhancer of Split1 (HES1) is transcriptionally regulated in quiescent fibroblasts, but not in fibroblasts that have undergone cell cycle arrest in response to ectopic expression of CDK inhibitory proteins (*8*). We confirmed

[1]Division of Basic Sciences, Fred Hutchinson Cancer Research Center, Seattle, WA 98109, USA. [2]Molecular and Cellular Biology Program, University of Washington, Seattle, WA 98195, USA. [3]Department of Molecular Biology, Princeton University, Princeton, NJ 08544, USA. [4]Department of Biochemistry, University of Washington, Seattle, WA 98195, USA.

*To whom correspondence should be addressed. E-mail: jroberts@fhcrc.org

the increased abundance of HES1 mRNA in quiescent human fibroblasts by quantitative real-time polymerase chain reaction (PCR). Compared with proliferating fibroblasts, serum-deprived or contact-inhibited cells expressed amounts of HES1 mRNA that were higher by factors of 12.2 and 8.6, respectively, whereas cells that were arrested by p21 did not increase transcription of the HES1 gene (fig. S1B). We thus tested whether HES1, which is part of a large chromatin modification complex (*9*–*11*), might influence the reversibility of cellular quiescence.

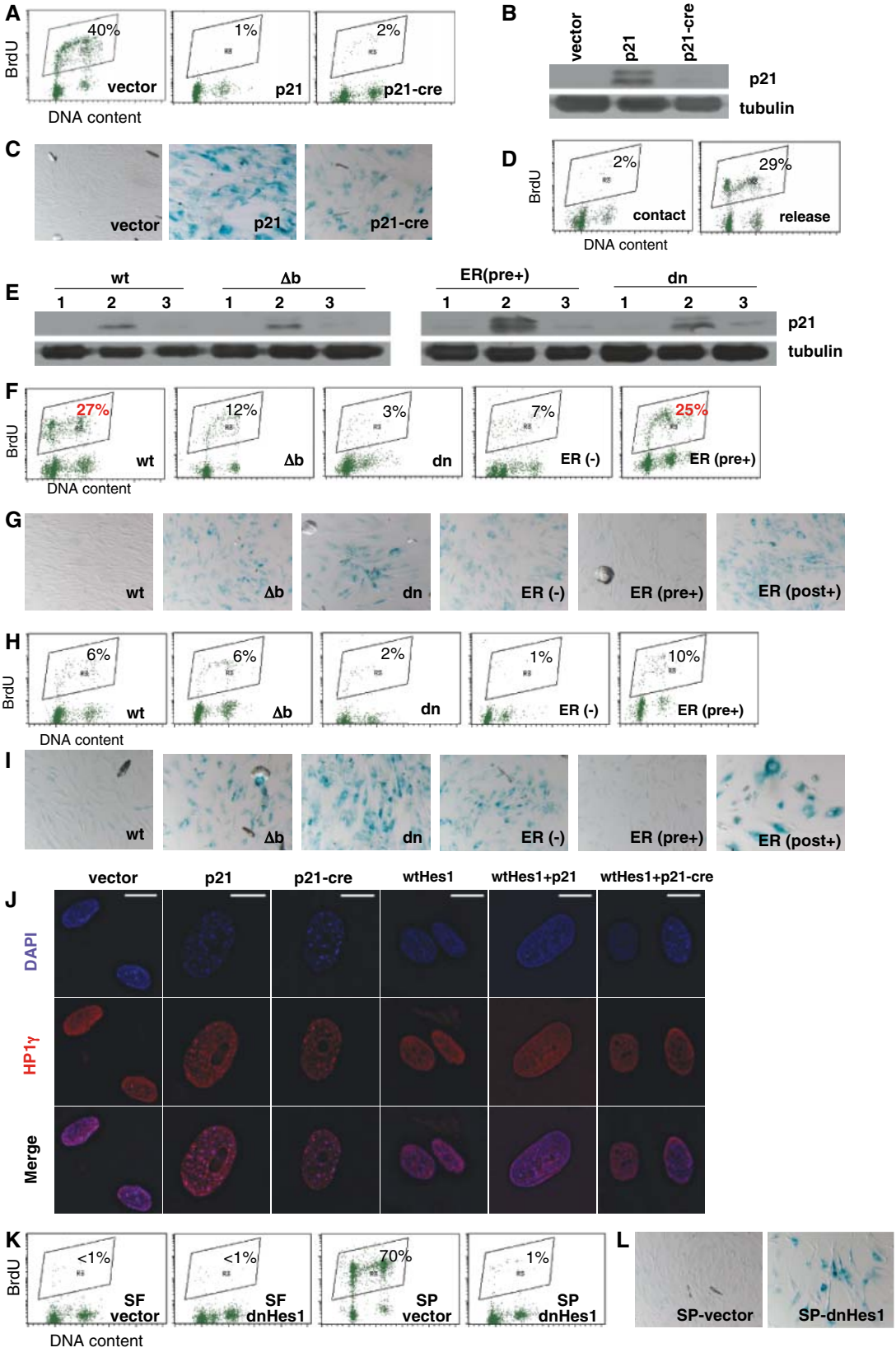

Fig. 1. Suppression of p21-initiated senescence by HES1. (**A** to **C**) Human fibroblasts (HFs) were transduced (day 0) with a $p21^{Cip1}$ expression cassette flanked by loxP sites (p21) or a loxp vector (vector). On day 4, p21-expressing cells were transduced with a vector expressing cre recombinase and GFP (p21-cre). On day 10, BrdU was added for 6 hours. (A) The percentage of BrdU-positive cells is indicated. (B) Abundance of p21 protein and (C) expression of senescence-associated β-galactosidase (SA-β-gal). (**D**) HFs were transduced with an empty vector, contact inhibited for 4 days (contact), then infected with cre-GFP and replated at lower density (release). The percentage of BrdU-positive cells is shown. (**E** to **I**) HFs were transduced with wtHES1, wtHES1-ER, DNA-binding mutant HES1 (Δb), or dnHES1, and then transduced with p21-loxP. 4-hydroxytamoxifen was added to wtHes1-ER cells before p21 transduction (pre +), 9 days after p21 transduction (post +), or not applied (–). Four days after p21 transduction, cells were either transduced with cre-GFP [(F) and (G)] or maintained with high p21 levels [(H) and (I)]. (E) Expression levels of p21. Lane 1, control; lane 2, p21; lane 3, p21 + cre. [(F) and (H)] Cells were incubated with BrdU for 6 hours. [(G) and (I)] Expression of SA-β-gal. (**J**) Cells were stained with DAPI and an antibody to HP1γ. (**K**) HFs were transduced with dnHes1 or an empty vector, serum deprived for 10 days (SF), and then restimulated with full-serum medium (SP). BrdU was added for 24 hours. The percentage of BrdU-positive cells is indicated. (**L**) Expression of SA-β-gal.

To determine whether HES1 is sufficient to prevent senescence associated with prolonged cell cycle arrest, we first transduced early-passage human lung fibroblasts with the following HES1 constructs: wtHes1, wtHes1-estrogen receptor fusion protein (wtHes1-ER), ΔbHes1 (a mutant defective in DNA binding), and dnHes1 (a dominant-negative HES1) (fig. S2B) (*12*). dnHES1 retains the DNA binding and dimerization domains of HES1 but lacks a C-terminal WRPW (Trp-Arg-Pro-Trp) domain, which mediates the interaction between HES1 and its co-repressors (*10*, *11*). dnHes1 competes with the endogenous HES1 for binding to DNA and therefore prevents the chromatin modifications caused by endogenous HES1 and its associated proteins. We then stably transduced these cells with the loxp-p21 vector and induced p21 expression and cell cycle arrest for 4 days. Cells were then transduced with cre-GFP to restore p21 expression to baseline, or maintained with p21 expression at high levels (Fig. 1E). Six days after down-regulation of p21, cells expressing ΔbHes1, dnHes1, or wtHes1-ER (–4-hydroxytamoxifen) failed to reenter the cell cycle and displayed a senescent phenotype. In contrast, cells expressing wtHes1 or wtHes1-ER (+4-hydroxytamoxifen) resumed proliferation after the removal of p21, and few cells showed β-galactosidase expression (Fig. 1, F and G). Wild-type HES1 also suppressed the appearance of a senescent morphology in cells maintained with high amounts of p21 (Fig. 1, H, to J). However, activation of the conditional Hes1-ER construct with 4-hydroxytamoxifen did not reverse senescence in cells that had already undergone this phenotypic transition (Fig. 1, G and I).

These experiments showed that HES1 was sufficient to prevent senescence associated with ectopic expression of p21, but is it necessary to prevent senescence in naturally quiescent cells? After 10 days of quiescence induced by serum-deprivation, control fibroblasts resumed proliferation after stimulation with serum (Fig. 1K). In contrast, fibroblasts that expressed dnHES1 during the 10 days of culture without serum became morphologically senescent, expressed senescence-associated β-galactosidase, and failed to resume proliferation after addition of serum (Fig. 1, K and L). Thus, HES1 controls the reversibility of cellular quiescence by blocking an alternative fate characterized by irreversible cell cycle arrest.

Premature senescence in normal human fibroblasts also occurs in response to oncogene activation and is thought to represent a physiological pathway for tumor suppression (*2*). To investigate whether HES1 influences oncogene-induced senescence, we transduced human fibroblasts (CCL153 and WI-38) with an empty vector or a construct expressing wtHes1. An activated oncogenic Ras gene (H-RasV12) was then introduced into these cells (*13*). Within 10 days of H-RasV12 expression, vector cells expressed increased amounts of the senescence-associated enzyme β-galactosidase and formed SAHF. HES1 suppressed these senescent phenotypes (Fig. 2, A to C), without affecting the abundance of Ras or p16 (Fig. 2D).

Quiescent fibroblasts are resistant to terminal differentiation and permanent cell cycle arrest induced by ectopic expression of the myogenic transcription factor MyoD, whereas fibroblasts arrested after ectopic expression of a CDK inhibitor p21 are fully MyoD responsive (*8*). This is another example of how quiescent cells actively maintain the ability to reversibly enter and exit the cell cycle. We now find that expression of HES1 in primary human fibroblasts is both

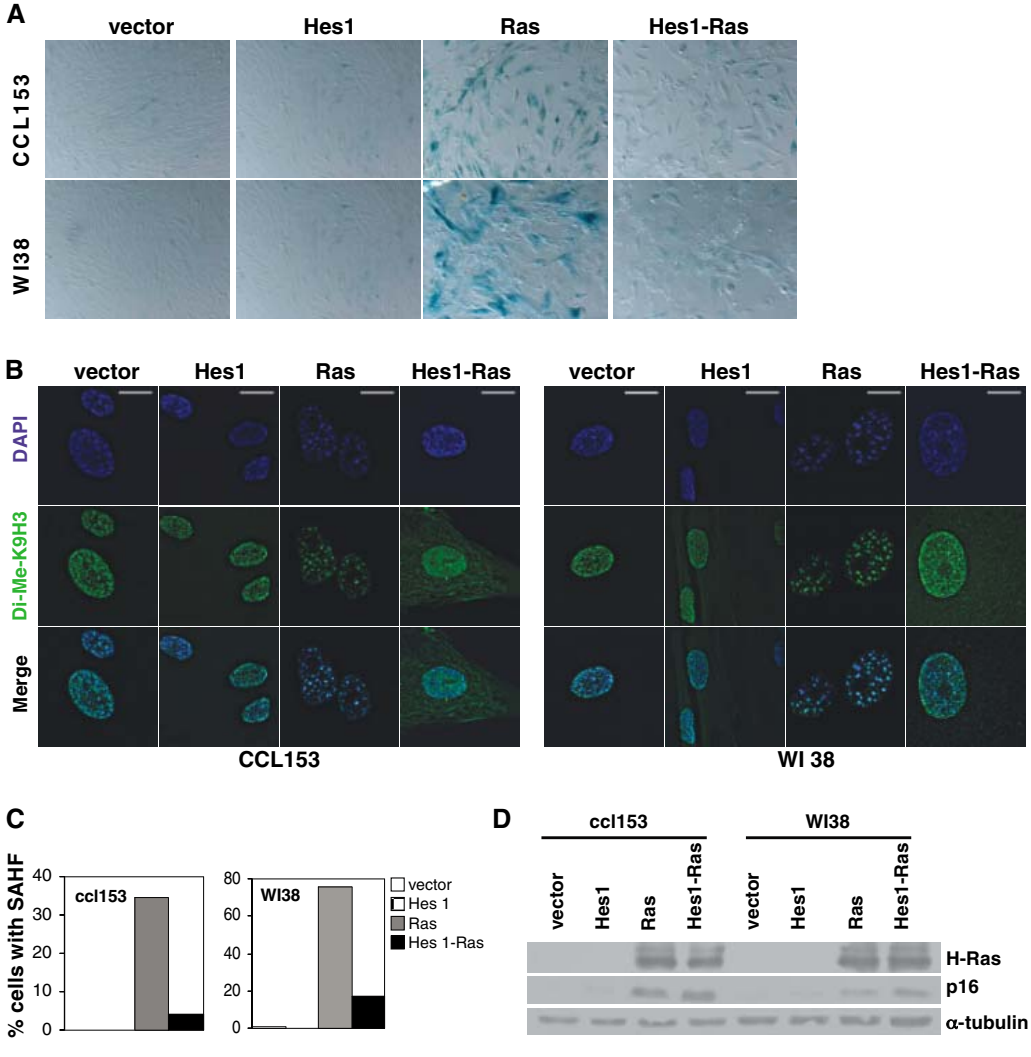

Fig. 2. Suppression of oncogene Ras-induced senescence by HES1. Primary human fibroblasts (CCL153 and WI-38) were transduced with an empty vector or wtHes1. Cells were then transduced with an activated form of H-Ras. Ten days after H-Ras expression, (**A**) cells were stained for senescence-associated β-galactosidase and (**B**) cells were stained with DAPI and an antibody to di-Me-K9H3. Scale bars, 20 μm. (**C**) Percentage of cells with SAHF. Results were quantitated by counting 100 cells on each slide, from two independent experiments. (**D**) Abundance of H-Ras and p16 protein.

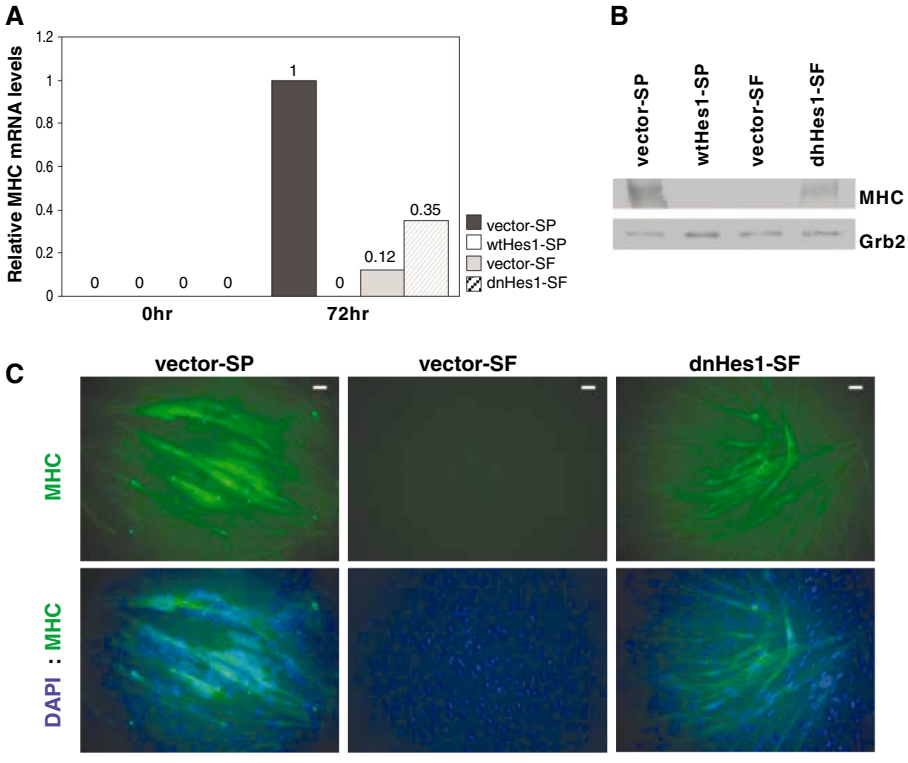

Fig. 3. Suppression of MyoD-induced muscle differentiation by HES1. Primary human fibroblasts (CCL153) were sequentially transduced with a MyoD-estrogen receptor fusion protein (MyoD-ER) and then with an empty vector (vector), wtHes1, or dnHes1. Proliferating cells were induced to differentiate by β-estradiol (SP) or were made quiescent for 4 days by serum starvation (SF) before induction of differentiation. (**A**) At 0 and 72 hours after addition of β-estradiol, MHC RNA was measured by real-time PCR normalized to glyceraldehyde phosphate dehydrogenase levels. Relative change compared with differentiated vector cells is plotted. Data are the average of duplicates. RNA amounts below the detection limit are indicated as "0." (**B**) The induction of MHC at 72 hours after differentiation is shown by immunoblot and (**C**) by immunostaining using an antibody to MHC. MHC is green; nuclei are blue (DAPI). Scale bars, 20 μm.

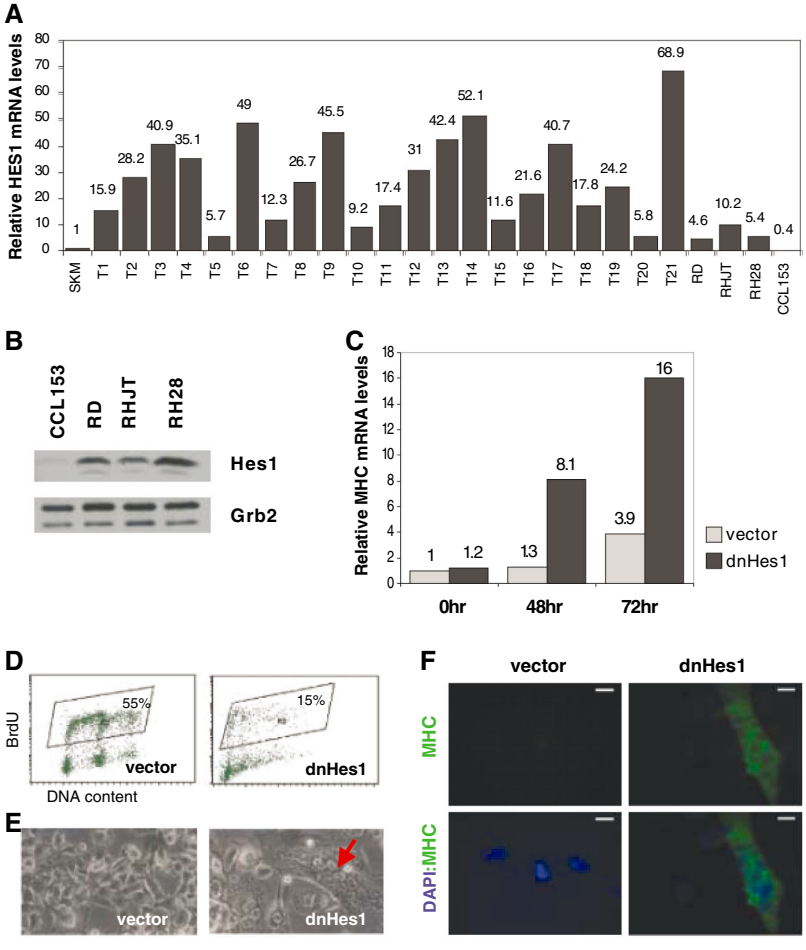

Fig. 4. Expression and function of HES1 in rhabdomyosarcomas. (**A**) The expression of HES1 was measured by real-time PCR in human rhabdomyosarcoma primary tumors (T1-T21) and cell lines (RD, RHJT, and RH28), in control skeletal muscle (SKM), and in primary human fibroblasts (CCL153). Relative change compared with control SKM is plotted. Data are the average of duplicates. (**B**) Abundance of HES1 protein in rhabdomyosarcoma cells. (**C**) RHJT cells were transduced with dnHes1 or vector control and then transferred to low-serum media to induce differentiation. At the indicated time points, MHC expression was measured as above. Relative change compared with control cells is plotted. Data are the average of duplicates. (**D**) RHJT cells were transduced with dnHes1 or vector control and were maintained in growth medium for 2 weeks. Cells were then incubated with BrdU for 6 hours and analyzed by flow cytometry. The percentage of BrdU-positive cells is indicated. (**E**) RHJT cells expressing dnHes1 formed multinucleated myotubes (red arrow) and (**F**) expressed MHC (green). Nuclei are blue (DAPI). Scale bars, 20 μm.

necessary and sufficient to inhibit MyoD-induced differentiation. We sequentially transduced cells with a vector expressing a MyoD–estrogen receptor fusion protein (MyoD-ER) and a vector expressing wild-type HES1 (wtHes1) or dnHes1. Cells were then induced to differentiate by exposure to β-estradiol. Expression of myosin heavy chain (MHC) RNA and protein, molecular markers for muscle differentiation, were detected in control proliferating fibroblasts but not in proliferating fibroblasts expressing wtHes1 (Fig. 3, A and B) (*14*). Quiescent fibroblasts did not express MHC in response to MyoD (Fig. 3, A to C) (*8*). However, expression of dnHes1 allowed quiescent fibroblasts to undergo myogenic differentiation in response to MyoD. Thus, MHC RNA and protein accumulated in dnHes1 cells but not in control cells (Fig. 3, A and B), and production of MHC was also detected by immunostaining with an antibody to MHC (Fig. 3C). Furthermore, dnHes1 cells fused to form multinucleated myotubes within 72 hours of MyoD-ER activation (Fig. 3C).

The WRPW domain of HES1 binds to Transducin-Like Enhancer of split 1 (TLE1), which functions as a co-repressor by recruiting histone deacetylases (*9*–*11*). Compared with proliferating fibroblasts, cells that were made quiescent after deprivation of serum or by contact inhibition expressed amounts of TLE1 that were higher by factors of 6.2 and 3.1, respectively, whereas cells that were arrested by p21 did not up-regulate TLE1 (fig. S1C). We investigated whether TLE1, like HES1, was necessary to suppress differentiation in quiescent fibroblasts. We sequentially transduced primary human fibroblasts with a vector expressing MyoD-ER and a vector expressing either shRNA-TLE1 or a control shRNA (short hairpin RNA). Expression of shRNA-TLE1 specifically reduced TLE1 expression by 64% but did not decrease the abundance of closely related TLE2 (fig. S3, A and B). Cells were deprived of serum for 4 days and then transferred to differentiation medium containing β-estradiol. Control fibroblasts did not undergo myogenic differentiation, whereas quiescent shRNA-TLE1 cells expressed MHC mRNA and protein and fused to form multinucleated myotubes within 72 hours (fig. S3, C and D).

Expression of HES1 can be increased by Notch-dependent and Notch-independent pathways (*15*–*18*). Exposure of quiescent fibroblasts to a pharmacological inhibitor of Notch signaling, the γ-secretase inhibitor N-[N-(3,5-difluorophenacetyl)-L-alanyl]-S-phenylglycine t-butyl ester (DAPT) (*19*), decreased the mRNA abundance of HES1 (fig. S4A). Furthermore, DAPT-treated quiescent fibroblasts accumulated MHC within 72 hours of activation of MyoD (fig. S4B). Therefore, activation of the Notch pathway appears to contribute at least partially to accumulation of HES1 and maintenance of a nondifferentiated state in quiescent fibroblasts.

Tumor cells might adopt pathways normally used by quiescent cells to suppress entry into irreversibly arrested states (*8*). Indeed, our results showed that HES1 may contribute to tumorigenesis by suppressing oncogene-induced senescence. Rhabdomyosarma (RMA) is an aggressive skeletal muscle tumor of childhood that originates from myogenic progenitor cells (*20*). RMA's constitutively express MyoD, but myogenesis is blocked by unknown mechanisms (*21*). HES1 mRNA amounts were increased by factors of 4.6 to 68.9 in 21 out of 21 primary RMAs of varying histology, location, and stage. The abundances of HES1 mRNA and protein were increased in 3 out of 3 RMA cell lines (Fig. 4, A and B). We transduced a human RMA cell line, RHJT, with a vector expressing dnHes1 or an empty vector control. After we transferred them to differentiation medium containing a low amount of serum, we observed a large time-dependent accumulation of MHC in RHJT cells expressing dnHes1 compared with that in control RHJT cells (Fig. 4C). Expression of dnHes1 also gradually reduced proliferation and promoted differentiation of RHJT cells in growth medium containing 10% serum. Both dnHes1 cells and control cells were maintained in growth medium and passaged every 3 days. After 2 weeks in culture, 55% of control cells became labeled with a brief pulse of 5-bromo-2-deoxyuridine (BrdU), whereas only 15% of dnHes1 cells showed incorporation of BrdU (Fig. 4D). In cells expressing dnHes1, exit from the cell cycle was accompanied by cell fusion to form multinucleated myotubes that expressed large amounts of myosin heavy chain (MHC) (Fig. 4, E and F). Exposure of RHJT cells to 5 μM DAPT to inhibit Notch signaling reduced the expression of HES1 by 70%, and after transfer of cells to differentiation medium, expression of MHC was increased in DAPT-treated cells (fig. S4, C and D). These results suggest that Notch signaling may contribute to tumor initiation and/or progression in rhabdomyosarcomas through increased expression of HES1 and suppression of MyoD-dependent differentiation.

In conclusion, we showed that HES1 maintained the reversibility of quiescence by controlling the choice between different out-of-cycle states. Inactivation of HES1 caused nondividing fibroblasts to spontaneously enter into an irreversible senescent state or allowed them to terminally differentiate in response to specific signals. Terminal differentiation and cellular senescence are both associated with the repackaging of nuclear DNA into stable heterochromatic structures that repress the expression of proliferation-related genes (*22*, *23*). These heterochromatic foci do not assemble in reversibly arrested, quiescent fibroblasts (*22*). We propose that HES1, which is part of a large chromatin-modifying complex (*9*–*11*), may counteract the heterochromatin assembly pathways present in irreversibly arrested cells. This hypothesis is supported by our demonstration that the HES1 DNA binding and co-repressor recruiting activities were required to prevent senescence and suppress differentiation in quiescent fibroblasts. Furthermore, we showed that expression of HES1 suppressed the formation of senescence-associated heterochromatin foci. Quiescent hematopoietic progenitor cells also up-regulate HES1 (*12*), which suggests that this function might be general.

Increased amounts of HES1 have been observed in ovarian carcinomas, breast cancers, non–small cell lung cancers, meningiomas, and medulloblastomas (*24*–*29*). HES1 expression is also increased in the stemlike cells in breast ductal carcinoma in situ (DCIS) and is associated with recurrence at 5 years after surgery (*26*). We showed in human rhabdomyosarcomas that the effect of pathological overproduction of HES1 was to cause these tumors cells to become refractory to cell cycle arrest and terminal differentiation and that inactivation of HES1 led to spontaneous tumor cell differentiation. The ability of HES1 to determine the fate of quiescent cells may underlie, at least in part, the widespread role of the Notch and HES1 pathways in maintaining stem cell lineages, regulating tissue regeneration, and promoting tumorigenesis.

References and Notes

1. C. J. Sherr, J. M. Roberts, *Genes Dev.* **9**, 1149 (1995).
2. J. Campisi, F. d'Adda di Fagagna, *Nat. Rev. Mol. Cell Biol.* **8**, 729 (2007).
3. C. M. Beausejour *et al.*, *EMBO J.* **22**, 4212 (2003).
4. K. Guo, J. Wang, V. Andres, R. C. Smith, K. Walsh, *Mol. Cell. Biol.* **15**, 3823 (1995).
5. O. Halevy *et al.*, *Science* **267**, 1018 (1995).
6. T. Cheng *et al.*, *Science* **287**, 1804 (2000).
7. Y. H. Kwon, A. Jovanovic, M. S. Serfas, H. Kiyokawa, A. L. Tyner, *J. Biol. Chem.* **277**, 41417 (2002).
8. H. A. Coller, L. Sang, J. M. Roberts, *PLoS Biol.* **4**, e83 (2006).
9. G. Chen, J. Fernandez, S. Mische, A. J. Courey, *Genes Dev.* **13**, 2218 (1999).
10. A. L. Fisher, S. Ohsako, M. Caudy, *Mol. Cell. Biol.* **16**, 2670 (1996).
11. D. Grbavec, S. Stifani, *Biochem. Biophys. Res. Commun.* **223**, 701 (1996).
12. X. Yu *et al.*, *Stem Cells* **24**, 876 (2006).
13. M. Serrano, A. W. Lin, M. E. McCurrach, D. Beach, S. W. Lowe, *Cell* **88**, 593 (1997).
14. Y. Sasai, R. Kageyama, Y. Tagawa, R. Shigemoto, S. Nakanishi, *Genes Dev.* **6**, 2620 (1992).
15. B. Jennings, A. Preiss, C. Delidakis, S. Bray, *Development* **120**, 3537 (1994).
16. S. Jarriault *et al.*, *Nature* **377**, 355 (1995).
17. C. L. Curry, L. L. Reed, B. J. Nickoloff, L. Miele, K. E. Foreman, *Lab. Invest.* **86**, 842 (2006).
18. W. J. Ingram, K. I. McCue, T. H. Tran, A. R. Hallahan, B. J. Wainwright, *Oncogene* **27**, 1489 (2008).
19. A. Geling, H. Steiner, M. Willem, L. Bally-Cuif, C. Haass, *EMBO Rep.* **3**, 688 (2002).
20. H. Scrable *et al.*, *Proc. Natl. Acad. Sci. U.S.A.* **86**, 7480 (1989).
21. S. J. Tapscott, M. J. Thayer, H. Weintraub, *Science* **259**, 1450 (1993).
22. M. Narita *et al.*, *Cell* **113**, 703 (2003).
23. S. A. Grigoryev, Y. A. Bulynko, E. Y. Popova, *Chromosome Res.* **14**, 53 (2006).
24. I. C. Cuevas *et al.*, *Cancer Res.* **65**, 5070 (2005).
25. O. Hopfer, D. Zwahlen, M. F. Fey, S. Aebi, *Br. J. Cancer* **93**, 709 (2005).
26. G. Farnie *et al.*, *J. Natl. Cancer Inst.* **99**, 616 (2007).
27. J. Konishi *et al.*, *Cancer Res.* **67**, 8051 (2007).
28. A. R. Hallahan *et al.*, *Cancer Res.* **64**, 7794 (2004).
29. X. Fan *et al.*, *Cancer Res.* **66**, 7445 (2006).

30. We acknowledge expert advice and materials from S. Tapscott and members of the Tapscott laboratory, J. Olson and members of the Olson laboratory, members of the Galloway laboratory, S. Parkhurst, V. Vasioukhin, X. Yu, C. Civin, K. Fitzgerald, W. Chien, K. Loeb, M. Mehaffey, R. Eisenman, M. Groudine, D. Gottschling, R. Zhang, P. Adams, and members of the Roberts laboratory. L.S. acknowledges support from the Howard Hughes Medical Institute. J.M.R. was supported by grants from NIH. H.A.C. is the Milton E. Cassel scholar of the Rita Allen Foundation and acknowledges support from the New Jersey Commission on Cancer Research and the Pharmaceutical Research and Manufacturers of America Foundation. H.A.C. is supported by National Institute of General Medical Sciences Center of Excellence grant P50 GM071508.

Supporting Online Material
www.sciencemag.org/cgi/content/full/321/5892/1095/DC1
Materials and Methods
Figs. S1 to S4
References

1 February 2008; accepted 22 July 2008
10.1126/science.1155998

Automatic Mental Associations Predict Future Choices of Undecided Decision-Makers

Silvia Galdi,[1]* Luciano Arcuri,[1] Bertram Gawronski[2]

Common wisdom holds that choice decisions are based on conscious deliberations of the available information about choice options. On the basis of recent insights about unconscious influences on information processing, we tested whether automatic mental associations of undecided individuals bias future choices in a manner such that these choices reflect the evaluations implied by earlier automatic associations. With the use of a computer-based, speeded categorization task to assess automatic mental associations (i.e., associations that are activated unintentionally, difficult to control, and not necessarily endorsed at a conscious level) and self-report measures to assess consciously endorsed beliefs and choice preferences, automatic associations of undecided participants predicted changes in consciously reported beliefs and future choices over a period of 1 week. Conversely, for decided participants, consciously reported beliefs predicted changes in automatic associations and future choices over the same period. These results indicate that decision-makers sometimes have already made up their mind at an unconscious level, even when they consciously indicate that they are still undecided.

Imagine the following scenario: It is election time and the available voting options include two political candidates. You do not have a strong party affiliation that could guide your voting decision, and you are still undecided which of the two candidates deserves your vote. Over the next couple of weeks, you pay close attention to the media coverage of the two candidates' political campaigns and to what the candidates say about various issues you care about. After several weeks of deliberation, you finally decide that you should give your vote to candidate A rather than candidate B, and that decision is ultimately reflected in your vote on election day.

Common wisdom, as well as theorizing in psychological science, suggests that such processes of decision-making are based on a given individual's weighting of the information that is acquired during a phase of deliberation about the available options (*1*–*3*). According to this view, future choices primarily depend on (i) the particular information that is acquired, and (ii) the decision-maker's personal weighting of that information. In this study, we investigated the differential effect of automatic mental associations and consciously held beliefs on future choices by individuals who claim to be decided versus undecided. Conceptually, automatic mental associations are defined as those associations that come to mind unintentionally, that are difficult to control once they are activated, and that may not necessarily be endorsed at a conscious level (*4*, *5*). Such automatic associations are often contrasted with consciously held beliefs, which can be described as mental contents that an individual explicitly endorses as accurate (*3*, *5*). The measurement of automatic associations has been advanced by the development of so-called implicit measures, most of which are based on participants' performance on computer-based, speeded categorization tasks (*6*, *7*). These implicit measures differ from explicit measures employed to assess conscious beliefs, which are based on standard self-report or survey methodology.

We provide evidence that future choices of undecided individuals can be predicted by their current automatic mental associations, even when these individuals consciously report that they are still undecided. This case is contrasted with future choices made by decided individuals, which we expected to be guided by consciously held beliefs about choice options rather than automatic mental associations. Our hypothesis that automatic associations may predict future choices of undecided decision-makers is inspired by earlier research on political decision-making (*8*) and biased information processing (*9*, *10*). The latter line of research has shown that automatic associations can bias the processing of new information in a manner that is consistent with the meaning

[1]Department of Developmental Psychology and Socialization, University of Padova, Via Venezia 8, 35131 Padova, Italy. [2]Department of Psychology, University of Western Ontario, Social Science Centre, London, Ontario N6A 5C2, Canada.

*To whom correspondence should be addressed. E-mail: silvia.galdi@unipd.it

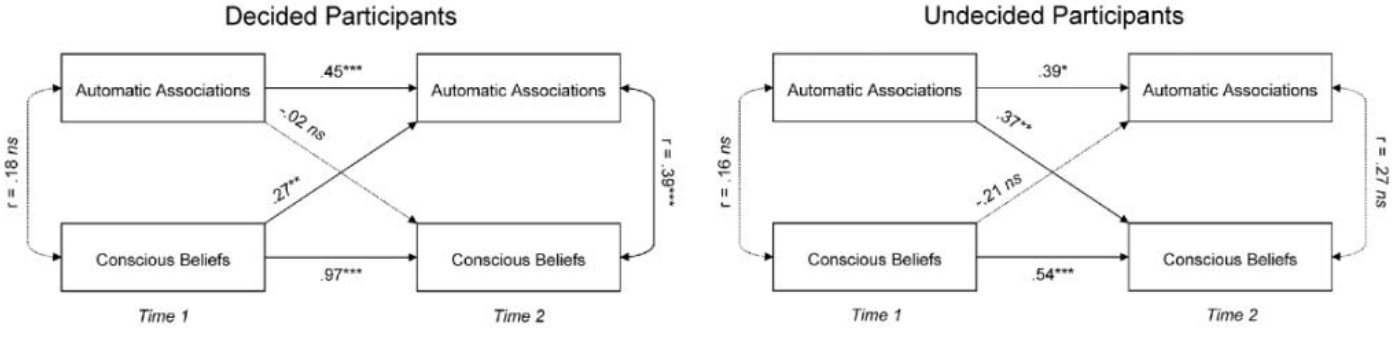

Fig. 1. Stability (horizontal arrows) and change (diagonal arrows) in automatic associations and consciously held beliefs from time 1 to time 2 (1 week apart) for participants who were indicated to be decided (n = 96) or undecided (n = 33) at time 1. The figure shows standardized beta values of simultaneous multiple regression analyses based on a two-wave-two-variable panel design (* P < 0.05; ** P < 0.01; *** P < 0.001; ns, not significant).

of previously existing associations. A useful example to illustrate such effects is a study on biases in face perception (*10*). In this study, white participants were presented with short movie clips in which the facial expressions of black and white faces that were fully controlled for physiognomic features changed from hostile to friendly or vice versa. Depending on the particular condition, participants' task was to indicate either the offset or the onset of hostility in the target's face. Results showed that participants identified hostility earlier or for a longer period in black compared to white faces. The relative size of these effects was correlated with participants' automatic associations—but not with their conscious beliefs—regarding blacks, such that enhanced perceptions of hostile expressions in black faces increased as a function of automatic negative associations regarding blacks. Expanding on these findings, other research has shown that such biasing effects of automatic associations remain unqualified by enhanced motivation to control biased or prejudiced responses (*9*), suggesting that automatic associations may influence information processing outside of conscious awareness (*11*).

Applied to the present question, these results suggest the possibility that future decisions of undecided individuals can be predicted by measuring their current automatic associations (*8*). Specifically, the available results (*9*, *10*) suggest that automatic associations could distort the processing of new information (e.g., by means of selective processing or biased interpretation), such that future decisions that are based on such distorted information will be in line with previously existing automatic associations. For instance, in our introductory example, an individual's automatic associations may be more favorable for candidate A compared to candidate B, even though this individual may not endorse a conscious preference for one candidate over the other (*12*, *13*). Yet, these associations may nevertheless influence the processing of new information about the two candidates, such that the subsequent conclusion drawn from this information is biased in favor of candidate A over candidate B. Hence, the individual may develop a conscious preference for candidate A over candidate B over the course of deliberating about the two options, which is rooted in the biasing influence of automatic associations on the processing of new information. From this perspective, the ultimate decision of an undecided individual may be determined, in a more or less probable sense, long before this individual consciously endorses a preference for one candidate over the other.

To test this assumption, we asked 129 residents of the city of Vicenza in Italy to complete various measures assessing their attitudes toward the enlargement of a U.S. military base in Vicenza. At the time of our data collection (October to December 2007), the enlargement plans were controversially discussed in the media, which led to a strong polarization among residents of the city. The measures included (i) a single-item question on whether participants are in favor of the enlargement, undecided, or against the enlargement (choice); (ii) a 10-item survey on participants' conscious beliefs about environmental, political, economic, and social consequences of the enlargement (conscious beliefs); and (iii) a computer-based response latency task designed to assess participants' automatic evaluative associations regarding the U.S. military base (automatic associations). The latter task was an adaptation of the Single-Category Implicit Association Test (*14*), in which participants had to categorize pictures of the U.S. military base, as well as positive and negative words, as quickly as possible. Automatic associations were inferred from participants' performance (i.e., response latencies, error rates) on different types of trials on this task (*15*). Participants completed all measures twice, with the two measurement occasions being 1 week apart.

To test the relations between automatic associations, consciously held beliefs, and future choices, we investigated the mutual relations between automatic associations and conscious beliefs for participants who were indicated to be decided versus undecided at time 1 using multiple regression and a two-wave-two-variable panel design (Fig. 1) (*16*). On the basis of *t* tests to determine the statistical significance of the standardized beta weights (*17*), the results indicated that automatic associations were relatively stable for both undecided participants [$t(30) = 2.30$, $P = 0.03$] and decided participants [$t(93) = 5.12$, $P < 0.001$]; conscious beliefs were relatively stable for undecided participants [$t(30) = 4.08$, $P < 0.001$] and highly stable for decided participants [$t(93) = 33.66$, $P < 0.001$]. Automatic associations at time 1 significantly predicted changes in conscious beliefs over time for undecided participants [$t(30) = 2.82$, $P = 0.009$], but not for decided participants [$t(93) = -0.86$, $P = 0.39$]. Conversely, conscious beliefs at time 1 significantly predicted changes in automatic associations over time for decided participants [$t(93) = 3.07$, $P = 0.003$], but not for undecided participants [$t(30) = -1.23$, $P = 0.23$] (*18*). These results suggest that for undecided participants, future conscious beliefs were to a significant extent determined by their earlier automatic associations, even though these participants had consciously reported being undecided at the time of the first measurement. In contrast, for decided participants, conscious beliefs predicted changes in automatic associations, presumably reflecting a consolidation of their consciously held beliefs (*5*). That is, conscious beliefs may have strengthened those associations that are in line with these beliefs, such that these associations become automatic over time.

To further investigate the relations of automatic associations and conscious beliefs to future choices, we simultaneously regressed participants' choices at time 2 (in favor, undecided, against) onto automatic associations and consciously held beliefs at time 1 (Fig. 2). Results showed that for decided participants, choices at time 2 were significantly predicted by their consciously held beliefs at time 1 [$t(93) = 15.40$, $P < 0.001$], with automatic associations being unrelated to future choices [$t(93) = -0.15$, $P = 0.88$]. Conversely, for undecided participants, choices at time 2 were significantly predicted by automatic associations at time 1 [$t(30) = 2.65$, $P = 0.01$], with consciously held beliefs showing a positive, albeit

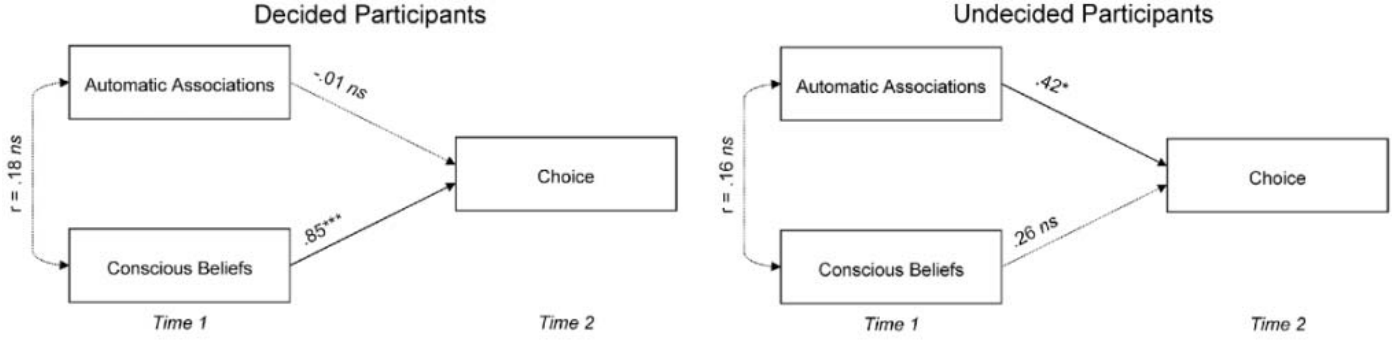

Fig. 2. Prediction of future choices (in favor, undecided, against) at time 2 by automatic associations and consciously held beliefs at time 1 (1 week apart) for participants who were indicated to be decided ($n = 96$) or undecided ($n = 33$) at time 1. The figure shows standardized beta values of simultaneous multiple regression analyses (* $P < 0.05$; *** $P < 0.001$; ns, not significant).

nonsignificant, relation to future choices [$t(30) = 1.69$, $P = 0.10$] (*19*). Taken together, these results suggest that (i) conscious beliefs and future choices of undecided decision-makers are to a significant extent determined by their earlier automatic associations; (ii) such effects occur only for undecided but not for decided decision-makers, whose choices are primarily based on earlier consciously held beliefs; and (iii) conscious beliefs of decided decision-makers influence their future automatic associations, such that these associations tend to become in line with consciously held beliefs over time.

These findings have important implications for social sciences that aim at predicting future choice decisions of public interest, one of the most intriguing examples being the prediction of voting decisions. Over the past decades, political scientists have been quite successful in predicting election outcomes by means of standard survey methodology. Yet, there have been repeated cases in which tight races between political candidates made the prediction of election outcomes rather difficult. Indeed, there have been several examples in which voters were indicated to be undecided until the day of the election. The present results suggest that in such cases, the prediction of election outcomes could be enhanced by including modern measures of automatic associations, such as the one used in the present study (*14*) or similar measures that have been developed by social psychologists in the past decade (*20*–*22*). Even though our longitudinal design did not include a direct measure of biased information processing, earlier research suggests that automatic associations can bias the processing of new information in a manner that is consistent with these associations (*9*, *10*). To the extent that information about choice options is often mixed and heterogeneous, biased processing of that information can bring future choices of undecided individuals in line with their already existing automatic associations. Thus, one could say that people sometimes have already made up their mind, even though they do not know it yet.

References and Notes

1. I. Ajzen, *Organ. Behav. Hum. Decis. Process.* **50**, 179 (1991).
2. P. M. Gollwitzer, *Am. Psychol.* **54**, 493 (1999).
3. F. Strack, R. Deutsch, *Pers. Soc. Psychol. Rev.* **8**, 220 (2004).
4. J. A. Bargh, in *Handbook of Social Cognition*, R. S. Wyer, T. K. Srull, Eds. (Erlbaum, Hillsdale, NJ, 1994), pp. 1–40.
5. B. Gawronski, G. V. Bodenhausen, *Psychol. Bull.* **132**, 692 (2006).
6. R. H. Fazio, M. A. Olson, *Annu. Rev. Psychol.* **54**, 297 (2003).
7. B. Wittenbrink, N. Schwarz, *Implicit Measures of Attitudes* (Guilford, New York, 2007).
8. L. Arcuri, L. Castelli, S. Galdi, C. Zogmaister, A. Amadori, *Polit. Psychol.* **29**, 369 (2008).
9. B. Gawronski, D. Geschke, R. Banse, *Eur. J. Soc. Psychol.* **33**, 573 (2003).
10. K. Hugenberg, G. V. Bodenhausen, *Psychol. Sci.* **14**, 640 (2003).
11. B. Gawronski, W. Hofmann, C. J. Wilbur, *Conscious. Cogn.* **15**, 485 (2006).
12. W. Hofmann, B. Gawronski, T. Gschwendner, H. Le, M. Schmitt, *Pers. Soc. Psychol. Bull.* **31**, 1369 (2005).
13. W. Hofmann, T. Gschwendner, B. A. Nosek, M. Schmitt, *Eur. Rev. Soc. Psychol.* **16**, 335 (2005).
14. A. Karpinski, R. B. Steinman, *J. Pers. Soc. Psychol.* **91**, 16 (2006).
15. A. G. Greenwald, B. A. Nosek, M. R. Banaji, *J. Pers. Soc. Psychol.* **85**, 197 (2003).
16. At time 1, 96 participants were decided (32 in favor, 64 against) and 33 participants were undecided. At time 2, 9 of the formerly undecided participants were in favor of the enlargement, 14 were still undecided, and 10 were against the enlargement. Even though no reminder of the responses at time 1 was given, all of the 96 decided participants indicated the same decision at time 1 and time 2.
17. The relevant requirements for an application of the employed statistical procedures were met.
18. Multiple regression moderator analyses that included decidedness as a dummy-coded moderator revealed that the impact of automatic associations at time 1 on conscious beliefs at time 2 was significantly moderated by decidedness [$t(123) = 3.43$, $P = 0.001$]; the moderating effect of decidedness on the impact of conscious beliefs at time 1 on automatic associations at time 2 failed to reach the conventional level of statistical significance [$t(123) = 1.64$, $P = 0.10$].
19. Multiple regression moderator analyses that included decidedness as a dummy-coded moderator revealed that the impact of automatic associations at time 1 on future choices at time 2 was significantly moderated by decidedness [$t(123) = 3.06$, $P = 0.003$]; the impact of conscious beliefs at time 1 on future choices at time 2 was not significantly moderated by decidedness [$t(123) = 0.83$, $P = 0.41$].
20. R. H. Fazio, J. R. Jackson, B. C. Dunton, C. J. Williams, *J. Pers. Soc. Psychol.* **69**, 1013 (1995).
21. A. G. Greenwald, D. E. McGhee, J. K. L. Schwartz, *J. Pers. Soc. Psychol.* **74**, 1464 (1998).
22. B. K. Payne, S. M. Cheng, O. Govorun, B. D. Stewart, *J. Pers. Soc. Psychol.* **89**, 277 (2005).

23. This research was supported by grants from the Department of Developmental Psychology and Socialization of the University of Padova, the Canada Research Chairs Program (202555), and the Social Sciences and Humanities Research Council of Canada (410-2005-1339). We thank G. Bodenhausen and K. Trzesniewski for helpful comments on an earlier version of this article.

Supporting Online Material

www.sciencemag.org/cgi/content/full/321/5892/1100/DC1
Methods
Appendices S1 to S4
References

21 May 2008; accepted 2 July 2008
10.1126/science.1160769

Nucleic Acid Standard

DNACON260/280 is a durable standard reference material that exhibits spectral characteristics similar to those of pure DNA for quick and reliable quality control of the DNA 260/280 nm measurement process. The material is designed to assure the wavelength accuracy in critical nucleic acid measurements. Suffering from none of the stability problems associated with DNA, it was created for use as a reliable National Institute of Standards and Technology traceable quality control standard by clinical and bioscience laboratories analyzing and evaluating the purity of a range of nucleic acids.
Starna Scientific
For information +44-(0)-20-8501-5550
www.starna.com

Microplate Thermoshakers

The Jitterbug 2 and Jitterbug 4 Benchtop Microplate Thermoshakers are available in two-plate and four-plate models. The three-in-one instruments can be used as a microplate thermoshaker, as a shaker without incubating, and as an incubator without shaking. Variable speed and temperature controls can be programmed to meet precise sample processing requirements. A programmable timer displays elapsed time and automatically sounds an alarm when the process is complete and the unit turns off. The Jitterbug thermoshakers are compact with a low profile and small footprint. The shaking function features a soft start that reduces splashing and spillage. A low-voltage power supply enables safe operation in a cold room or incubator.
Boekel Scientific
For information 800-336-6929
www.boekelsci.com

Compact Automated Workstation

The BenchCel R Platform is the heart of a fast and compact automation workstation that can handle applications ranging from simple microplate processing tasks to sophisticated applications such as polymerase chain reaction preparation that previously required high-priced, full-size systems. It handles a variety of integrations, rack styles, types of labware, and capacity options. Features include the flexibility to work with lidded microplates, deep-well plates, and tip boxes and a choice of two-rack, four-rack, and six-rack configurations. The platform is an integrated benchtop robot and microplate storage system that features a unique high-speed plate shuttle that accesses integrated microplate stacks and peripheral microplate-based instruments including liquid handlers, dispensers, readers, sealers, washers, centrifuges, microplate storage devices, and more.
Velocity11
For information 650-846-6600
www.velocity11.com

Nanosphere Conjugates

The Kodak X-Sight Nanosphere Conjugates labeled with Streptavidin provide an effective means for life science researchers to detect biotinylated probes in fluorescent molecular biology research applications. These streptavidin conjugates are fully biocompatible and suitable for both in vivo and in vitro applications, providing outstanding photostability and brightness. Offered in four wavelengths from ultraviolet to near infrared, they provide a robust platform for translating molecular imaging experiments from in vitro to in vivo applications. The Kodak X-Sight imaging agent family also includes Kodak X-Sight Nanospheres and Large Stokes Shift Dyes, which are also offered in a variety of conjugated forms. Although they have been optimized for Kodak In-Vivo Imaging Systems and Kodak Image Systems, they are compatible with other commercially available digital imaging systems.
Carestream Health
For information 585-781-5364
www.carestreamhealth.com

Gel Documentation System

Red is a plug-and-play gel documentation system that features a touch-screen panel to control all aspects of imaging, from lighting control to image capture. It includes a computer with embedded Windows XP. Its scientific-grade sensor and innovative optical design provide the flexibility critical to imaging a wide variety of flourescent one-dimensional gels. Images can be saved to a memory stick or printed directly using any USB-compatible printer.
Alpha Innotech
For information 510-904-5647
www.redimager.com

Gel Scalpels

Target bands can be excised without scratching the expensive screen of an ultraviolet transilluminator by using nuclease-free Gel Scalpels. These polystyrene plastic scalpels have a thin, blade-like end that accurately cuts through gels and a spatula end that lifts and transfers agarose gel bands effortlessly. They are manufactured in a nuclease-free process and packaged in nuclease-free plastic bags.
Bel-Art Products
For information 800-423-5278
www.belart.com

Vacuum Concentrator

The Vacufuge plus is for concentration, drying, and purification of DNA, RNA, nucleotides, and proteins. This vacuum concentrator provides fast evaporation, worry-free concentration, and no sample loss. The Vacufuge plus features a new liquid crystal display with a user-friendly control panel that offers intuitive operation. The device reduces evaporation times by allowing for solvent preselection as well as four heating levels. It offers 13 fixed-angle rotors for vessels of various sizes and capacities.
Eppendorf
For information 800-645-3050
www.eppendorfna.com

Electronically submit your new product description or product literature information! Go to **www.sciencemag.org/products/newproducts.dtl** for more information.

Newly offered instrumentation, apparatus, and laboratory materials of interest to researchers in all disciplines in academic, industrial, and governmental organizations are featured in this space. Emphasis is given to purpose, chief characteristics, and availabilty of products and materials. Endorsement by *Science* or AAAS of any products or materials mentioned is not implied. Additional information may be obtained from the manufacturer or supplier.

POSITIONS OPEN

ASSISTANT PROFESSOR
Amherst College
Biochemistry or Bio-Organic Chemistry

The Amherst College Department of Chemistry (**website: https://cms.amherst.edu/academiclife/departments/chemistry**) invites applications for a full-time tenure-track Assistant Professorship in biochemistry or bio-organic chemistry beginning in July 2009. The position requires a Ph.D. and calls for teaching chemistry at the introductory and advanced undergraduate levels. Opportunities for teaching in interdisciplinary courses and programs are also available. The successful candidate will be expected to establish a vigorous research program in which undergraduates can substantively participate. The research program can span the boundaries between biochemistry and other sciences.

Applicants should submit curriculum vitae, undergraduate and graduate transcripts, a statement of teaching philosophy, and a detailed description of their research plans, and should arrange for the forwarding of three letters of reference, all to: **Prof. Mark D. Marshall, Chair, Department of Chemistry, Amherst College, P.O. Box 5000, Amherst, MA 01002-5000.** Review of materials will begin October 13, 2008, and will continue until the position is filled.

Amherst College is a private undergraduate liberal arts college for men and women, with 1,600 students and 200 faculty members. Located in the Connecticut River Valley of western Massachusetts, Amherst participates with Hampshire, Mount Holyoke, and Smith Colleges and the University of Massachusetts in the Five-College Consortium.

Amherst College has taken a leadership role among highly selective liberal arts colleges and universities in successfully diversifying the racial, socioeconomic, and geographic profile of its student body. The College now aims to enrich the diversity of its faculty, administration, and staff to ensure that full participation and inclusion become desired norms across the culture of the Institution. Amherst aspires to become a learning community in which everyone, not just those individuals whom we identify with minority cultures or perspectives, is informed about and responsive to all aspects of diversity. The administration, faculty, and student body are committed to attracting qualified candidates from groups currently underrepresented on our campus. *Amherst College is an Equal Opportunity Affirmative Action Employer and encourages women, persons of color, and persons with disabilities to apply.*

MOLECULAR NEUROBIOLOGIST

The Department of Biology and the Neuroscience Program at Amherst College invite applications for a tenure-track position at the **ASSISTANT PROFESSOR** level in molecular neurobiology. The research program of the successful candidate will be one that can involve undergraduate biology and neuroscience majors. Teaching duties include development of a laboratory course in molecular neurobiology, rotation in team-taught introductory biology and neuroscience courses, and teaching other courses in the candidate's area. A completed Ph.D. is required, and postdoctoral experience is expected. Send curriculum vitae and statements of research and teaching interests to: **Neurobiology Search Committee, Department of Biology, Amherst College, P.O. Box 5000, Amherst, MA 01002-5000.** Electronic submissions will not be accepted. Have three letters of recommendation sent separately. Review of applications will begin October 15, 2008, and continue until the position has been filled.

Amherst is a private undergraduate liberal arts college for men and women, with 1,600 students and a teaching faculty of 200. Located in the Connecticut River Valley of western Massachusetts, Amherst participates with Hampshire, Mount Holyoke, and Smith Colleges and the University of Massachusetts in the Five College Consortium. More information about the College can be found at **website: http://www.amherst.edu.** Amherst College aims to enrich the diversity of its faculty, administration, and staff to ensure that full participation and inclusion become desired norms across the culture of the Institution.

POSITIONS OPEN

華中科技大學
Huazhong University of Science and Technology

FULL-TIME PROFESSOR POSITIONS

The College of Life Science and Technology at Huazhong University of Science and Technology is seeking qualified candidates to fill 20 positions at the Professor level in biophysics and molecular physiology, molecular genetics and developmental biology, biochemistry, molecular and cellular biology, biomedical engineering, bioinformatics and system biology, and chemical biology and nanomedicine. Candidates must hold a Ph.D. or M.D., and have publications in high profile journals. The University will offer a generous startup package, competitive salaries, and benefits and housing. Interested candidates should submit curriculum vitae, statements of research interests and accomplishments, and the names and contact information of two to five references to **e-mail: qkwang@mail.hust.edu.cn,** or **e-mail: zhsqe@mail.hust.edu.cn.**

FACULTY POSITIONS in CHEMICAL ENGINEERING
Princeton University

The Department of Chemical Engineering seeks outstanding applicants for tenure-track positions at the **ASSISTANT PROFESSOR** level, effective as early as July 1, 2009. The search is open to candidates in any area of chemical engineering, including those specializing in energy and sustainability, and in bioengineering. The successful candidates should have a Ph.D. in chemical engineering or related field, demonstrated excellence in academic research, and a strong commitment to teaching and advising undergraduate and graduate students. Candidates must complete a required online faculty application at **website: https://jobs.princeton.edu;** curriculum vitae, detailed descriptions of teaching and research interests, reprints of selected publications, and the names and addresses of at least three references may be attached as PDF documents to the online application, or sent to: **Faculty Search Committee, Department of Chemical Engineering, Princeton University, Princeton, NJ 08544-5263.** Applicants are encouraged to apply before December 1, 2008. For additional information on applying for positions at Princeton University, please link to **website: http://www.princeton.edu/dof/about_us/dof_job_openings/.** *Princeton University is an Equal Opportunity Employer and complies with applicable Equal Employment Opportunity and Affirmative Action regulations.*

The Department of Biology at Western Kentucky University (WKU) invites applications and nominations for the position of **HEAD of the DEPARTMENT of BIOLOGY.** The successful candidate will provide visionary leadership for an active, collegial department with an established record of excellence in undergraduate education, a growing graduate program, and an active, multidisciplinary, international research program. Interested applicants should submit a letter of interest, a current resume, a statement of philosophy and priorities for teaching, research and departmental leadership, and the names and contact information for five references. Deadline for receipt of application materials is October 1, 2008. Potential applicants may view the full position description and learn more about the WKU Department of Biology at **website: http://bioweb.wku.edu/headsearch2008/.** Submit applications and nominations to:

Biology Department Head Search
Western Kentucky University
1906 College Heights Boulevard #11080
Bowling Green, KY 42101-1080

Review of applications will begin on October 10, 2008, and will continue until the position is filled. *All qualified individuals are encouraged to apply including women, minorities, persons with disabilities, and disabled veterans. Western Kentucky University is an Affirmative Action/Equal Opportunity Employer.*

POSITIONS OPEN

DIRECTOR
The National Study Center for Trauma and Emergency Medical Services: An Organized Research Center in Trauma and Anesthesiology

The University of Maryland School of Medicine (UMSOM) is seeking qualified applicants for the position of Director of the National Study Center for Trauma and Emergency Medical Services (EMS), a newly formed Trauma and Anesthesiology Organized Research Center (ORC) dedicated to injury prevention and care. The ORC's charter is to perform basic translational and clinical research focused on injury. It is anticipated that the successful candidate will have research interests in one or more of the ORC's signature programs. Related areas of expertise are also welcome.

This ORC will encompass current research efforts from the Shock Trauma Center, the National Study Center and the UMSOM Department of Anesthesiology. The R. Adams Cowley Shock Trauma Center is a world class clinical, multidisciplinary research and educational center in injury and critical illness. The Department of Anesthesiology has a long history of excellence and funding in neuroprotection. The current National Study Center has extensive expertise with epidemiologic research and managing large databases. The current portfolio of the ORC is $22 million; it is expected that funding will grow substantially over the next few years. An endowed **CHAIR in TRAUMA RESEARCH** exists for the successful candidate, who will report directly to the Dean, UMSOM.

Minimal requirements include an M.D., Ph.D., or M.D./Ph.D. with a minimum of at least five years of experience at the level of Associate Professor or above. A record of sustained accomplishments and evidence of leadership in his/her field, relevant administrative experience and evidence of effective interpersonal, and collaborative and communication skills are also required. The successful candidate is expected to have a distinguished record of scholarly activity, a history of extramural funding, and the ability to build an interdisciplinary program and experience with successfully teaching/mentoring medical and graduate students.

Interested applicants should send or e-mail a letter of inquiry and curriculum vitae to:

Thomas M. Scalea, M.D., FACS, FCCM
Physician-in-Chief
R. Adams Cowley Shock Trauma Center
Francis X. Kelly Professor of Trauma Surgery
22 South Greene Street, Third Floor
Baltimore, MD 21201
E-mail: tscalea@umm.edu

The University of Maryland, Baltimore is an Affirmative Action/Equal Employment Opportunity/ADA Employer, and has a strong institutional commitment to the principle of diversity in all areas.

ECOLOGICAL/EVOLUTIONARY THEORIST

The Department of Ecology, Evolution, and Organismal Biology (EEOB) at Iowa State University seeks a tenure-track **ASSISTANT PROFESSOR** developing theory relevant to evolutionary and/or ecological processes. EEOB **(website: http://www.eeob.iastate.edu)** comprises 30 faculty who use integrative approaches that bridge disciplines and span multiple levels of biological organization. The successful candidate is expected to develop a nationally recognized research program and skillfully teach undergraduate and graduate students. Applicants should have a Ph.D. in ecology, evolution, or related field and demonstrate excellent research and teaching potential. Following the instructions on **website: http://www.iastatejobs.com,** submit cover letter, curriculum vitae, and research and teaching statements, plus up to three reprints as PDF files, each not to exceed 1MB, by 1 October 2008 (see **website: http://www.eeob.iastate.edu/search.html** for additional information). In addition, arrange to have three letters of recommendation sent by e-mail as PDF files to **e-mail: searches@iastate.edu.** For further information, contact **e-mail: brent@iastate.edu.** *ISU values diversity and is an Affirmative Action/Equal Employment Opportunity Employer with National Science Foundation ADVANCE funding to enhance the success of women faculty in science and engineering.*

POSITIONS OPEN

California State University Northridge

ASSISTANT PROFESSOR, MOLECULAR BIOLOGY/BIOTECHNOLOGY
Department of Biology
Annual Salary: Up to $70,000

California State University, Northridge invites applications for a tenure-track Assistant Professor of Biology in Molecular Biology/Biotechnology to begin August 2009. Candidates must hold a Ph.D. in the biological sciences and have postdoctoral experience. The successful candidate is expected to develop a vigorous research program involving undergraduate and graduate (M.S.) students, seek extramural research funding, demonstrate teaching excellence, and provide effective instruction to students of diverse backgrounds in a multicultural setting. Teaching may include biotechnology, recombinant DNA techniques, graduate seminars, specialty, or introductory biology courses.

Applicants should submit a letter of application, curriculum vitae, statements of teaching philosophy and research interests, three representative publications, and arrange for three letters of recommendation to be sent to **e-mail: biology.dept@csun.edu (Attn.: Chair of Search and Screen Committee)** or to mailing address: **Chair of Search and Screen Committee, Department of Biology, California State University, 18111 Nordhoff Street, Northridge, CA 91330-8303.**

Application deadline: Screening will begin on October 1, 2008. Priority will be given to applications received by October 15, 2008, and remain open until filled.

California State University is an Equal Opportunity Affirmative Action Employer and does not discriminate on the basis or race, religion, national origin, sexual orientation, gender, marital status, age, disability, disabled veteran, or Vietnam-era veteran status.

MICROBIOLOGIST. The Biology Department of Franklin and Marshall College invites applications for a tenure-track **ASSISTANT PROFESSOR** position in microbiology, beginning fall 2009. Candidates should have the Ph.D. and demonstrated strengths in teaching and research.

The teaching load is 3/2. Teaching responsibilities include: lecture and laboratory sections of a sophomore-level core course in cell biology, a laboratory elective in microbiology, a seminar elective in the candidate's area of expertise, and participation in the general education curriculum. In addition to the biology major, we offer interdisciplinary majors in neuroscience and animal behavior, biochemistry and molecular biology, and environmental studies/science.

Franklin and Marshall has a tradition of excellence in science and student research. A new life sciences building opened in 2007. In 2008, the Howard Hughes Medical Institute awarded the College a substantial grant to launch a bioinformatics program.

Please send a letter of application, a statement that explains plans for actively engaging undergraduates through teaching and research and explains goals for developing as a teacher and scholar, curriculum vitae, teaching evaluations, and undergraduate and graduate transcripts to: **Prof. Peter Fields, Department of Biology, Franklin and Marshall College, P.O. Box 3003, Lancaster, PA 17604-3003.** Applicants should also have three reference letters sent directly to **Prof. Fields.** Priority will be given to completed applications received by October 1, 2008. Electronic submissions cannot be accepted. **Telephone: 717-291-4118; fax: 717-358-4548; e-mail: janice.kaufman@fandm.edu; website: http://www.fandm.edu/biology.xml.**

Franklin and Marshall College is a highly selective liberal arts college with a demonstrated commitment to cultural pluralism. *Equal Opportunity Employer.*

POSITIONS OPEN

MICROBIOLOGIST

Goucher College's Department of Biological Sciences has a tenure-track opening at the **ASSISTANT PROFESSOR** level for a broadly trained Microbiologist beginning fall 2009. Expertise in environmental microbiology preferred. Candidates must possess a Ph.D. and a commitment to teaching and research at a liberal arts college. Postdoctoral work and teaching experience are preferred. Responsibilities include teaching intermediate or advanced courses in microbiology, participation in the introductory courses for majors and/or nonmajors, and developing a research program that includes undergraduates. The College's strategic plan emphasizes environmental sustainability and international and intercultural experiences, which creates opportunities for faculty to participate in developing an Environmental Studies Program and major, as well as an opportunity to develop courses with an international focus. Applicants should send curriculum vitae, summary of teaching philosophy, research interests, transcripts, and three letters of recommendation to: **Human Resources, Goucher College, 1021 Dulaney Valley Road, Baltimore, MD 21204-2794.** Application deadline is November 1, 2008. *The successful candidate will be subject to a background check as a condition of employment.* Goucher College is committed to increasing the diversity of the campus community and encourages applicants that will fulfill that mission.

Goucher College is an Equal Opportunity Employer.

FACULTY POSITION

The Department of Genetics and Development at Columbia University Medical Center is expanding its faculty and seeks outstanding applicants with the ability to develop an independent research program for a tenure-track position at the **ASSISTANT PROFESSOR** level. In special circumstances, applicants at other levels will also be considered. Applicant's research program should use molecular genetic approaches to study, in any model organism, any question relevant to vertebrate physiology and to the molecular and genetic bases of human degenerative diseases. Our Department spans a broad range of interests including developmental biology, physiology, DNA repair and recombination, cancer, and human genetics. Applicants should include curriculum vitae and a summary of current and proposed research programs, and arrange for three letters of reference to be sent. Completed applications should be submitted as one single document. Applications and letters of reference should be sent electronically to **Developmental Biology Search, Attn.: Celia Morales, e-mail: cr2020@columbia.edu.** Consideration for completed applications will begin October 1, 2008.

Columbia University is an Equal Opportunity/Affirmative Action Employer. Women and minorities are encouraged to apply.

UNIVERSITY of ROCHESTER. The Department of Chemistry invites applications in all areas of chemistry at the **ASSISTANT PROFESSOR** level. Candidates are expected to establish an outstanding program of original research, and be effective teachers at the graduate and undergraduate levels. Applicants should send curriculum vitae indicating Ph.D. and postdoctoral advisors, and a statement of research plans, teaching interests; and arrange for three letters of recommendation to be sent to **Ms. Karen Dean** (preferably in electronic form) at **e-mail: dean@chem.rochester.edu;** or by mail to: **Chemistry Faculty Search Committee, c/o Ms. Karen Dean, Department of Chemistry, University of Rochester, RC Box 270216, Rochester, NY 14627-0216.** Review of completed applications will begin on October 1, 2008. *The University of Rochester, an Equal Opportunity Employer, has a strong commitment to diversity and actively encourages applications from candidates from groups underrepresented in higher education.*

POSITIONS OPEN

FACULTY POSITION in IMMUNOLOGY
Department of Microbiology and Immunology
University of Western Ontario

The Department of Microbiology and Immunology invites applications for a probationary (tenure-track) faculty position at the level of **ASSISTANT or ASSOCIATE PROFESSOR** in immunology.

The successful candidate will hold a Ph.D., M.D., D.D.S., or equivalent degree and is expected to establish an independent, externally funded research program, collaborate with other faculty members at the University and its affiliated institutes, and to participate in the teaching programs of the Department at the undergraduate and graduate levels. Special emphasis will be given to individuals using molecular and cellular approaches to study in vivo adaptive and/or innate immune responses, including those using infection models. The Department of Microbiology and Immunology is home to one of the worldwide Federation of Clinical Immunology Societies Centers of Excellence, has strong research programs in the area of infection and immunity, including autoimmunity, tumour immunology, transplantation, viral immunology, innate immunity and molecular and cellular microbiology, as well as state-of-the-art core facilities in genomics, proteomics, flow cytometry, cellular and molecular imaging, and animal care.

Please send detailed curriculum vitae, a brief description of research accomplishments and future plans, copies of representative publications, and the names of three references to:

Miguel A. Valvano, Chair
Department of Microbiology and Immunology
Room 3014, Dental Sciences Building
The University of Western Ontario
London, Ontario, Canada
N6A 5C1

Applications will be accepted until the position is filled. Review of applications will begin after December 1, 2008.

These positions are subject to budget approval. Applicants should have fluent written and oral communication skills in English. All qualified candidates are encouraged to apply; however, *Canadian citizens and permanent residents will be given priority. The University of Western Ontario is committed to employment equity and welcomes applications from all qualified women and men, including visible minorities, aboriginal people and persons with disabilities.*

FACULTY POSITION
Department of Anatomy
University of California, San Francisco

The Department of Anatomy at the University of California, San Francisco (UCSF) invites applications for a full-time academic appointment in the Adjunct Professorial series (nontenure track). The successful applicant will have experience in the direction of complex human anatomy curricula and documented excellence in the teaching of human anatomy and neuroanatomy. The position will include responsibilities as **FACULTY DIRECTOR** of the Willed Body Program and administrative oversight of the human anatomy laboratory. A Ph.D or M.D. or equivalent doctoral-level degree is required. Research experience (including a record of publications) that will bring a scientific perspective to the teaching is highly desirable. UCSF seeks candidates whose experience, teaching, research, or community service has prepared them to contribute to our commitment to diversity and excellence.

Please send written applications, prior to September 30, 2008, including curriculum vitae and three letters of reference, to:

Human Anatomy Search Committee
Department of Anatomy
University of California San Francisco
513 Parnassus Avenue, P.O. Box 0452
San Francisco, CA 94143-0452

UCSF is an Affirmative Action/Equal Opportunity Employer. All qualified applicants are encouraged to apply, including minorities and women.

AWARDS

The Debiopharm Life Sciences Award 2008 goes to Dr Manel Esteller !

On August 21, 2008, Dr. Manel Esteller* from the Spanish National Cancer Center (CNIO) in Madrid, Spain, received the Debiopharm Life Sciences Award for his outstanding research in fundamental and translational oncology.

Dr. Esteller's work focuses on the epigenetics of cancer, a field that has been receiving growing attention from the international biomedical research community, and to which he has contributed major advances. Over the past 10 years of his still young career, Dr. Esteller has received numerous awards and his articles, published in the highest profile journals including Nature, Science, New England Journal of Medicine, EMBO Journal or PNAS, have generated considerable impact.

The Award ceremony, which took place at the Ecole Polytechnique Fédérale de Lausanne (EPFL) in Switzerland, during the EPFL Life Science Symposium 2008, was funded by Debiopharm S.A. and organised by the EPFL. With this nomination, Dr. Esteller and his laboratory received CHF 100'000, a certificate and an etched crystal tribute commemorating this honour.

The objective of the Debiopharm Life Sciences Award is to mentor and motivate young innovative European researchers in the field of life sciences, with a focus this year on oncology. Potential candidates for the Award are required to be under the age of 40, with research having therapeutic and industrial potential. Selection criteria include novelty and originality of the work, as well as its importance and significance in connection with targeted therapeutic fields.

The topic for the Debiopharm Life Sciences Award 2009 is Biology and Immunology of Infection

EPFL ÉCOLE POLYTECHNIQUE FÉDÉRALE DE LAUSANNE

DEBIOPHARM LIFE SCIENCES AWARD

* Dr Esteller is Head of the Cancer Epigenetics Laboratory at CNIO in Madrid, Spain

POSITIONS OPEN

FACULTY POSITION
Columbia University
Department of Chemical Engineering

The Department of Chemical Engineering announces a faculty position to be filled at the rank of **ASSISTANT or ASSOCIATE PROFESSOR.** The Department seeks outstanding individuals with the motivation to excel in research, teaching, and service. Candidates at the Associate level should have a record of continued strong leadership in research. A Doctorate in chemical engineering or a related field is required. Department research is in biological, soft materials, electrochemical, or environmental engineering, and candidates who complement current departmental research will be given the highest priority. Columbia University offers an attractive, highly intellectual, and collaborative environment. Assistance with faculty housing is available. Starting date is July 1, 2009. Candidates should submit a brief research plan, a statement of teaching objectives that demonstrates a commitment to chemical engineering education, the names and contact information of three references, curriculum vitae, and reprints of recent key research publications. Send curriculum vitae and materials in a single PDF file to **e-mail: facultyposition@cheme.columbia.edu.**

This search will close on November 30, 2008.

Columbia University is an Affirmative Action/Equal Opportunity Employer. We encourage women and minorities to apply.

An immediate **POSTDOCTORAL FELLOW POSITION** is available for a highly motivated individual within the Center for Microbial Pathogenesis at the Research Institute at Nationwide Children's Hospital. The Fellow will help formulate hypotheses, as well as design and execute experiments to further our understanding of the structure, function and role in pathogenesis of the type IV pilus of *H. influenzae*. The Fellow will also prepare abstracts, scientific papers, and presentations. Experience in the following areas is desired: protein purification, protein-protein interaction, molecular biology (DNA and RNA), and immunological assays. This position is funded by a grant from the NIH/National Insititute on Deafness and Other Communications Disorders. The Fellow will be under the mentorship of two established investigators, **Lauren Bakaletz** and **Robert Munson,** working toward the goal of becoming independent in his/her research effort. The Fellow will also be responsible for supervising student trainees and eventually obtaining external research funding. Interested candidates should submit a letter describing experience, curriculum vitae, and three references to **Dr. Robert Munson (e-mail: munson.10@osu.edu).**

Minimum requirements: M.D., Ph.D., or equivalent degree. Desire to pursue a career in biomedical research and knowledge of the research process. Necessary technical skills in the appropriate area of research, good technical writing skills, and good communication skills are required.

ASSISTANT PROFESSOR of NEUROSCIENCE

Oberlin College invites applications for a continuing position in neuropharmacology beginning July 1, 2009. Candidates able to employ a variety of approaches (molecular, physiological, pharmacological, and behavioral) to understanding functional systems and behavior or to understanding disease-related processes are particularly encouraged to apply. Teaching responsibilities include contributions to introductory neuroscience lecture and laboratory courses, upper-level courses for neuroscience majors, and establishing a research program that includes undergraduate research opportunities. The candidate must have a Ph.D. degree in-hand or expected by July 1, 2009. Submit applications including curriculum vitae, three letters of recommendation, and transcripts to: **Dr. Catherine McCormick, Neuroscience Department, Oberlin College, Oberlin, OH 44074** by October 17, 2008. *Affirmative Action/Equal Opportunity Employer.*

POSITIONS OPEN

HIGH-LEVEL CAREER OPPORTUNITIES in EXPOSURE SCIENCE
U.S. Environmental Protection Agency
Office of Research and Development

The Envionmental Protection Agency (EPA)'s Office of Research and Development (ORD) is seeking highly qualified candidates to fill two positions within the National Exposure Research Laboratory (NERL): (1) **DIRECTOR** of the Environmental Sciences Division in Las Vegas, Nevada, (2) **DIRECTOR** of the Human Exposure and Atmospheric Sciences Division in Research Triangle Park, North Carolina.

Directors in both positions will be required to provide critical capabilities and leadership in the area of exposure research. Activities will include planning, developing, organizing, directing, and implementing a highly technical and complex science research and development organization that has a nationwide impact and includes a staff of 70 to 100 employees.

These positions will be filled using EPA's Title 42 Authority, which allows us to hire the highest caliber science leaders through renewable term appointments of up to five years and at annual salaries of up to $200,000 depending upon qualifications, experience, and other factors. Selected applicants will be eligible for full benefits including relocation, health and life insurance, retirement, and vacation and sick leave.

Specific information on the positions and instructions for applying can be found at **website: http://www.epa.gov/nerl/.** Applications must be submitted by October 10, 2008.

The U.S. EPA is an Equal Opportunity Employer.

BIO-ORGANIC CHEMIST. The Williams College Chemistry Department invites application for a tenure-track position at the **ASSISTANT PROFESSOR** level for fall 2009. (Senior appointment possible in exceptional circumstances.) Initial teaching assignment, depending upon the successful candidate's subspecialty, will include two courses from: sophomore-level organic chemistry, enzyme kinetics and reaction mechanisms, biochemistry, and a course for nonscience majors. A semester teaching load normally includes complete responsibility for one course and two laboratory sections, and supervision of student research projects. Candidates should hold a Ph.D. or have completed their dissertation by September 2009 (postdoctoral experience is preferred). The successful candidate must have a strong commitment both to teaching at the undergraduate level and to developing a productive research program. Williams College is a highly selective, coeducational liberal arts institution of approximately 230 faculty and 2,000 undergraduates, located in northwestern Massachusetts. The Chemistry Department is composed of 12 faculty members, and graduates about 25 to 30 majors each year; the Department has excellent facilities for teaching and research. The College is actively working to increase the diversity of its science majors and seeks an individual who can help us meet these goals. Mail resume, undergraduate and graduate transcripts, descriptions of teaching philosophy and research projects for undergraduates, and three letters of recommendation to: **Prof. Enrique Peacock-López, Chair, Department of Chemistry, Williams College, Williamstown, MA 01267,** by October 1, 2008. Electronic applications will not be accepted. For additional information about the Chemistry Department, please visit our **website: http://www.williams.edu/Chemistry.** *Beyond meeting fully its legal obligations for nondiscrimination, Williams College is committed to building a diverse and inclusive community where members from all backgrounds can live, learn, and thrive.*

POSITIONS OPEN

University of Wisconsin, Oshkosh seeks two tenure-track **ASSISTANT PROFESSOR** positions in biology beginning 1 September 2009.

(1) **ANIMAL PHYSIOLOGIST.** Ph.D. required; postdoctoral and teaching experience desirable. Responsibilities: teach animal and human physiology, molecular/cell biology, introductory biology; develop research program in animal physiology; pursue extramural funding; supervise M.S. theses; and advise majors.

(2) **ENVIRONMENTAL HEALTH.** Ph.D. required; postdoctoral and teaching experience desirable. Responsibilities: teach epidemiology, environmental toxicology, topics in environmental health, introductory microbiology; develop introductory biostatistics course; establish research program in environmental health; pursue extramural funding; supervise M.S. theses; and advise majors.

Submit application letter, brief statements of teaching philosophy and research interests, curriculum vitae, reprints, three current letters of recommendation and transcripts (official or photocopy) to: **Chair, Department of Biology and Microbiology, University of Wisconsin Oshkosh, Oshkosh, WI 54901-8640** by 17 October 2008. Employment requires criminal background check. For additional information, see **website: http://www.uwosh.edu/departments/biology/.** *Affirmative Action/Equal Opportunity Employer.*

Additional job postings not featured in this issue can be viewed online at **website: http//www.sciencecareers.org.** New jobs are added daily!

MARKETPLACE